ABSTRACT

Aerodynamic Design Considerations for Small-Scale, Fixed-Pitch, Horizontal-Axis Wind Turbines Operating in Class 2 Winds

Timothy A. Burdett, M.S.M.E.

Mentor: Kenneth W. Van Treuren, D. Phil.

Renewable sources of energy, such as wind, are necessary to meet the growing demand as conventional energy sources are depleted. Very little research has been accomplished to improve wind turbine performance in Class 2 winds. This work experimentally analyzed techniques to improve the aerodynamic performance of small-scale, fixed-pitch, horizontal-axis wind turbines in Class 2 winds. Experimental data for the S823 airfoil was taken for Reynolds numbers from 50,000 to 200,000. A trip strip was shown to improve airfoil performance for Reynolds numbers below 100,000. Additional wind tunnel studies validated the wind turbine testing procedure. Using blade element theory (BET) and blade element momentum theory (BEMT), wind turbine blades with optimum angle of twist were designed and tested. Results suggest the BEMT-optimized blades will perform better at the design point. The sensitivity of the design angle on power production was also examined, resulting in negligible difference for the conditions tested.

Aerodynamic Design Considerations for Small-Scale, Fixed-Pitch, Horizontal-Axis Wind Turbines Operating in Class 2 Winds

by

Timothy A. Burdett, B.S.E.

A Thesis

Approved by the Department of Mechanical Engineering

_____
William Jordan, Ph.D., Chairperson

Submitted to the Graduate Faculty of
Baylor University in Partial Fulfillment of the
Requirements for the Degree
of
Master of Science in Mechanical Engineering

Approved by the Thesis Committee

_____
Kenneth W. Van Treuren, D. Phil., Chairperson

_____
Stephen T. McClain, Ph.D.

_____
Ian A. Gravagne, Ph.D.

Accepted by the Graduate School
May 2012

_____
J. Larry Lyon, Ph.D., Dean

Page bearing signatures is kept on file in the Graduate School.

TABLE OF CONTENTS

LIST OF FIGURES

LIST OF TABLES

NOMENCLATURE

A_c	=	Cross-sectional area
A_{ts}	=	Test section area
AEP	=	Annual energy production
a	=	Axial induction factor
a_{prev}	=	Axial induction factor of previous iteration
a'	=	Tangential induction factor
B	=	Number of blades on wind turbine
BF	=	Blockage factor for wind turbine testing
BR	=	Blockage ratio for wind turbine testing
b	=	Span
c	=	Chord
c	=	Scale parameter used in Weibull probability function
C_D, c_d	=	Coefficient of drag
C_{D_u}	=	Uncorrected coefficient of drag
C_L, c_l	=	Coefficient of lift
C_{L_u}	=	Coefficient of lift
C_M	=	Coefficient of moment
C_P	=	Coefficient of power
C_p	=	Coefficient of pressure
C_{P_u}	=	Uncorrected coefficient of power
C_T	=	Coefficient of thrust

C_{T_r} = Elemental coefficient of thrust at radius r

C_τ = Coefficient of torque

$D, \mathfrak{D}$ = Drag force

D = Diameter

F = Loss factor

F_c = Centrifugal forces

F_{hub} = Hub loss factor

F_{tip} = Tip loss factor

f = Generic function

h_{ts} = Height of test section

I = Current produce by generator

K = Constant used in solid blockage correction factor

K_{vel} = Correction factor for wind tunnel velocity

k = Shape parameter used in Weibull probability function

k_τ = Torque constant

L = Lift force

M = Molecular weight

M = Moment

M_A = Aerodynamic moment

N = Number of elements in turbine blade

N_{cr} = Log of the amplification factor of the most-amplified frequency which triggers transition used in the transition model of XFOIL

P = Power

$P_{D_{wind}}$ = Power density in the wind

P_{rotor} = Power produced by the wind turbine blades

P_{wind} = Power available in the wind

P_W = Average wind turbine power

Pr = Probabilty

p = Freestream static pressure

p^+_d = Pressure just upstream of wind turbine rotor disk

p^-_d = Pressure just downstream of wind turbine rotor disk

p_{loc} = Local static pressure

p_∞ = Freestream pressure

p_S = Static pressure

p_T = Total pressure

Q = Torque

R = Radius of the wind turbine blade

Re, R_N = Reynolds number based on chord

r = Local radius of the wind turbine blade

S = Sutherland constant

S = Planform area

sc = Geometric scaling factor

T = Thrust

T = Temperature

T_0 = Reference temperature

TI = Turbulence intensity

TSR = Tip speed ratio

TSR_u = Uncorrected tip speed ratio

U = Wind velocity

U_d = Velocity at wind turbine actuator disk

U_{rel} = Relative velocity of flow over each blade element

U_u = Uncorrected velocity

U_w = Relative velocity of flow over each blade element

U_∞ = Upstream air velocity

$\bar{u}$ = Mean of the velocity

u' = Standard deviation of the velocity

u_∞ = Velocity at the edge of the boundary layer

V = Voltage

V_m = Volume of wind tunnel model

W = Weight

x = distance in the x direction

x = Mole fraction

z = Height above the surface of the earth

z_r = Reference height above the surface of the earth

Greek

α = Exponent used in power law

α = Angle of attack

$\alpha_{max\ L/D}$ = Angle of attack that maximized the L/D value

α_u	=	Uncorrected angle of attack
β	=	Pitch angle
ε	=	Roughness parameter
ε_b	=	Blockage for airfoil testing in a wind tunnel
ε_{rel}	=	Relative error between iterations
ε_{sb}	=	Solid blockage for airfoil testing in a wind tunnel
ε_{wb}	=	Wake blockage for airfoil testing in a wind tunnel
θ	=	Angle of twist
λ	=	Tip speed ratio
λ_r	=	Local tip speed ratio at radius r
μ	=	Dynamic viscosity
μ_0	=	Reference dynamic viscosity
μ_{mix}	=	Dynamic viscosity of the air and water vapor mixture
ν	=	Kinematic viscosity
ρ	=	Density
σ	=	Streamline blockage for airfoil testing in a wind tunnel
σ_r	=	Elemental wind turbine solidity at radius r
τ	=	Torque generated by turbine rotor
φ	=	Flow angle
Ω	=	Turbine rotor rotational velocity
ω	=	Angular velocity imparted to the wake

ACKNOWLEDGMENTS

First and foremost, I must express my deepest gratitude to Dr. Kenneth Van Treuren for guiding my research and helping me develop both professionally and personally. His invaluable insight into low Reynolds numbers flows has made this work possible, and his vision for developing small-scale wind turbine technology in low wind areas has guided this research from its outset.

I would also like to thank Jason Gregg for the past work he has done in small-scale wind turbine research at Baylor. In his research, he developed the wind turbine test stand, demonstrated the effect of roughness, and began work on airfoil testing. Jason Gregg, along with Andrew Hanks and Josh Kinnaird, installed the meteorological tower used for the wind site survey detailed in this work.

Many other faculty members at Baylor have contributed to this research. Dr. Stephen McClain has provided very meaningful insight in the effect of roughness, as well as contributing LabVIEW® code used in the automation of the experiments. He has also provided the basic foundation for my understanding the computational side of fluid dynamics. Dr. Ian Gravagne has provided vital insight into the electrical components of the testing system. Dr. Lesley Wright has given important guidance about experiment design and data reduction. None of the airfoil testing would have been possible without the help of Ashley Orr in machining the airfoil mounts and helping change out equipment for the experimental tests. I am indebted to Dr. David Jack, from whom I have learned much about numerical modeling and optimization. Without the help of Mr. Dan Hromadka, the experimental testing could not have been completed. Mr. Hromadka

helped troubleshoot and repair the experimental equipment multiple times. Additionally, Max Blose at Waco Hobby Stop donated materials for developing the airfoil surface as well as providing guidance in making the best finish.

I must also thank my fellow students at Baylor who have contributed to my research. Steven Mart developed the basis of a number of LabVIEW® programs and helped me multiple times in developing LabVIEW® code. Brandon Blakely performed flow visualization studies to help us understand the flow over an airfoil at low Reynolds numbers. Evan Martin, Neil Jordan, Lance Case, Jimmy Becker, Cassius Elston, Logan Tecson, and Russell Mailen have helped me set up experiments, complete coursework, and enjoy grad school.

I am also very grateful for the opportunities my parents have given me and the direction they have provided me over the years. I would not be the person I am today with their support and encouragement.

Finally, I must thank my wife for supporting me through this processing and making sure I get enough sleep. She put up with the long hours and encouraged me throughout the entire process.

DEDICATION

To my wife and family

CHAPTER ONE

Introduction

Wind turbine power generation is a growing industry both in the U.S. and around the world. However, the need for renewable energy sources, like wind energy, is debated and even contested by some [1]. By providing the general energy framework into which renewable energy sources and, more specifically, wind turbine technology fits, this chapter serves to explain the motivation for investing time and resources into improving wind turbine technology. In particular, this thesis examines small-scale, fixed-pitch, horizontal-axis wind turbines designed for Class 2 wind and its potential role with distributed generation.

The Energy Challenge

The energy future for both the U.S. and the world is very uncertain because of the increasing energy demand and limited energy resources. The Energy Information Administration (EIA) documents the primary energy consumption for the U.S. by source and sector for 2010 as seen in Figure 1.1 [2]. Notably, 92% of the U.S. energy production comes from non-renewable sources (fossil fuels and nuclear). While renewable energy only contributes a fraction of non-renewable sources, it does contribute to all sectors of energy consumption. In 2009, 93.4% of world consumption was generated by non-renewable resources [3]. These statistics demonstrate how dependent both the U.S. and the world are on finite energy resources.

On a global level, significant increase in energy consumption is expected, especially when considering the demands of the growing economies of India and China

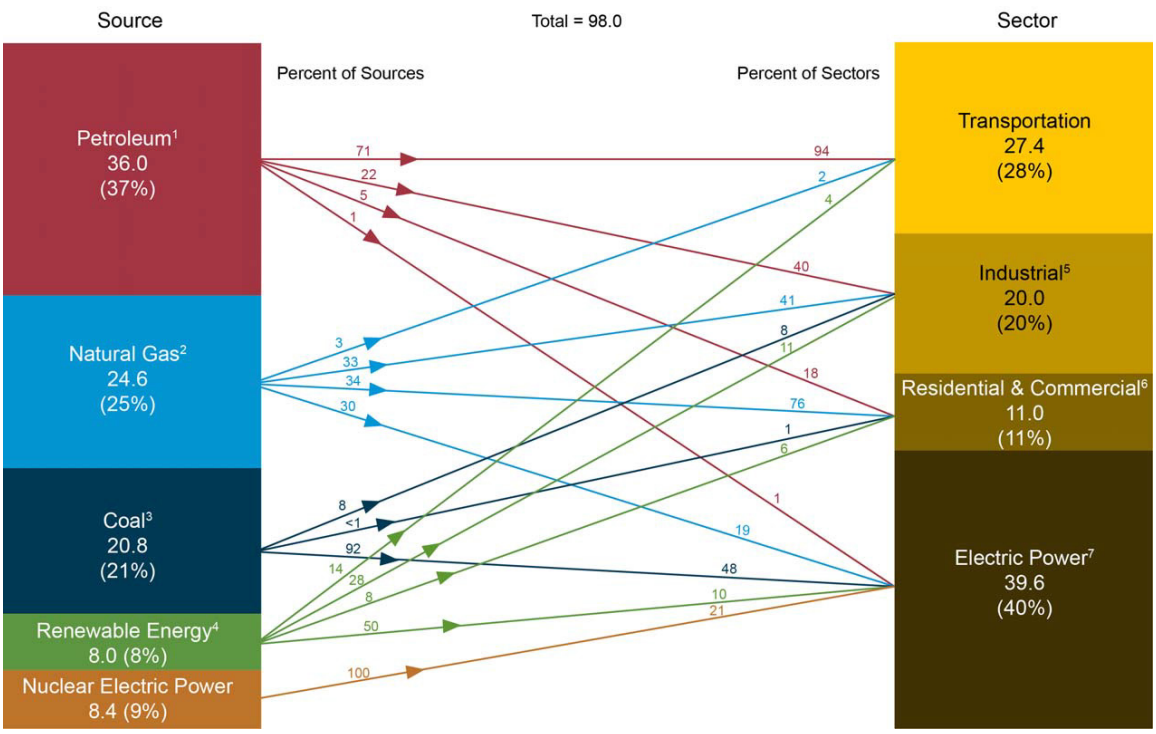

Figure 1.1: Primary Energy Consumption by Source and Sector, 2010 (Quadrillion Btu) [2]

[4, 5], as seen in Figure 1.2. This figure has been developed by the EIA in their prediction of international energy use [5]. Currently, the largest consumer of fossil fuel resources in the world is the U.S., which also consumed nearly three times more oil than it produced in 2009 [3].

Based on published energy data from the EIA, analysts have come to many conclusions on the state of global energy. The Institute for Energy Research (IER) argues that the vast fossil-fuel resources of the U.S. provide such energy security that pursuing "expensive" renewable energy resources is detrimental to the U.S. economy and energy future [1]. However, this analysis is simplistic and not comprehensive. Additionally, it neglects the fact that wind energy is cost-competitive with coal and nuclear for energy production (as will be discussed later), and, thus, not all renewable

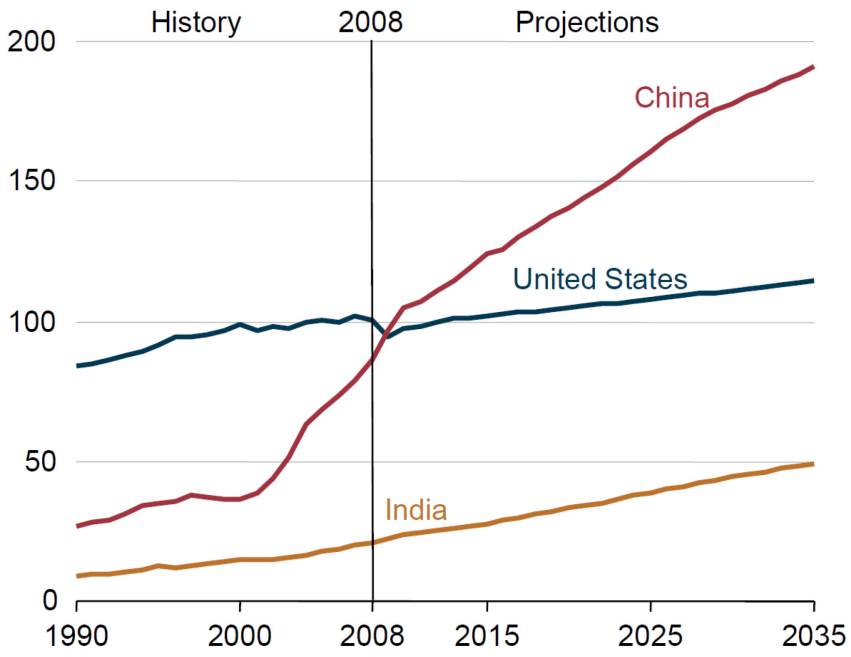

Figure 1.2: U.S., China, and India Energy Consumption, 1990-2035 (Quadrillion Btu) [5]

technologies are "expensive" when compared with tradition fuels. Other analysts, such as Fronk et al., estimate that half of the known world fossil fuels reserves and nuclear sources will be depleted within 45 years and that a major shift to renewable energy must occur in the next 100 years [4]. This analysis, on the other hand, neglects any additional discoveries adding to the current fossil fuel reserves that will likely occur. Such additions can occur simply through the discovery of more resources or through technological advances that allows economic recovery of resources currently thought not recoverable. Because of the uncertainty associated with both the energy demand and the finite resources in the U.S. and the world, it is only logical to invest in energy sources that are both economical and sustainable, such as wind. The EIA, which, in the author's opinion, has a more realistic model of world energy demand and production, projects the world energy consumption by fuel from 2008 to 2035, as seen in Figure 1.3 [5]. Notably, their prediction includes no silver bullet technology; instead all energy sources must

increase production, including renewable resources, and the energy portfolio must be diverse to meet projected energy demand [4, 6].

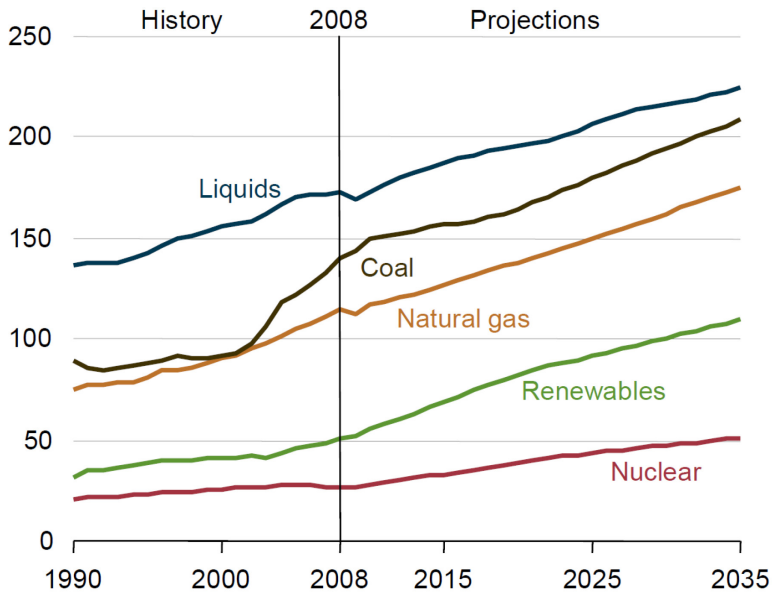

Figure 1.3: World Energy Consumption by Fuel, 1990-2035 (Quadrillion Btu) [5]

In addition to the growing energy needs and limited energy resources, copious amounts of water are used in fuel processing and/or in power generation. The most significant water use is by thermoelectric power plants, which are fueled by coal, natural gas, or nuclear fission. In 2005, 39% of the 349 billion gallons of freshwater withdrawals in the U.S. were used for thermoelectric power generation. Because many areas in the U.S. are facing freshwater limitations, this can result in a higher cost of freshwater, and, thus a higher cost of energy [2, 7]. Notably, wind technology uses a negligible amount of water in its manufacture and power production.

Role of Wind Energy

In 2010, 8% of the energy consumed by the U.S. was generated using renewable energy [2]. Only 11% of that renewable energy was produced from wind. Larger

contributions came from hydroelectric power, wood, and biofuels, as seen in Figure 1.4. In terms of renewable energy used for electricity generation, however, wind was second only to hydroelectric generation and is projected to increase significantly as seen in Figure 1.5 [8]. In fact, wind technology was the fastest growing renewable resource in 2010 [9]. The primary market for wind energy is electric power bought by utilities, although wind energy is also used for residential and commercial electricity as well.

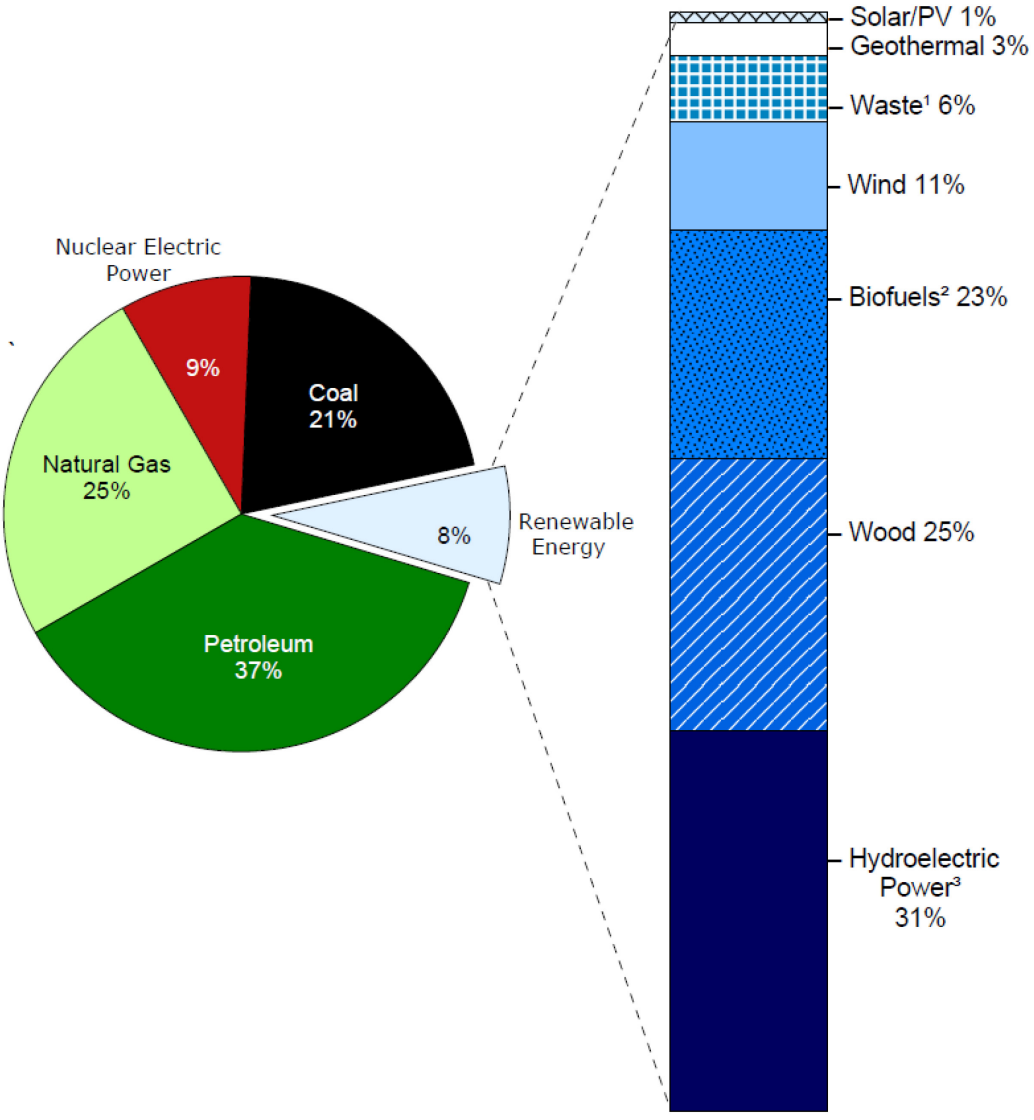

Figure 1.4: U.S. Renewable Energy as Share of Total Primary Energy Consumption by Source, 2010 [2]

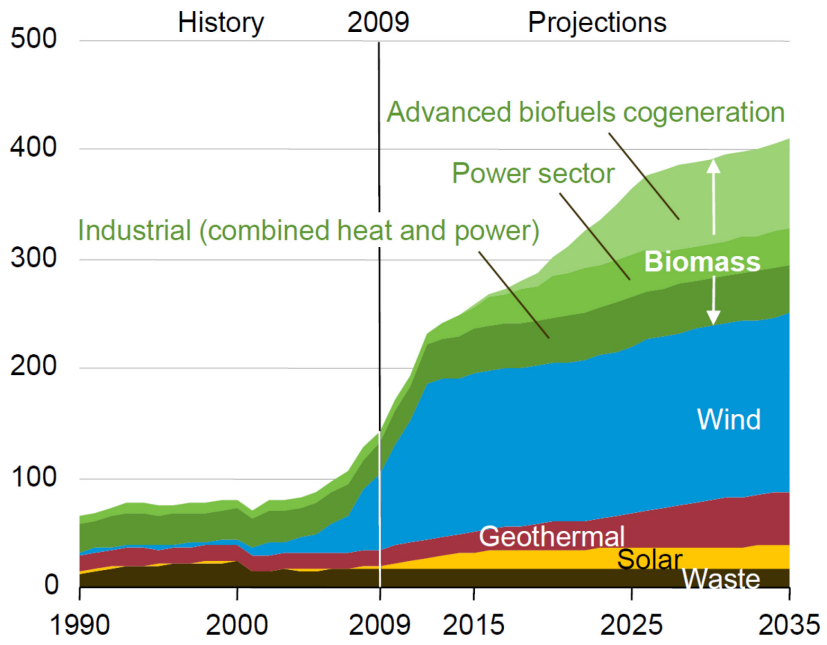

Figure 1.5: U.S. Non-Hydropower Renewable Electricity Generation, 1990-2035 (billion kilowatts per year) [8]

In comparing energy sources, energy cost to the consumer is the bottom line. The standard method of comparison is using the levelized cost of energy (LCOE), which is defined as the price per unit energy that causes the initial investment in the technology to break even. The EIA estimates the current LCOE for new power plants, which "reflects overnight capital cost, fuel cost, fixed and variable [operations and maintenance] cost, financing costs, and an assumed utilization rate for each plant type." Neither state nor federal incentives are included in the LCOE, but a "3-percentage point increase in the cost of capital" is included for fossil-fuel plants without carbon control and sequestration [10]. Because some types of new power plants have long construction lead times and if started today would not be completed until 2016, the LCOE comparison is projected for 2016, as seen in Figure 1.6. While land-based wind is more expensive than natural gas, generally speaking, it is cheaper than nuclear and most types of coal power plants, demonstrating the cost-competitiveness of land-based wind energy.

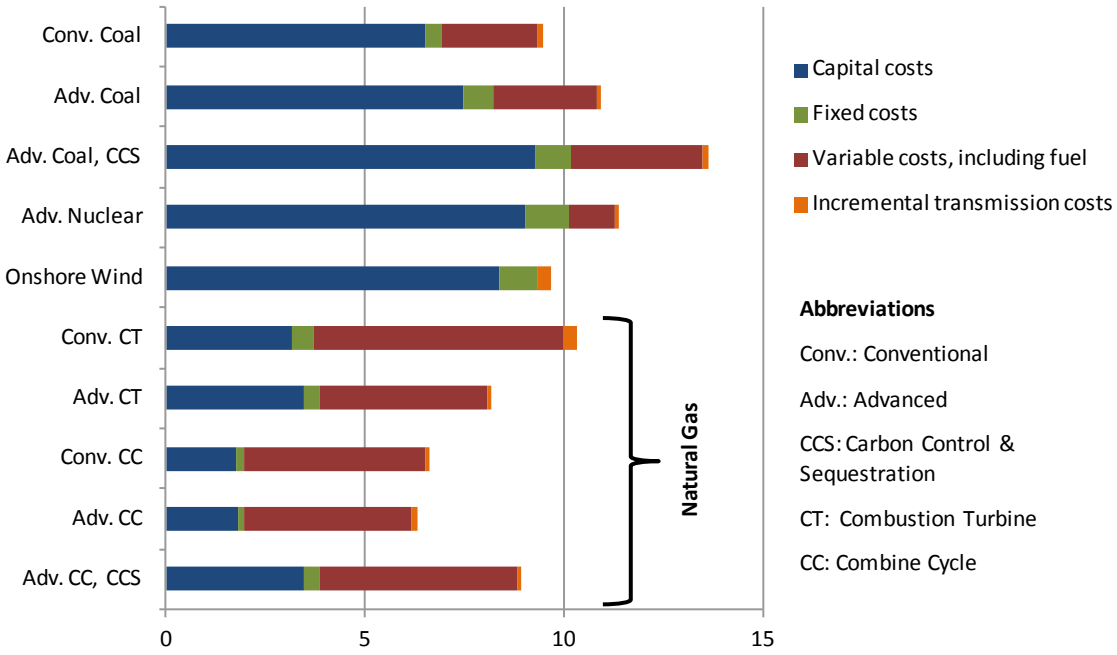

Figure 1.6: LCOE for New Power Plants, 2016 (2009 cents per kWh) [10]

The EIA also projects the LCOE for some types of new power plants in the years of 2020 and 2035, as seen in Figure 1.7. For all these cases, installing new wind turbines is more cost-effective than a new nuclear or coal power plant, again demonstrating the expected cost-effectiveness of wind. These economics are what is driving the expected increase in wind generation seen in Figure 1.5. Many other aspects of wind energy generation add to its attractiveness as an alternative energy source, such as its renewable nature as well as its negligible water use in turbine construction and power generation as previously discussed.

Aspects of Wind Energy Conversion that Affect Cost of Energy

While many wind energy extraction devices exist, most concepts fit into two categories, horizontal-axis or vertical-axis wind turbines (HAWT or VAWT). Generally speaking, HAWTs have the potential to be more efficient. Additionally, they have shown

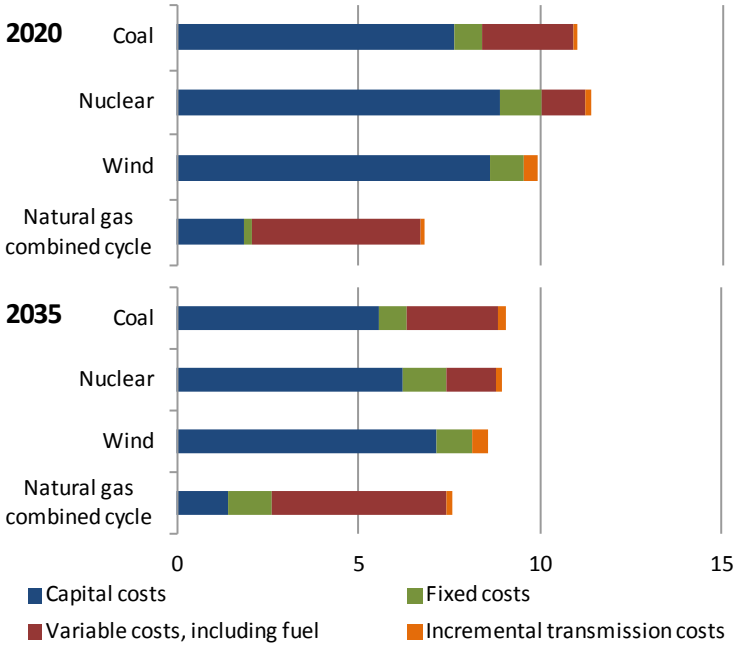

Figure 1.7: LCOE for New Power Plants, 2020 and 2030 (2009 cents per kWh) [8]

to be more cost effective than VAWTs and are, thus, the most common design in the industry. For similar reasons, the most common HAWT rotor configuration is a three-bladed, upwind rotor, which is the subject of this study.

Wind Classification

The wind conditions in a region are typically classified by wind power density and average wind speed. Table 1.1 contains the National Renewable Energy Laboratory (NREL) classification for wind at 10 and 50 m heights, as well as an additional column containing the NREL assessment of each class in terms of usefulness for power generation. This assessment reflects NREL's determination that Class 3 winds and above are "suitable for most wind turbine applications" and Class 1-2 winds are not [11].

Figure 1.8 shows the wind resource map of the U.S. by wind class at a height of 50 m. The Midwest region contains the largest geographic area of land-based wind

Table 1.1: Class Breakdown of Average Wind Speed at 10 and 50 m [11]

Height	10 m (32.8 ft)		50 m (164.0 ft)		
Wind Power Class	Wind Power Density, W/m^2	Speed, m/s	Wind Power Density, W/m^2	Speed, m/s	Qualitative Assessment
1	0 - 100	0.0 - 4.4	0 - 200	0.0 - 5.6	Poor
2	100 - 150	4.4 - 5.1	200 - 300	5.6 - 6.4	Marginal
3	150 - 200	5.1 - 5.6	300 - 400	6.4 - 7.0	Fair
4	200 - 250	5.6 - 6.0	400 - 500	7.0 - 7.5	Good
5	250 - 300	6.0 - 6.4	500 - 600	7.5 - 8.0	Excellent
6	300 - 400	6.4 - 7.0	600 - 800	8.0 - 8.8	Outstanding
7	>400	>7.0	>800	>8.8	Superb

resources, which are primarily Class 3-4 winds. Additionally, around the Rocky Mountains and the Appalachian Mountain Ranges there are small regions of primarily Class 3-4 winds. The Atlantic and Pacific coasts as well as the Great Lakes have largely Class 4-7 winds offshore. Any region without color has Class 1-2 winds, which makes up approximately two-thirds of the U.S.

Figure 1.9 shows the U.S. population density by county based on the 2010 census. As seen in this figure, the majority of the population lives either near the coasts or on the eastern half of the U.S. When comparing with Figure 1.8, it is clear that the wind resources in the Midwest and near the Rocky Mountains are located away from the majority of the population. As noted by Calvert et al., Class 6 sites are an average distance of 500 miles from load centers, and Class 4 sites are an average distance of 100 miles from load centers [12].

Because most promising wind sites are not near population centers, large-scale wind turbine deployment with current technology will require a significant investment in new power transmission lines. Generally speaking, new transmission lines cost about $2 million dollars per mile, a considerable expense [13]. Figure 1.10 documents one attempt to determine an economical way to build the new transmission lines required for energy

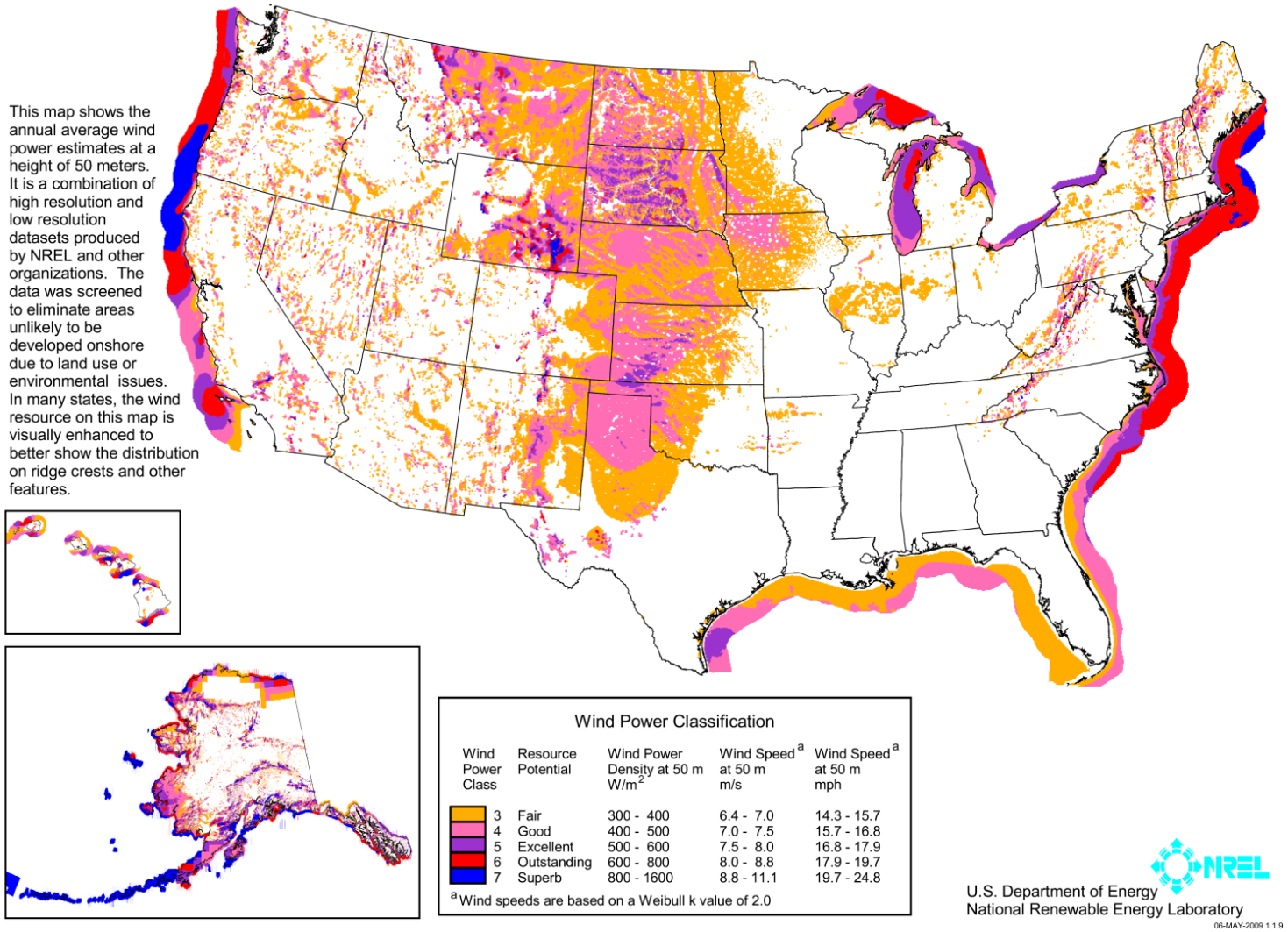

Figure 1.8: U.S. Annual Average Wind Speed at 50 m [14]

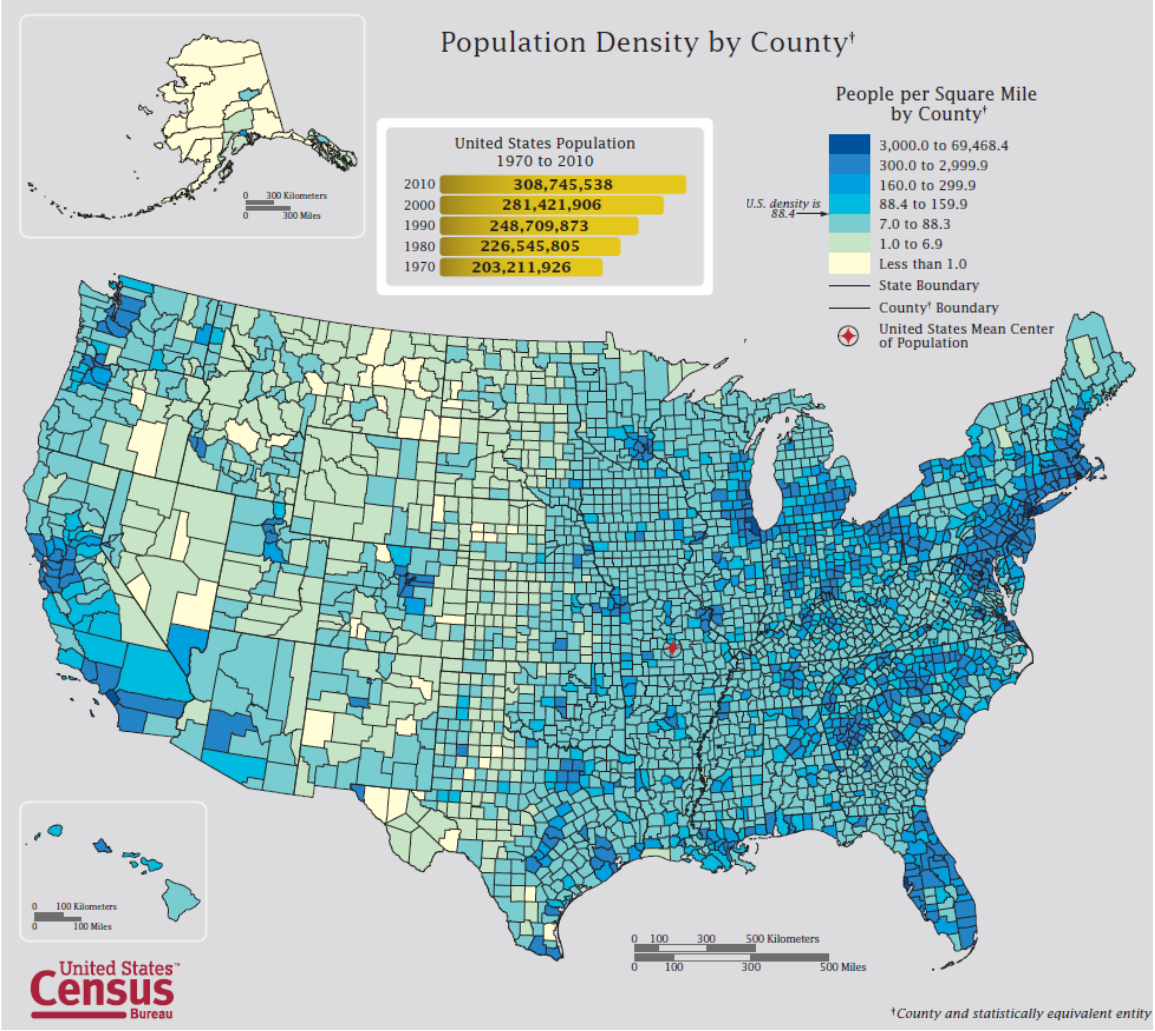

Figure 1.9: U.S. Population Density by County, 2010 Census [15]

production if wind is to supply 20% of the U.S. energy requirement by 2030. This analysis adds approximately 12,650 miles of new transmission lines at an estimated cost of $20 billion dollars [16].

The wind class in which a wind turbine operates in is one of the most significant factors in determining cost of energy. Figure 1.11 shows the levelized cost of wind energy excluding the cost of transmission and grid integration (bus-bar cost) for each wind class. This figure demonstrates very clearly the dependence of energy cost on wind conditions, with the cost of energy decreasing as class and, thus, average wind speed

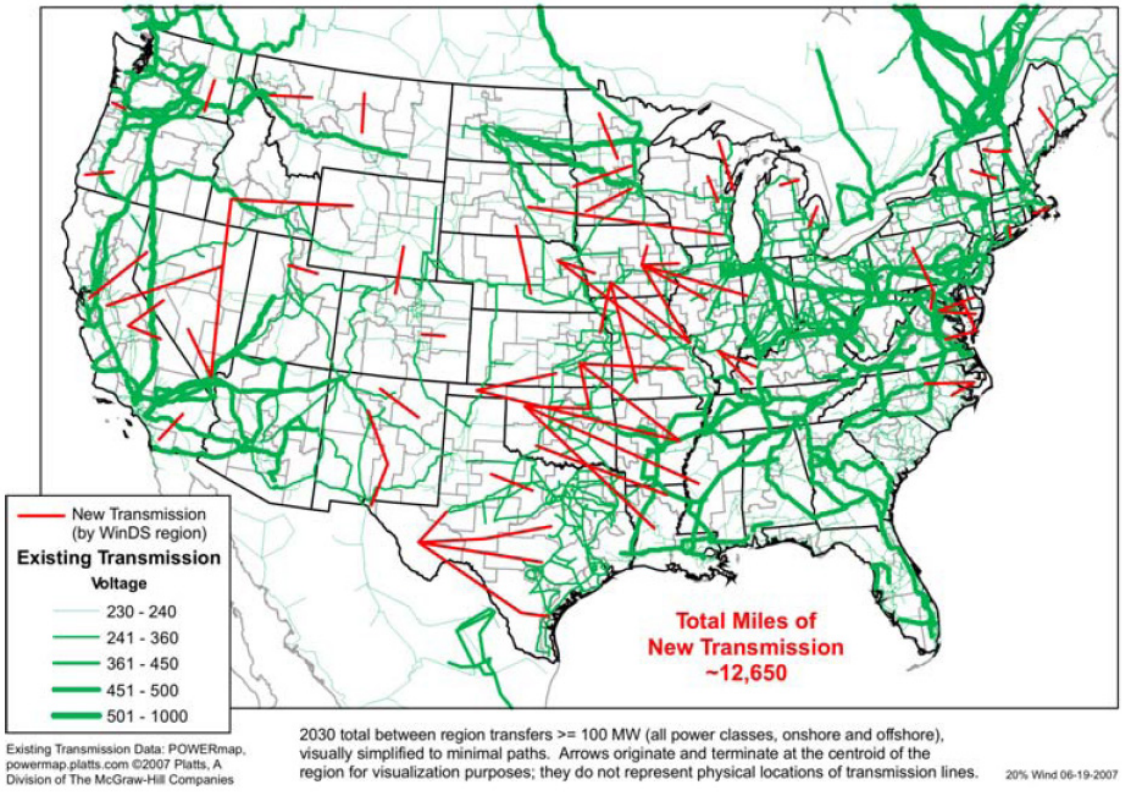

Figure 1.10: Conceptual New Transmission Line Scenario by WindDS region [16]

increases. Additionally, there is a significant difference in LCOE between land-based, shallow-offshore, and deep-offshore wind energy capture because of the additional infrastructure required for installing turbines offshore.

Notably, Class 2 wind is not included in Figure 1.8 and Figure 1.11, largely because it is considered a "marginal" resource by NREL. Additionally, in the Department of Energy (DOE) proposal for 20% of U.S. energy being supplied from wind energy by 2030, offshore wind is part of the solution and Class 2 wind is neglected [16]. However, Womeldorf estimates the LCOE of Class 2 wind, found by extrapolating the data in Figure 1.11, to be significantly less than even the most cost-effective offshore wind, as seen in Figure 1.12 [17]. This strongly suggests that land-based Class 2 wind should be considered, especially in view of the costly offshore wind technologies being

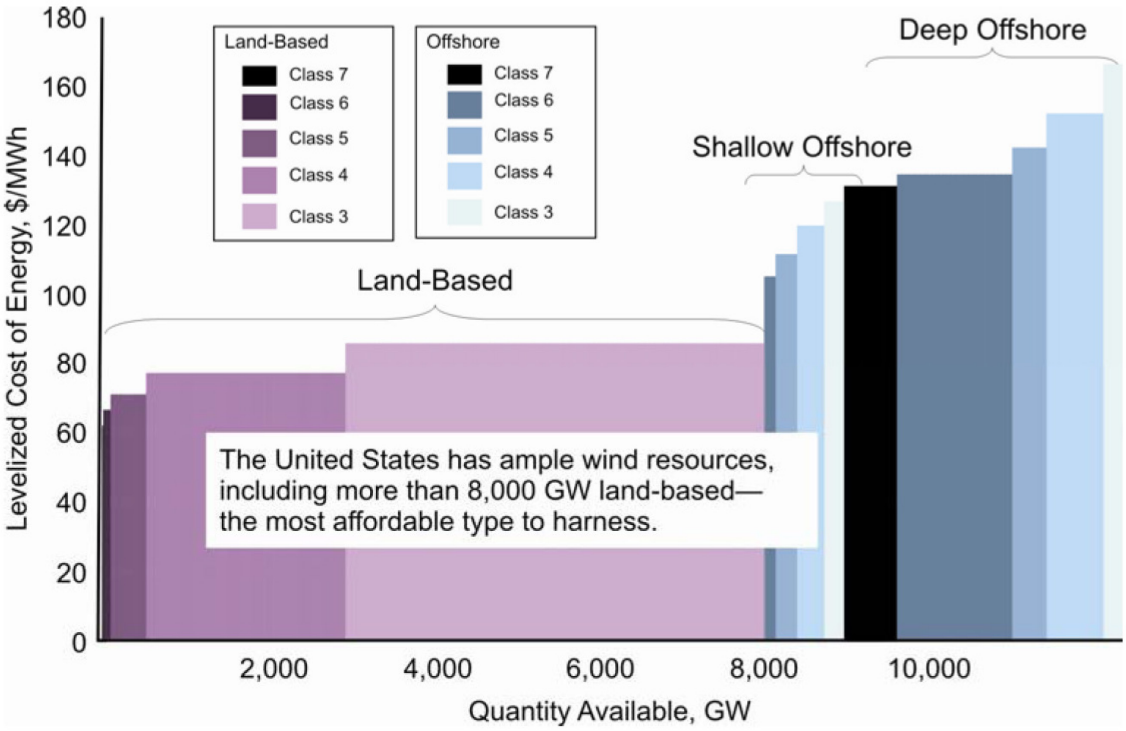

Figure 1.11: U.S. Supply Curve for Wind Energy—Current Bus-Bar Energy Costs [16]

developed. Additionally, developing a cost-effective wind turbine for Class 2 winds opens up nearly two-thirds of the U.S. to onshore wind energy extraction.

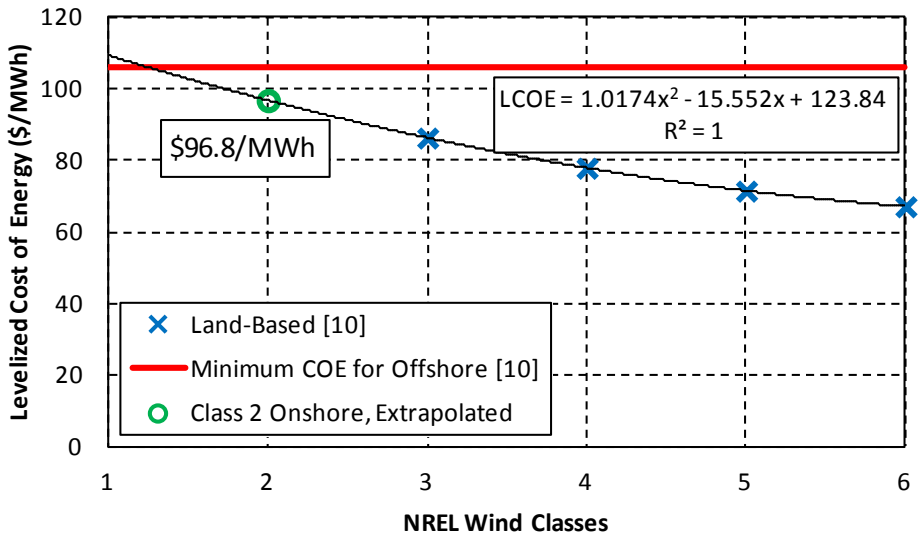

Figure 1.12: Extrapolated Cost of Class 2 Wind [17]

Within current wind turbine technology and literature, there is a lack of cost-effective turbines designed for Class 2 wind sites. Sangpanich et al. use existing wind turbine technology to determine if developing a Class 2 wind site in Turkey is economical [18]. In their analysis, they determined that with current technology it is not economical, but suggested that new technology should be developed. For example, two common large- and small-scale HAWTs are the GE 1.5-77 and Southwest Windpower Skystream 3.7. The GE 1.5-77 turbine, a 1.5-MW-rated machine with 37 m blades, is the "most widely deployed turbine" globally [19]. It was designed to be installed on a 77 m tower in a 10 m/s average wind speed, which requires a Class 7 site [20]. Figure 1.13 shows the maximum efficiency of the turbine to be approximately 48% at 9 m/s based on the manufacturer's power curve. The Skystream 3.7 turbine is rated at 3 kW and has a 3.7 m diameter. Its maximum coefficient of power is 28% at 8 m/s. According to the manufacturer, the Skystream 3.7 can be installed in areas with a 4.5 m/s average wind speed, although by analyzing the power curve in Figure 1.14, the Skystream turbine only begins to produce power at 4 m/s. The manufacturer recommends installing the turbine in regions that have 5.4 m/s or greater, and by analyzing the coefficient of power curve in Figure 1.14, it appears that the turbine was designed for a wind speed of approximately 8 m/s. The turbine was also designed to be installed on 10.2-21.0 m towers, which, with 8 m/s average wind speeds, means the site must be a Class 6-7 site [21]. Additionally, these turbines reach their rated power around 13-15 m/s, which most Class 2 sites rarely experience. Because most wind turbines are designed neither for Class 2 winds nor to produce very much power in Class 2 winds, this thesis investigates methods to increase performance of HAWTs operating in Class 2 winds and reduce the cost of energy.

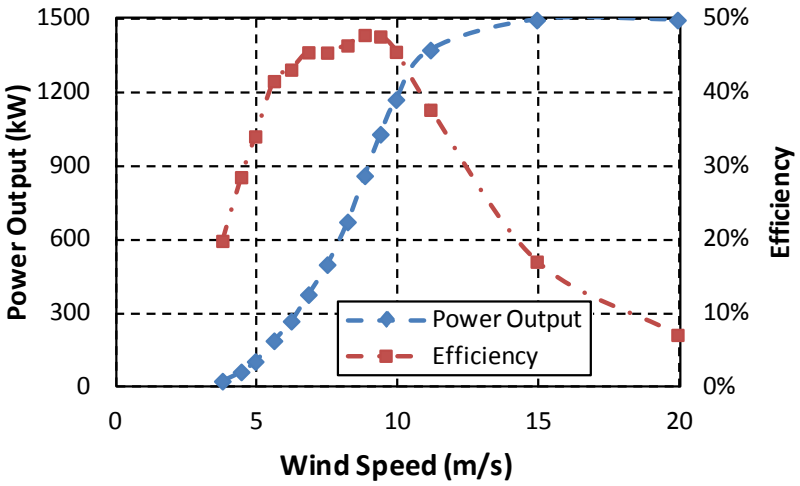

Figure 1.13: GE 1.5-77 and Power and Efficiency Curves [20]

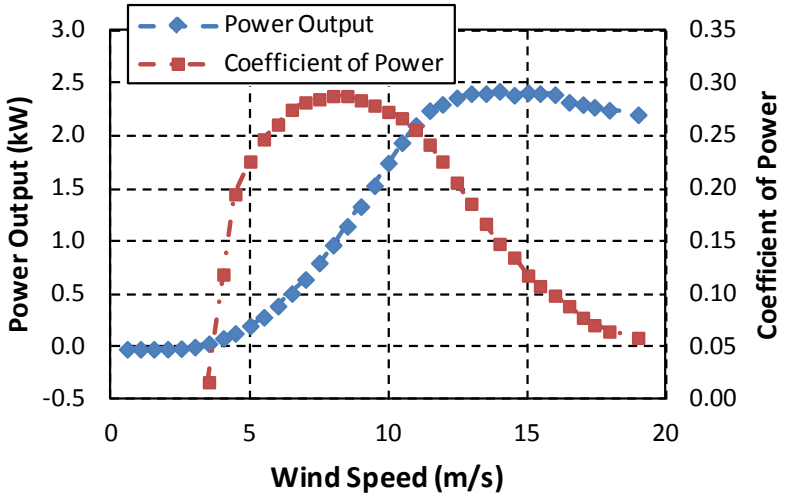

Figure 1.14: Skystream 3.7 Power and Coefficient of Power Curves [22]

Wind Turbine Scale

Horizontal-axis wind turbine technology is typically classified by the scale of the turbine, which relates to the physical size and the electrical output of the turbine. Table 1.2 lists a classification by scale of HAWTs, with the typical markets for each scale.

Medium- and large-scale wind turbines, typically installed in large numbers on wind farms, are generally accepted as the most cost effective wind turbine technology.

Table 1.2: Scale Breakdown of HAWT Technology [16, 23]

Scale	Output (kW)	Diameter (m)	Market
Large	>500	>50	Electric Power
Medium	100 - 500	20 - 50	Industrial
Small	10 - 100	3 - 20	Commercial
Small	0.5 - 10	0.5 - 3	Residential, On-Grid
Micro	<0.5	<0.5	Residential, Off-Grid

This is due to economy of scale relationships, which drives towards larger turbines and taller towers to reduce the cost of energy [24]. These wind farms are typically built in regions that have Class 3 average winds or better to be economically feasible. As can be seen in Figure 1.8, the two largest regions of wind potential are the Midwest and offshore on either the Atlantic of Pacific coasts.

Another significant issue for large-scale wind turbines is gearbox failure. In 2002, DOE proposed developing low-speed, permanent-magnet generators to eliminate the gearbox [12], yet in 2008 gearbox failure is still reported as a significant cost that often occurs fairly early in the life of the turbine [16]. Figure 1.15 demonstrates both aspects graphically in comparison to other unplanned failures. Finally, because of the scale of these turbines and wind farms, the initial investment and risk are significant, particularly when considering the uncertainty of building new transmission lines.

Small- and micro-scale wind turbines are typically installed individually or in small groups to generate power locally. Known as distributed generation, this requires no additional transmission lines to be built because the energy is being generated at the site of use. However, current commercially available turbines need to be installed in regions that have Class 3 average wind speeds or better to be economical, generally speaking. Since most of the population in the U.S. does not live in areas with Class 3 winds or higher, distributed generation using wind turbines is not an economic option for most of

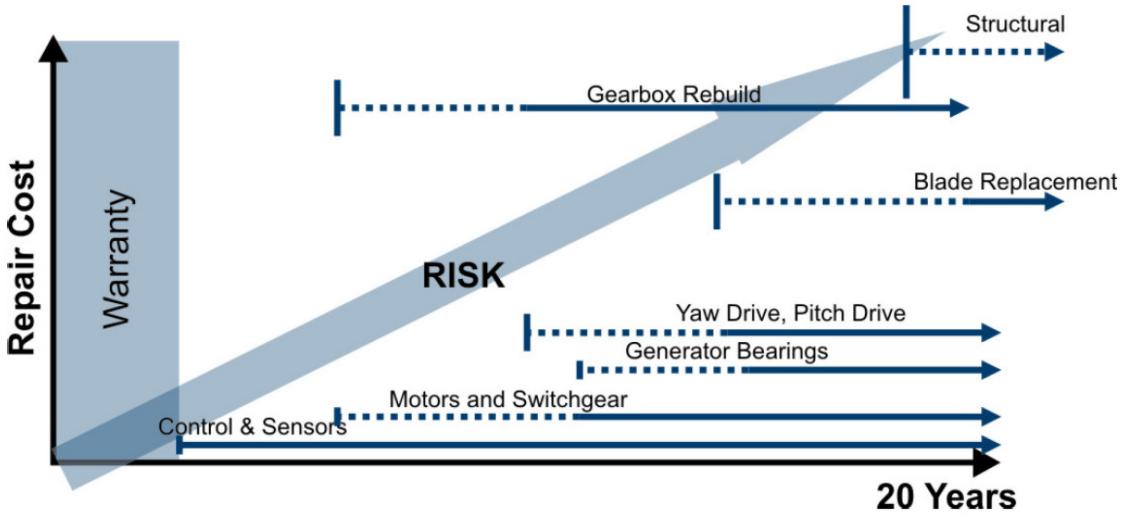

Figure 1.15: Unplanned Repair Cost, Likely Sources, and Failure Risk with Plant Age [16]

the U.S. Small- and micro-scale wind turbines have several advantages. Because they have higher rotational speeds than medium and large scale turbines, they can be designed without a gearbox, using a direct-drive, permanent-magnet generator. Also, when installed in residential and commercial areas, the size of small-scale turbines makes them the obvious choice when considering safety and aesthetics. For these reasons, small-scale technology has the advantage of avoiding dependence on costly transmission lines and the significant risk of gearbox failure even though the cost of energy is typically higher than for medium- and large- scale turbines due to economies of scale. Thus, it is expected that the cost of energy of small-scale units will be less over the life of the turbine, particularly when considering the cost-savings associated with not building new transmission lines (typically not included in cost comparisons). Demonstrating the value of small-scale technology and the growth of this market, Flower reports the number of small-scale installations increased 26% and the sales revenue grew 53% in 2010 [23].

Wind Turbine Efficiency

The final determining factor for cost of energy is wind turbine efficiency. Typically a turbine is designed to be most efficient at a specific wind speed. However, large scale turbines typically have pitch control to increase efficiency over a range of wind speeds. Most small- and micro-scale turbines, on the other hand, typically do not have pitch control and are designed with a fixed pitch to be most efficient at a particular wind speed. Thus, optimizing wind turbine performance for a specific wind speed is the design strategy for developing small-scale wind that is the subject of this study.

Objectives and Scope of this Study

The goal of this study is to improve the design of small-scale, fixed-pitched, horizontal-axis wind turbines for Class 2 wind speeds. Small wind turbines coupled with generated distributed generation are proposed to eliminate dependence on high cost transmission lines. Fixed-pitch blades are used in the design to reduce the cost of the turbine. Wind turbine performance in Class 2 winds is analyzed because the cost of harvesting Class 2 wind energy is expected to be less expensive than offshore. Additionally, current commercial technology is not designed for Class 2 sites.

In this work, the aerodynamic efficiency has been maximized by improving the blade shape as well as controlling the unique aerodynamic conditions that occur with flow over the blade in these low wind speeds. Simulations and wind tunnel experiments of two-dimensional wind turbine airfoils and scaled wind turbines have been performed to demonstrate the efficiencies and power output possible for low wind conditions of approximately 5 m/s.

Presentation Outline

This work experimentally explores multiple aspects of small-scale, fixed-pitch, horizontal-axis wind turbine aerodynamic design for Class 2 winds. The organization of the document is divided as follows. Chapter 2 provides both the theoretical and experimental background necessary to understand the airfoil and wind turbine studies. Chapter 3 contains documentation of the experiment design, procedures used in the studies performed, as well as the data reduction used in the wind site survey, airfoil studies, and wind turbine studies. Chapter 4 presents the results of the wind site survey, airfoil studies, and wind turbine studies. Chapter 5 concludes the discussion with a summary of this work as well as recommendations for further study and guidelines for design.

CHAPTER TWO

Technical Background

The intent of this chapter is to provide the necessary aerodynamic background to understand the flow phenomena encountered in this study as well as discuss previous, pertinent research. The goal of this thesis is to add to the current understanding of the aerodynamic design of small-scale wind turbines through the experimental investigations performed.

HAWT Aerodynamic Theory

Current aerodynamic theory has been developed from a combination of the three primary fluid flow equations—conservation of mass, momentum, and energy—as well as airfoil aerodynamic theory. The conservation of mass and energy equations have been used to derive the power in the wind passing through the turbine as shown by the equation

$$P_{wind} = \frac{1}{2}\rho\pi R^2 U^3 \tag{2.1}$$

where ρ is the air density, R is the turbine radius, and U is the wind velocity. The amount of energy the actual turbine extracts is simply the power available in the wind multiplied by the rotor efficiency, known as the coefficient of power, C_P, as seen in the following equation

$$P_{rotor} = P_{wind}C_P = \frac{1}{2}\rho\pi R^2 U^3 C_P \tag{2.2}$$

This equation shows that the power extracted by a particular rotor is proportional to the density, efficiency, square of the radius, and cube of the velocity. Since the air density of

a region cannot be controlled, changing the density is not an option for increasing the power output of a wind turbine. The remaining three variables have been discussed in Chapter 1, as scale (radius), wind class (wind velocity), and efficiency (coefficient of power). Noticeably, a small increase in radius or a small increase in wind velocity produces a significant increase in power because of the square and cube relationships, respectively. This is what has driven turbine manufacturers to make larger diameter turbines on taller towers. However, this work is focused on improving the efficiency of small-scale HAWTs through better blade design.

Critical Parameters

Two dimensionless parameters are typically used in characterizing aerodynamic conditions and wind turbine performance. The first is coefficient of power, as previously mentioned, which is the wind turbine aerodynamic efficiency and is defined by the equation

$$C_P = \frac{P_{rotor}}{P_{wind}} = \frac{\tau\Omega}{\frac{1}{2}\rho\pi R^2 U^3} \tag{2.3}$$

where τ is the torque generated by the rotor and Ω is the rotational velocity of the rotor. Also, the tip speed ratio (TSR) non-dimensionalizes the rotational velocity of the turbine and is defined by the equation

$$\lambda = \frac{\Omega R}{U} \tag{2.4}$$

Momentum Theory

The general approach to analyzing the air flow over a wind turbine uses the conservation of momentum equation. First, a control volume is drawn around the turbine as a streamtube with one-dimensional axial flow, seen in Figure 2.1. In their analysis of

ship propellers, Rankine and Froude simplified the rotor in the streamtube to an actuator disk that is extracting energy by creating a pressure drop, as seen in Figure 2.2 [25]. This assumes that the rotor is acting uniformly on the fluid, which implies the rotor has an infinite number of blades. From this analysis, the axial induction factor, a non-dimensional parameter used to simplify equations and calculations, can be defined as

$$a = \frac{U_\infty - U_d}{U_\infty} \tag{2.5}$$

where U_∞ is the upstream air velocity and U_d is the velocity at the actuator disk. Using this analysis, Betz was able to determine the efficiency of an ideal rotor to be 59.3%, which is commonly taken to be the maximum efficiency or coefficient of power possible for a HAWT [25, 26]. This point of maximum efficiency occurs when the axial induction factor is equal to 1/3.

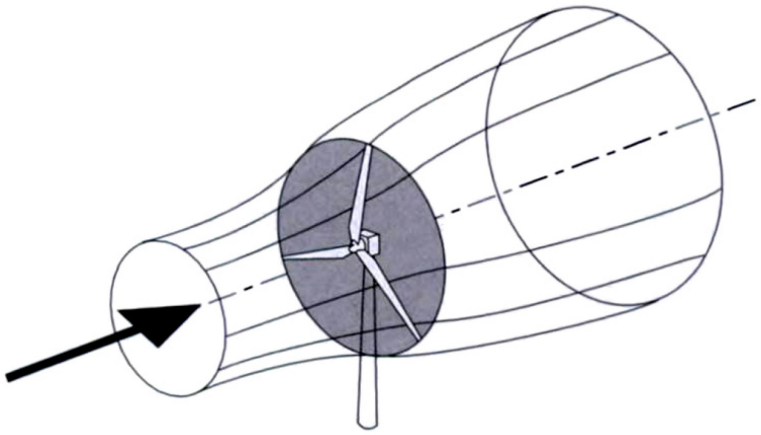

Figure 2.1: The Energy Extracting Stream-tube of a Wind Turbine [27]

Joukowski furthered this theory by including rotation in the wake of the streamtube, making the problem two-dimensional [25]. From this analysis, the tangential induction factor, a second non-dimensional parameter used to simplify equations, can be defined as

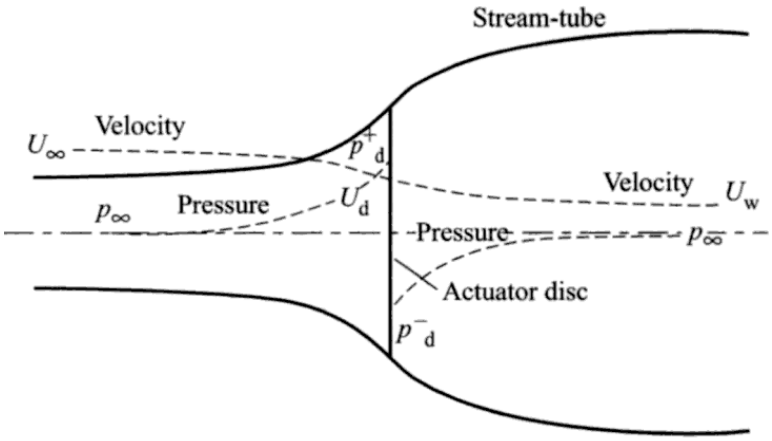

Figure 2.2: An Energy Extracting Actuator Disc and Stream-tube [27]

$$a' = \frac{\omega}{2\Omega} \tag{2.6}$$

where ω is the angular velocity imparted to the wake. Gipe notes that greater wake rotation, which can be seen in a higher tangential induction factor, will decrease the overall rotor efficiency [28].

Figure 2.3 shows typical induction factors for an ideal wind turbine with a TSR of 7.5. Notably, the axial induction factor is at the optimum of 1/3 over the entire blade except near the hub. Additionally, the tangential induction factor, indicative of the rotation imparted to the streamtube, is near zero over most of the blade, but increases significantly near the hub where the efficiency will also be lower.

Airfoil Aerodynamic Theory

The second portion of current aerodynamic theory for HAWTs is based on the aerodynamics of airfoils, which are two-dimensional streamlined bodies designed to generate desired forces while moving relative to a fluid. These forces are defined as lift, which acts normal to the fluid flow, and drag, which acts in the direction of the fluid flow. Additionally, a moment is generated due to the interaction between the fluid and

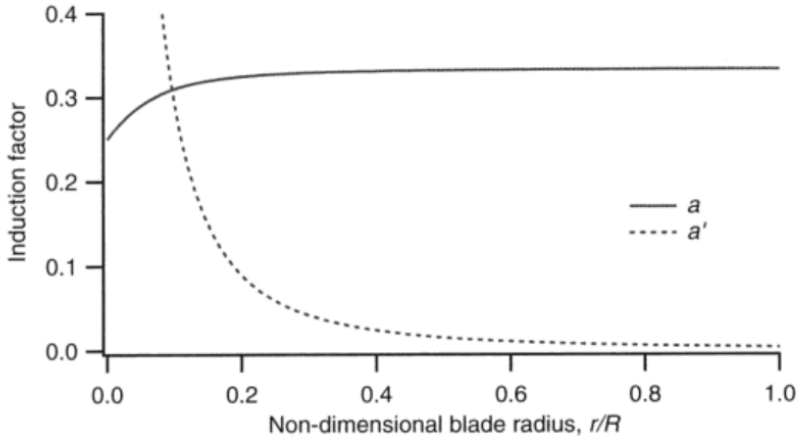

Figure 2.3: Induction factors for an ideal wind turbine with wake rotation, TSR = 7.5 [26]

the airfoil. The lift and drag forces as well as the moment are all generated as a results of two-dimensional phenomena. The first is skin friction over the surface of the airfoil causing drag. The second is the pressure distribution over the airfoil, caused by flow acceleration over the surface. This pressure distribution causes both lift and drag forces as well as the moment. The orientation of the airfoil with respect to the freestream flow is known as the angle of attack, α, which is defined as the angle between the chord line of the airfoil and the direction of the freestream velocity. Figure 2.4 shows a symmetric airfoil at a positive angle of attack. Also shown are the streamlines over the airfoil and the forces and moment (shown as coefficients) that are generated. For this case, the pressure gradients over the surface of the airfoil cause, in general, the pressure on the upper surface to be less than the pressure on the lower surface, and this pressure difference creates an upward lift force and a backward drag force.

Important non-dimensional parameters for airfoil study are the coefficients of lift, drag, moment, and pressure as well as the Reynolds number. The following equations document the definitions of these important parameters.

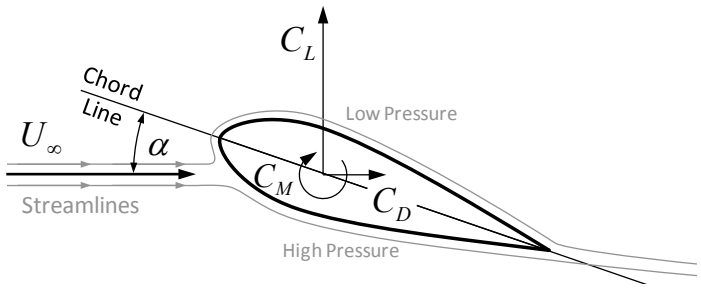

Figure 2.4: Symmetric Airfoil at a Positive Angle of Attack

$$C_{L,D} = \frac{L,D}{\frac{1}{2}\rho \cdot U^2 \cdot \mathrm{S}} \tag{2.7}$$

$$C_M = \frac{M}{\frac{1}{2}\rho \cdot U \cdot S \cdot c} \tag{2.8}$$

where

$$S = c \cdot b \tag{2.9}$$

$$C_p = \frac{p_{loc} - p}{\frac{1}{2}\rho \cdot U^2} \tag{2.10}$$

$$Re = \frac{\rho \cdot U \cdot c}{\mu} \tag{2.11}$$

where L is lift, D is drag, ρ is the freestream fluid density, S is the planform area of the airfoil, c is the airfoil chord, w is the airfoil width, p_{loc} is the local static pressure at a particular point on the surface of the airfoil, p is the freestream static pressure, μ is the dynamic viscosity, and U is the freestream wind velocity (for a stationary airfoil).

Figure 2.5 shows typical lift coefficient, drag coefficient, and L/D curves versus angle of attack. As angle of attack increases, lift typically increases until the stall point is reached where the flow separates and lift begins to decrease. Additionally, drag remains relatively constant until stall occurs, at which point the drag increases significantly. The extent of the post-stall decrease in lift and increase in drag determines whether the airfoil has hard (significant change in lift and drag) or soft (minimal change in lift and drag) stall characteristics. Generally, speaking, airfoils with soft stall characteristics are more

desirable for fixed-pitch wind turbines. As the angle of attack increases further, the deep stall region will be reached, at which point the lift decreases and the drag increases steeply. The L/D curve is important because it shows the angle of attack at which the lift to drag ratio is maximized. The L/D ratio is significant because it is directly related to the torque produced by the wind turbine blade. For a particular rotational velocity, or TSR, the torque is directly related to the power production. Thus, a higher L/D ratio directly translates to more power production.

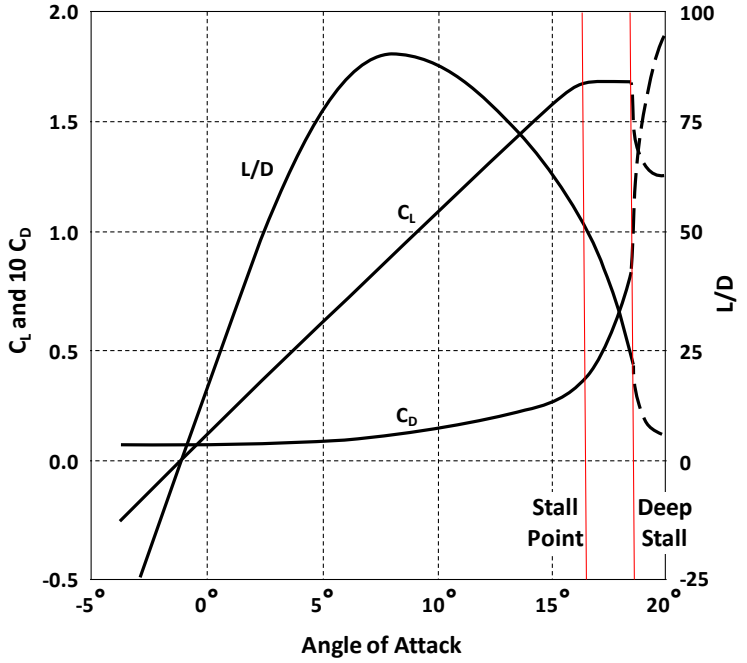

Figure 2.5: Typical Airfoil Performance Curves [29]

Potential flow theory, panel methods. While flow over an airfoil can be modeled using the full Navier-Stokes equations and CFD, potential flow and boundary layer theory provide a simpler and faster way to model flow over an airfoil. Using potential flow theory, four simple, inviscid "potential" flows can be easily represented mathematically. They are uniform, source, sink, and vortex potential flows, as seen in

Figure 2.6. While these flows are very elementary, using superposition they can be combined into more practical geometries such as an airfoil. Figure 2.7 shows how uniform, source, and sink flows can be combined to simulate flow over an oval. By dividing the surface of an airfoil into discrete panels, as shown in Figure 2.8, and using conformal mapping, sources, sinks, and vortex flows of varying strengths are applied at each of the nodes with a uniform flow applied to the whole domain to model flow over an airfoil. However, this theory is only valid for inviscid flows and, thus, is only valid outside the boundary layer. To accurately model flow over an airfoil, particularly for the low Reynolds numbers of interest to this work, boundary layer theory must be employed.

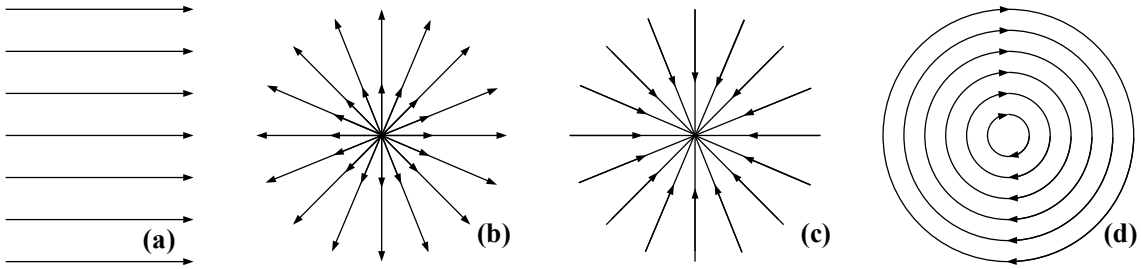

Figure 2.6: (a) Uniform (b) Source, (c) Sink, and (d) Vortex Potential Flows

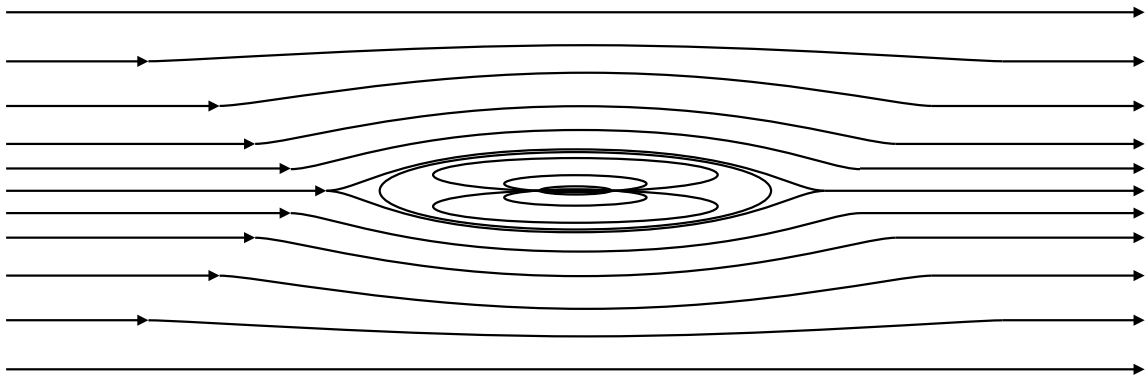

Figure 2.7: Superposition of Uniform Flow, Source, and Sink

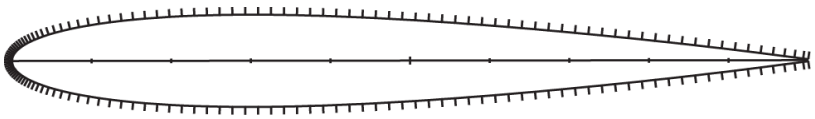

Figure 2.8: Default Airfoil Panel Divisions in XFOIL (160 nodes) for NACA 0012

Boundary layer theory. The boundary layer phenomenon is caused by friction and occurs when a fluid moves relative to a solid. For the example of a fluid flowing around a stationary curved surface (such as a cylinder or an airfoil) as seen in Figure 2.9, the fluid velocity profiles show that at the surface of the plate the velocity is zero due to friction and at the edge of the boundary layer the fluid velocity is approximately the freestream velocity. Between the boundary layer edge and the plate surface, the velocity profile is a smooth, continuous curve. This figure illustrates the phenomenon of flow separation when the edge of the boundary layer "separates" from the edge of the surface. Flow separation is caused by a negative, or adverse, pressure gradient, which decelerates the flow until the direction of the flow is reversed near the surface and the flow separates. Downstream of the separation point, a large wake region forms between the edge of the boundary layer and the surface as seen in Figure 2.9.

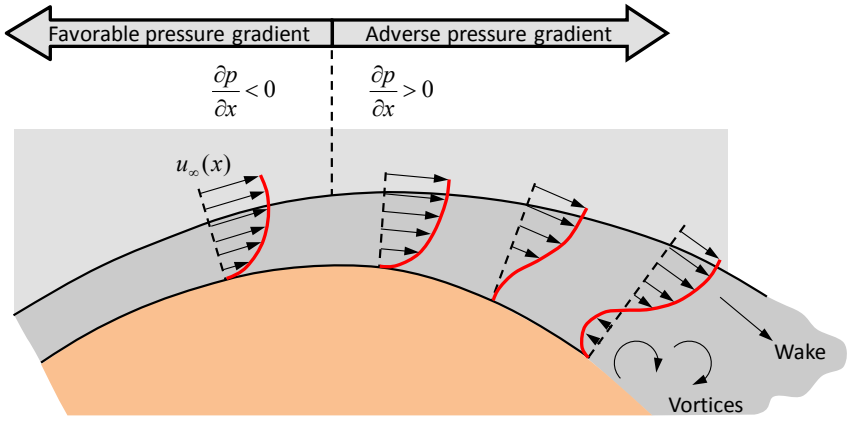

Figure 2.9: Illustration of Separation and Wake Region in a Boundary Layer [30]

There are two types of boundary layers, laminar and turbulent, as seen in Figure 2.10. A laminar boundary layer is generally thinner, creates less skin friction on a surface, and is also more susceptible to flow separation than a turbulent boundary layer. A laminar separation bubble, unique to the Reynolds number regimes of interest to this work, occurs when a laminar boundary layer separates, transitions to a turbulent boundary layer, and reattaches downstream, as seen in Figure 2.10. This type of flow is notable because it typically occurs on a small-scale wind turbine operating at low wind speeds.

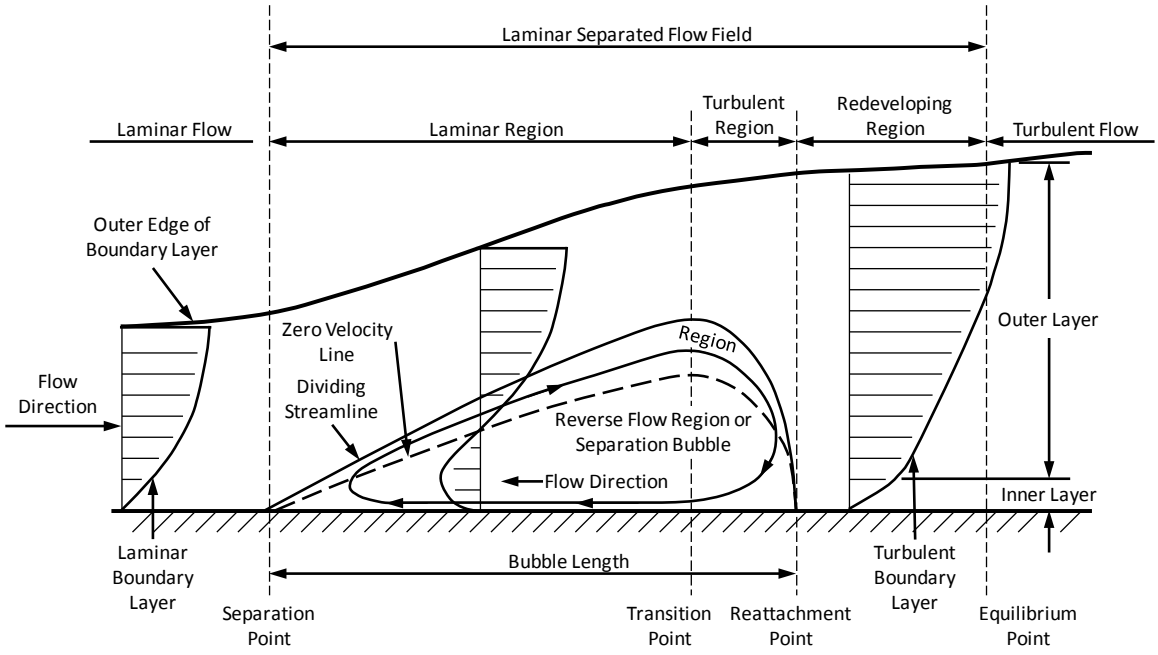

Figure 2.10: Schematic Diagram of Laminar Separation Bubble [31]

Multiple factors affect the location where transition from a laminar to a turbulent boundary layer will occur along a surface, such as freestream turbulence, surface roughness, pressure gradients, and flow separation. Specifically, increases in freestream turbulence, surface roughness, an adverse pressure gradient or the occurrence of laminar

separation all generally promote transition. Promoting transition increases skin friction over a surface because a turbulent boundary layer generates more skin friction than a laminar boundary layer. Depending upon where transition occurs, this can delay separation. A turbulent boundary is less susceptible to flow separation than a laminar boundary layer because it pulls in energy from the freestream flow to the surface. As seen Figure 2.10, if the boundary layer transitions to turbulent after separation, the flow can reattach. When the flow reattaches, the region of separation is known as a separation bubble.

Promoting flow transition for separation control can be accomplished using both passive and active flow control methods. Both methods have been applied for reducing separation on the wings of an airplane as well as on low-pressure turbine blades in a gas turbine engine. Passive methods include adding surface roughness [32], a trip wire [33], trip strip [34], leading-edge tape [35], riblets [36], or vortex generators [37]. Active flow control methods include flaps [38], vortex-generator jets [39], plasma-actuated jets [40], piezoelectric actuators [41], or even acoustic excitation [42].

While models for laminar and turbulent flow are very developed, predicting the location transition and separation, as well as the extent of the separated region, is difficult. This is because few models have been proposed that even attempt to take into account all the factors that affect transition and separation [43]. For this reason, modeling the flow in Reynolds number regimes where transition and separation often occur is difficult.

For a fixed geometry, varying the Reynolds number will vary the freestream velocity and, thus, the pressure gradient over that geometry. Figure 2.11 shows the drag coefficient on a sphere versus Reynolds number. This figure shows two distinct regions

of flow over a sphere, one with a higher coefficient of drag and one with a lower coefficient drag. For the smooth sphere, the flow is naturally laminar at lower Reynolds numbers. At the higher Reynolds numbers, the flow is naturally turbulent. While a turbulent boundary layer produces more drag and should have a higher coefficient of drag, this trend is reversed for the sphere. This is because the flow is laminarly separating at the lower Reynolds numbers but is staying attached when the boundary layer is turbulent. The reduction of separated flow and coefficient of drag is due to the fact that a turbulent boundary layer is less susceptible to flow separation than a laminar boundary layer. This figure also shows the effect of adding surface roughness, represented by the roughness parameter, ε, divided by the sphere diameter, D. Adding surface roughness to the sphere shifts the Reynolds number at which transition naturally occurs to a lower Reynolds number and the drag is reduced. The irregular surface of a golf ball is a good example as it operates in the lower Reynolds number range.

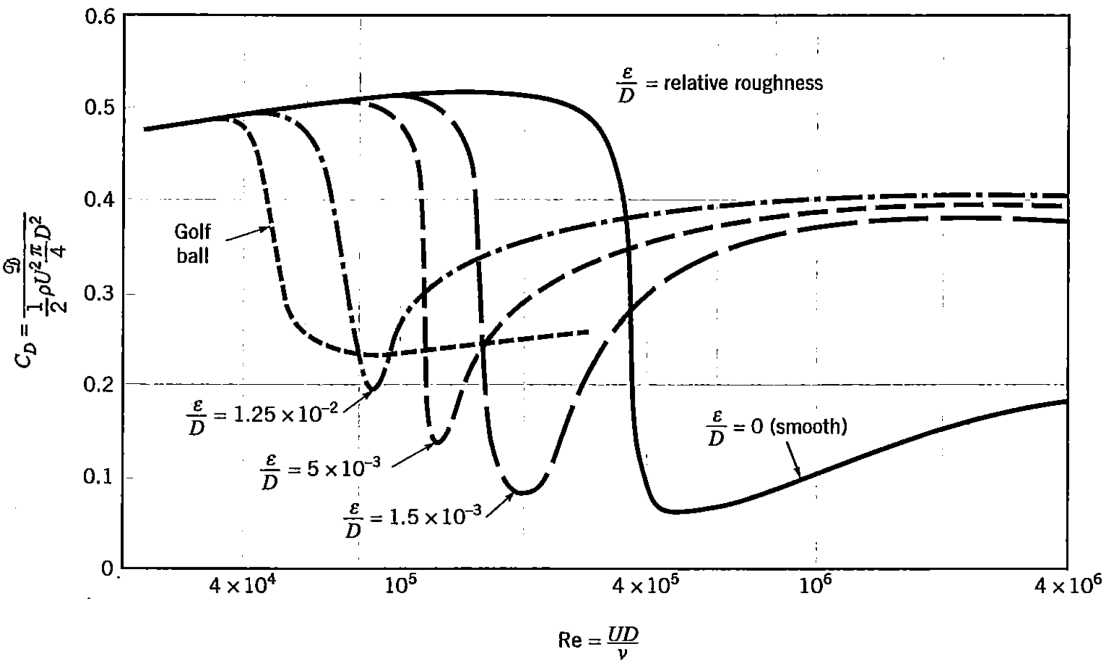

Figure 2.11: Drag on a Sphere [44]

This phenomenon can also be seen when analyzing drag on an airfoil surface. While an airfoil is streamlined to eliminate flow separation, decreasing Reynolds number can cause flow separation to occur at angles of attack in the normally attached flow region, increasing the drag. However, by adding roughness, the drag can be reduced. This has been done for the S823 airfoil at an angle of attack of 0 deg by applying a sandpaper (180 grit) trip strip with a height of 0.35% of the chord at a location 25% of the chord from the leading edge on the upper surface. The results are shown in Figure 2.12. Figure 2.12 (b) shows that the drag can be reduced by over 30% at a Reynolds number of 50,000. Flow separation also decreases the lift generated, as seen in Figure 2.12 (a). For Reynolds numbers below 100,000, the addition of the trip strip decreases drag and increases lift. For Reynolds number above 150,000, the addition of the trip strip has the opposite effect, increasing drag and decreasing lift. The L/D parameter, shown in Figure 2.12 (c), is of interest because a higher L/D indicates greater wind turbine power production. For Reynolds numbers of 150,000 and above, the addition of the trip strip always decreases the L/D value, by as much as 15.7%. However, for Reynolds number below 150,000, the addition of the trip strip always increases the L/D value. At a Reynolds number of 50,000, the smooth airfoil actually has a negative L/D value of -0.735, but the airfoil with a trip strip has an L/D value of 1.034, an increase of nearly 250%.

Figure 2.13 shows the general trend of how L/D_{max} varies with Reynolds number on smooth and rough airfoils. While the rough airfoils have a lower L/D_{max} for Reynolds numbers greater than 10^5, they have a higher L/D_{max} for values less than 10^5. Because of the relationship of L/D to power production, the proper addition of roughness to a wind turbine blade should improve performance at these low Reynolds numbers.

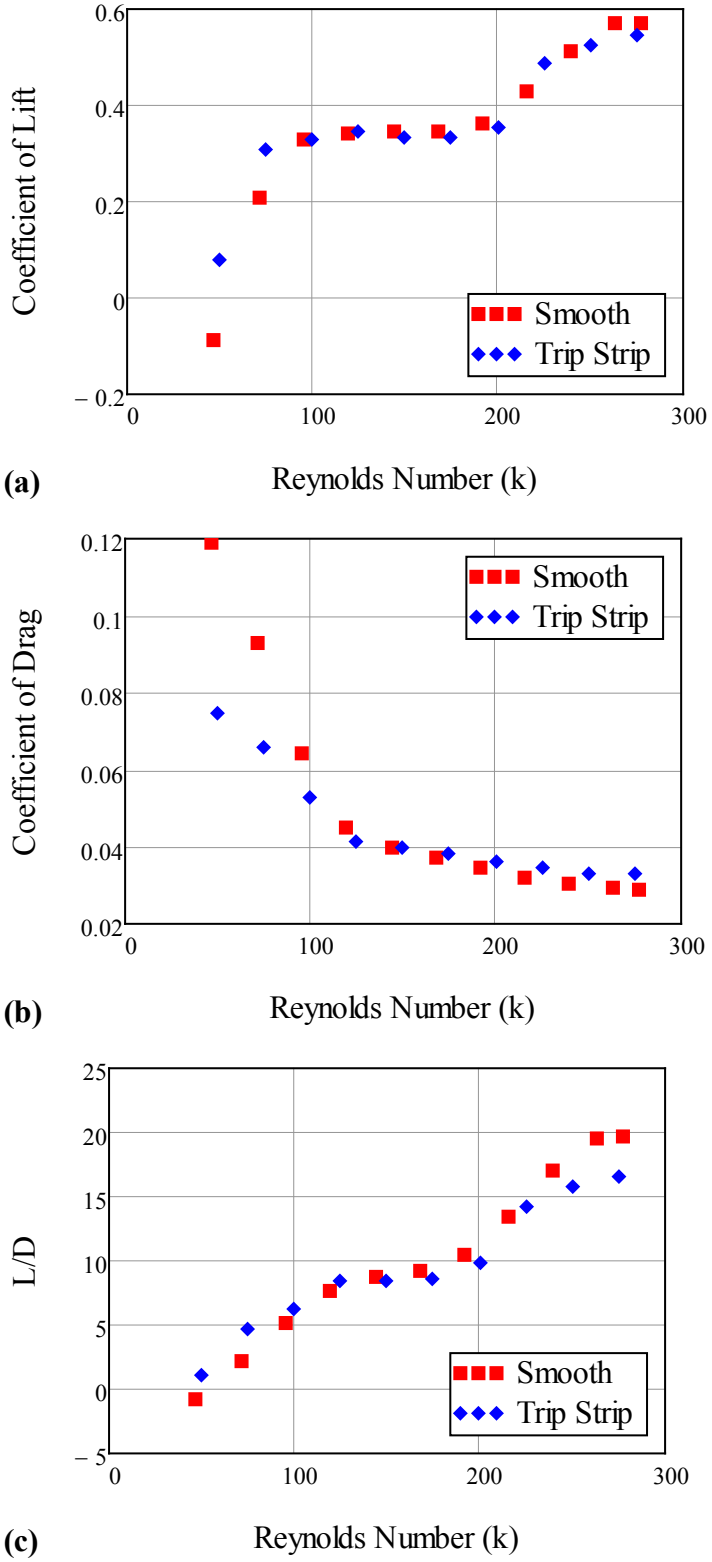

Figure 2.12: S823 Airfoil, at an Angle of Attack of 0 deg, (a) Lift Coefficient, (b) Drag Coefficient, and (c) L/D Dependence on Reynolds Number

Past research at Baylor by Gregg et al. has studied the effect of roughness on small-scale wind turbines in wind tunnel testing, which suggest an increase by as much as 50% by applying roughness to a wind turbine with a TSR of 3 [45]. Additionally, Gross and Fasel studied ways to reduce flow separation on a wind turbine airfoil, the S822, at a Reynolds number of 100,000 by applying pulsed vortex generator jets, flip-flop jets, and plasma actuators [46].

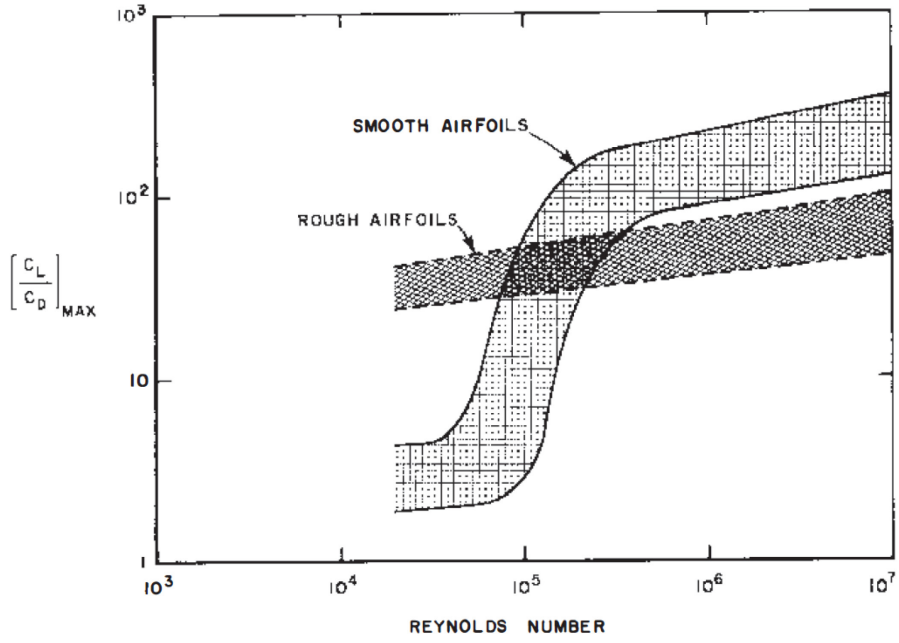

Figure 2.13: Low Reynolds Airfoil Performance [47]

Airfoil aerodynamic codes. By combining potential flow theory to model the inviscid flow outside the boundary layer and boundary layer theory to model the flow in the boundary layer, flow over an airfoil can be simulated quickly and with reasonable accuracy for a wide range of flow conditions. Two codes that combine these theories are the commercial Eppler Airfoil Design and Analysis Code (also known as PROFIL, which is the name that will be used in this work) and the public-domain code XFOIL.

PROFIL is widely used in research and industry for airfoil design and analysis [48-50], and "has been successfully applied at Reynolds numbers from 3 x 10^4 to 5 x 10^7" [51]. However, in previous studies the code has been shown not to capture the effect of separation bubbles. Rather it just notes when a separation bubble may be present on the airfoil [52]. Additionally, PROFIL was used to design all the NREL airfoils designed for wind turbines [53].

XFOIL, on the other hand, was designed for transonic and low-Reynolds numbers flows. Because the flows over a small-scale wind turbine blade are low Reynolds numbers, this code is of particular interest. Figure 2.14 shows the graphical output while using XFOIL. The coefficient of pressure profile has been plotted as well as streamlines over the airfoil. This code combines high-order panel methods with theory developed by Drela and Giles [54] and implemented in their "ISES" code. This theory solves the steady 2-D Euler equations with viscous corrections using a global Newton method, and prediction transition using the Orr-Sommerfeld equation [55]. XFOIL was developed to accurately predict a range of flow conditions over an airfoil in a fraction of the time that Navier-Stokes-based computational fluid dynamics (CFD) programs require. Pertinent to this paper is XFOIL's accuracy of prediction for low Reynolds number flows, as demonstrated by Drela and Giles [54] and McGranahan and Selig [56], due to an accurate representation of separation bubble losses. Granahan and Selig demonstrated experimentally that XFOIL predicts transition and reattachment very well for a number of airfoils at low Reynolds numbers. However, their experiments show XFOIL's prediction of laminar and turbulent separation to be significantly inaccurate at high angles of attack. In particular, their data showed the location of turbulent separation to be off by as much as 60% of the chord length from the experimental value. For almost all the conditions

tested, XFOIL predicts that the turbulent separation occurs later (more toward the trailing edge) than it does experimentally. This inaccuracy will increase the predicted value of lift and decrease the predicted value of drag when compared with the experimental results.

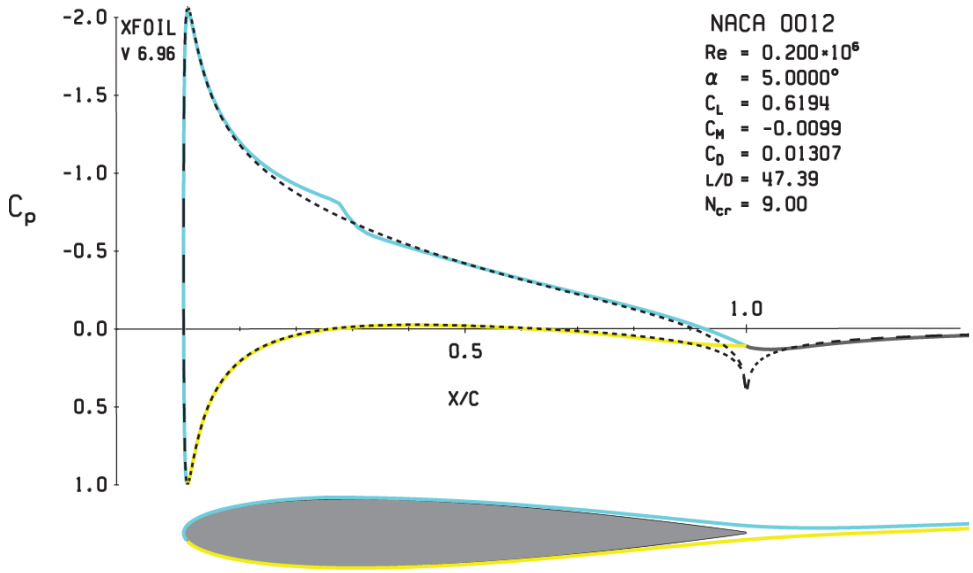

Figure 2.14: Pressure Profile and Streamlines Generated using XFOIL for NACA 0012

Figure 2.15 shows a comparison of two sets of experimental data with PROFIL and XFOIL simulation lift and drag coefficients for the E387 airfoil over a range of angles of attack at a Reynolds number of 60,000. The coefficient of drag curve shows the presence of a separation bubble between the angles of -1 and 5 degrees. Both experimental data sets capture the flow fully separating between 5 and 8 degrees. While PROFIL does not capture the effect of the separation bubble on the drag between the angles of -1 and 5 degrees, which increases the drag coefficient, XFOIL does. However, neither code captures the flow fully separating between the angles of 5 and 8 degrees, which reduces the lift and increases the drag.

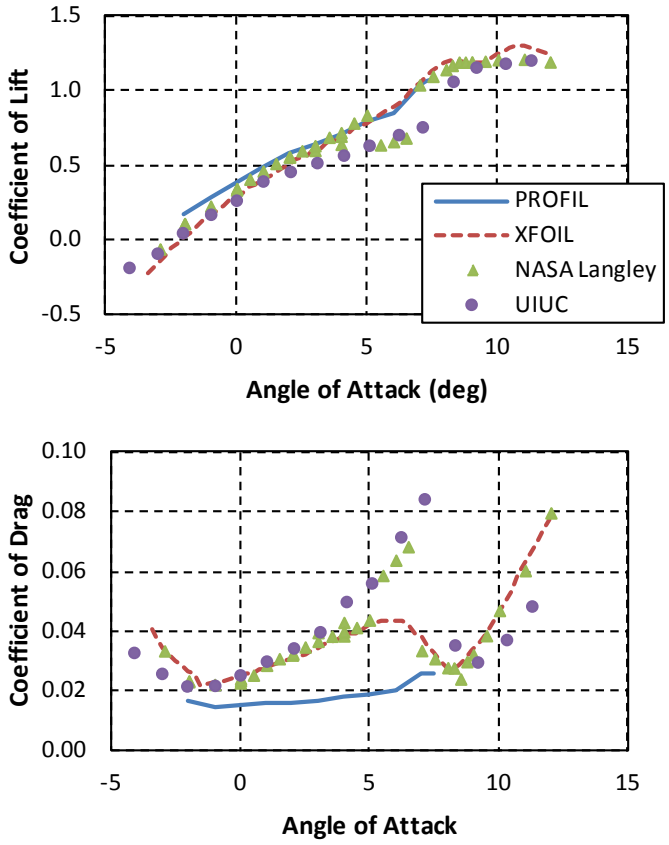

Figure 2.15: Comparison of E387 Airfoil Data at a Reynolds Number of 60,000 [52, 57]

Other airfoil analysis tools. While computational fluid dynamics (CFD) is widely used for fluid flow modeling, the transition models in commercial CFD packages do not adequately capture the physical phenomenon for airfoils very well, as detailed by Menter et al. [43] and Maughmer and Coder [58]. Additionally, the setup and computational time is generally at least two orders of magnitude greater than for the panel codes.

Blade Element Theory

Because the momentum theory does not account for blade shape and the aerodynamic effects of the individual blades, a more specific approach was developed known as the blade element theory (BET). The primary assumption behind this theory is that a wind turbine blade can be divided into discrete elements in the radial direction of

the blade, and the flow can be analyzed over each element as two-dimensional and independent of the other elements. In this way, each element can be analyzed as an airfoil that is producing lift and drag. Figure 2.16 shows the vectors of the wind velocities acting on a given blade element and the forces (shown as coefficients) it generates. Using this theory, wind turbine performance can be calculated based on a given wind speed, turbine rotational speed, and empirical or numerical lift and drag airfoil data. However, this theory is does not account for the general streamtube aerodynamics that are modeled using the general momentum theory.

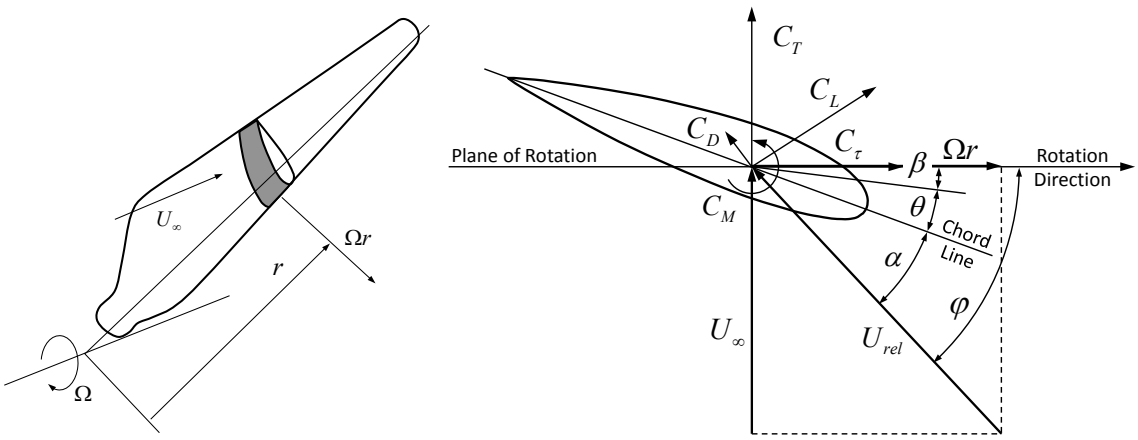

Figure 2.16: Blade Element (a) [27] and 2D Analysis of the Blade Element (b)

Figure 2.16 shows a number of important parameters. U_{rel} is the resultant vector of the freestream flow, U_∞, and flow generated by the rotation, Ωr. φ is the angle of the flow. β is the pitch angle, which for a fixed-pitch blade, is zero. θ is the angle of twist, and α is the angle of attack with respect to the relative flow of air. C_L, C_D, and C_M are the coefficients of lift, drag, and moment defined for airfoil, and C_τ and C_T are the coefficients of torque and thrust generated by the element of the blade.

BET Optimization

Using BET analysis, the only parameter that can be optimized for power output is the angle of twist. Based on this analysis, the optimal angle of twist is the angle that puts each element at the angle of attack that maximizes the lift to drag ratio, which is the peak on the L/D curve (shown in Figure 2.5). To calculate the optimum angle of twist distribution over the blade, the flow angle and the angle of attack at which the maximum L/D value occurs must be known. The angle of twist can be calculated by the equation

$$\theta = \varphi - \alpha_{max\ L/D} \tag{2.12}$$

where

$$\varphi = (\lambda_r)^{-1} \tag{2.13}$$

where

$$\lambda_r = \frac{\Omega r}{U} \tag{2.14}$$

In these equations, λ_r is the local TSR. The BET theory is appealing for a small-scale wind turbine designer because the application of the theory to design a blade with an optimum angle of twist is very simple.

Reynolds Number Regimes over Small-Scale HAWT Blades

For a wind turbine blade, the Reynolds number is still defined based on the chord of the airfoil, but the velocity used is no longer the freestream velocity, but the relative velocity, U_{rel}, as shown in Figure 2.16 (b) and detailed in the following equation

$$Re = \frac{\rho U_{rel} c}{\mu} \tag{2.15}$$

For small-scale HAWTs, the Reynolds number can vary from approximately 10,000 to 1,000,000 for a wind speed of 5 m/s, depending on the chord and diameter of the blade. Within this range, the flow is naturally laminar over most of the airfoil in the attached flow region. However, the flow conditions can change drastically, which is largely due to the effect of laminar separation and whether or not the flow reattaches and forms a separation bubble. Figure 2.17 illustrates the significant variation in airfoil

performance with Reynolds number for the NACA 66_3-018 airfoil. This behavior is both hard to model and hard to measure experimentally.

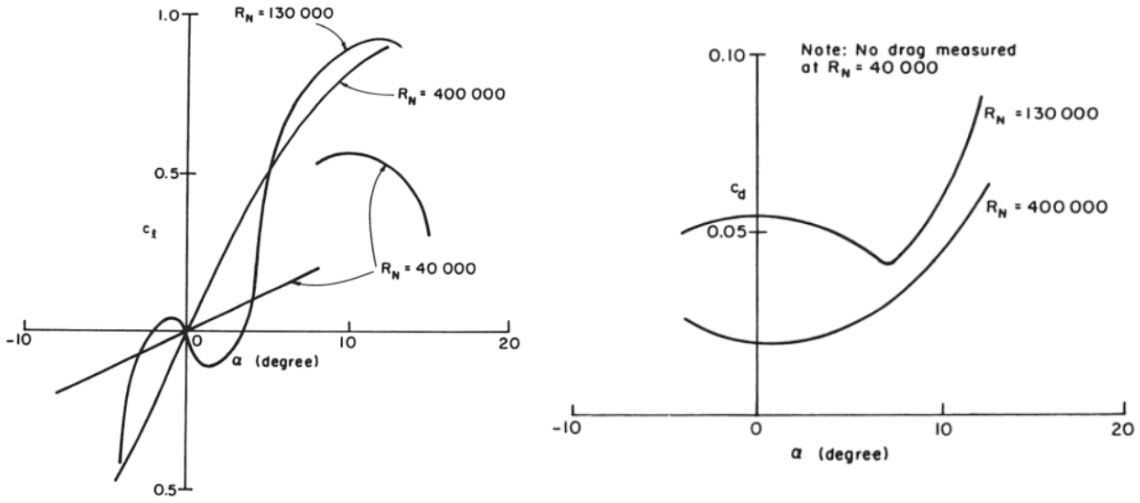

Figure 2.17: NACA 66_3-018 Airfoil Experimental Performance [59]

Based on this behavior, the flow conditions can be divided into general Reynolds number regimes. The first regime is 10,000 to 30,000, for which the flow is completely laminar over the airfoil for small angles of attack and mild pressure gradients. However, the lift coefficient is limited to about 0.5, because the flow laminarly separates. In this regime, once the flow separates it will not reattach [31]. The next regime is from 30,000 to 70,000. Carmichael expressed the average separation bubble length as a Reynolds number by using the average separation bubble length as the characteristic length. This resulted in an average separation bubble Reynolds number of 50,000 [31]. Thus, in this region, the flow may reattach once it separates, however, it is not likely. Forcing transition has shown to reduce separation and increase performance for some airfoils [31]. The third regime ranges from 70,000 to 200,000. In the generally attached flow region (angle of attack between -5 and 10 degrees), a laminar separation bubble will

likely be present and can significantly increase drag. In the lower end of this region, forcing flow transition near the leading edge of the airfoil can reduce drag and improve performance, but forcing transition is not typically needed at the higher end of this regime [47]. For the two regions between 30,000 and 200,000, a hysteresis effect has been noted and can produce different results in performance. Another region exists between 200,000 and 700,000. In this range of Reynolds number it is easy to obtain laminar flow. The laminar separation bubble can still be of significant length and worsen performance [31]. In this Reynolds number regime "extreme and unusual behavior is caused by anomalous transition, separation and [separation] bubble formation phenomena" [60]. Additionally, because of the presence of a laminar separation bubble and/or flow separation and natural transition, the flow is very sensitive to changes in freestream turbulence, surface finish, and airfoil shape [47]. The final region is between 700,000 and 3,000,000 and is the best quantified range with a vast amount of high-quality airfoil data. Within this regime, a laminar separation bubble is sometimes present but is typically small and causes only a small increase drag [31]. Because of the minimal effect of the laminar separation bubble on airfoil performance, the change in airfoil performance in this Reynolds number range is minimal, as shown by the coefficient of lift for the S809 airfoil in Figure 2.18. Figure 2.19 shows the coefficient of drag curves change fairly significantly with Reynolds number and decrease nearly 40% as Reynolds number increases from a Reynolds number of 1,000,000 to 2,500,000. However, the actual drag forces are generally minimal compared to the lift forces and this variation in drag will not produce a significant variation in power production on a turbine. For the wind turbine tested in this study, the Reynolds numbers at the design wind speed of 5 m/s

range from approximately 15,000 to 300,000 depending upon the scale and chord distribution of the blade.

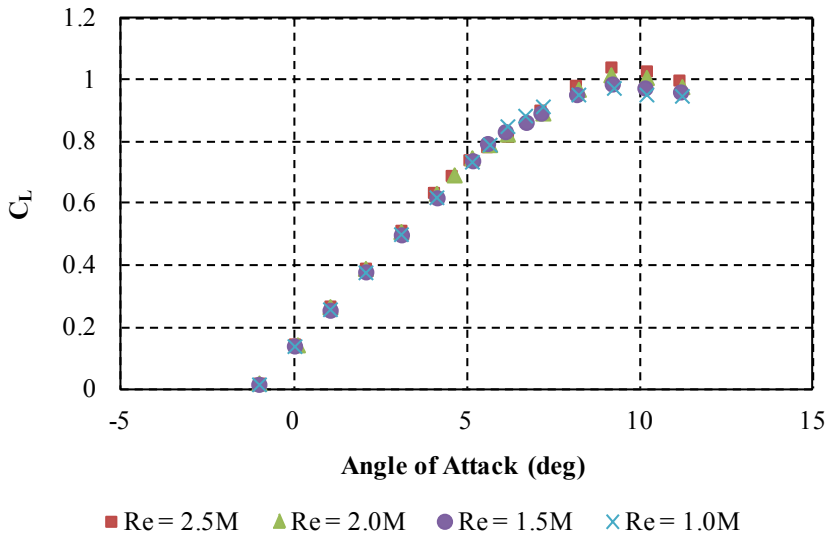

Figure 2.18: S809 Coefficient of Lift Curve [61]

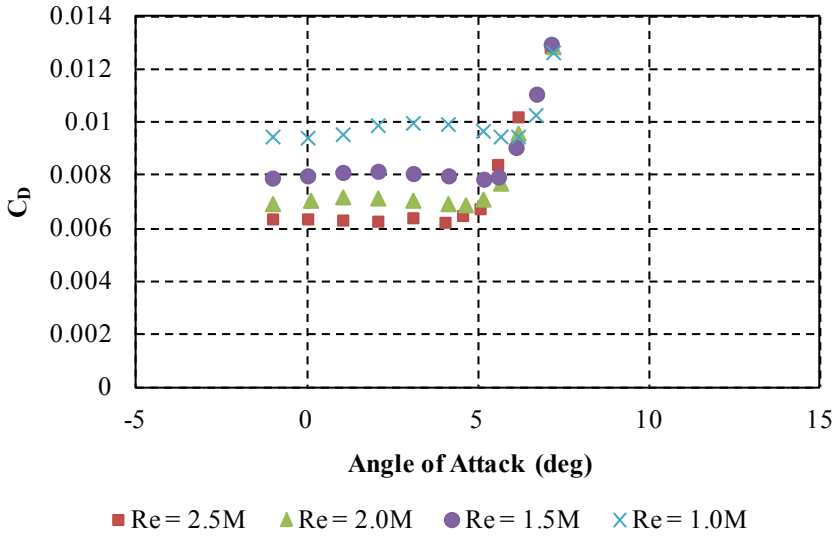

Figure 2.19: S809 Coefficient of Drag Curve [61]

Dependence of Design Angle of Attack on Reynolds Number

In using airfoil data to design a wind turbine using BET, the angle of attack at maximum lift-to-drag ratio is critical. In general, this angle of attack will change with

Reynolds number, as seen in Figure 2.20 for the S809 airfoil. However, the optimum design angle only changes from 4.1 to 6.2 degrees over a range of 2 million Reynolds number, and the magnitude of the peak lift-to-drag ratio for ranges from approximately 120 to 90. For low Reynolds numbers, this change in design angle is similar, as seen in Figure 2.21 [52, 62]. This figure shows data for the E387 airfoil taken at the NASA Langley Low-Turbulence Pressure Tunnel (LTPT) for Reynolds numbers between 60,000 and 460,000. For the E387 airfoil over the range of Reynolds numbers shown in the figure, the design angle changes from 6.5 to 8.5 deg over a range of Reynolds number of 0.4 million, and the magnitude of the peak lift-to-drag ratio ranges from approximately 40 to 100. Obviously, the range of change in the design angle will be different for every airfoil; however, both the angle and magnitude of the maximum lift to drag ratio varies more with Reynolds number for the lower Reynolds numbers. This is due to the effect of the laminar separation bubble mentioned previously and needs to be taken into account in wind turbine design.

The obvious follow-up question to the discussion of the design angle changing with Reynolds number is an analysis of how much wind turbine performance actually changes with a specified change in design angle. Data is currently available from the NREL Phase VI experiments [63], which was a wind tunnel test of a 10-m diameter, variable-pitch wind turbine. In the testing, the pitch was fixed at multiple angles and the wind turbine was tested while spinning at a constant speed of 72 rpm. The results from this experiment are shown in Figure 2.22. Noticeably, while there is a measureable difference in the coefficient of power at wind speeds below 10 m/s, the difference is not significant in the actual power produced, as the measurements are all within approximately 0.5 kW. These wind speeds are in the pre-stall region, where the flow

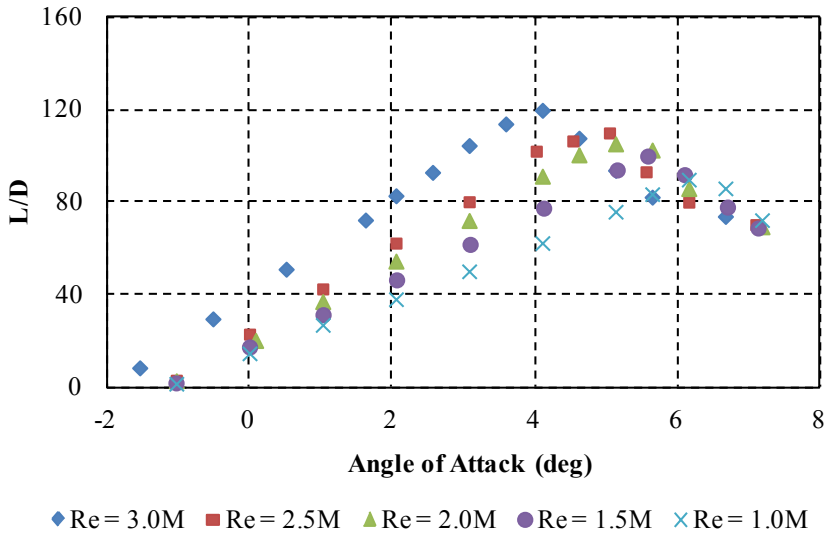

Figure 2.20: S809 Airfoil Data from Delft University of Technology [61]

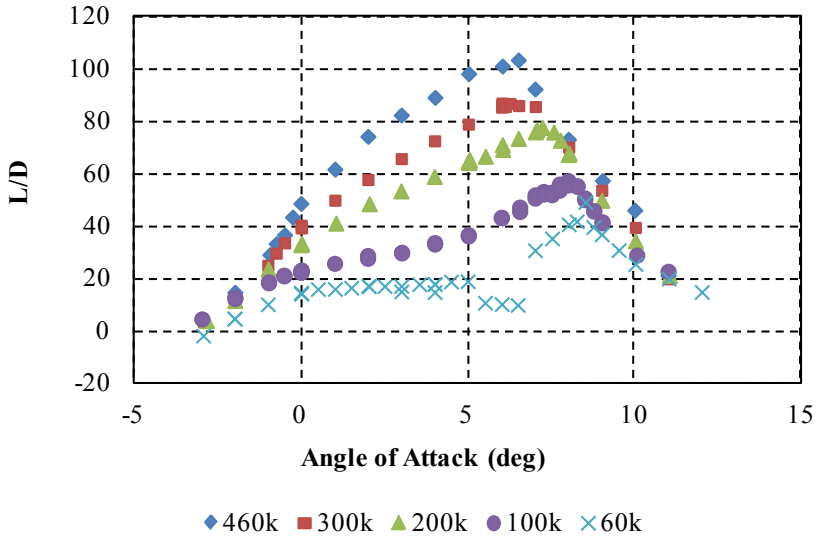

Figure 2.21: E387 Airfoil Data from the NASA Langley LTPT [52]

over the blades is largely attached and turbine operating efficiently. However, at wind speeds of 10 m/s and higher, there is a significant difference in the Power measurement, with a difference of up to 2.72 kW. These wind speeds correspond to the stalled region, when the turbines are no longer operating efficiently. While the wind turbine in this test

was operating at a constant rotational velocity, it is notable that changing the pitch angle does not have a significant effect on power production in the pre-stall region but does in the stall region. The obvious question after analyzing this data is how much changing the design angle affect the power output of a fixed-pitch wind turbine.

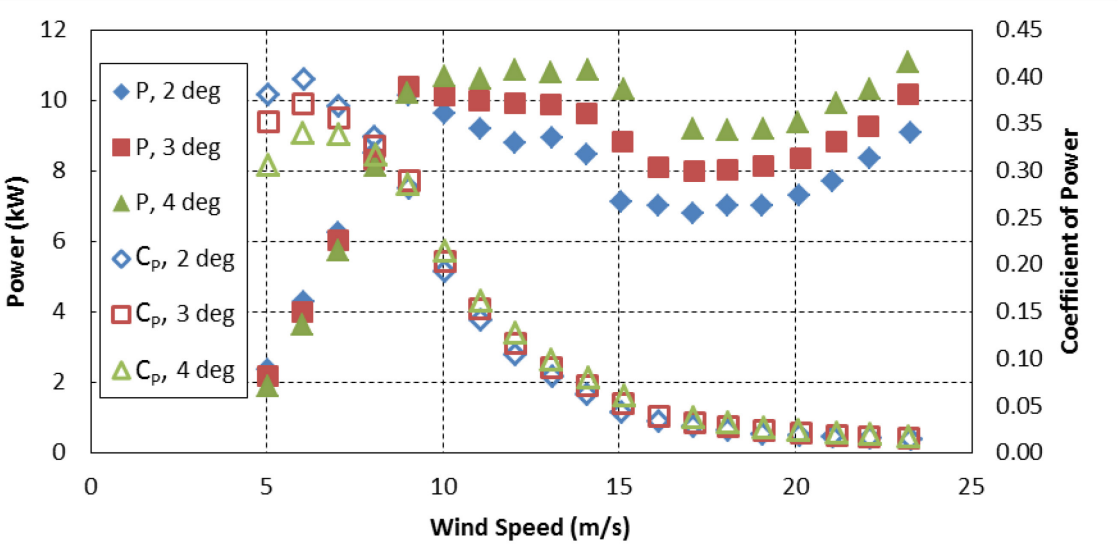

Figure 2.22: Power and Coefficient of Power for NREL Phase VI Experiment for Multiple Pitch Angles at 72 RPM [63]

Blade Element Momentum Theory

Because the momentum theory only captures the general aerodynamics and the blade element theory only captures the blade-specific aerodynamics, the two have been combined to achieve a realistic model that accounts for blade geometry. The combination of the two theories is known as and referred to in this work as the Blade Element Momentum Theory (BEMT). This theory is also known as strip theory because it divides the streamtube into strips coinciding with the blade elements for analysis. Figure 2.23 shows both an example blade element division on a blade (a) as well as an example annular strip division in the streamtube (b) that would be used in BEMT.

Comparing the elemental analysis of BEMT to BET, the only change is the inclusion of the induction factors, which reduces the freestream component of velocity and increases the rotational component of the velocity (as seen in Figure 2.24), thereby reducing the airfoil angle of attack from the BET analysis.

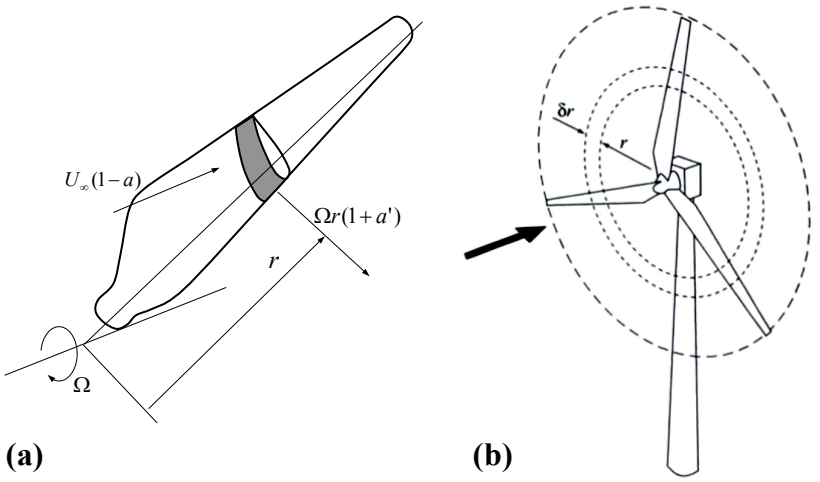

Figure 2.23: (a) Blade Element and (b) Annular Strip analyzed in BEMT [27]

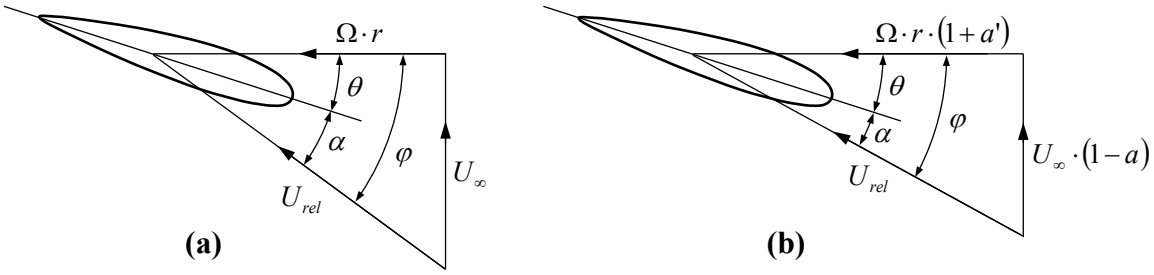

Figure 2.24: Elemental Velocity Triangle for (a) BET and (b) BEMT [27]

Even though the assumptions of both the momentum theory and blade element theory are not realistic, BEMT, with a few corrections, has been shown to yield reasonable accuracy for some flow conditions, as in the study by Anderson et al. [64]. However, in a blind comparison with the NREL Phase VI experiment in the NASA Ames 80 ft by 120 ft wind tunnel, the BEMT predictions differed from the experimental data by

25% to 175% when the flow was completely attached over the wind turbine blade, which BEMT should be able to predict reasonably well [65]. Some studies since the original comparison, however, have been able to match the experimental data from the Phase VI [66, 67] or MEXICO [68, 69] experiments.

In BEMT models the largest source of inaccuracy is often the airfoil data used [60, 70]. This can be due to limited airfoil data at both the appropriate Reynolds number and in the stall region. As previously mentioned, the Reynolds numbers of interest in this study range from 15,000 to 300,000. For Reynolds numbers from 100,000 to 500,000, experimental data taken by Selig et al. and Lyon et al. is available for a wide range of airfoils, including the S823 airfoil [57, 71, and 72]. Some data was also taken at Reynolds numbers of 40,000 and 60,000, although this is not available for the S823 airfoil. For the lower range of Reynolds numbers from 15,000 to 100,000, no experimental S823 airfoil data has been published. Additionally, aerodynamic codes do not always capture the flow accurately depending upon the flow phenomena present in this Reynolds number range as previously mentioned [62].

Predicting wind turbine performance in off-design conditions requires airfoil data in the stall region for fixed-pitch blades. This is problematic because there is a general lack of experimental airfoil data outside the traditional attached flow region. It is also difficult to simulate the aerodynamics outside this region with codes such as XFOIL or PROFIL, as noted earlier. Various models have attempted to extrapolate airfoil data outside of the typical attached flow region with limited success in only a few cases. The models have not demonstrated the ability to predict well for a wide variety of flow cases [60, 67, 73-75]. While the data from these models are better than to having post-stall data, experimental two-dimensional airfoil data taken in the post-stall region rather than a

post-stall model will produce the most accurate turbine model. To model constant-rpm, fixed-pitch wind turbines, it is essential to model post-stall airfoil data. However, for constant-TSR, fixed-pitch wind turbines, modeling the post-stall airfoil data is only necessary at higher wind speeds when the rotational speed is limited by the controller. Nonetheless, a well-designed wind turbine of this type should only require rotational speed limitation at high wind speeds that do not occur often and have minimal impact on the annual energy production (AEP) of the wind turbine.

Many other corrections have been developed to increase the accuracy of the BEMT modeling methods. Some corrections deal with flow over the turbine blades in general, the most notable being the tip loss correction derived by Prandtl (in an appendix to a work written by Betz) [76] and applied to rotors by Glauert [77]. The same idea can be applied to account for hub loss [78]. While both tip-loss and hub-loss corrections can be significant in reducing the power production, the tip-loss correction generally has a much greater impact because more torque is generated at the tip of the blade than at the root. Other corrections deal with the flow over each element, and, thus, "correct" the airfoil data for the three-dimensional flows that actually occur on the blade due to rotation. However, for attached flow there should not be a significant difference between the two-dimensional airfoil flow and the rotating conditions [78-81]. The primary three-dimensional flow phenomenon that occurs is airfoil stall delay, which is discussed extensively by Hansen and Butterfield [82]. The phenomenon of stall delay occurs when flow separation is delayed on a wind turbine blade due to the favorable pressure gradients developed by rotation [82, 83]. For a fixed-pitch wind turbine, the effects of stall delay are not significant except in the stall-controlled portion of the wind turbines performance when flow over the blade is largely separated [84]. Because of stall delay, wind turbine

power production in this region is often under-predicted by models even if a stall-delay correction is used [82]. Multiple stall delay corrections have been proposed and evaluated experimentally by Snel [80, 81], Du and Selig [85], Bak et al. [86], and Tangler and Selig [87]. In a review of wind turbine aerodynamics, Sorenson presents a simple and general approach to corrections for stall delay [25]. Additionally, Spera documents a correction to account for a cascade effect, or flow interactions between blades [60]. The cascade effect is only significant at the root of the blades where the circumferential distance between the blades is minimal, and, similar to the hub-loss correction, is generally much less than the effect of the tip-loss correction because of the greater torque generated near the tip of the blade.

Additionally, the classical solution for the coefficient of thrust violates the basic assumptions used in derivation for axial induction factors greater than 0.5. Notably, axial induction factors this high do not occur at the optimum design, which should have an axial induction factor of 1/3. To correctly calculate the thrust coefficient for high axial induction factors, Glauert's turbulent wake state or windmill state empirical correction [88] is commonly applied to the local thrust coefficient when the axial induction factor is greater than 0.4, the intercept of the two curves, shown by the equation

$$C_{T_r} = 0.889 - \frac{0.0203 - (a - 0.143)^2}{0.6427} \tag{2.16}$$

where C_{T_r} is the local coefficient of thrust. Other variations of Glauert's correction have chosen the intercept to be 0.326 or 0.368 [27]. Figure 2.25 shows the comparison of the classical thrust coefficient theory versus axial induction factor curve contrasted with the empirical corrections by Glauert [88], Burton et al. [27], and Wilson [60]. However, when including the hub and tip loss factors in the thrust coefficient equation, the classical

and empirical curve no longer intercept, as seen in Figure 2.26. For this reason, Buhl [89] developed an empirical equation that intercepts the classical thrust coefficient equation at an axial induction factor of 0.4 when the loss factor is applied, shown by the equation

$$C_{T_r} = \frac{8}{9} + \left(4F - \frac{40}{9}\right) a + \left(\frac{50}{9} - 4F\right) a^2 \tag{2.17}$$

where F is the local loss factor. Using an empirical thrust coefficient correction that has a gap with tip- and hub-loss factors less than unity and the axial induction factor is near the intercept of the two lines, has potential to prevent convergence in the BEMT algorithm.

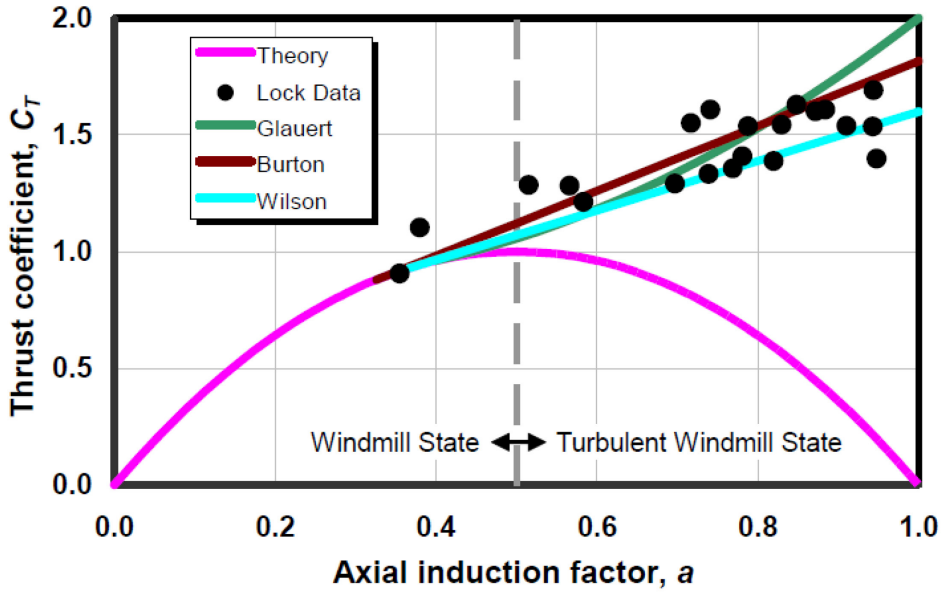

Figure 2.25: Thrust Coefficient vs. Angle of Attack curves when tip/hub losses are ignored [89]

Other corrections to the BEMT theory exist for predicting off-design conditions such as non-uniform wind inflow and the turbine operating at a yaw angle, but because the theory in this work is being compared with wind tunnel experiments with uniform

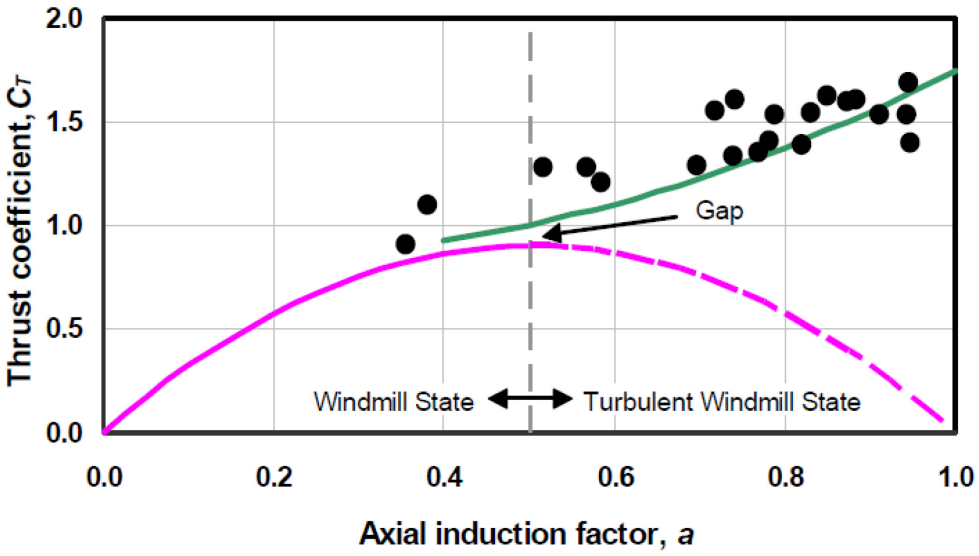

Figure 2.26: Classical Thrust Coefficient vs. Angle of Attack curve with Glauert's empirical relation when losses (F = 0.9) are included in the equations [89]

inflow and no-yaw conditions, these corrections are unnecessary. For small-scale HAWTs, the inflow is essentially uniform and the turbines do not experience yaw angles for a significant period of time.

BEMT Algorithms

The BEMT equations cannot be solved analytically for most cases, but must be solved numerically. A number of algorithms exist for solving these equations, most notably the algorithm employed in the NREL codes Aerodyn and WT_Perf [90] and the two algorithms detailed by Manwell et al. [26]. These algorithms are notable for the small-scale wind designer because they are reasonably-documented and should prove relatively easy to implement without a significant investment of time or money. For this work, the second method employed by Manwell et al. will be used because it is well documented [26]. In this algorithm, the flow conditions over each element are solved

iteratively and individually. An important parameter used in this algorithm is known as the local blade solidity, defined by the equation

$$\sigma_r = \frac{B \cdot c}{\pi \cdot r} \tag{2.18}$$

where B is the number of blades, c is the local chord length, and r is the local radius. Beginning with the innermost element and working out to the outermost element, the algorithm presented by Manwell et al. starts solving the flow over each element with a guess for the induction factors. The induction factors for maximum power production according to momentum theory are used for initial guesses, 1/3 for the axial induction factor and zero for the tangential induction factor. Next, the flow angle is calculated by the equation

$$\varphi = \frac{1-a}{(1+a\prime)} {\lambda_r}^{-1} \tag{2.19}$$

Subsequently, the angle of attack for that element can be calculated by the following equation

$$\alpha = \varphi - \theta \tag{2.20}$$

where θ is the angle of twist for the blade being simulated. Further, the coefficients of lift and drag can be calculated for that blade element, which are functions of the angle of attack and the Reynolds number as seen in the equations

$$C_L = f(\alpha, Re) \tag{2.21}$$

$$C_D = f(\alpha, Re) \tag{2.22}$$

Because only discrete airfoil data is typically available, the airfoil data for Reynolds numbers greater and less than the flow Reynolds number can be splined to determine the coefficients of lift and drag for those angles of attack. Further, the coefficients of lift and drag were calculated by linearly interpolating between the data a Reynolds number above

and below the Reynolds number experienced by that element. Next, the coefficient of thrust was calculated using the equation

$$C_{T_r} = \frac{\sigma_r(1-a)^2(C_{\mathrm{L}}\cos\varphi + C_{\mathrm{D}}\sin\varphi)}{\sin^2\varphi} \tag{2.23}$$

Further, the tip loss factor was calculated using Prandtl's tip-loss equation

$$F_{tip} = \frac{2}{\pi}\cos^{-1}\left[\exp\left(-\left\{\frac{B/2(1-r/R)}{r/R\sin\varphi}\right\}\right)\right] \tag{2.24}$$

The axial induction factor was calculated using BEMT theory in the follow equation if C_{T_r} was less than 0.96

$$a = \left[1 + \frac{4F_{tip}\sin^2\varphi}{\sigma_{\mathrm{r}}C_L\cos\varphi}\right]^{-1} \; if \; C_{T_r} < 0.96 \tag{2.25}$$

but was calculated using Glauert's empirical turbulent wake-state correction if C_{T_r} was greater than 0.96 using the equation

$$a = \frac{1}{F}\left[0.143 + \sqrt{-0.55106 - 0.6427C_{T_r}}\right] if \; C_{T_r} \geq 0.96 \tag{2.26}$$

The tangential induction factor was calculated using the equation

$$a' = \left[\frac{4F_{tip}\cos\varphi}{\sigma_r C_L} - 1\right]^{-1} \tag{2.27}$$

Equations 2.19-2.27 were iterated until the relative error between the previous value and current value for the axial induction factor was less than 10^{-6}. The relative error was calculated by the equation

$$\varepsilon_{rel} = \left|\frac{a - a_{prev}}{a}\right| \tag{2. 28}$$

After the above convergence criteria was met, the coefficient of power was calculated with the equation

$$C_P = \frac{8}{B\cdot\lambda}\sum\left[F_{tip}\sin^2\varphi\,(\cos\varphi - \lambda_r\sin\varphi)(\sin\varphi + \lambda_r\cos\varphi)(1 - C_D/C_L\cot\varphi)\lambda_r{}^2\right] \tag{2.29}$$

Optimizing Blade Shape with BEMT

For maximum power output, momentum theory dictates that the axial induction factor (a) is equal to 1/3. Applying this assumption and assuming there is no wake rotation (i.e. the tangential induction factor, a', equals zero), it is possible to analytically derive an optimum flow angle and chord, as derived by Manwell et al. [26] and Hansen [91]. The optimum flow angle is shown by Equation 2.30,

$$\varphi = \tan^{-1}\left[\frac{2}{3}{\lambda_r}^{-1}\right] \tag{2.30}$$

and the angle of twist can be calculated using Equation 2.12. The optimal chord can be calculated using the equation

$$\frac{c}{r} = \frac{8\pi \sin\varphi}{3BC_L\lambda} \tag{2.31}$$

where B is the number of blades and C_L is the coefficient of lift for the chosen angle of attack used in the blade design. Burton et al. include wake rotation in the derivation of the optimum flow angle and chord by neglecting the contribution of drag [27]. Thus, the optimal tangential induction factor is shown by the equation

$$a' = \frac{2}{9}{\lambda_r}^{-2} \tag{2.32}$$

The optimal flow angle is shown by the equation

$$\varphi = \tan^{-1}\left\{\frac{2}{3}[\lambda_r(1+a')]^{-1}\right\} \tag{2.33}$$

Again, the angle of twist can be calculated using Equation 2.12. Additionally, the optimal chord distribution is given by the equation

$$\frac{c}{r} = \frac{16\pi}{9B\lambda C_L}\left\{\frac{4}{9} + [\lambda_r(1+a')]^2\right\}^{-1/2} \tag{2.34}$$

Further, Burton et al. discusses tip and hub losses and the Prandtl tip- and hub-loss correction, given by the equations

$$F_{tip} = \frac{2}{\pi}\cos^{-1}\left[e^{-\frac{B}{2}\frac{(R-r)}{r}\sqrt{1+{\lambda_r}^2/(1-a)^2}}\right] \tag{2.35}$$

$$F_{hub} = \frac{2}{\pi}\cos^{-1}\left[e^{-\frac{B}{2}\frac{(r-r_{hub})}{r}\sqrt{1+{\lambda_r}^2/(1-a)^2}}\right] \tag{2.36}$$

which can be combined into one loss factor using the equation

$$F = F_{tip}F_{hub} \tag{2.37}$$

Burton et al. continue to analytically solve for the optimum tangential induction factor, given by the equation

$$a' = \frac{1}{3}\left(1 - \frac{1}{3F}\right){\lambda_r}^{-2} \tag{2.38}$$

as well as the optimum flow angle

$$\varphi = \tan^{-1}\left[\left(1 - \frac{1}{3F}\right)\left(\lambda_r\left(1 + \frac{a'}{F}\right)\right)^{-1}\right] \tag{2.39}$$

Finally, the optimum chord distribution is given by the equation

$$\frac{c}{r} = \frac{16\pi}{9B\lambda C_L}\left\{\left(1 - \frac{1}{3F}\right)^2 + \left[\lambda_r\left(1 + \frac{a'}{F}\right)\right]^2\right\}^{-1/2} \tag{2.40}$$

However, these BEMT-optimized equations only apply for blades with the given optimal chord distribution, and these equations cannot be used to predict wind turbine performance.

Multiple studies have been performed using BEMT codes to optimize blade shape. Using a BEMT code rather than just the analytically derived equations (shown in Equations 2.30-2.40) allows evaluation of off-design performance as well as optimization for a range of different parameters. Rather than optimizing for power production at the design wind speed and TSR, the blade shape can be optimized based on the AEP and/or a

cost function. Additionally, physical or practical constraints on chord length can be applied since the optimal chord distribution is not always the feasible.

Other HAWT Analysis Tools

Additionally, other theoretical models for analyzing the flow over wind turbines exist, such as vortex theory or CFD. Vortex theory, while providing more information about the flow field, excludes wake expansion [27]. CFD is too computationally expensive to use in design for the small-scale wind turbine designer. However, CFD is often used to improve an existing design by varying a few parameters like in the study performed by De Bellis and Catalano [92]. Optimization in CFD for all the parameters defining a blades shape is not reasonable because each variable added increases the computational time exponentially and the necessary computational time and computational resources are not practical.

Quantifying and Comparing Wind Turbine Performance

In quantifying and comparing the performance of wind turbines, coefficient of power is often utilized (defined in Equation 2.3). Additionally, the actual power output that the wind turbine will produce at a particular site, known as the average wind turbine power, can be used to compare how much power different turbines will produce at a specific site. The average wind turbine power is defined by the equation

$$P_W(U) = P_{rotor}(U)Pr(U) \tag{2.41}$$

where $P_{rotor}(U)$ is the power produced by the turbine blades at a particular wind speed (defined by Equation 2.2) and $Pr(U)$ is the probability that the wind will be blowing at that particular speed for that particular site. The AEP is the total power produced over the course of a year, as defined by the equation

$$AEP = \int_0^\infty P_{rotor}(U)Pr(U)\mathrm{d}U = \int_0^\infty P_W(U)\mathrm{d}U \quad (2.42)$$

While the actual data is discrete, a cubic spline can be fitted to the data and the resulting spline numerically integrated. However, unless a wind site survey is performed, calculating the AEP requires assuming the wind distribution, which may or may not be reasonable. A final parameter for comparison is the cut-in wind speed of a turbine, defined as the lower wind speed at which the wind turbine produces power.

Optimum Theoretical HAWT Blade Design

Multiples studies have analyzed the optimum theoretical HAWT blade design with many definitions of what is "optimum." The purpose of this section is to discuss the ways that a wind turbine can be optimized theoretically, including the parameters that can be varied in the optimization as well as the criteria for the optimization.

To improve the performance of a wind turbine with a particular diameter and operating in specified wind conditions, the primary method to improve performance is to change the blade shape. Three parameters define the blade shape: the chord distribution, the twist distribution, and the airfoil or airfoils used in the blade. Additionally, fixed-pitch turbines can be designed for a constant TSR or for a constant rotational velocity; however, the latter is less efficient. Thus, a final parameter in addition to the blade shape is the TSR. Using BET or BEMT, the effect of changing the chord distribution, twist distribution, or TSR is fairly simple to calculate once the model is developed. However, calculating a change in the airfoil used to design the blade requires an entirely new set of airfoil data. Thus, a significant amount of thought and planning should go into the airfoil selection.

Choosing an appropriate airfoil for the flow conditions which the prospective wind turbine will experience is critical to achieving the desired performance. This will include the Reynolds number range that the wind turbine blade will operate under as well as the range of angles of attack. Some airfoils perform well at high Reynolds numbers and others are designed specifically to perform well at low Reynolds numbers with minimal flow separation. Specific to a fixed-pitch wind turbine, an airfoil with a gentle stall is desirable.

NREL has designed families of airfoils for multiple size wind turbines using the aerodynamic code PROFIL. One of the primary concerns in designing an airfoil for use on a wind turbine blade is the lift-to-drag ratio because of its direct relationship to torque and to power production. Thus, a high lift-to-drag ratio is one of the most critical aspects of a wind turbine airfoil [53]. A unique parameter for wind turbine airfoil design is that the airfoils must be relatively insensitive to roughness. While this is not critical for an airplane because the wing can be cleaned upon landing, wind turbine blades are rarely cleaned [93]. For an airfoil used at the root of the blade, it is desirable to have a thick airfoil to increase the structural integrity of the blade [93]. Another problem with airfoils used for fixed-pitch wind turbines is that they have produced excessive power at high wind speeds. To remedy this, NREL designed airfoils for the root, outboard, tip regions of the blade that have a low maximum lift coefficient. This also reduces the stresses over the blade [94]. Additionally, thin airfoils have been design for the tip of the blade to reduce the weight of the blade and thus the cut-in speed and the cost of the blade [53]. As a final consideration, NREL has designed airfoils that produce minimal noise [95].

Other researchers have also designed airfoils for wind turbines. Giguere and Selig have designed airfoils that have at least 10% thickness as well as a very high

maximum lift to drag ratio over a wide range of Reynolds numbers [96]. Additionally, Fuglsang and Bak [97] document the airfoils designed by the Riso National Laboratory. These airfoils were designed for Reynolds numbers greater than one million and are not applicable to this study. Also, extensive wind tunnel tests have been performed on airfoils for wind turbines at low Reynolds numbers [57, 71, 72, 98, and 99]. However, the lower limit of the experimental tests is most often a Reynolds number of 100,000. A few tests were performed at Reynolds numbers of 40,000 and 60,000.

The S823 was tested in this research because of its design for small-scale, low wind speed HAWTs. The National Renewable Energy Laboratory (NREL) designed this family of airfoils, the S822 to S823, for fixed-pitch wind turbines 3-10 meters in diameter [48]. This family of airfoils has been "designed and analyzed theoretically" using PROFIL [48]. The S823 is used specifically for this research because it has been designed for the root of the blade, the part of the turbine that sees the lowest Reynolds numbers. Notably, the S833 to S835 family of airfoils should be more applicable to this research because they were designed for a smaller wind turbine, 1-3 meters in diameter. However, on initial comparison of the S823 with the S835 [100] (both of these airfoil shapes are for the root of the blade where the Reynolds number is lowest) using the published PROFIL data, the S823 has a higher maximum lift coefficient and lift to drag ratio over the range of Reynolds numbers of interest in this study.

Typically in wind turbine optimization, a specific wind speed or wind class is chosen at which to perform the optimization. For example, Ceyhan et al. utilized a genetic algorithm to optimize the wind turbine performance for a chosen wind speed and TSR by varying the chord and twist distribution [101]. The optimization was applied to an existing design and improved the performance by 80% at the design point.

Additionally, the starting performance of the wind turbine can be considered, because if the cut-in speed is lowered, then the wind turbine can produce power where it was initially producing none. Clifton-Smith and Wood utilized evolutionary optimization to optimize the chord and twist distributions as well as the TSR for maximum power output and starting performance [102].

Rather than choosing a specific wind speed or wind class to optimize turbine performance, a wind distribution can be used. This is more difficult because the wind turbine performance over a range of wind speeds must be known. For example, Mendez and Greiner used a genetic algorithm combined with BEMT to optimize the blade chord and twist to optimize the AEP [103]. In another study, Dossing et al. applied an unconstrained steepest descent optimization algorithm with the length step determined by the golden section method to maximize the power output of the turbine at a specific TSR by a geometry parameter that accounted for the chord and twist distributions [104]. Another consideration can be noise reduction, as in the study performed by Xuan et al [105]. In their study, genetic algorithm was used to maximize the AEP and minimize the noise level by varying the airfoil shape of each element. Since the airfoil performance data was not a fixed input, it was evaluated using XFOIL.

A final parameter that can be included in the optimization can be the cost of energy. For example, Xudong et al. minimized the cost of energy by varying the chord, twist, and relative thickness of the blade using the "fmincon" function in MATLAB® [106]. Additionally, Benini and Toffolo applied a multi-objective optimization using an evolutionary optimization algorithm to maximize the AEP per square meter of a wind park and minimized the cost of energy by varying TSR, hub-to-tip ratio, chord distribution, and twist distribution [107]. Further, Eke and Onyewudiala applied a

genetic algorithm for minimum cost of energy and maximum AEP by varying the chord and twist distributions as well as relative thickness [108]. In another study, Raju both optimized the power with a mass constraint and optimized the mass with a power constraint by varying the chord distribution [109]. While a cost function was not used, a mass constraint was applied because reducing the mass of the blades reduces the cost of the turbine.

Experimental Wind Tunnel Testing

Airfoil Testing

Measurement techniques. Multiple techniques exist for quantifying airfoil performance experimentally. Generally speaking, there are two sets of parameters of interest. One is the pressure profile over the airfoil, and the second includes the aerodynamic forces generated by the airfoil. The pressure profile is typically measured using static pressure ports along the surface of the airfoil. The pressure profile can also be used to calculate the lift and drag forces over the airfoil. However, it is more common to directly measure the forces generated by the airfoil using a force measurement device. Most often, the airfoil will be mounted on a sting, which is connected to a force balance like the one seen in Figure 2.27. This particular model is a three-dimensional model because the airfoil does not span the whole wind tunnel. However, a model can be mounted on a force balance that spans the whole tunnel so that no three-dimensional corrections are necessary. Figure 2.28 shows a two-dimensional model that would have a load cell mounted on the tunnel wall to measure lift and moment. Typically with this type of model the drag is measured using the momentum-wake deficit method. However,

the momentum-wake deficit method can be limited to the range of angles of attack that can be measured if the extent of the wake cannot be quantified because of interactions with the upper and lower wind tunnel walls. Additionally, Barlow et al. notes that momentum-wake deficit method is considered questionable for airfoils with flow separation present [59]. Selig et al. measure lift, moment, and drag using wall-mounted load cells and the momentum-wake deficit method [99, 110]. The experimental tests performed in this work use a two-dimensional model and a force balance with a single mounting location.

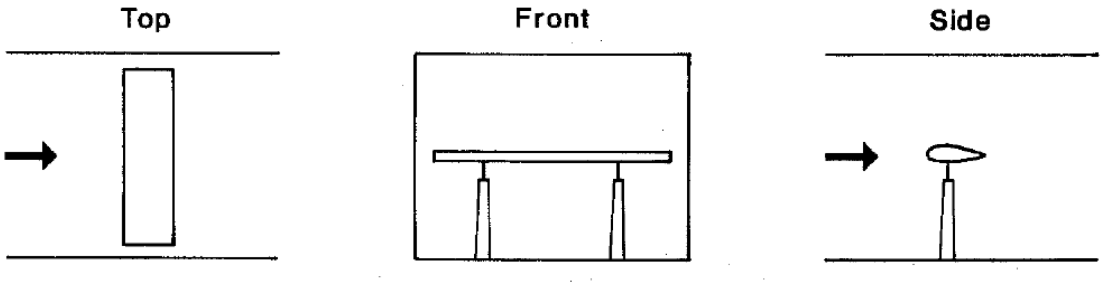

Figure 2.27: Three-dimensional Airfoil Model with Force Balance [111]

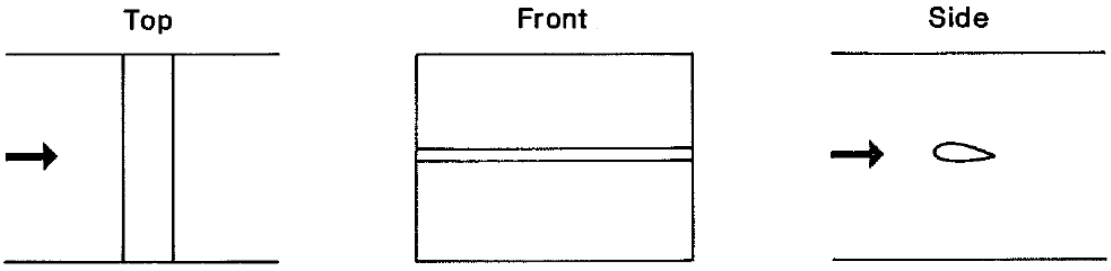

Figure 2.28: Two-dimensional Airfoil Model [111]

Wind tunnel corrections. While wind tunnel corrections are often only applied if the wind tunnel blockage is greater than 10%, for airfoil testing wind tunnel corrections have become standard. Two sets of wind tunnel corrections are clearly documented, one

in the textbook *Low Speed Wind Tunnel Testing* by Barlow et al. [59] and the other in documentation of low speed wind tunnel testing by Selig et al. [99]. These corrections apply for a range of effects caused by the wind tunnel wall, and these effects can be divided into three categories: blockage, streamline curvature, and buoyancy.

The first type of blockage is solid blockage, which is caused by the presence of a model within the wind tunnel test section. This decreases the effective area that the stream tube of air is flowing through. Applying Bernoulli's equation shows that the velocity must increase when it flows through the decreased area, effectively increasing all aerodynamic forces and moments for that angle of attack. The correction for solid blockage can be calculated using the following equation

$$\varepsilon_{sb} = \frac{K \cdot V_m}{{A_{ts}}^{3/2}} \tag{2.43}$$

where K is a constant of 0.74 for a wing spanning the tunnel breadth, V_m is volume of the model, and A_{ts} is the cross-sectional area of the test section. Notably, the solid blockage correction factor is merely a function of model volume and wind tunnel cross-sectional area. Additionally, accounting for only the model volume does not account for the change that occurs with airfoil orientation. However, since the airfoil will be operating over a relatively small range of angles, this correction factor is sufficient.

The second type of blockage is wake blockage, which is caused by a decreased velocity in the airfoil wake. According to the continuity equation for a closed test section, the freestream velocity must increase. The effect of the blockage is proportional to the size of the wake, thus, it is proportional to the measured value for drag. The constant of proportionality only depends on the chord of the airfoil and the height of the test section, as seen in the equation

$$\varepsilon_{wb} = \left(\frac{c}{2h_{ts}}\right) C_{D_u} \tag{2.44}$$

where c is the chord of the airfoil, h_{ts} is the height of the test section, and C_{D_u} is the uncorrected, measured drag coefficient.

The second effect caused by the wind tunnel walls is streamline curvature. This is because the physical boundaries of the walls interfere with the natural curvature of the free air over the model, effectively increasing the airfoil effective camber and a subsequent increase in lift, moment, and angle of attack. However, the drag is not affected by this phenomenon. Equation 2.45 documents the streamline correction factor.

$$\sigma = \frac{\pi^2}{48}\left(\frac{c}{h_{ts}}\right)^2 \tag{2.45}$$

Buoyancy, or boundary layer growth, is the third notable effect of the wind tunnel walls. As the air moves through the wind tunnel, the boundary layer will grow increasingly large and the static pressure will decrease. Since the freestream velocity is measured upstream of the model, the actual freestream velocity at the model is higher. This correction factor must be determined experimentally for each unique wind tunnel and has not been completed for the Baylor Subsonic Wind Tunnel, so this analysis will not include this correction. Equation 2.46 shows the form of the correction factor, and Equation 2.47 shows the correction factor equation used by Selig et al. [112].

$$K_{vel} = f(U_u) \tag{2.46}$$

$$K_{vel} = 1.015755 - 0.0002391U_u + 0.00001712\sqrt{U_u} + \frac{0.1296}{\sqrt{U_u}} \tag{2.47}$$

where U_u is the uncorrected velocity and $f(U_u)$ is a function of the uncorrected velocity. Figure 2.29 shows the variation of the velocity correction factor with Reynolds number. While this correction is insignificant for Reynolds numbers above 400,000, the correction

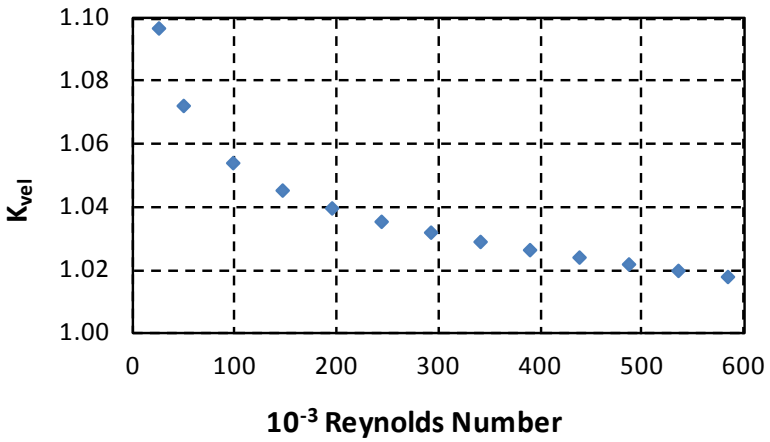

Figure 2.29: Buoyancy Correction Factor Variation

factor increases as Reynolds number decreases, suggesting that such a correlation should be determined for low Reynolds number testing.

Multiple methods of combining these correction factors have been published; for this study, however, the method presented by Barlow et al. [59] is used and documented in the following equations

$$U = U_u(1 + \varepsilon_b) \tag{2.48}$$

$$\alpha = \alpha_u + \left(\frac{1}{8\pi}\frac{c^2}{{h_{ts}}^2 + (c/4)^2} + \frac{1}{2\pi}\sigma\right) C_{L_u} \tag{2.49}$$

$$C_L = C_{L_u}(1 - \sigma - 2\varepsilon_b) \tag{2.50}$$

$$C_{\mathrm{D}} = c_{D_u}(1 - 3\varepsilon_{sb} - 2\varepsilon_{wb}) \tag{2.51}$$

where

$$\varepsilon_b = \varepsilon_{sb} + \varepsilon_{wb} \tag{2.52}$$

Considerations for low Reynolds number airfoil testing. In addition to the wind tunnel corrections mentioned above, a number of considerations should be kept in mind when performing wind tunnel tests at low Reynolds numbers. In general for wind tunnel testing, the flow uniformity should be maximized and flow angularity minimized. Barlow et al. suggest that the dynamic pressure variation should be less than 0.5% and

the maximum flow angle variation should be less than ±0.2 deg, although ±0.1 deg is preferable [59]. The primary consideration for low Reynolds number airfoil testing is the freestream turbulence intensity, defined by the equation

$$TI = \frac{u'}{\bar{u}}$$

where u' is the standard deviation and $\bar{u}$ is the mean of the velocity. Typically the turbulence will be measured with hot wire anemometry and sampled at a rate on the order of 10,000 Hz. For low Reynolds number airfoil testing where laminar separation and a laminar separation bubble are expected, the freestream turbulence intensity needs to be minimal to prevent the boundary layer from prematurely transitioning to a turbulent boundary layer. Selig et al. and Barlow et al. both suggest that the freestream turbulence intensity should be lower than 0.1%, which can be obtained through a large contraction ratio and multiple screens to smooth the flow [59, 110]. If the freestream turbulence intensity is higher than 0.1%, the laminar separation bubble effects may not be captured. Another consideration is the scale of the forces, which are significantly lower than the forces generated at higher Reynolds numbers. As previously mentioned concerning the airfoil data in Figure 2.17, the drag forces at a Reynolds number of 40,000 were not able to be measured because the forces were too small.

Wind Turbine Testing

Wind tunnel blockage. The blockage of an ideal wind turbine test should be minimal, less than 10% if possible. Tunnel blockage, or blockage ratio, is defined as the ratio of rotor swept area to wind tunnel cross-sectional area. Bahaj et al. derived a blockage factor (BF) for wind turbine testing based on a momentum analysis of an actuator disk [113], defined by the equation

$$BF = \frac{U_u}{U} \tag{2.53}$$

where U_u is the freestream velocity measured in the wind tunnel with the turbine model in the wind tunnel and U is the freestream velocity measured in the wind tunnel without the turbine model in the tunnel while the wind tunnel fan is operating at the same speed. The blockage factor can be applied to the TSR measured with the turbine in the wind tunnel, as seen by the equations

$$TSR_u = \frac{\Omega R}{U_u} \tag{2.54}$$

$$TSR = TSR_u BF = \frac{\Omega R}{U} \tag{2.55}$$

where TSR_M is the uncorrected tip speed ratio and TSR is the corrected tip speed ratio. The coefficient of power is corrected as seen by the following equations

$$C_{P_u} = \frac{\tau\Omega}{\frac{1}{2}\rho\pi R^2 U_u^3} \tag{2.56}$$

$$C_P = C_{P_u} BF^3 = \frac{\tau\Omega}{\frac{1}{2}\rho\pi R^2 U^3} \tag{2.57}$$

where $C_{P,u}$ is the uncorrected coefficient of power and C_P is the corrected coefficient of power. The blockage ratio of a wind turbine is defined by the equation

$$BR = \frac{\pi R^2}{A_c} \tag{2.58}$$

where R is the radius of the wind turbine and A_c is the cross-sectional area of the wind tunnel. Thus, the blockage ratio is a ratio of the swept area of the wind turbine and the cross-sectional area of the wind tunnel. Chen and Liou demonstrate experimentally that the blockage correction is less than 5% for a blockage ratio of 10% and, thus, does not need to be applied under these conditions. However, for cases with higher blockage, this correction must be applied [114].

Wind turbine scaling. While often difficult, wind tunnel testing of wind turbines can provide very meaningful results and minimize research and development risks. For example, wind tunnel data can be used for optimizing designs. Gregg et al. studied the effect of TSR, number of blades, and surface roughness on wind turbine performance in a wind tunnel with a 2 ft (0.61 m) square cross-section [45]. Additionally, wind tunnel tests can be used to develop and validate aerodynamic modeling tools such as the UAE and the MEXICO wind tunnel tests [65, 68]. Other tests of this nature have been performed by Ronsten [79] and Snel et al. [80] to better model the stall delay phenomena.

In wind tunnel testing of wind turbines, scaling is often a necessary topic of discussion. For wind tunnel testing, a large turbine design is typically scaled down to be small enough to allow testing in a wind tunnel without corrections due to low tunnel blockage. As noted by Simms et al. in the case of the UAE and MEXICO tests [65], it is sometimes necessary instead to test a full-scale turbine because scaling is impractical. Nonetheless, full-scale wind turbine testing in a wind tunnel would be difficult because common wind tunnel sizes are too small to accommodate most wind turbines while keeping blockage minimal.

When scaling a turbine for design or wind tunnel testing, only geometric scaling and TSR matching are typically applied. In *Wind Energy Explained*, these are the only types of aerodynamic scaling discussed [26]. Table 2.1 lists the scaling relationships for quantities of interest based on rotor radius. Multiple studies have been performed using only these scaling criteria. For example, Cho et al. tested a 12% scaled model of the NREL Phase VI turbine and analyzed the acoustic noise produced [115]. Chen and Liou tested multiple scaled models and analyzed the significance of the blockage correction with wind tunnel blockage between 10.2-28.3% [114]. Jackson studied the scaling of

fatigue loads with good correlation for most of the conditions studied [116]. Hulskamp et al. scaled trailing edge flaps to determine their ability to reduce dynamic loading [117].

Table 2.1: Wind Turbine Scaling Laws without Reynolds Number Matching [26]

Quantity	Symbol	Relation	Scale dependence
Power	P	$P_1/P_2 = (R_1/R_2)^2$	$\sim R^2$
Torque	Q	$Q_1/Q_2 = (R_1/R_2)^3$	$\sim R^3$
Thrust	T	$T_1/T_2 = (R_1/R_2)^2$	$\sim R^2$
Rotational speed	Ω	$\Omega_1/\Omega_2 = (R_1/R_2)^1$	$\sim R^{-1}$
Weight	W	$W_1/W_2 = (R_1/R_2)^3$	$\sim R^3$
Aerodynamic moments	M_A	$M_{A,1}/M_{A,2} = (R_1/R_2)^3$	$\sim R^3$
Centrifugal forces	F_c	$F_{c,1}/F_{c,2} = (R_1/R_2)^2$	$\sim R^2$

Note: R, radius

Another important aspect of scaling is Reynolds number matching (Reynolds number based on chord as defined in Equation 2.15). Without applying Reynolds number matching in addition to TSR matching and geometric scaling, the aerodynamic conditions between the two turbines are not truly identical.

As shown in Figure 2.18, airfoil performance does not typically change significantly for Reynolds numbers above 700,000 because of the limited effect of the laminar separation bubble if it is even present at all. Thus, if the Reynolds numbers are kept above 700,000, Reynolds number matching is not necessary and the test results should not be significantly affected. Most medium to large turbines (> 20 m) operate at higher Reynolds numbers [60], and the Reynolds number effect does not need to be taken into account. This is documented by Jackson, who states that fatigue loads for larger turbines can be scaled without Reynolds number matching and reasonable agreement can be achieved [116].

Due to the sensitivity of flow separation and transition to multiple factors, the specific Reynolds number below which the unusual flow phenomena occurs is also sensitive to similar changes such as airfoil shape. For this reason, Carmichael locates this Reynolds number at 700,000 [31], and it is also documented at 500,000 [60]. Additionally, Gao and Hu predicted in a computational fluid dynamics (CFD) model that this Reynolds number should be closer to 200,000 and that the airfoil lift and drag coefficient changed little in the Reynolds number range of 200,000 to 2,500,000 [118]. This study in particular is specific to the wind turbine blade geometry and flow conditions modeled.

The Reynolds number below which Reynolds number matching should be used will be taken as 500,000 for this study, although this Reynolds number will heavily depend upon airfoil shape and wind turbine geometry. Table 2.2 lists the scaling relationships of key parameters based on a geometric scaling factor, sc, when Reynolds number scaling is used. As can be seen in the table, the freestream velocity must increase by the geometric scaling factor, and the rotational velocity must increase by the square of the scaling factor. Because these relationships were derived from Reynolds number matching in addition to geometric scaling and TSR matching, scaling in this manner can lead to impractical freestream and rotational velocities.

Table 2.2: Wind Turbine Scaling Laws with Reynolds Number Matching [119]

Parameter	Symbol	Relation
Radius	R	$R_1/R_2 = sc$
Chord	c	$c_1/c_2 = sc$
Kinematic Viscosity	ν	$\nu_1/\nu_2 = 1$
Freestream Velocity	U	$U_1/U_2 = 1/sc$
Rotational Velocity	Ω	$\Omega_1/\Omega_2 = 1/sc^2$
Rotor Power	P_{rotor}	$P_{rotor_1}/P_{rotor_2} = 1/sc$
Torque	τ	$\tau_1/\tau_2 = sc$

Two situations exist when scaling down a turbine for wind tunnel testing which will result in Reynolds numbers below 500,000 and necessitate Reynolds number matching. First, if the original full-scale turbine already experiences low Reynolds numbers, Reynolds matching must be used in scaling, as in the testing of a scaled 1.15 m turbine optimized for 5 m/s by Burdett et al. [120]. Second, if scaling down the turbine results in Reynolds numbers below 500,000, either Reynolds number matching must be used or some other test parameters must be controlled such that the Reynolds numbers on the blade remain above 500,000. One such test was performed by Wainauski in scaling a 3.5 MW turbine by a 1:30 ratio to an 8 ft (2.44 m) diameter for testing in an 18 ft (5.49 m) octagonal test section [121]. In this test, a TSR was chosen to keep the Reynolds numbers over the blade near 600,000 and the tip speed below 183 m/s. Because of this, Reynolds number matching was not necessary and compressibility effects did not need to be taken into account. However, this study was very beneficial in demonstrating the effects of scaling, surface roughness, and blade shape modifications on the full-scale 3.5 MW turbine. After correcting the data for scaling effects, the wind tunnel data agreed with the full-scale annual energy production (AEP) within 1%.

A few other considerations exist for scaling. An obvious parameter for scaling is mass, which is difficult to scale. For steady-state wind turbine tests, however, mass scaling will not change the measured values. Additionally, the starting torque for the full-scale generator is very difficult to scale. For this reason, cut-in speed (the wind speed at which the turbine begins to spin), cannot be scaled very easily. Peterson notes that small variations in turbine geometry, such as radius, may cause the scaling projections to be inaccurate [122].

Wind Site Survey

Typically, a wind site survey is conducted for at least two years to determine the wind conditions at a particular site [13]. As previously discussed, knowing the wind distribution as well as the wind turbine performance are necessary to predict the AEP of a turbine at a specific site.

Wind characteristics are generally displayed using two types of figures. The first type of figure is a wind rose, which displays the frequency of direction from which the wind originates as well as the frequency of wind velocity in any particular direction. Most wind sites have either one or two prevalent wind directions. Figure 2.30 shows a wind rose using wind data from the Waco Region Regional Airport (ACT) from 1984 to 1992. The height at which the wind speed was measured is not recorded [123]. This figure illustrates the bipolar nature of the wind in Waco. Approximately 20% of the wind comes from the north (this includes north, north-northeast, and north-northwest), and approximately 42% of the wind comes from the south (this includes south, south-southeast, and south-southwest). The second type of figure is a histogram of the wind speed distribution, a generic example of which can be seen in Figure 2.31. This data does not correspond to the wind rose data from the Waco Regional Airport, but is merely an example of a typical histogram. Multiple characteristics of the wind can be determined using this type of analysis. First, the most common wind speed is easily identified by the peak. Additionally, the histogram gives an indication of the wind speeds a wind turbine will most often experience, which should influence the design process.

A Weibull probability function is the accepted distribution for representing a wind distribution [26], defined by the equation

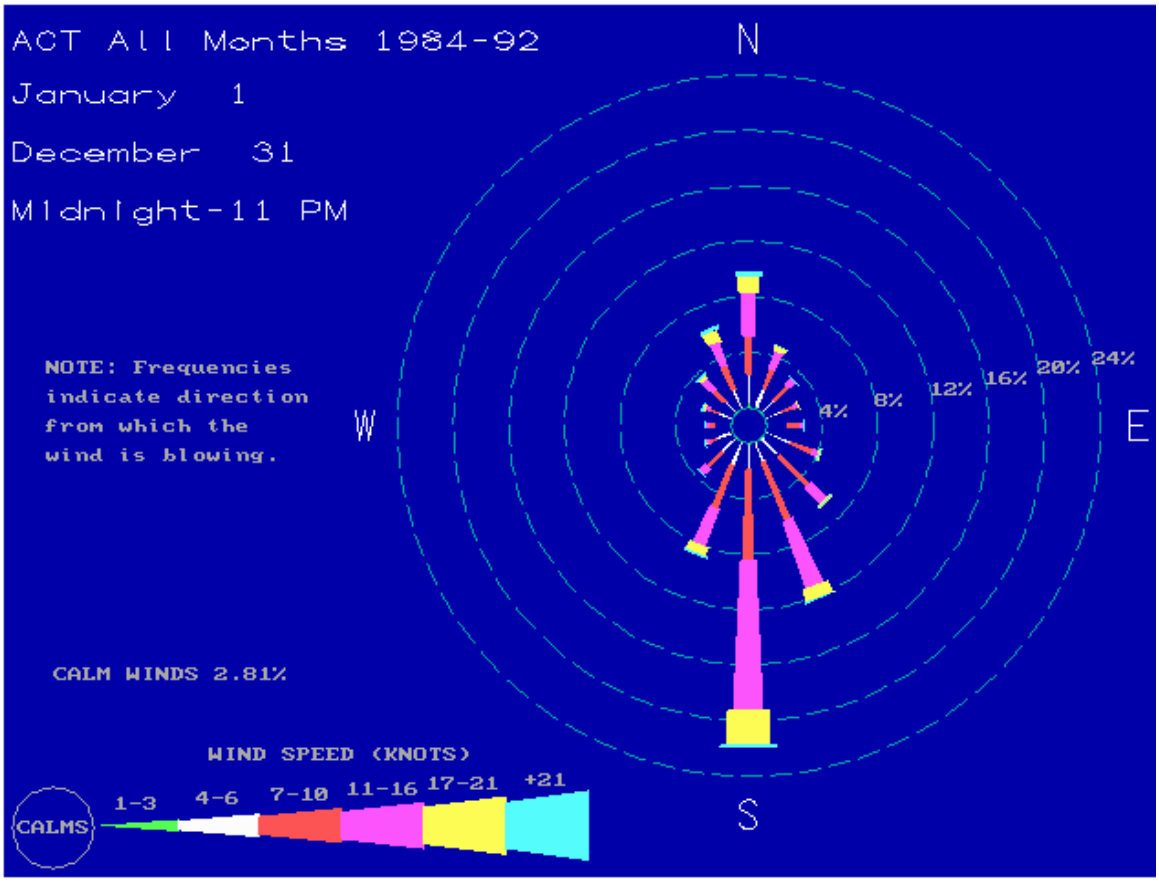

Figure 2.30: Wind Rose from Waco Airport [123]

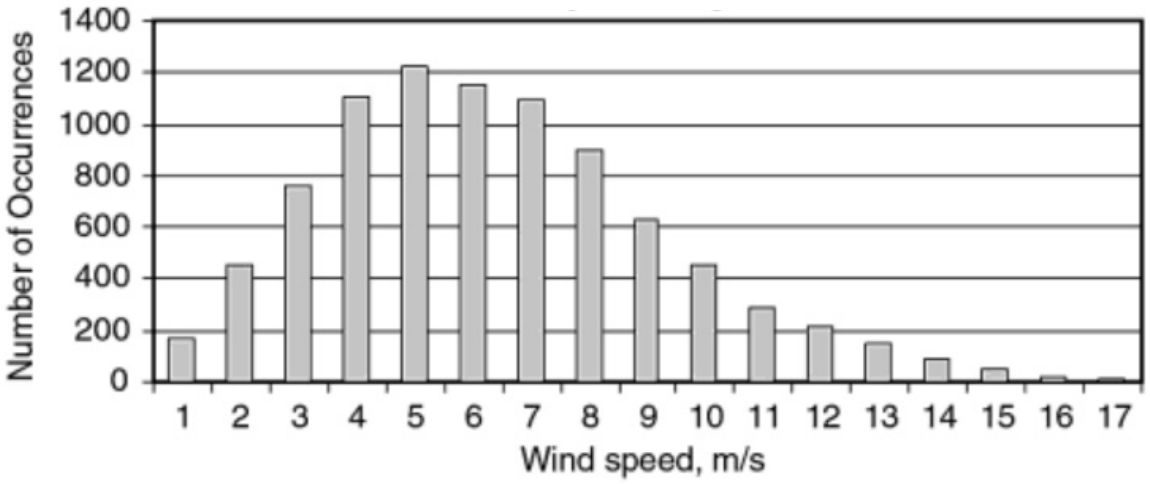

Figure 2.31: Typical Weibull Shape of Wind Speed Histogram [26]

$$P_{wind}(U) = \frac{k}{c}\left(\frac{U}{c}\right)^{k-1} e^{-\left(\frac{U}{c}\right)^{k}} \tag{3.1}$$

where U is the wind speed, k is the shape parameter, and c is the scale parameter. If wind data is available, a Weibull probability function is fit to the data. Multiple empirical methods exist for approximating the shape and scale parameters and are outlined by Manwell et al. [26]. Additionally, a linear regression can be performed on the cumulative probability function after transforming the variables or maximum likelihood estimation can be used [124]. If the wind data is not available for a particular site, an average wind speed can usually be estimated from a nearly site, and a Rayleigh probability function is used to estimate the wind distribution. A Rayleigh probability function is a Weibull function with a shape parameter of 2.0.

If data is missing or invalid because of anemometer failure during the test, some measures may be taken to correct the data, as outlined by Prasad et al. [125]. Ozgur and Kose suggest as long as less than 10% of the data is invalid, corrections may be applied [126]. Artificial neural networks have been applied to determine reasonable corrections by Kalogirou et al. with less than 1.8% error in validation [127]. However, this method requires years of data to train the artificial neural network. Kline and Milligan outline three other ways to correct the missing data, which utilize wind data from a nearby site or previous months [128]. Additionally, if multiple anemometers are installed at the same height on the same site, data from one anemometer can be used to fill in the missing data from the faulty anemometer. This correction can only be performed, however if one of the anemometers is functioning properly at any particular moment in time for the duration of the wind site survey. Further, if the wind speed is being measured at two

additional heights, boundary layer theory can be used to extrapolate what the data would be at the height with the missing data.

Contributions of this Work

In this work, multiple aspects of wind turbine design are addressed in efforts to improve the design process for small-scale wind turbine designers, particularly with application to low-speed or Class 2 wind sites. The first part of this work involves the analysis of a partially-complete wind site survey in Waco, Texas, a Class 2 wind site by NREL classifications. While all the data from the wind site survey has not yet been collected, the purpose of this study is to develop and document a method for analyzing the wind data and utilizing it in developing the average wind turbine power and AEP for a wind turbine operating in Waco.

The second part of this work experimentally investigates various aspects of airfoil performance at low Reynolds numbers that have not been tested before the for S823 airfoil in order to improve wind turbine modeling and design at these Reynolds numbers. This includes comparing the experimental results with the aerodynamic codes PROFIL and XFOIL and a brief roughness study aimed at determining the best trip strip height and location to reduce flow separation and improve airfoil performance at the Reynolds numbers tested.

The final part of this work involves three experimental wind turbine tests of designed wind turbines. For all the tests, the wind turbines were designed for a wind speed of 5 m/s. This wind speed was chosen for design based on preliminary data from the wind site survey (at a height of 50 ft) detailed in Chapters 3 and 4. Based on the wind speed and height, the NREL classification is Class 2, as seen in Table 2.3. Additionally,

the wind speed classifications at 100 ft are included in the table because that is the maximum height of the wind site survey. The average wind speeds in this table have been extrapolated from a height of 50 m to the specified heights using the $1/7^{th}$ power law, and the wind power densities were calculated using the equation

$$P_{D_{wind}} = \frac{3}{\pi}\rho U^3 \tag{2.2}$$

derived by Celik for a Rayleigh distribution, which is a standard wind distribution used for general estimates of wind distribution [129].

Table 2.3: Class Breakdown of Wind Speed at 50 and 100 ft

Height	50 ft (15.2 m)		100 ft (30.5 m)		
Wind Power Class	Wind Power Density, W/m^2	Speed, m/s	Wind Power Density, W/m^2	Speed, m/s	Qualitative Assessment
1	0 - 130	0.0 - 4.7	0 - 160	0.0 - 5.2	Poor
2	130 - 190	4.7 - 5.4	160 - 240	5.2 - 5.9	Marginal
3	190 - 250	5.4 - 5.9	240 - 320	5.9 - 6.5	Fair
4	250 - 310	5.9 - 6.4	320 - 400	6.5 - 7.0	Good
5	310 - 380	6.4 - 6.8	400 - 480	7.0 - 7.5	Excellent
6	380 - 500	6.8 - 7.4	480 - 640	7.5 - 8.2	Outstanding
7	>500	>7.4	>640	>8.2	Superb

The first experimental test evaluates a scaling technique including Reynolds number matching and determines the validity of the blockage correction applied in wind tunnel tests. Validating the scaling technique and blockage correction experimentally enables the use of scaled wind tunnel tests for small-scale wind turbines. The second experimental test applied the scaling relationships and blockage correction from the previous study to compare the performance of blades with optimized angles of twist for power production at the design wind speed and TSR using BET and the BEMT algorithm documented in Equations 2.18-2.29. The power performance was optimized for a design wind speed and TSR rather than for the AEP because BET cannot be used to optimize for

AEP. Only the angle of twist was optimized in this study because BET cannot be used to optimize any other parameter. The equations derived for the optimal twist and chord distributions based on BEMT theory are not used in this study because the intent was to isolate the twist distribution. One additional part of this study involved optimizing the design TSR, which effectively changes the angle of twist, for power production at a design wind speed. This was done using the BEMT model. The MATLAB® code used to numerically determine these optimums can be found in Appendix A. A second additional part of this study involved comparing the optimized BEMT blade with a commercial wind turbine with the same diameter. The third and final experimental wind turbine test involves an analysis of the performance output of wind turbines designed using a design angle modified by ±2 degrees. As noted previously, the effect of changing the design angle (using BET) or pitch angle for a fixed-pitch, variable-speed wind turbine has not been previously studied. It is important to know the sensitivity of this optimum angle when designing a wind turbine.

CHAPTER THREE

Experiment Design, Procedure, and Data Reduction

Multiple experiments have been undertaken to improve the design process of small-scale, fixed-pitch, horizontal-axis wind turbines by quantifying and comparing wind turbine performance. This chapter provides the details of the experimental design, procedure, and data reduction used for each of the three types of experiments performed. The first experiment involved measuring wind speed and direction at a potential site in Waco being evaluated for a possible wind turbine installation. While the wind site survey is currently incomplete, the methods for processing and analyzing the data are outlined. The second experiment involved measuring the lift and drag forces generated by an airfoil under the Reynolds numbers present on a small-scale wind turbine. The third and final experiment involved measuring the power output of a wind turbine tested under the wind conditions experienced at the Waco site.

Wind Site Survey

Goal of Experiment

The purpose of a wind site survey is to quantify the wind conditions in Waco at a site chosen for potentially installing a wind turbine. The results of this study can be used to predict the AEP of a wind turbine installed at the site.

Site and Measurement Equipment

The Region 12 Education Service Center (ESC) was chosen to install the wind site survey tower because it is one of the highest locations in Waco and has very few

surrounding obstructions. The meteorological (met) tower used for the data acquisition is an NRG 30 m TallTower, located at approximately +31° 29' 50.40", -97° 10' 6.46". The tower has four anemometers located on the tower with one at approximately 50 ft (15.2 m) and 75 ft (22.8 m), and two anemometers and a wind vane are installed at approximately 100 ft (30.5 m), as seen in Figure 3.1. The anemometers are NRG #40C models with a minimum wind speed measurement of 0.4 m/s (Figure 3.1). The wind vane used is an NRG #200P model (Figure 3.1). The wind vane was calibrated so that zero degrees was measured when the wind was blowing from true north. The measurement equipment is mounted on the 8-inch diameter tower on side-mount booms 2.4 m out horizontally from the tower. The uncertainty in the anemometer measurement is ± 0.45 m/s, and the wind vane has 1% linearity. The equipment is monitored with a Symphonie Data Logger model 3090, a newer model of which is shown in Figure 3.2. The data is sampled at 1 Hz and the average, standard deviation, maximum, and minimum for 10 minutes of data is recorded in a data file for each day.

Data Reduction

The first step in analyzing the data is determining the validity of the data. While the anemometers and wind vane have been calibrated by the manufacturer, various weather conditions and other external factors, such as a possible frozen anemometer, can prevent the equipment from measuring wind speed and direction properly. These phenomena can cause one or more of the anemometers to measure values lower or higher than the true value, so these values must be either ignored or corrected. Since the goal of this study is to quantify the wind conditions over two years (although only one year of data is currently available), eliminating data has the potential to skew the statistical

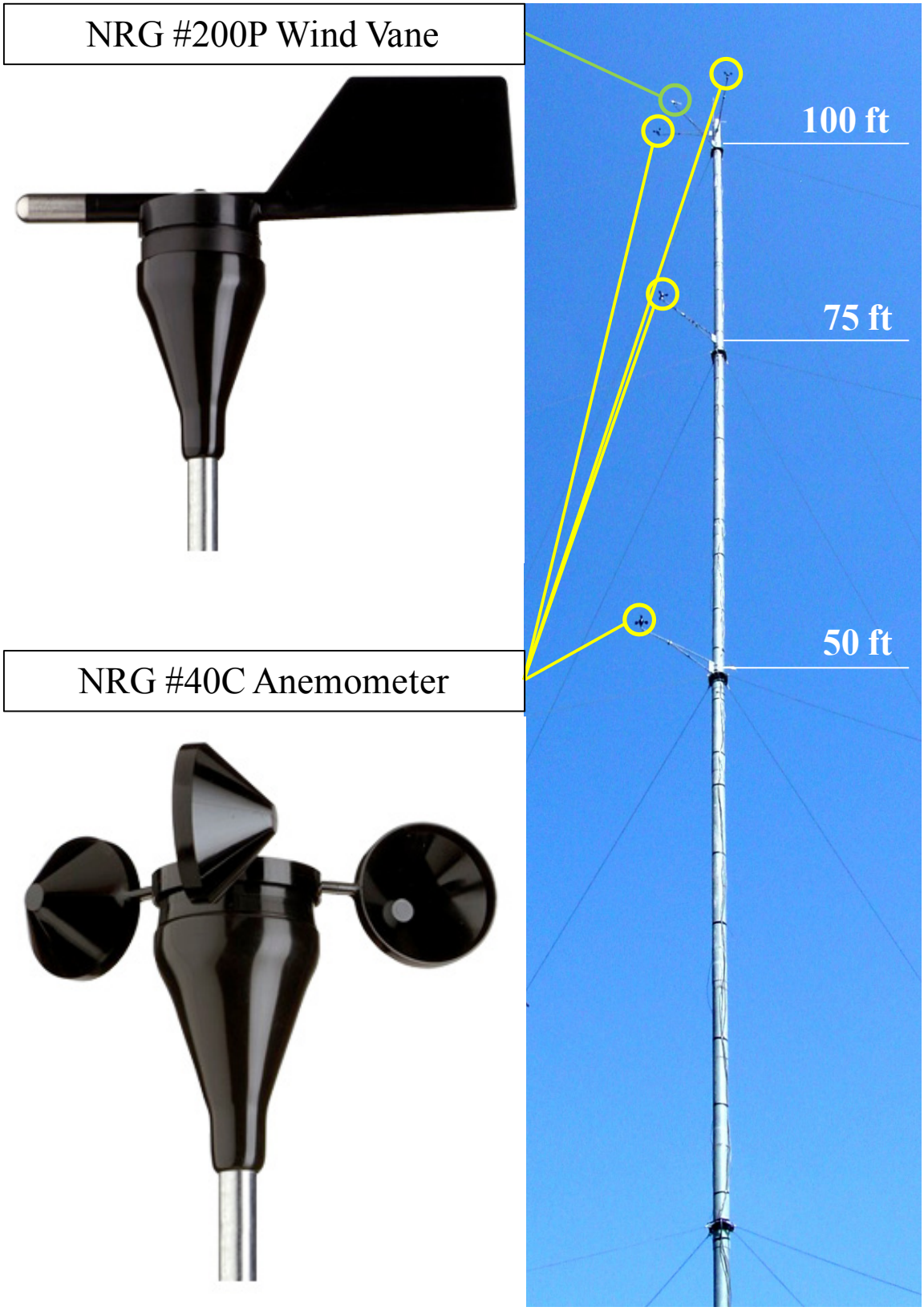

Figure 3.1: Anemometers and Wind Vane on Wind Site Survey Tower [130, 131]

Figure 3.2: Symphonie Data Logger [132]

distribution of the data. Thus, it is better to correct the data if a reasonable method for correction is available. Identifying invalid data is problematic because standard statistical methods for eliminating an invalid data point such as Chauvenet's criteria cannot be used because the conditions of the test are not steady-state. Further, correcting the data requires making assumptions about the nature of the flow and the earth's boundary layer.

Two commonly-employed methods exist for determining the validity of measured wind speed data. Both of these methods involved comparing the measurements of two anemometers and isolating outliers based on what the comparison of the two measurements should be. This analysis assumes that both of the anemometers will not measure an incorrect wind speed at the same time, which, upon inspection, proves to be true for this data. Additionally, it must be noted that the primary mode of anemometer malfunction causes a reading of 0.4 m/s, which is the minimum measurable wind speed. This could be due to a mechanical problem preventing the anemometer from spinning or an electrical problem preventing the correct signal from being recorded. The first method

is to plot the measurements of two anemometers on two separate axes. If the anemometers are measuring the velocity at the same height, the data should form a line with a slope of approximately one. If one of the anemometers is not working properly for a period of time, there will be a group of data at or near 0.4 m/s. The second method is to plot the ratio of anemometer measurements versus sample number or time. If the anemometers are measuring the velocity at the same height, the anemometer ratio should be near one for the entire data set. If the anemometer in the denominator is not measuring data properly, the ratio will be greater than one as it will be measuring a lower value than the other anemometer. If the anemometer in the numerator is not measuring properly, the ratio will be less than one as it will be measuring a lower value than the other anemometer. The first method has the advantage of displaying the true values of the data while the second method has the advantage of showing temporal resolution.

The second consideration in the analysis is to determine a reasonable correction for the invalid data. The number of anemometers at a particular height and the quality of the other anemometer data will determine the best correction method to use, which are presented in the discussion of data recorded at each height.

A comparison of the measured data for both anemometers at 100 ft can be seen in Figure 3.3 and Figure 3.4. The uncorrected data in Figure 3.3 (a) show most of the data for the two anemometers agree and that the data in general has a slope of one as expected. However, both anemometers have periods of time when the anemometer is not working properly and is producing a value of 0.4 m/s when the other anemometer is measuring a value as high as 13 m/s (circled in red). Figure 3.4 (a) shows the uncorrected data in a plot of anemometer ratio versus sample number. In general, the ratio of the anemometers is very near one. However, three distinct periods occurred when one of the anemometers

was not working properly, highlighted by the red circles. During the first of these periods, the 100 ft (B) anemometer is not functioning properly. During the second and third of these periods, the 100 ft (A) anemometer is not functioning properly. Figure 3.5 shows that actual wind speed measurements from sample number 30,000 to 35,000 to show what is happening with the actual data when one of the anemometers is not functioning properly. In general, the two anemometers follow each other very closely. When the two anemometers differ, however, one of the anemometers is measuring a value of 0.4 m/s, which occurred for a period of nearly two weeks.

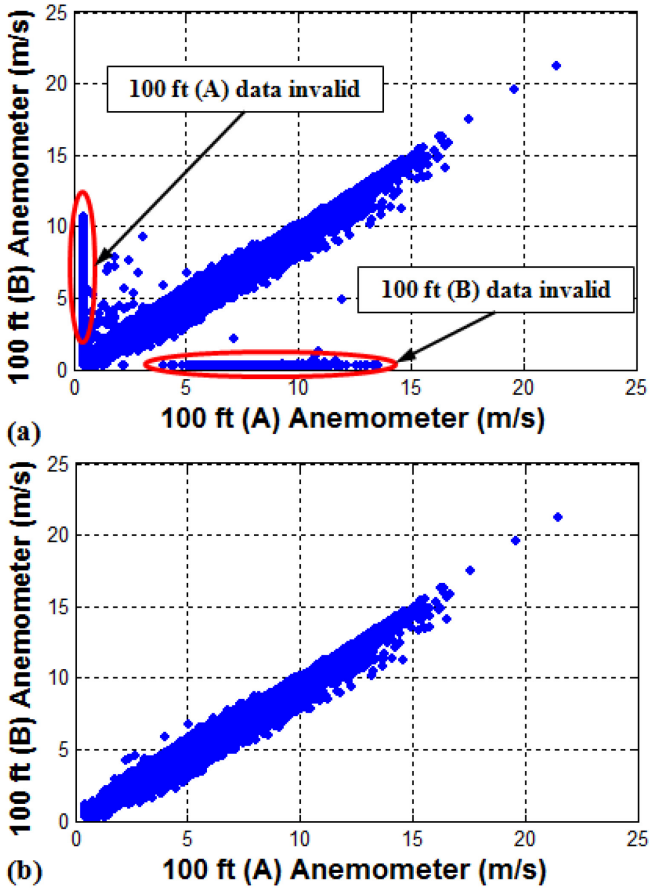

Figure 3.3: Comparison of Anemometer Measurements of Two Anemometers at 100 ft for the (a) uncorrected and (b) corrected data

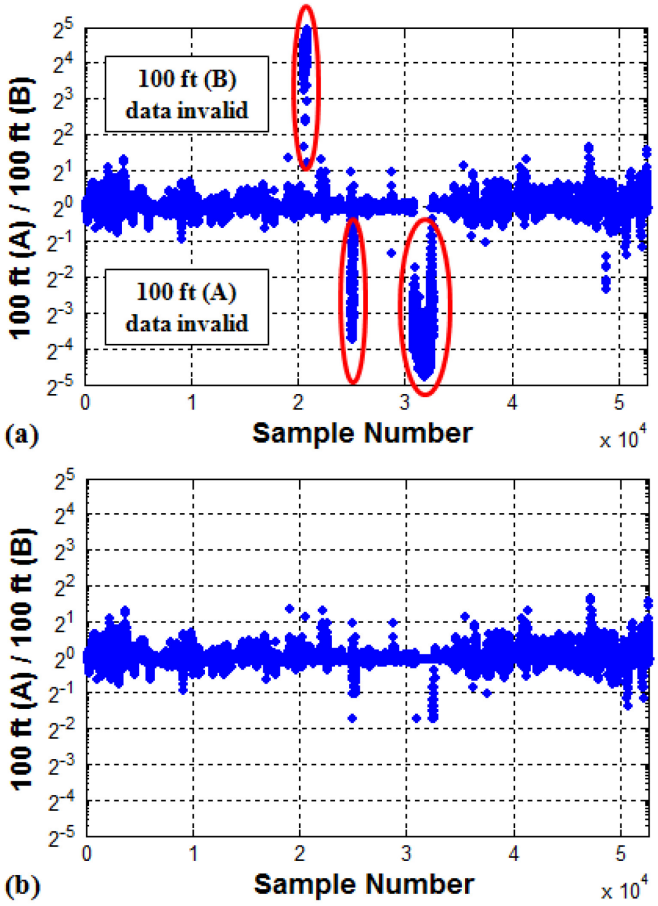

Figure 3.4: Anemometer Ratio of Two Anemometers at 100 ft for the (a) uncorrected and (b) corrected data

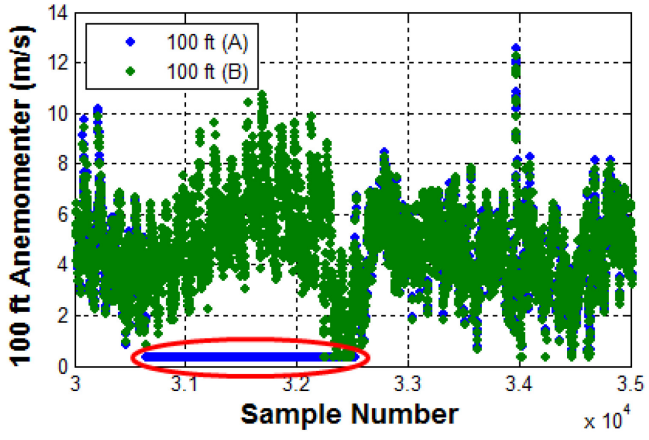

Figure 3.5: Comparison of Data from Anemometers at 100 ft for Sample Numbers between 30,000 and 35,000

To correct the invalid data, the measurement from the other anemometer was assigned to the malfunctioning one. Because of the vast amount of data, this process was automated. After careful consideration of the data, two criteria were used to determine if a data point was invalid. First, the difference in the output values of the two anemometers must be greater than the uncertainty of the anemometers, ±0.45 m/s, or 0.9 m/s. Second, the ratio of the anemometers must be outside the bounds of 2^{-1} and 2^{1}, at which point one anemometer would be measuring more than twice or less than half the measurement of the other anemometer. With these criteria, the data was corrected and is shown in Figure 3.3 (b) and Figure 3.4 (b). Using this correction method, 3.687% of the data from the 100 ft (A) anemometer was corrected, and 0.694% of the data from the 100 ft (B) anemometer was corrected.

Applying the same analysis to compare the data at 75 ft with the readings of the two anemometers at 100 ft reveals that the anemometer at 75 ft is consistently functioning properly and that the correction was successful. Figure 3.6 shows the plot of both sets of anemometer data at 100 ft versus the anemometer data at 75 ft. Because the anemometers being compared are not at the same height, the slope should not be one, but should still be near one. In this case, the slope should be a little less than one. Notably, there is no instance when the anemometer is measuring 0.4 m/s and the anemometers at 100 ft are reading significantly higher. In this case, the corrected and uncorrected data only applied to the data from the anemometers at 100 ft using the correction mentioned previously. Figure 3.7 shows the ratios, which also shows the ratio to be less than one for the same three periods of time noted in the discussion of the 100 ft anemometer data. Again, the data at 75 ft is consistently accurate even when comparing with the corrected 100 ft data.

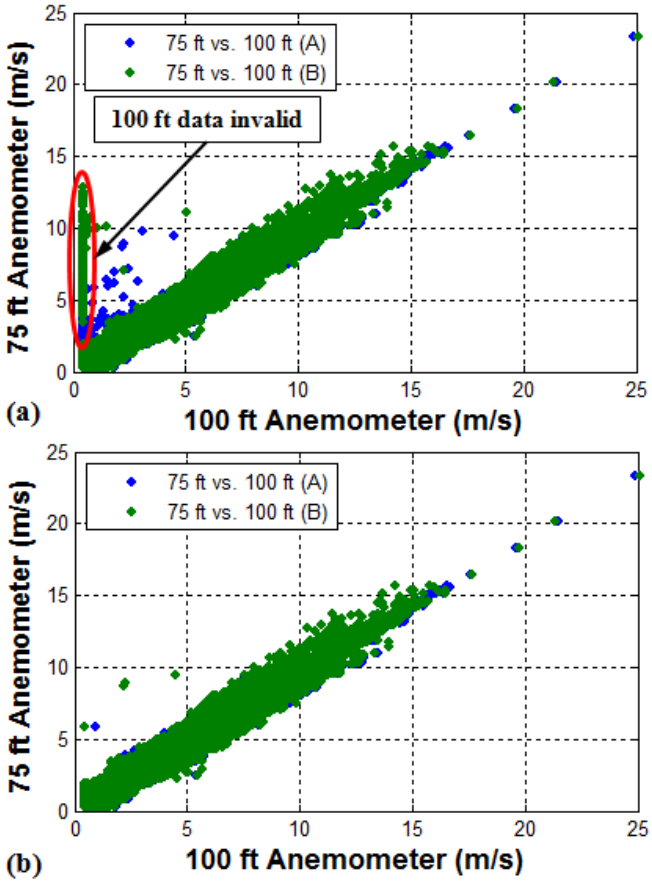

Figure 3.6: Comparison of Anemometer Measurements of Both Anemometers at 100 ft with the Anemometer at 75 ft for the (a) uncorrected and (b) corrected data

The final analysis is of the data from the anemometer at 50 ft, as seen in Figure 3.8 (a) and Figure 3.9 (a). Both these figures show the 75 ft data is valid, but there are a number of instances when the anemometer at 50 ft is not recording data properly, as circled in red in both figures. To correct this data, boundary layer equations were required because only one anemometer was measuring wind speed at this height. Because the boundary layer over the earth is considered turbulent, the power law for a turbulent boundary layer was used, defined by the equation

$$\frac{U(z)}{U(z_r)} = \left(\frac{z}{z_r}\right)^{\alpha} \tag{3.3}$$

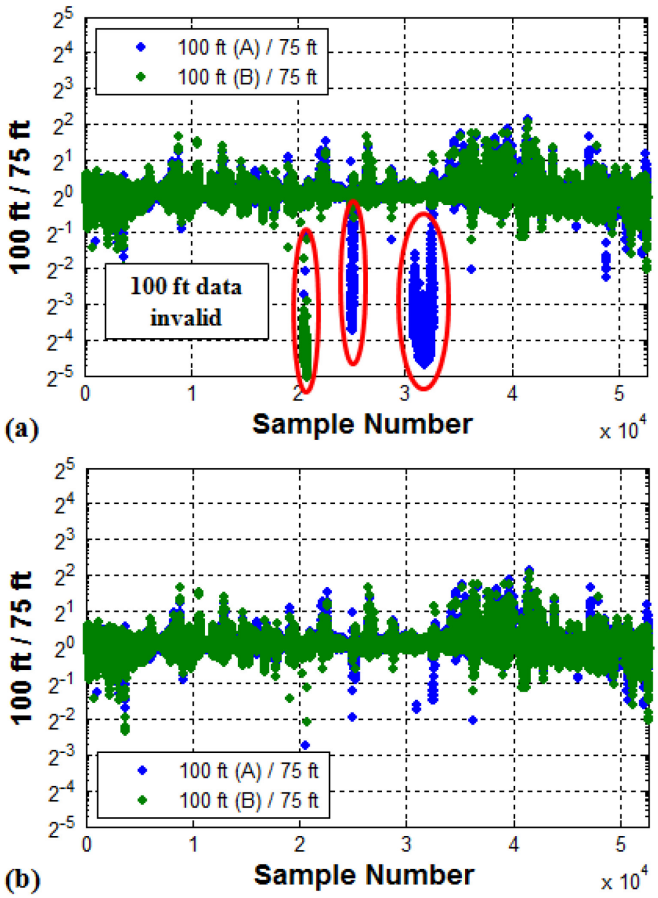

Figure 3.7: Anemometer Ratios of Anemometers at 100 ft with Anemometer of 75 ft for the (a) uncorrected and (b) corrected data

where z is the height above the ground, z_r is the reference height above the ground, $U(z)$ and $U(z_r)$ are the wind velocities at the given heights, and α is the exponent that characterizes the shape of the boundary layer. While a steady, fully turbulent boundary layer over a flat plate has an exponent, α, of approximately 1/7, this is not the case with the atmospheric boundary layer because of the local terrain, macro-scale pressure gradients, and unsteady nature of the flow over the surface of the earth.

Using the corrected data at 100 ft and the data at 75 ft, the exponent in the power law equation can be calculated at a particular moment in time. Thus, the exponent was solved for each 10-minute averaged set of measurements. Figure 3.10 shows the

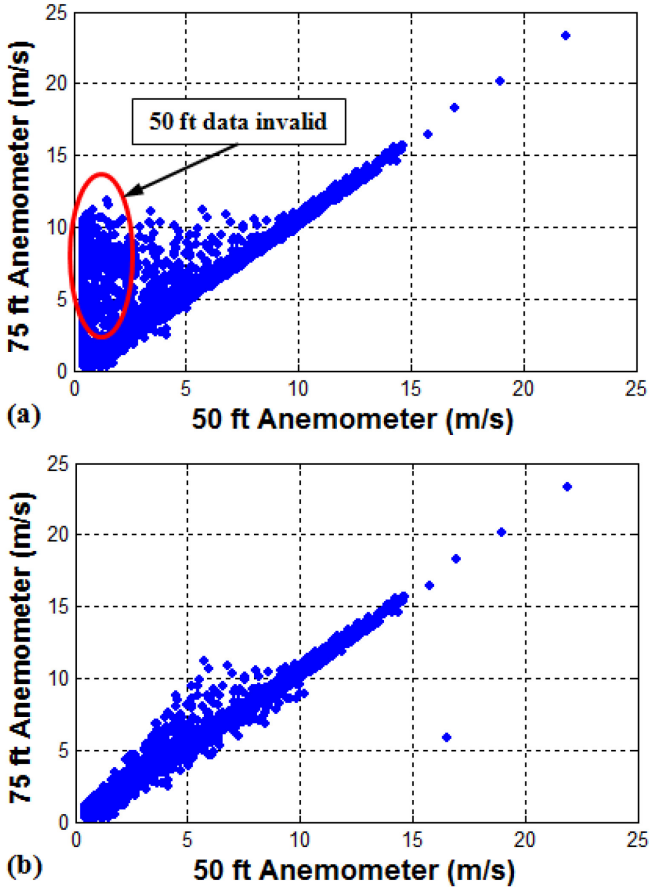

Figure 3.8: Comparison of Anemometer Measurements of the Anemometer at 75 ft with the Anemometer at 50 ft for the (a) uncorrected and (b) corrected data

distribution of exponents solved for using the power law for each data point, showing an average value near 2/7. Using the calculated exponent and the data at 75 ft, the wind speed at 50 ft can be calculated. This prediction has been compared to the measured wind speed at 50 ft in the histogram in Figure 3.11. As seen in the figure, 76.712% of the predicted data is within ±0.45 m/s of the actual measured data. Additionally, only 0.255% of the predicted data is greater than 2 m/s from the measured data, which is likely due to erroneously measured wind speed at 50 ft and accounts for the spike in the histogram on the far right side of Figure 3.11.

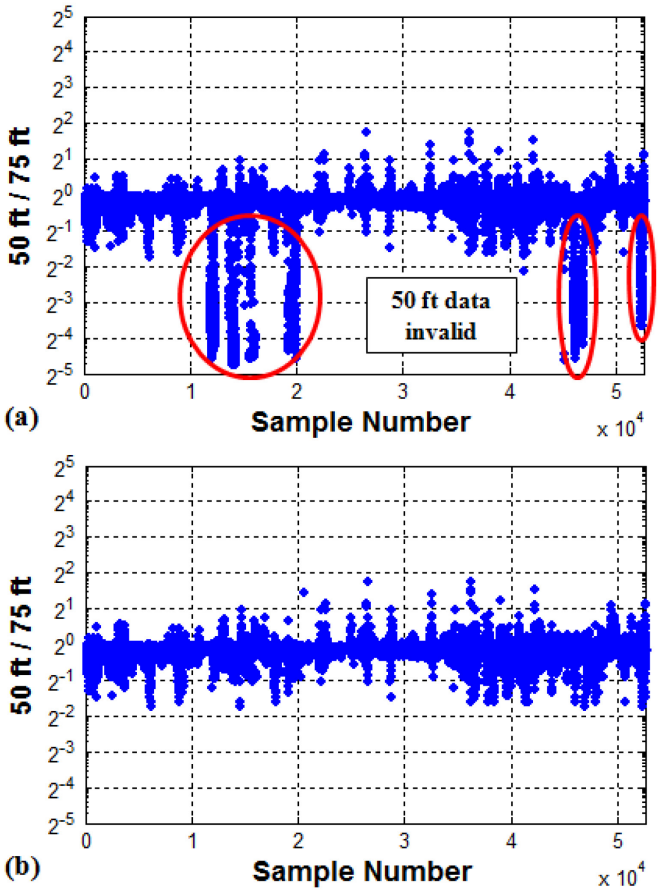

Figure 3.9: Anemometer Ratio of the Anemometer at 75 ft with the Anemometer at 50 ft for the (a) uncorrected and (b) corrected data

In correcting the data at 50 ft, the same algorithm was used that was outlined for the correction of data for the 100 ft anemometers. Additionally, the correction was only applied if the value of the exponent was physically meaningful, with a value between 0 and 0.75, the upper limit of which was chosen after careful consideration and analysis of the data. In this case, however, the data from the anemometer at 50 ft was compared with the boundary layer extrapolation applied using the previously mentioned exponent and the data from the anemometer at 75 ft. This correction was applied to 3.115% of the data measured at 50 ft. The comparison of uncorrected vs. corrected data can be seen in Figure 3.8 and Figure 3.9. Additionally, Figure 3.12 shows the uncorrected and corrected

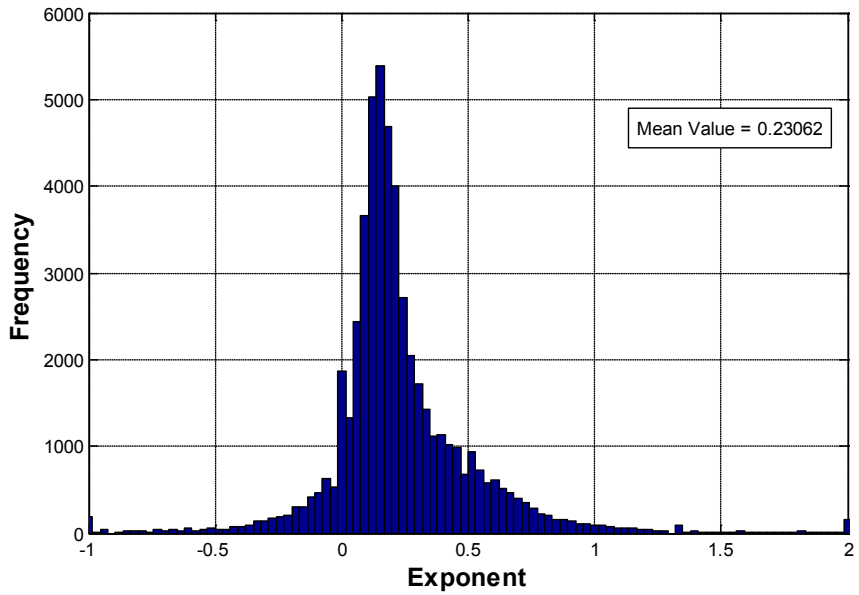

Figure 3.10: Histogram of the Exponent from the Power Law for each data point

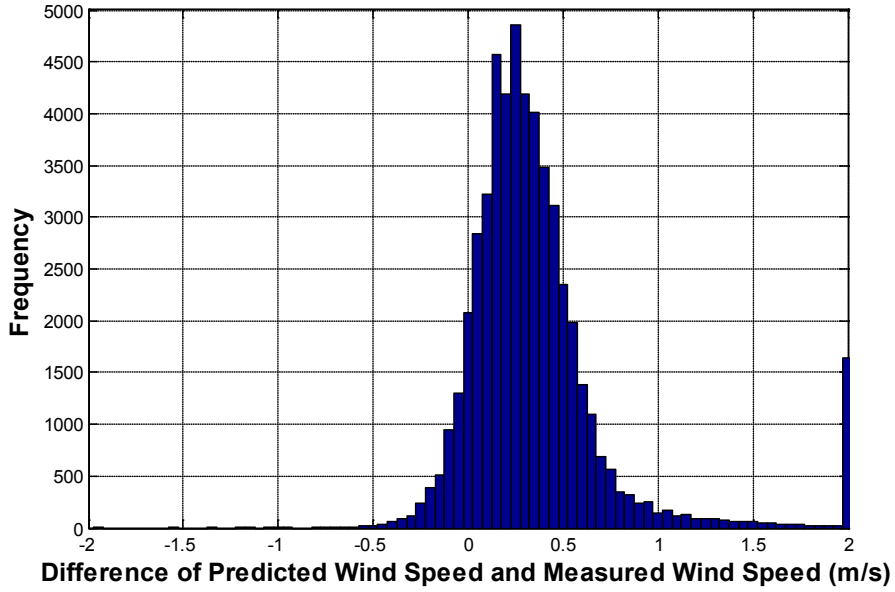

Figure 3.11: Histogram of the Difference between Predicted (using Power Law) and Measured Wind Speed

data from sample number 10,000 to 15,000. This data shows two periods, circled in red, when the anemometer was measuring a speed of 0.4 m/s for an unlikely period of time; however, the correction results in a more expected trend in the data.

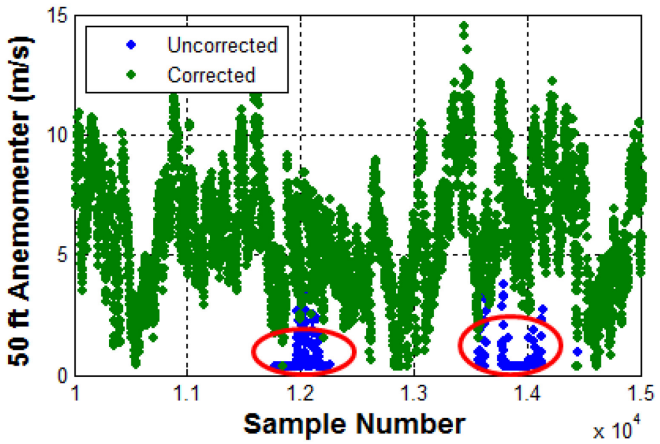

Figure 3.12: Comparison of Uncorrected and Corrected 50 ft Anemometer Data

Finally, in generating the wind rose, when the all three of the anemometers were reading 0.4 m/s, which is the minimum speed recorded by the anemometers, the angle value for the wind direction was not included. Thus, 0.358% of the angle measurement data was not included in the wind rose. The MATLAB® code used for both importing and analyzing the data can be found in Appendix B.

Baylor Subsonic Wind Tunnel

Facility and Measurement Equipment

All wind tunnel tests were performed in the Baylor Subsonic Wind Tunnel (Figure 3.13), an Engineering Laboratory Design, Inc. (ELD) Model 406B. This wind tunnel is open-circuit and has a constant-pitch fan driven by a variable-speed, 40-hp motor, which allows wind speeds in the tunnel to range from 0.1-50 m/s. The test section is 4 ft long with a 2 ft square cross section. The tunnel velocity variation is ±1% and the turbulence intensity is less than 0.2% at the inlet to the test section. The wind tunnel speed was remotely controlled by sending a 0-10 VDC signal to the wind tunnel controller. The signal was generated using a LabVIEW® program and a CDAQ National

Instruments (NI) 9263 module, an analog DC voltage output unit with a range of 0-10 VDC. An overview of the LabVIEW® interface is detailed in Appendix C.

Figure 3.13: Baylor Subsonic Wind Tunnel

To determine atmospheric conditions used in calculating the air density and viscosity, LabVIEW® software and NI hardware were used to automate the process. However, the absolute pressure was measured using a wall-mounted Oakton barometer (model 03316-80), which cannot interface with LabVIEW®. Thus, the pressure reading (in mbar) was input into the LabVIEW® program manually. The atmospheric temperature was measured using a T-type thermocouple and an NI 9211 CDAQ module with a built-in cold junction compensation. The relative humidity (RH) was measured using a Siemens QFM3101 RH duct sensor. At the beginning of each test, 10,000 samples of temperature and relative humidity were measured over a period of 30 seconds in order to calculate the density. The RH does not have a significant effect on density when compared to a calculation based on ideal gas law, which decreases the density on

the order of 1%. However, the effect on dynamic viscosity can be on the order of 10%, which will subsequently affect the Reynolds number calculation.

To measure the dynamic pressure, an Omega PCL-2A pressure transducer was used. This unit was connected to the computer using a 9-pin serial port and data could be read from the unit using LabVIEW® at a rate of approximately 20 Hz.

Data Reduction

The freestream velocity was calculated using Bernoulli's equation, as seen in Equation 3.4.

$$U = \sqrt{\frac{p_T - p_S}{\frac{1}{2}\rho}} \tag{3.4}$$

In this equation, U is the wind velocity, P_T is the total pressure, P_S is the static pressure, and ρ is the air density. Using this equation assumes inviscid and steady flow along a streamline with constant density.

The measured atmospheric conditions, temperature, pressure, and relative humidity, were used to calculate density. This was performed using polynomial functions fit to the tables for psychometric relationships of moist air published by the International Association for the Properties of Water and Steam [133].

The viscosity of humid air was also calculated using the atmospheric conditions measured. First, the viscosity of dry air was calculated using Sutherland's Law [134] as defined by the equation

$$\frac{\mu}{\mu_0} \approx \left(\frac{T}{T_0}\right)^{3/2} \frac{T_0 + S}{T + S} \tag{3.5}$$

where T_0 and μ_0 are reference values of temperature and viscosity, respectively, and S is the Sutherland constant which is a characteristic of the gas. For air, T_0 = 273 K, μ_0 =

1.716E-5 (N·s)/m^2, and S = 111 K. Second, the viscosity of humid air was calculated using Wilke's viscosity equation (Equations 3.6 and 3.7) [135] for a two species gas mixture, defined by the equations

$$\mu_{mix} = \frac{\mu_1}{1+\left(\frac{x_2}{x_1}\right)\varphi_{12}} + \frac{\mu_2}{1+\left(\frac{x_1}{x_2}\right)\varphi_{21}} \tag{3.6}$$

where $$\varphi_{12} = \frac{1}{\sqrt{8}}\left(1+\frac{M_1}{M_2}\right)^{-1/2}\left[1+\left(\frac{\mu_1}{\mu_2}\right)^{1/2}\left(\frac{M_2}{M_1}\right)^{1/2}\right]^2 \tag{3.7}$$

In these equations, the subscripts 1 and 2 represent the two species, air and water, x is the mole fraction, μ is the viscosity of a pure sample of either species calculated using Sutherland's Law, and M is the molecular weight.

Airfoil Study

Goal of Experiment

To better understand the aerodynamics over a wind turbine and to acquire two-dimensional data for use in wind turbine blade design, an airfoil study was performed under the same aerodynamic conditions (Reynolds numbers) that a small-scale HAWT experiences. The airfoil performance was quantified under these conditions by measuring the lift and drag forces over a range of Reynolds numbers. The Reynolds numbers tested ranged from 15,000 to 200,000. Additionally, the results of this study were compared with published data when available. As part of this study, roughness in the form of a trip strip was added to the airfoil surface to determine the effect on performance over the range of Reynolds numbers investigated. Typically, airfoil data is experimentally measured from about -5 to 15 degrees, which is how this test was performed. However, to use the data in the design of a stall-controlled wind turbine, it is ideal to quantify the airfoil performance over a range of -90 to 90 degrees because the

airfoil cross-section may see these extreme angles of attack that extreme on the turbine blade during normal operation. However, this is not possible with the current experimental setup at Baylor University because of the limitations of the force balance.

Facility and Measurement Equipment

All airfoil experiments were performed in the Baylor University Subsonic Wind Tunnel. In addition to measuring atmospheric conditions and wind velocity, the lift and drag forces generated by the airfoil being tested were measured using an ELD dynamometer, more commonly known as a force balance. The airfoil performance was measured over a range of angle of attacks from -5 to 15 deg. The angle of attack was set manually and measured with a Craftsman 7-inch Digital Torpedo Level. The range for the lift is 0-7 kgf and for the drag is 0-3 kgf, as specified by the manufacturer. However, for the purposes of the airfoil testing, the dynamometer was calibrated for a range of 0-3 kgf for lift and 0-2 kgf for drag. The dynamometer was calibrated by hanging weights from the force balance in the direction of lift and drag, as seen in Figure 3.14. The DC voltage output from the force balance was measured using a NI BNC 2110 and recorded using LabVIEW®. The data from the calibration is recorded in Figure 3.15 and results in a linear regression, which is used in calculating the conversion factor from voltage to lift and drag forces.

The airfoils used in this experiment were the E387 and S823. An airfoil chord of 6 inches was chosen because it provided minimal wind tunnel blockage over the range of angles of attack tested but also generated large enough aerodynamic forces to minimize measurement uncertainty with the dynamometer. The manufacture of the airfoils is detailed in Appendix D, and Appendix E describes the testing performed in the process of

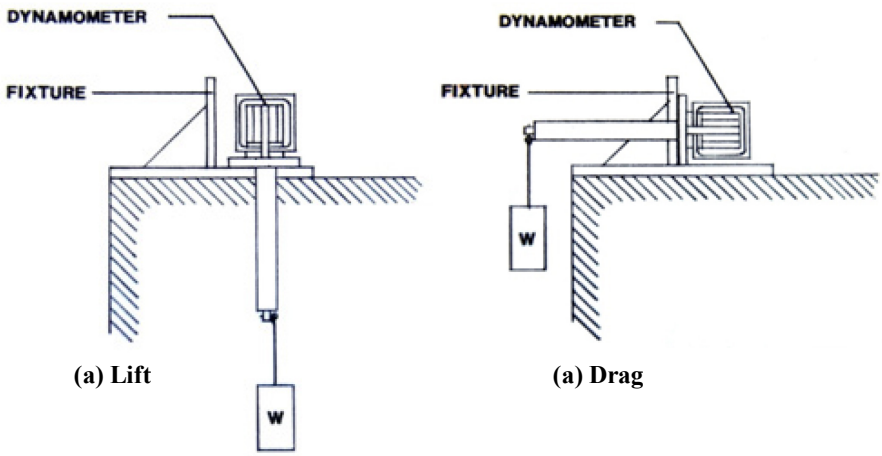

Figure 3.14: Dynamometer Calibration Setup [136]

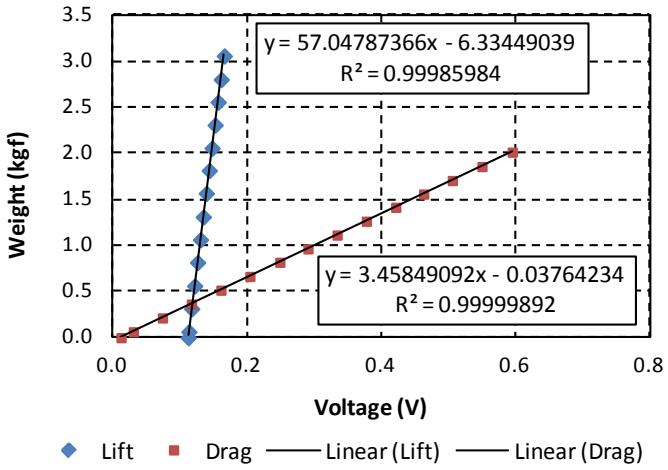

Figure 3.15: Calibration Result of Dynamometer

arriving at the airfoil surface used in this testing. A schematic of the instrumented wind tunnel test section can be seen in Figure 3.16. The pitot-static tube is 10.16 cm from the wind tunnel wall, which is outside the boundary layer. Additionally, it is approximately 10 cm upstream of the airfoil. The angle of attack of each airfoil was varied by rotating about the front screw in the airfoil mount, and tightening the back screw to keep it in place. Figure 3.17 shows the actual airfoil mounted on the dynamometer in the wind tunnel test section.

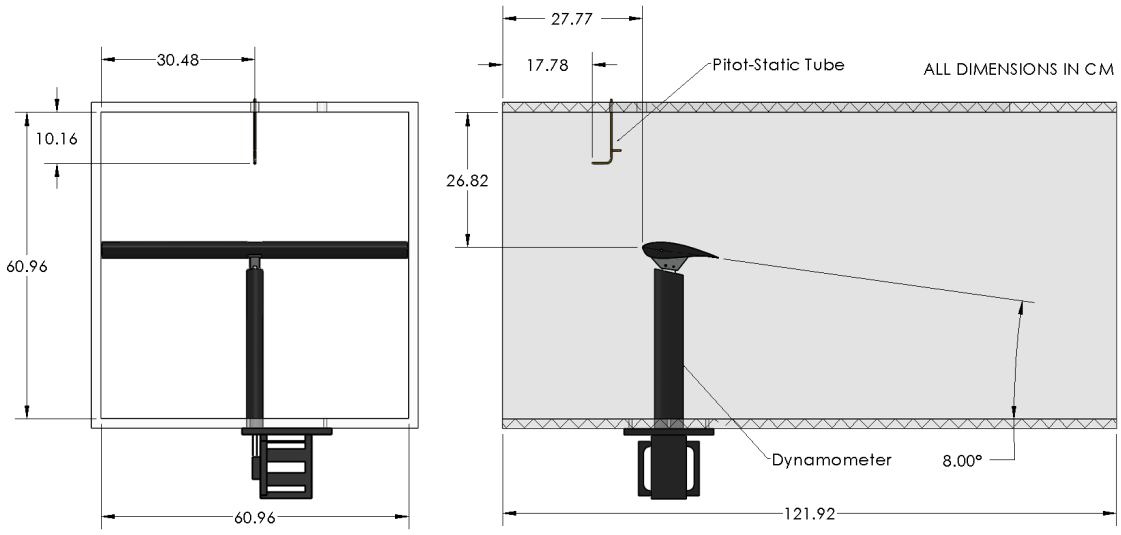

Figure 3.16: S823 Airfoil and Measuring Equipment Installed in Wind Tunnel

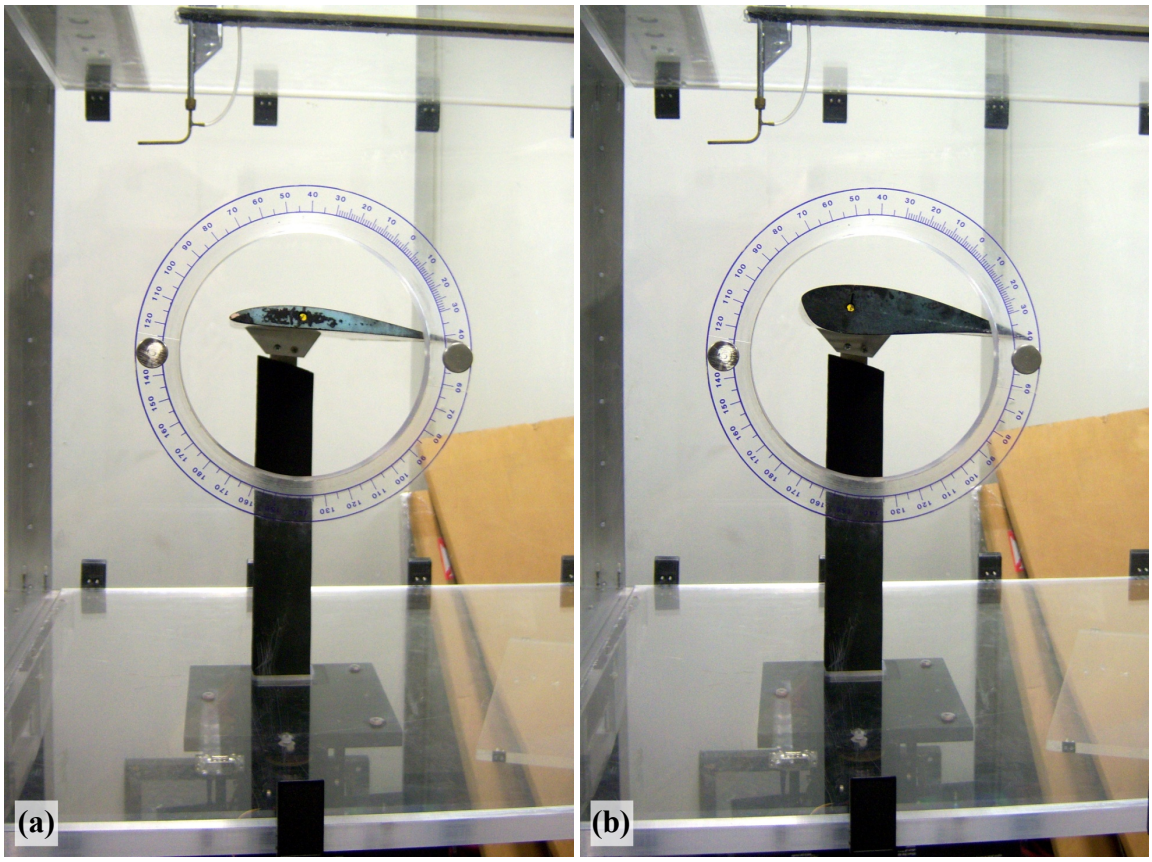

Figure 3.17: (a) E387 and (b) S823 Airfoils Mounted on Dynamometer in Wind Tunnel

Testing Procedure

The following procedure was used in airfoil testing. First, the angle of attack was set and measured. Next, the wind tunnel was run at the desired Reynolds numbers from highest to lowest, taking data at each speed after the tunnel reached steady state. The flow over the airfoil generally reached steady state within 60 seconds of changing the velocity; however, steady state was determined when the freestream velocity, lift, and drag measurements were not changing with time. This condition was tested in the LabVIEW® program by calculating the slope of the data with respect to time and comparing it with an experimentally determined value. After careful consideration, 5×10^{-4} and 3×10^{-5} were chosen as the thresholds for the lift and drag, respectively.

Automation

The majority of the data acquisition process was automated and integrated into a single program using LabVIEW®. This included measuring atmospheric conditions, controlling the wind tunnel speed, and measuring lift and drag. However, because of the design of the dynamometer, the angle of attack was adjusted and measured manually. Sample LabVIEW® code can be found in Appendix F.

Figure 3.18 shows a flowchart of the algorithm used in the automation of the airfoil testing process. The inputs to the program include the atmospheric pressure, planform area of the wind, chord or characteristic length used in Reynolds number calculation, the voltage to lift and drag conversion factors for the dynamometer (which is the slope of the linear regression from the calibration seen in Figure 3.15), the DAQ settings, and an array of voltages that set the wind tunnel speed to the desired Reynolds numbers. The wind speeds must be arranged from highest to lowest so that the flow is

initially attached (for most angles tested, the flow is attached at a Reynolds number of 200,000, but not necessarily at a Reynolds number of 75,000 and below). After setting the wind tunnel speed, the program was paused for 60 seconds to give the aerodynamics time to reach steady state. This pause also occurred when decreasing the wind speed to a lower Reynolds number. After that, 3 sets of data averaged over 30 seconds and used to determine if the data was steady. If the data was not steady, more data would be taken. Once the steady criterion was satisfied or 20 minutes of data has been taken at that Reynolds number, the wind tunnel would be set to the next wind speed. When all wind speeds have been tested for the desired angle of attack, the wind tunnel is stopped and the angle of attack can be adjusted. After all angles of attack have been tested, the experiment is considered complete for that airfoil.

Data Reduction

Standard corrections were applied to the airfoil data to account for the increased drag due to the airfoil mount as well as the flow conditions altered by the wind tunnel walls, as previously described in Chapter 2. To account for the increased drag due to the airfoil mount, the bottom bracket of the mount (detached from the airfoil) was installed in the wind tunnel and secured at an angle of 0.0 degrees. Subsequently, the wind tunnel was run over the range of Reynolds numbers tested and the measured drag was converted to a coefficient. This value was then subtracted off the measured values for drag at the corresponding Reynolds numbers. Additionally, the wind tunnel blockage corrections documented by Barlow et al. [59] and outlined in Equations 2.43-2.45 and 2.48-2.52 have been applied. A sample Mathcad® sheet used in data reduction for data taken for the S823 airfoil at a Reynolds number of 200,000 can be found in Appendix G.

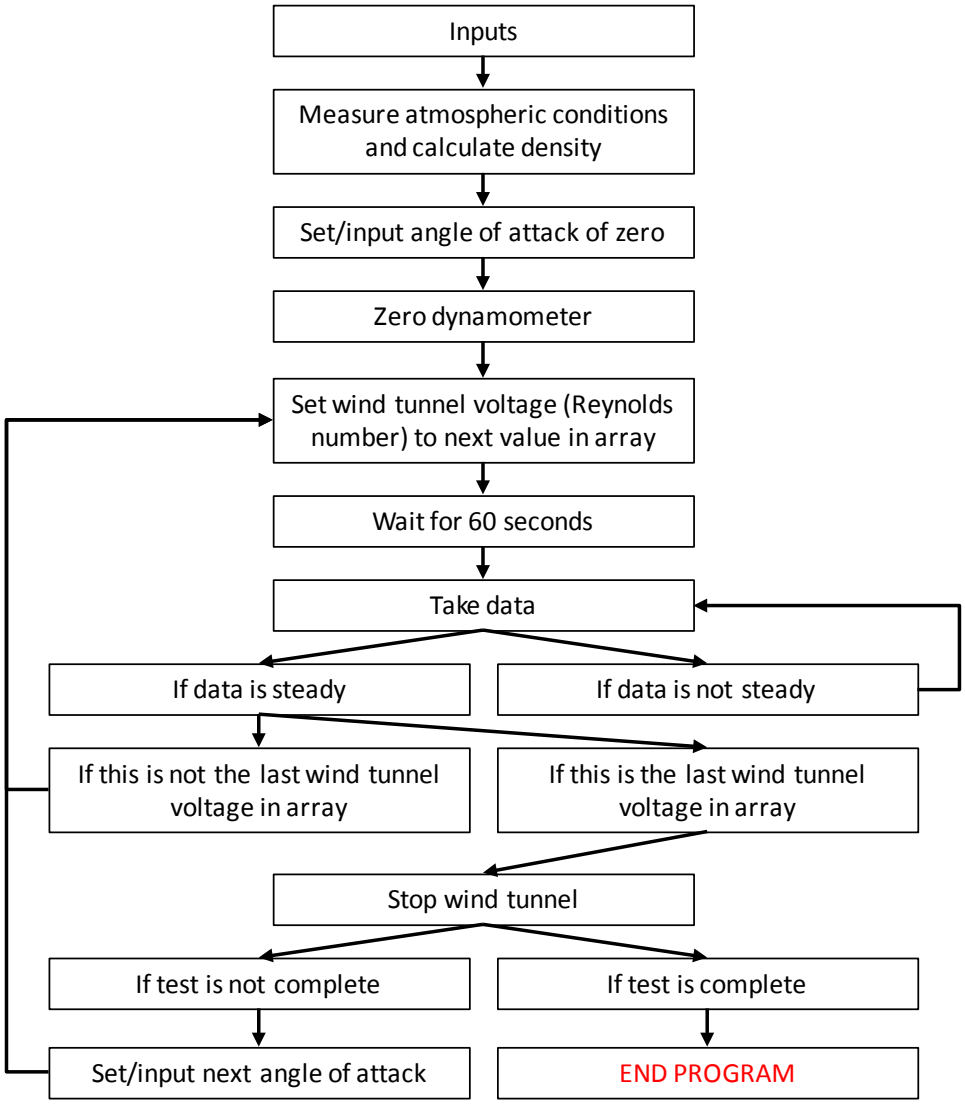

Figure 3.18: Flowchart of Airfoil Testing Automation Algorithm

Uncertainty Analysis

Experimental uncertainty was determined using the method outlined by Kline and McClintock [137]. A sample uncertainty calculation for the S823 airfoil at a Reynolds number of 200,000 and the entire range of angles of attack has been included in Appendix G. Angle of attack measurements were within ±0.1 degrees. Velocity measurements ranged from 0.562-3.608% uncertainty, coefficient of lift measurements ranged from 1.160-18.726% uncertainty for coefficient of lift with a magnitude greater

than 0.13, and the coefficient of drag measurements ranged from 1.201-8.928% uncertainty.

Wind Turbine Study

Goal of Experiment

The purpose of the wind turbine experiments performed in this study is threefold: first, to experimentally validate a correction factor for wind tunnel blockages up to approximately 50%; second, to show the experimental difference between optimizing the angle of twist using BET and BEMT; finally, to determine the sensitivity of changing the BET design angle on a wind turbine blade ±2 degrees has on wind turbine performance.

To experimentally validate the scaling and experimental techniques used in wind tunnel testing, a 0.5 m diameter rotor was scaled down to 0.4 m and 0.3 m diameter turbine and all three blade sets were then tested. Calculated frontal wind tunnel blockage area ratios and radial wake expansion can be seen in Table 3.1. The radial wake expansion was calculated using axial momentum theory. For this wake expansion calculation, the maximum coefficient of power measured in the experimental tests was used, 0.35. Additionally, Table 3.2 contains the general parameters for the three turbines that were scaled using geometric scaling, TSR matching, and Reynolds number matching. Figure 3.19 shows the twist and chord distribution used for these blades. These blades were designed with a constant chord for simplicity of blade design as well as to ensure the power output of the turbines was measurable.

Two blade sets were designed using both BET and BEMT to optimize the twist angle for power production at a design wind speed and TSR. The power production was experimentally measured and compared. Table 3.3 shows the general parameters for the

Table 3.1: Wind Tunnel Blockage and Radial Wake Expansion for Scaling Study

Parameter	Large	Medium	Small
Diameter (m)	0.5	0.4	0.3
Wind Tunnel Blockage Ratio (%)	52.8	33.8	19.0
Radial Wake Expansion (mm)	6.60	5.28	3.96

Table 3.2: General Turbine Parameters for Scaling Study

Parameter	Large	Medium	Small
Scaling Factor	1	1.25	1.667
Radius (m)	0.25	0.2	0.15
Hub Radius (mm)	50.0	40.0	30.0
Chord (mm)	40.0	32.0	24.0
Design Wind Speed (m/s)	5	6.25	8.333
Design Tip Re # (10^3)	69.8	69.8	69.8
Design Hub Re # (10^3)	19.4	19.4	19.4

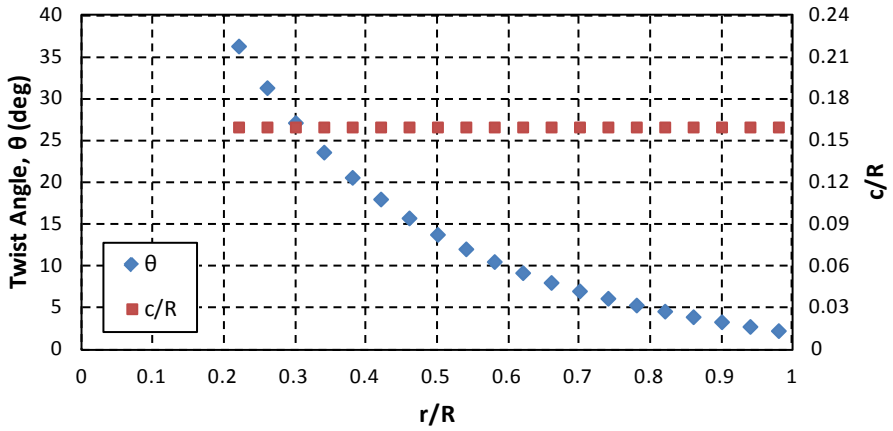

Figure 3.19: Twist and Chord Distribution for Scaling Study

full size design and scaled model tested in the wind tunnel. In this study a constant chord was also used to keep the parameters being varied minimal and isolate the effect of changing only the angle of twist.

Finally, to determine the effect of changing design angle and, thus, the pitch angle, three blades sets were designed with a predetermined angle of twist and no change in pitch, a two-degree increase in pitch, and a 2 degree decrease in pitch. Table 3.4 lists

Table 3.3: General Turbine Parameters for BET/BEMT Study

Parameter	Full Size	Scaled Model
Scaling Factor	1	2.3
Diameter (m)	1.15	0.5
Radius (m)	0.575	0.25
Hub Radius (mm)	57.5	25.0
Chord (mm)	92.0	40.0
Design Wind Speed (m/s)	5	11.5
Design Tip Re # (10^3)	160.6	160.6
Design Hub Re # (10^3)	35.2	35.2

the general parameters for the turbines used in this study. Figure 3.20 shows the twist and chord distribution for the "zero-pitch" turbine blade set.

Table 3.4: General Turbine Parameters for Pitch Study

Parameter	Value
Design TSR	5
Diameter (m)	0.5
Radius (m)	0.25
Hub Radius (mm)	25
Chord (mm)	40
Design Wind Speed (m/s)	5
Design Tip Re # (10^3)	69.814
Design Hub Re # (10^3)	15.308

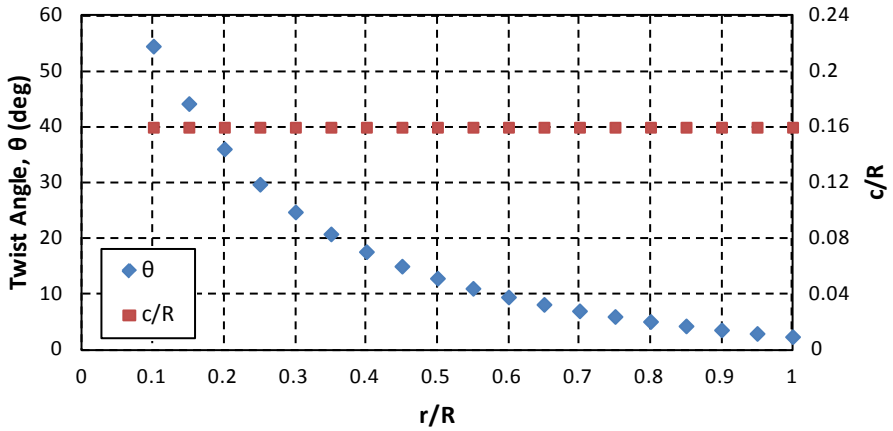

Figure 3.20: Twist and Chord Distribution for Pitch Study

Turbine Rotor CAD and Manufacture

The rotor assembly that was mounted onto the test stand included three blades, a dovetail hub, and a nosecone, which were all modeled in SolidWorks®. The blades were drawn by lofting S823 airfoil profiles and rotating each profile around the quarter chord to obtain the design angle of twist. To strengthen the blade, a chamfer (at 45 deg with a leg height equal to 6.25% of the chord) was drawn around the base of the blade. Additionally, the trailing edge of the blade was filleted (with a radius equal to 0.25% of the chord) to ensure a smooth trailing edge was printed. The wind turbine blades and dovetail hub were printed on an Objet30 desktop printer, with a layer resolution of 0.0011 inches (27.9 μm) using VeroWhite material. The blades were not sanded after manufacture, thus, any surface roughness from the printing process is on the order of the printer resolution. The nosecone was printed on a Dimension 768 3D printer, which has a layer resolution of 0.01 inches (0.254 mm) and uses ABS plastic.

Using the chord and twist distribution seen in Figure 3.19, three blade sets were printed with diameters of 0.5, 0.4, and 0.3 m, as seen in Figure 3.21. These blades were geometrically scaled with Reynolds number and TSR matching.

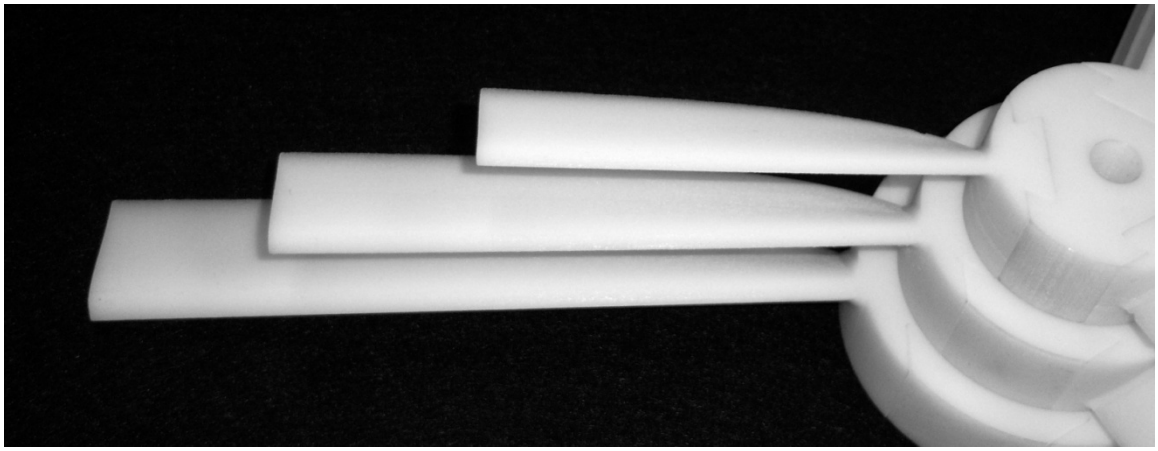

Figure 3.21: Printed Wind Turbine Blades used in Scaling Test

The SolidWorks® models of the BET- and BEMT-optimized blades can be seen in Figure 3.22. The actual printed blades can be seen in Figure 3.23, which highlights the differences in the twist distribution between the two blade designs. Additionally, these blades were printed with a trip strip, which was seen to improve performance in the airfoil study. The trip strip can be seen in the SolidWorks® model (Figure 3.22) as well as in an up-close picture of a BEMT-optimized blade in Figure 3.24.

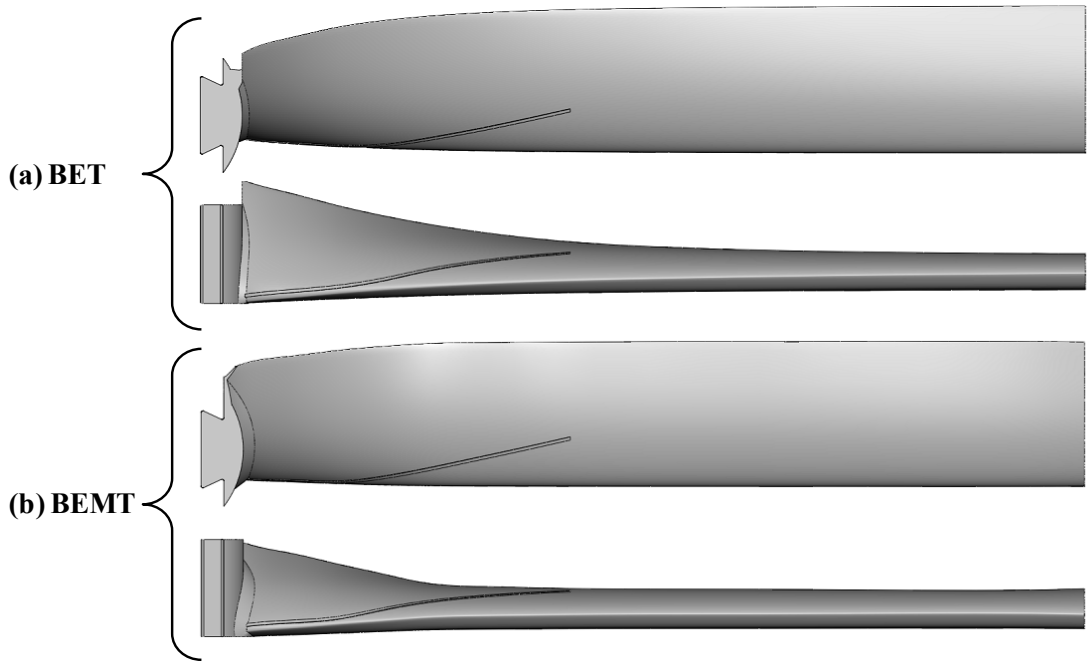

Figure 3.22: SolidWorks model of (a) BET- and (b) BEMT-optimized blades

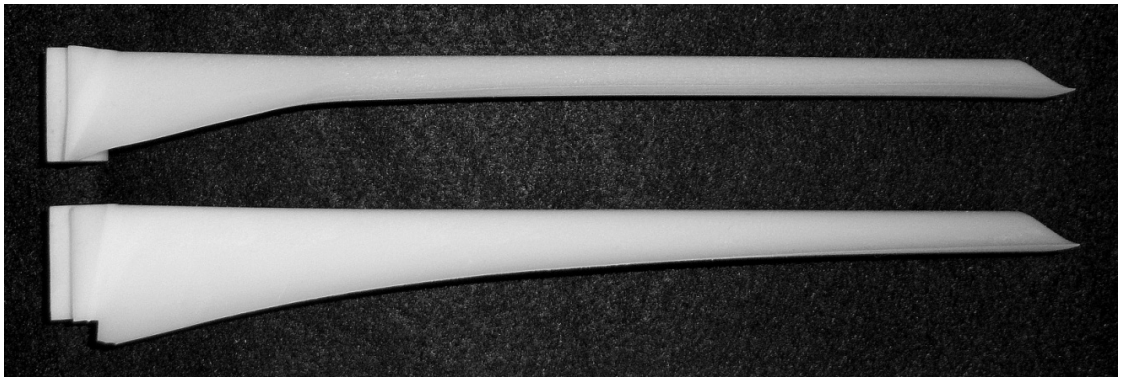

Figure 3.23: Printed BET- (top) and BEMT- (bottom) designed blades

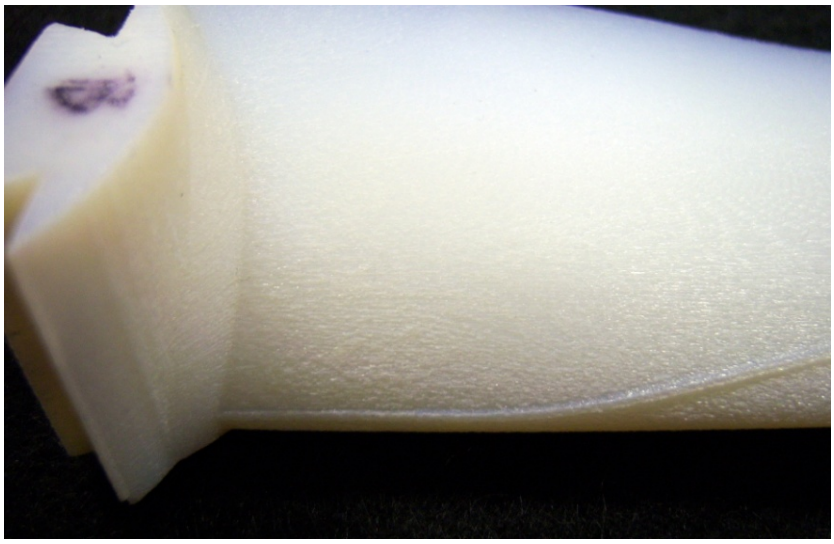

Figure 3.24: Printed Trip Strip on BEMT Blade

Finally, the printed blades used in the pitch study can be seen in Figure 3.25, which highlights the difference in the pitch angle. The blade in the center has the twist distribution seen in Figure 3.20, and the other two blades have the same twist distribution offset by 2 degrees.

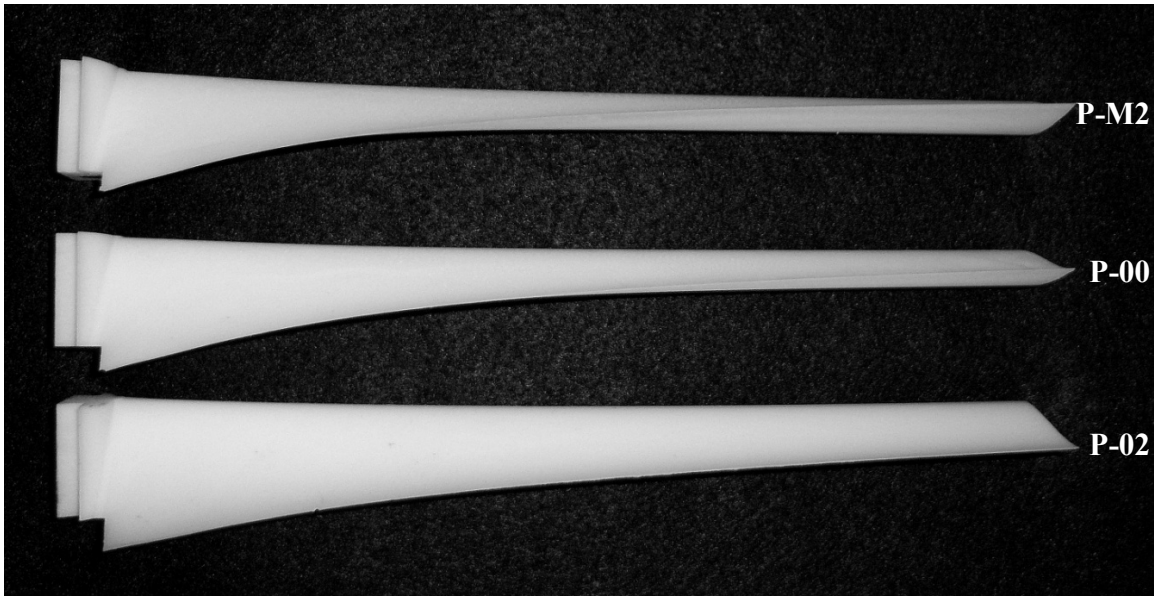

Figure 3.25: Printed Wind Turbine Blades used in Pitch Study

Facility and Measurement Equipment

To achieve these goals, the designed rotors were tested in the Baylor Subsonic Wind Tunnel. The atmospheric conditions were measured as detailed previously. The wind turbine test stand (Figure 3.26) was designed in previous research at Baylor University [138] in which a comparison of multiple motors was performed. As a result of that study, a maxon RE-40 motor was used as a generator. The motor specifications are listed in Table 3.5. A shaft adapter increased the size of the generator shaft to a ½-13 inch threaded shaft, 1-3/8 inches long with 1 inch of threads.

Figure 3.26: Wind Turbine Test Stand

Output voltage from the generator was measured using a voltage divider connected to an NI 9263 CDAQ. The voltage divider was designed to divide the voltage

Table 3.5: Re-40 Motor Data

Specification	Value
Model Number	148877
Type	Brushed, Graphite
Diameter	40 mm
Assigned Power Rating	150 W
Maximum Permissible Speed	8200 rpm
Maximum Continuous Current	3.33 Amps
Maximum Continuous Torque	201 mNm
Max Efficiency	92%
Torque Constant	60.3 mNm/A

by three (schematic shown in Figure 3.27) and keep the output voltage below 10 VDC, the maximum voltage input of the NI 9263 CDAQ module. It was constructed with three 100,000 Ω, 0.5 Watt resistors with a tolerance of ±0.05% and calibrated by generating a voltage from 0-30 VDC over the voltage divider using a BK Precision 1760A DC Power Supply. The voltage applied to the voltage divider circuit was measured using an Agilent 34401A Digital Multimeter. The voltage divider output was measured using the NI 9263 CDAQ module, which was controlled using LabVIEW®. The resulting calibration curve can be seen in Figure 3.28.

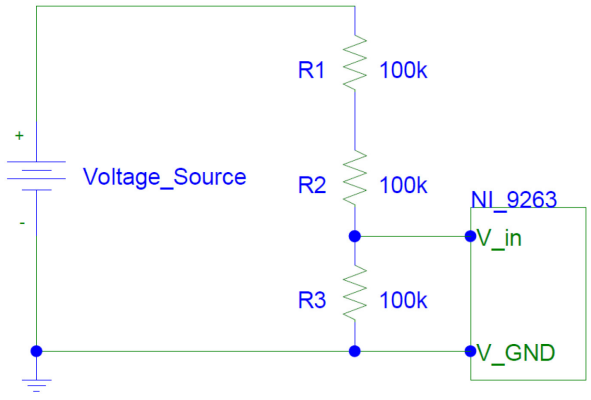

Figure 3.27: Voltage Divider Schematic

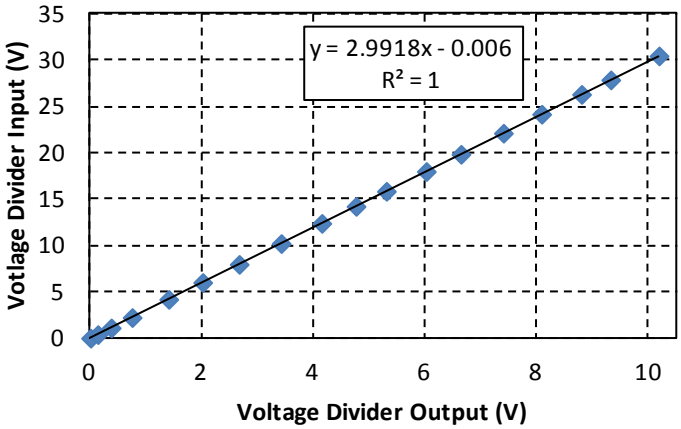

Figure 3.28: Voltage Divider Calibration Data

The maximum power point (MPP) of the turbine was determined by varying its rotational speed at a specified wind speed and applying a resistive load to the generator. A sample power curve can be seen in Figure 3.29 showing both the variation of power output with resistive loading and TSR. A custom-designed decade box with two decades and a resistive range of 1-99 Ω was used to varying the resistive load. This decade box was designed to set the resistance based on a 0-5 VDC input signal, which was output by an NI BNC 2110. The resistors in this decade box are Bourns Thick Film Resistors in the 652-PWR2202 family, with a power rating of 30 W. TE Connectivity T9A relays were used to switch between resistors. A full schematic of the circuit as well as the code used by the microcontroller can be found in Appendix H. In verification of the resistor values of this decade box, it was determined that the relays did not consistently operate properly and added an unpredictable resistance to the circuit depending upon how well they short circuited their respective resistors. Because of this, a Clarostat 240-C Decade Box was used instead of the custom-designed decade box for all tests. The resistances of both units were determined using an Agilent 34401A multimeter.

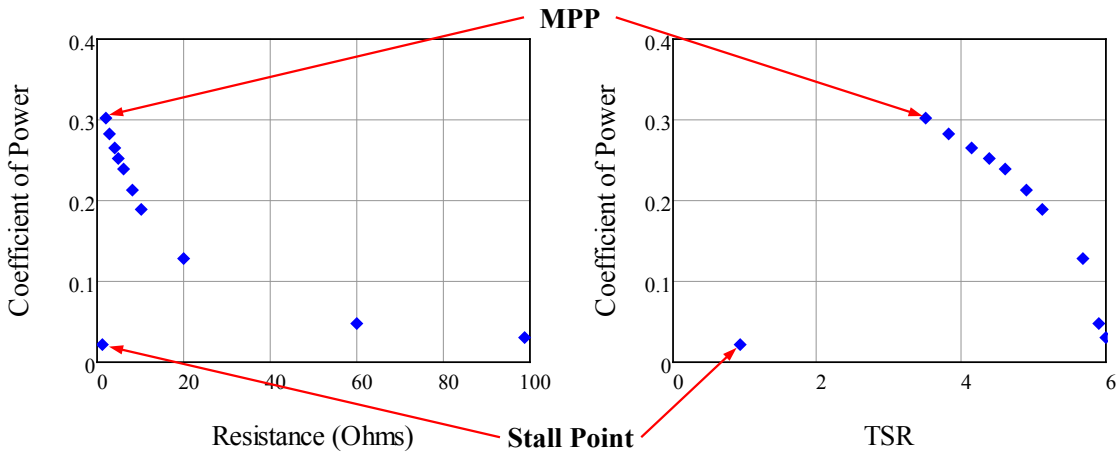

Figure 3.29: Sample Power Curve at a Specific Wind Speed

The rotational velocity of the wind turbine was measured using a HOTO ET-1 External Trigger Kit for use with the ESL-20 LED Stroboscope. The output of the external trigger was connected to a 2.2 kΩ pull-up resistor, which was connected to a +5 VDC signal output from the NI BNC 2110. The resulting voltage output of the external trigger kit varied from 5 VDC under no excitation and approximately 0.75 VDC when the trigger was excited. When the turbine was spinning, this produced a square wave which was subsequently used to calculate frequency and rotational velocity based on the number of pulses using LabVIEW®. The number of pulses was determined by counting the leading edge of each pulse in one second. However, at rotational velocities lower than 120 rpm, there will only be one, if any, pulse in a second. Thus, by increasing the sampling duration if the turbine was spinning (detected by a single pulse), rotational velocities as low as 30 rpm can be measured.

A schematic of the experimental setup of the largest rotor used the scaling test can be seen in the wind tunnel in Figure 3.30. The only difference between this setup and the other wind turbine tests is the rotor used in the test. The other rotors used in the scaling

test have a smaller diameter, and the other wind turbine tests had the same diameter as the large turbine seen in the figure. The pitot-static tube was mounted upstream of the wind turbine by 33.29 cm. It was also 13.34 cm from the ceiling, and 17.15 cm from the side wall, far outside of the boundary layer on the wall. The RPM sensor is mounted at the back of the motor and measuring the rotational velocity on the shaft extruding out of the back of the generator. Both the large rotor used in the scaling test and the BEMT-designed rotor are seen in the wind tunnel in Figure 3.31.

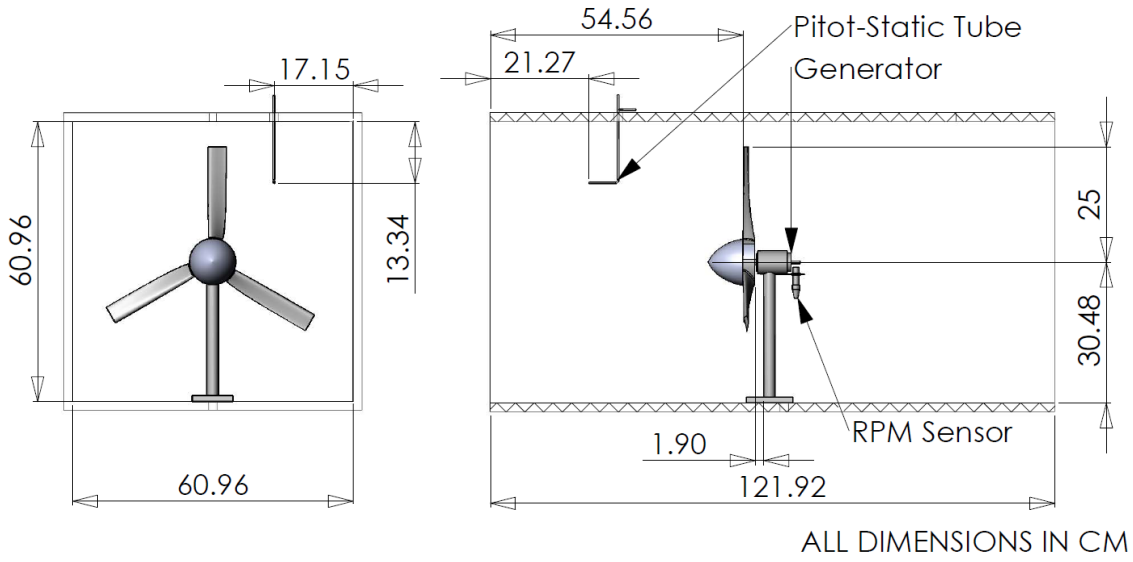

Figure 3.30: Largest Scaling Test Wind Turbine and Measurement Equipment Installed in Wind Tunnel

Testing Procedure

The experimental process required developing a power curve for each wind speed to determine the MPP. Depending upon the turbine blade being tested, the wind speed range was as wide as 1-10 m/s in increments of 0.5 m/s. Because of the blockage correction, the wind speeds were set by running the wind tunnel with an empty test section to determine the "corrected" velocity. The MPP at each test wind speed was then

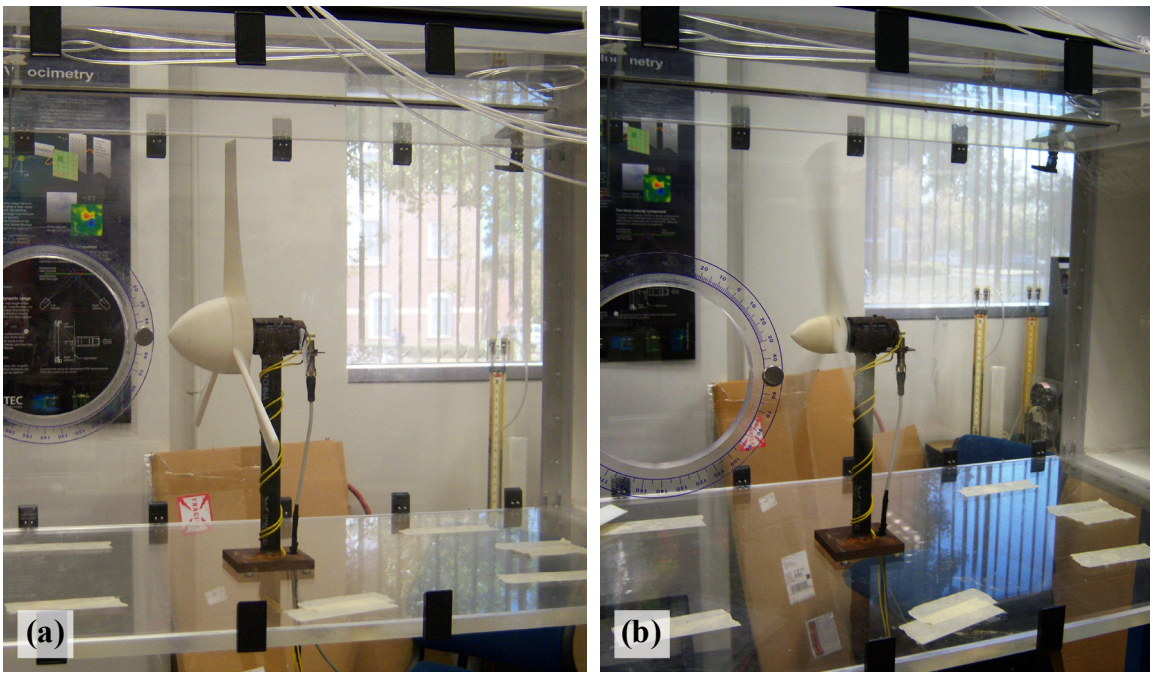

Figure 3.31: Pictures of (a) Largest Scaling Study Rotor and (b) BEMT-Designed Rotor on Test Stand in Wind Tunnel

used to develop a curve of coefficient of power versus wind speed. The coefficient of power curve at each wind speed was developed by connecting the generator to a resistive load, reducing the resistance from 99 Ω until stall occurred, and measuring the power output and rotational velocity at each loading. Additionally, the rotational velocity was measured when the generator was disconnected and the turbine unloaded.

Automation

The wind turbine testing procedure and measurement process was mostly automated using LabVIEW®. This includes controlling the wind tunnel, measuring atmospheric conditions, measuring rotational velocity, measuring output voltage from the generator. While a custom decade box was automated for testing, the resistance was changed manually because of the previously mentioned issue with the relays. Thus, the only manual part of testing was changing the resistance.

Figure 3.32 shows a flowchart of the algorithm used in automating the wind turbine testing. The inputs to the program included the atmospheric pressure, the radius of the turbine, the scaling factor, the DAQ settings, the maximum current allowable based on generator specifications, and the maximum safe rotational velocity. The maximum current allowable for the maxon motor is 3.33 Amps. The maximum safe rotation velocity was limited between 2500 and 3800 depending upon the turbine being tested to prevent structure failure of the blades. Additionally, and array of voltages for setting the wind tunnel at desired wind velocities was input. These voltages were determined by running the wind tunnel with an empty test section from the lowest test speed to the highest test speed while recording the corresponding voltages.

The freestream velocity, rotational velocity, and current being produced by the generator were monitored to determine if the aerodynamics had reached a steady-state and to ensure the limits for these parameters were not exceeded. If any of these parameters exceeded their maximum limits or after the highest velocity in the voltage array was reached and tested, the wind tunnel was stopped and the program was ended. A final input to the program was the bounds and step sizes used in calculating the next resistance. Figure 3.33 shows an example set of inputs for the resistance calculation and resulting series of resistances. The program begins the series with the starting resistance, then subtracts from that value the number in "Step1" and rounds to the nearest half-set (in this case, 10 Ω). This continues until the resistance value is the series is equal to or less than the value in "Mid1." At this point, "Step2" is used for the step size. This pattern continues until stall occurs, and enables quick and easy modification of the series depending upon when stall is expected to occurs (stall occurs at a lower resistance as wind speed is increased). The resistance series in Figure 3.33 would fully characterize

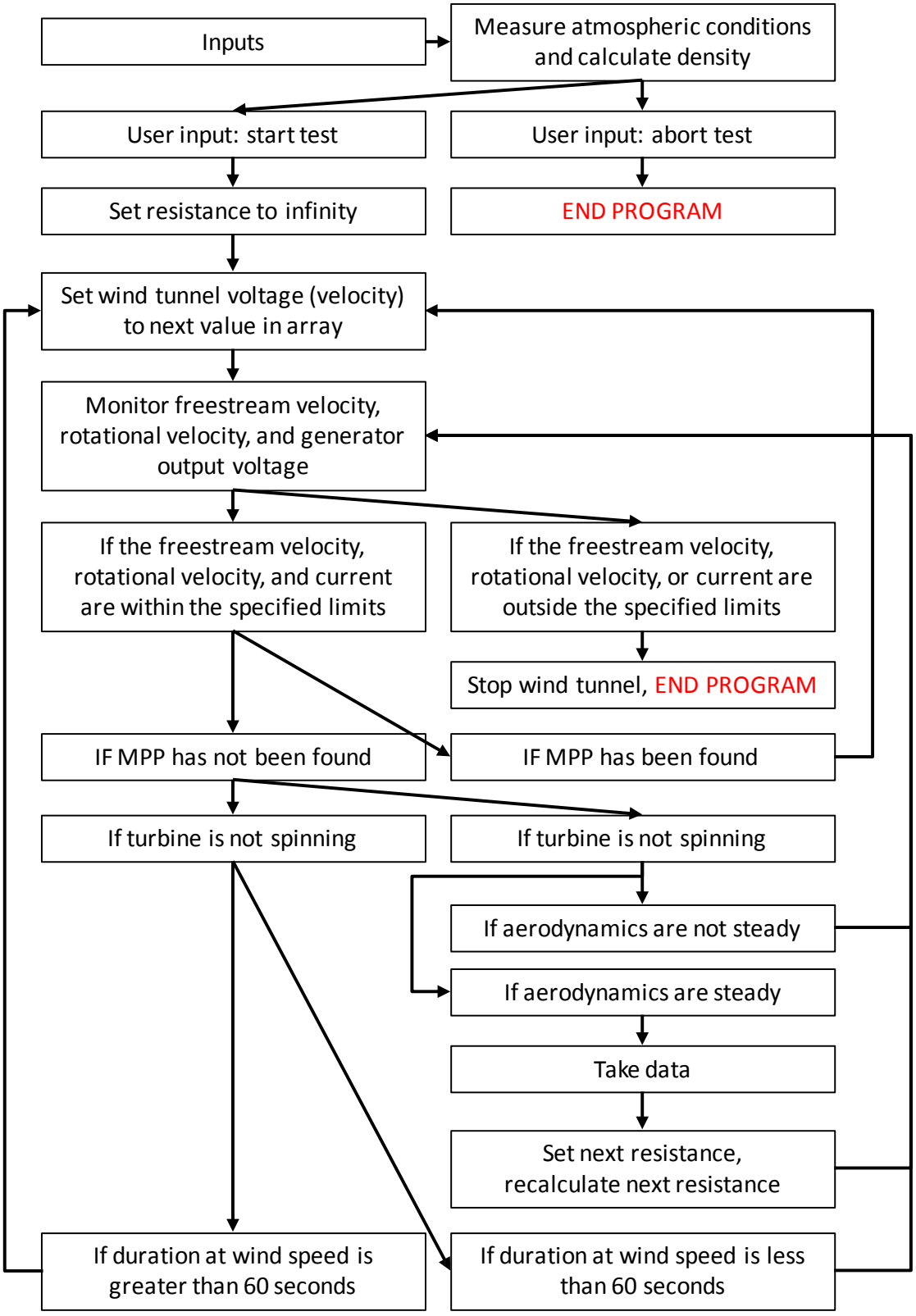

Figure 3.32: Flowchart of Wind Turbine Automation Algorithm

the performance at a particular wind speed and find the MPP if stall occurs below a resistance of 10 Ω. However, if stall occurs at 17 Ω, the MPP will not actually be found. At this point, the next resistance calculation will begin with the lowest pre-stall resistance, then increment the resistance by 1 Ω until stall occurs again. In this way, the program was able to determine the maximum power point and the resistance at which stall occurs within 1 Ω even without any prior knowledge of what loading at which stall will occur. The maximum power point MPP was considered "found" when the wind turbine power output decreases by more than 50%, and was accomplished by incrementing the resistance down by 1 Ω (the minimum resolution of the decade box) until the wind turbine stalled. Since the MPP is typically occurs just prior to stall, after having done this the MPP was considered found.

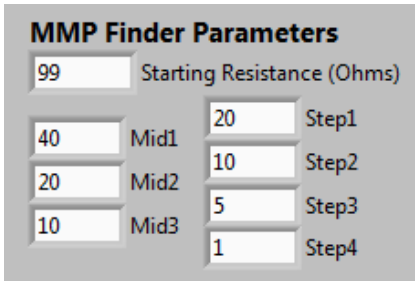

Resulting sequence:
99, 80, 60, 40, 30,
20, 15, 10, 9, 8, 7…

Figure 3.33: Example Bounds and Step Sizes for Next Resistance Calculation

The turbine was considered to be spinning if there was a change in the output voltage from the External Trigger Kit. While a full two pulses may not have been captured and the RPM cannot be calculated, the turbine is spinning. The aerodynamics were determined to be steady when the slope (from a linear regression) of 30 samples (taken approximately every second) was within a specified limit. The limit was determined experimentally as a threshold below which the data was always steady. The

slope for the wind velocity, RPM, and output voltage were 0.05, 10, and 0.2, respectively. In recording data, the dynamic pressure, rotational velocity, and voltage output of the generator were measured 6 times over a period of approximately 10 seconds, from which the parameters of interest could then be calculated. This provided a secondary check to determine whether the data was steady, because if a clear trend existed in the 6 averages, the data was not steady. Sample schematics of the LabVIEW® code and front panel can be found in Appendix I.

Data Reduction

The primary parameters of interest in the wind turbine tests are the TSR and power coefficient. Because the frontal area wind tunnel blockage for the experiments performed ranged from 19.0-52.8%, the corrections outlined in Equations 2.53-2.57 were applied to the calculation of TSR and power coefficient. To calculate the coefficient of power, the torque must be known. In order to determine the torque, the current was calculated with Ohms Law using the measured resistance and voltage. The torque was calculated based on the manufacturer specified torque constant for the maxon RE-40 motor used in testing, shown by the equation

$$\tau = Ik_{\tau} \tag{3.8}$$

where I is the generator current and k_{τ} is the torque constant. For scaled wind tunnel tests, the parameters and measurements were scaled using the relationships detailed in Table 2.2. Sample data reduction performed in Mathcad® can be found in Appendix J.

Uncertainty

The experimental uncertainty was calculated using the method outlined by Kline and McClintock [137]. The velocity uncertainty ranged from 0.870-7.192%, TSR from

0.915-8.587%, coefficient of power from 2.17-23.285%. Sample uncertainty calculations can be found in Appendix J.

CHAPTER FOUR

Results and Discussion

The results of the experiments detailed in the previous chapter and their impact on wind turbine design are described in this chapter. While the site survey will continue until two full years of data have been collected, one full year of data is presented here. The airfoil study performed and its use in wind turbine design is also presented. Additionally, the wind turbine blade sets designed and tested demonstrate both the validity of the experimental process and the advantages of better design procedures.

Wind Site Survey

Data collection at the wind site began on October 13, 2010. While approximately 17 months of data have been collected, only one full year of data has been used in this study in order to calculate the AEP. Figure 4.1 shows a wind rose generated using the wind vane data and wind speed measurements from the anemometer at 50 ft. Analyzing this data shows that 23.24% of the wind blows from the north and 57.97% of the wind blows from the south. Additionally, the mode, or most common, wind direction is 176 degrees from true north, which agrees with the Waco Regional Airport wind rose which indicated the primary wind direction to be south. Figure 4.2 shows the histograms and curve fits for each of the anemometers in 0.5 m/s bins. The curve fits were generated using the wblfit function in MATLAB®, which uses maximum likelihood estimation to determine the shape and scale parameters for the best fit and estimates confidence intervals for those parameters. In general the Weibull fit is very reasonable, however the peak of the fit is lower and to the right of the peak of the measured data. Additionally,

the curve is generally higher than the measured data on either side of the peak, but at wind speeds above 8-10 m/s the curve fit is lower than the measured data. Figure 4.3 shows the monthly averages compared with the yearly average to show seasonal trends. The data shows that in 2011, the average wind speeds are higher than the yearly mean between February and June. The months of July through January, with the exception of November, are lower than the yearly mean. More generally speaking, the highest monthly average wind speeds are in the spring, and the lowest occur between late summer and early winter. Also, the yearly mean wind speed increases with the height of the anemometer, as expected.

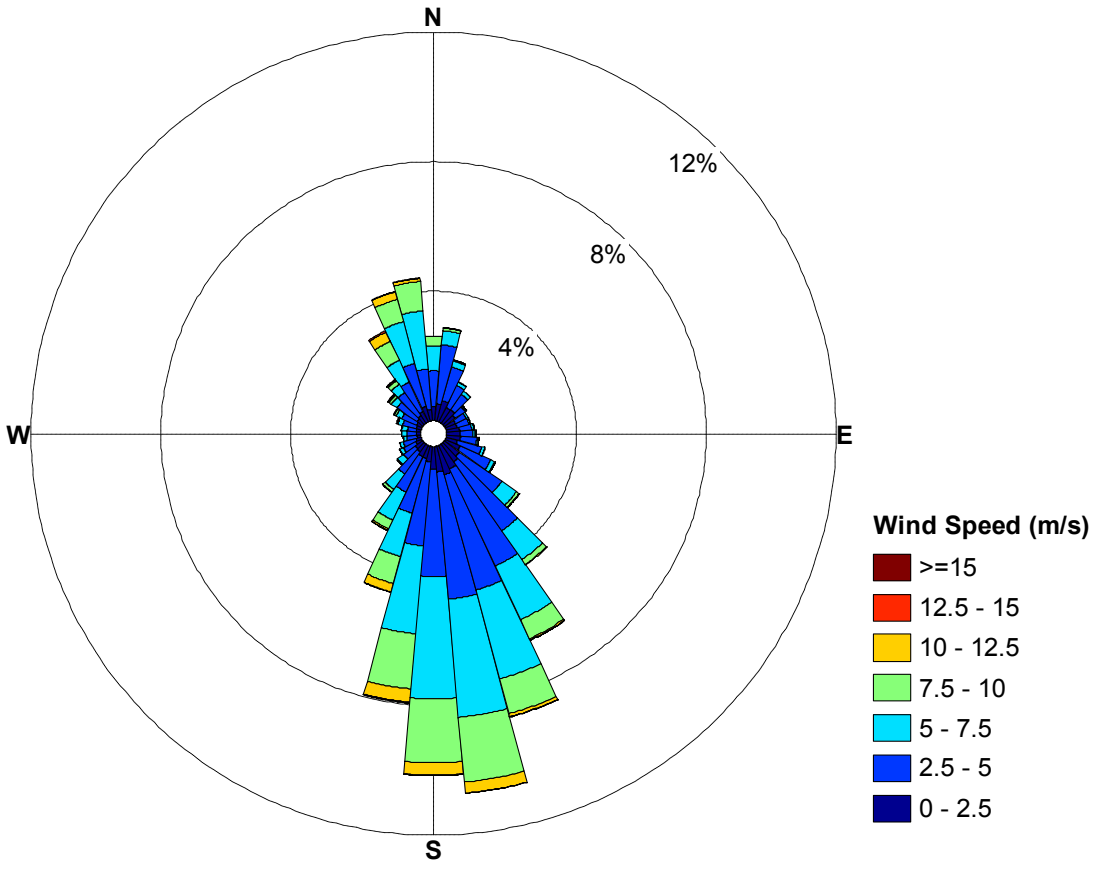

Figure 4.1: Wind Rose at 50 ft

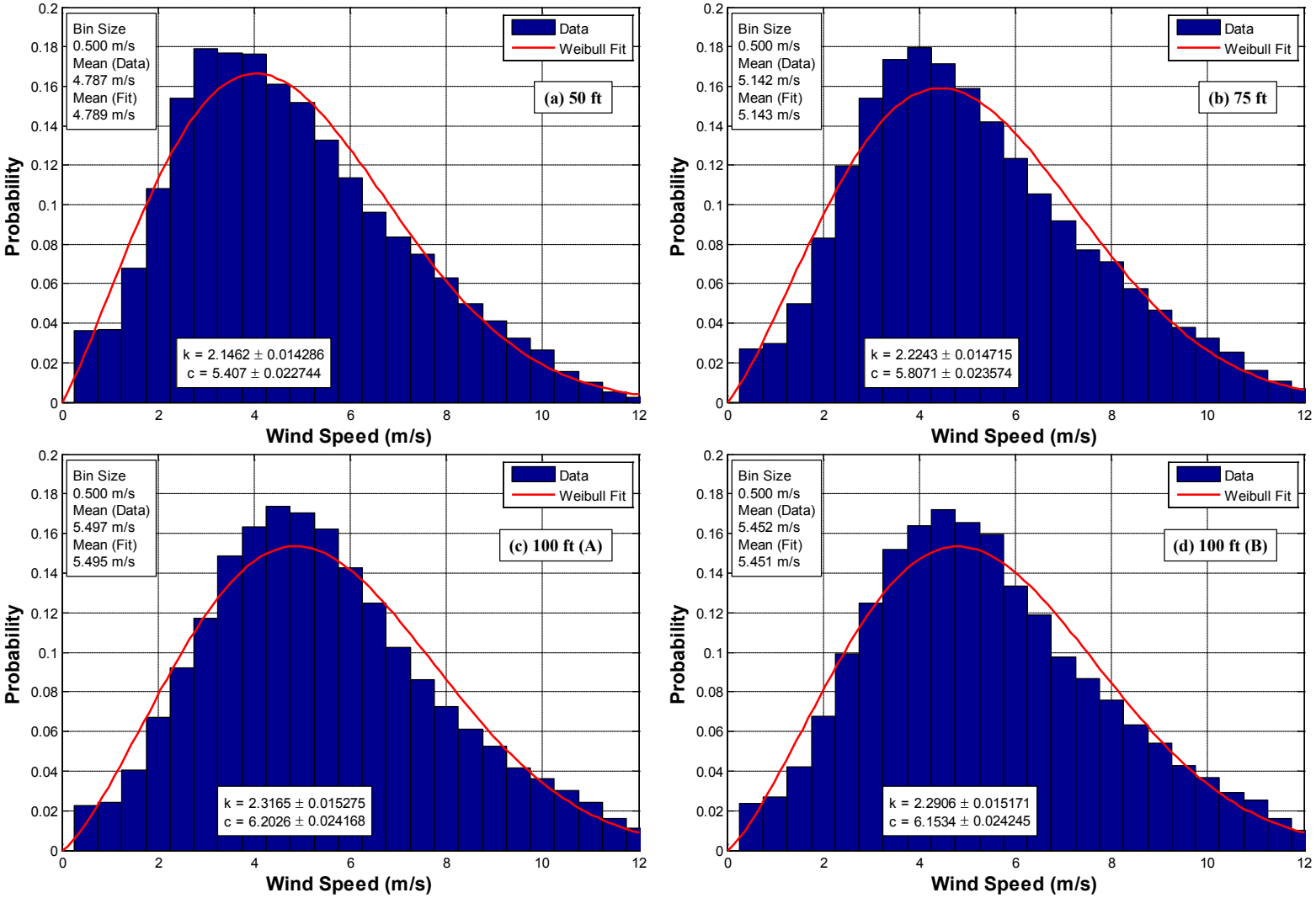

Figure 4.2: Wind Speed Distribution from each Anemometer

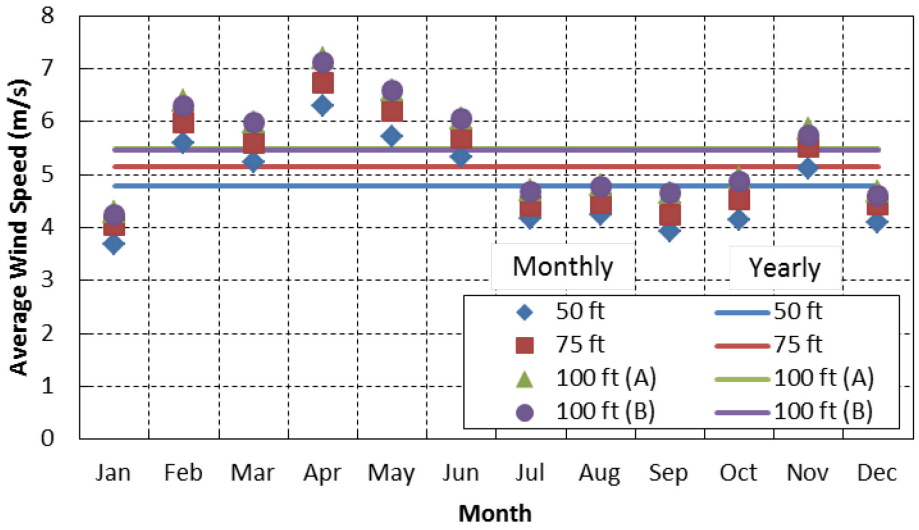

Figure 4.3: Monthly Average Wind Speed with Yearly Average Wind Speed

Airfoil Study

The purposes of the following airfoil study are twofold: first, to analyze the effect of roughness in the Reynolds number regime that a small-scale wind turbine experiences, and second, to acquire airfoil data over the range of Reynolds numbers necessary to design of a small-scale wind turbine for a wind speed of 5 m/s. As an initial validation of the airfoil testing process, data was taken at Reynolds numbers of 200,000 and 100,000 and compared with published experimental and numerical data. The published experimental data was taken at the Univeristy of Illinois, Urbana-Champagne [71]. The numerical data was generatued using PROFIL and was published in the S823 airfoil design report [48]. Additional numerical data was generated using XFOIL version 6.96.

E387 Airfoil Study

Airfoil data for the E387 airfoil was taken in order to validate the Baylor Subsonic Wind Tunnel for low-Reynolds number testing. This airfoil was chosen because of the extent of airfoil data available for this airfoil. The data taken in this work is compared

with PROFIL and XFOIL data. The PROFIL data was published in a study by McGhee et al. [52]. Experimental data taken by McGhee et al. [52] in a study in the NASA Langley Low Turbulence Pressure Tunnel (LTPT) and by Selig et al. in the University of Illinois, Urbana-Champagne, (UIUC) Low Turbulence Subsonic Wind Tunnel [71] are also included in the comparison. Airfoil data from Stuttgart and Delft are included in the report by McGhee et al. [52], but not included in this study because all the data agrees very well. The turbulence intensity for both the data taken at NASA Langley as well as UIUC is approximately 0.1%. The turbulence intensity in the Baylor Subsonic is under 0.2%.

Figure 4.4 shows the lift and drag data at a Reynolds number of 200,000. For the coefficient of lift curve the agreement between all the data is very good. The coefficient of drag also agrees well, however, the Baylor data does not seem to capture the increase in drag due to a laminar separation bubble between angles of attack between 0 and 7 degrees. The Baylor data is nearly 37% lower than the rest of the experimental data at an angle of attack of 5.3 deg. This may be due to the differences in drag measurement techniques noted by Miley [111], either using a force balance or the momentum-wake deficit technique.

Figure 4.5 shows the comparison of data for a Reynolds number of 100,000. In this case, the coefficient of lift data all agrees very reasonably. Similarly to a Reynolds number of 200,000, the Baylor data does not seem to capture the effect of the separation bubble like the NASA Langley and UIUC data. At this point it is notable that the Baylor data was taken with higher turbulence intensity than the other two experimental tests. Since higher turbulence intensity can make the flow transition from a laminar boundary layer to a turbulent boundary layer earlier on the surface of the airfoil, it is likely that the

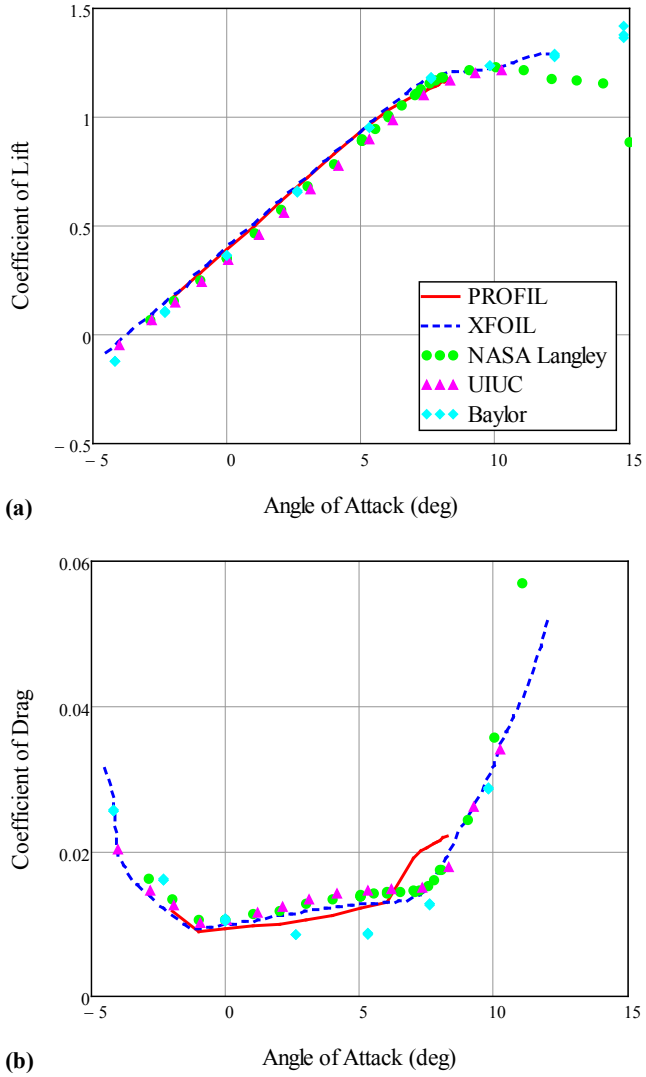

Figure 4.4: E387 Coefficient of (a) Lift and (b) Drag at a Reynolds Number of 200,000 [52, 71]

reduced separation bubble effects present in the Baylor data is due to transition occurring earlier.

Figure 4.6 shows the E387 airfoil at a Reynolds number of 60,000. Notably, the effects of the separation bubble on the coefficient of drag are larger for this Reynolds number with the Baylor data showing a lower peak coefficient of drag between the angles of attack of 0 and 8 deg. Analyzing the coefficient of lift data, an interesting

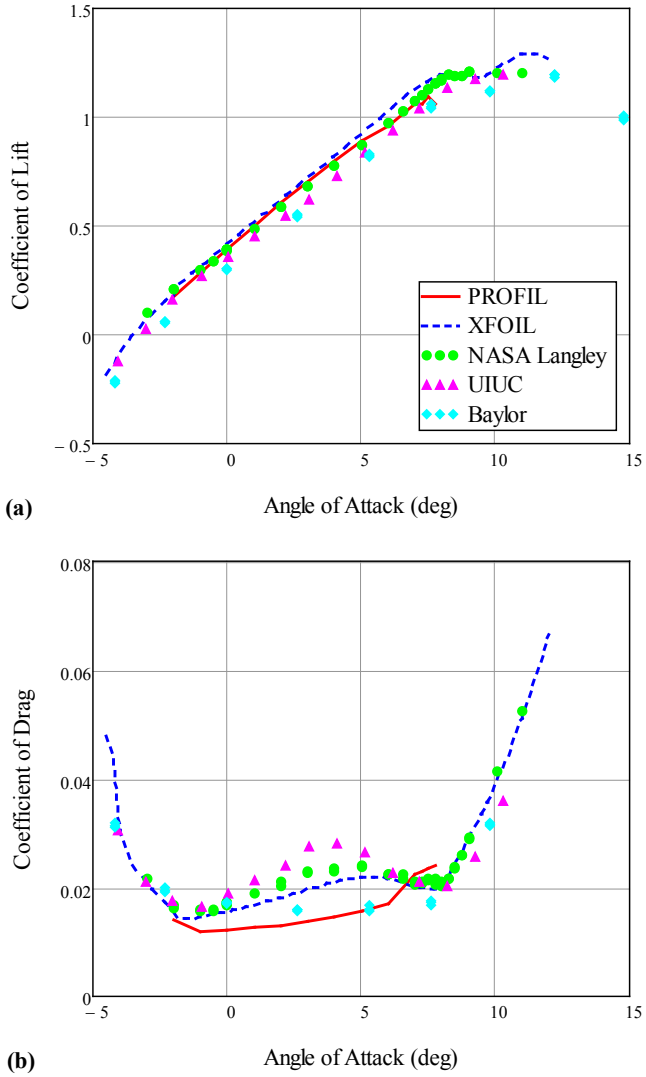

Figure 4.5: E387 Coefficient of (a) Lift and (b) Drag at a Reynolds Number of 100,000 [52, 71]

phenomenon occurs experimentally in both the NASA Langley and UIUC data between angles of attack of 5 and 7 degrees. For these angles, the flow is laminarly separating but not reattaching. However, at both higher and lower angles of attack, the flow separates laminarly and reattaches [52]. The NASA Langley experiments tested a Reynolds number of 60,000 with freestream pressures of 5.15 and 2.96 psi, and the test with a lower pressure had higher turbulence intensity. For an angle of attack of 7 deg, the test

with higher turbulence intensity separated earlier on the suction surface of the airfoil and never reattached, as shown in Figure 4.7. It is possible that the flow over the airfoil in the Baylor data is separating earlier on the airfoil surface than the other data due to the higher turbulence intensity and the flow is not reattaching, as in the case of a laminar separation bubble. However, this requires a flow visualization study to determine what is actually happening with the flow.

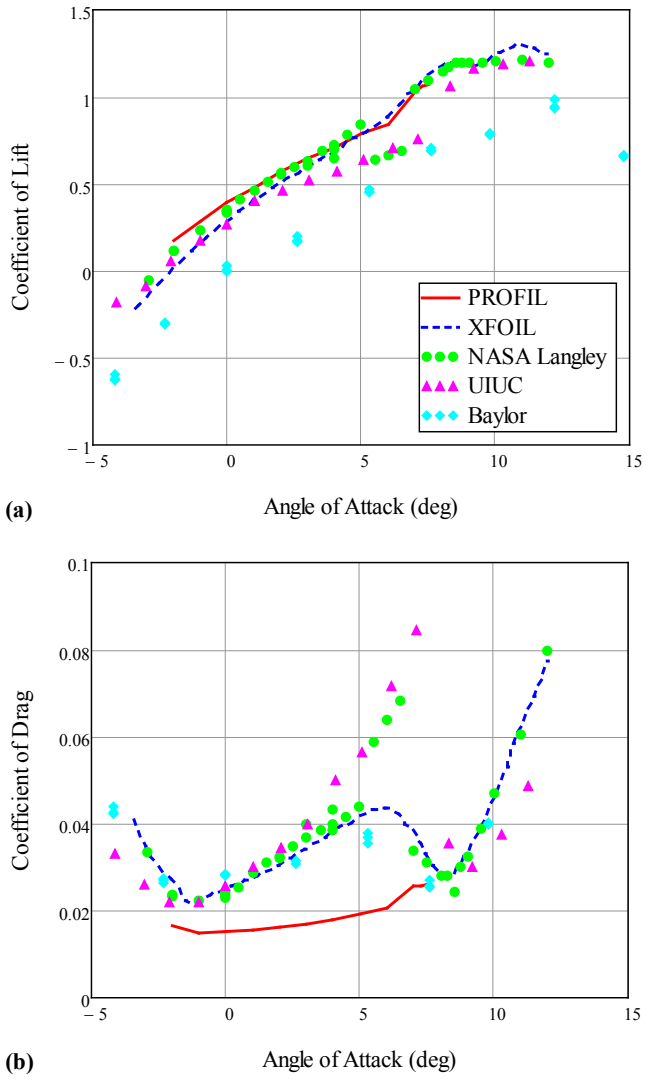

Figure 4.6: E387 Coefficient of (a) Lift and (b) Drag at a Reynolds Number of 60,000 [52, 71]

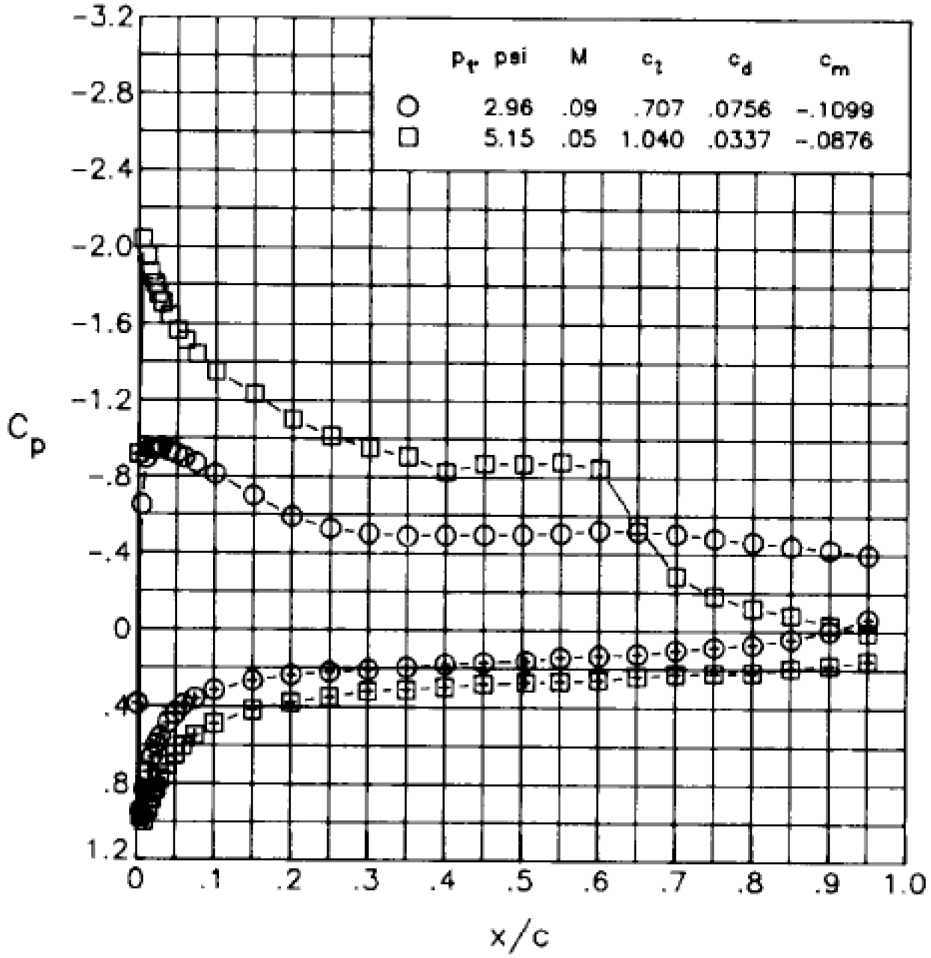

Figure 4.7: Experimental Coefficient of Pressure for the E387 Airfoil at an Angle of Attack of 7 deg, taken in the NASA Langley LTPT [52]

S823 Airfoil Study

Figure 4.8 and Figure 4.9 show the results of the experimental and numerical studies performed at Baylor University compared with published data. For both Reynolds numbers, all the data agrees very reasonably. Analyzing the coefficient of lift curves for both Reynolds numbers, all the data matches the basic theoretical solution that predicts a lift slope of approximately 0.1/degree, which is valid in the attached flow region. Additionally, both the experimental data sets capture stall within 1 degree of each other, as noted in Table 4.1 and Table 4.2. While the numerical tools do not predict deep

stall, both sets of experimental data capture a significant decrease in lift when deep stall occurs. However, the Baylor data captures this phenomena at a lower angle of attack than the UIUC data, which is may be due to the difference in turbulence intensity mentioned previously. A very interesting phenomena occurs at low angles of attack (below approximately 0 deg), resulting in an increase in lift and an increase in drag in the experimental data. However, for a Reynolds number of 200,000, the UIUC data does not capture the increase in drag at low angles of attack that the Baylor data does. This is because two sets of data were taken in the UIUC test, one in which lift and drag were measured, and one in which only lift was measured. The increase in lift, suggesting flow separation on the bottom of the airfoil, occurred during the test when only the lift was measured but not in the test when drag was also measured, thus the UIUC data does not show an increase in drag at low angles of attack for a Reynolds number of 200,000. No explanation is given for this behavior by Selig et al. [71]. While neither XFOIL nor PROFIL capture the phenomena present in the experimental data, XFOIL does predict the same phenomena at an angle of attack of -8 degrees and Reynolds number of 200,000. Figure 4.10 shows the streamlines over the surface of the airfoil pedicted by XFOIL, with flow separation occuring on the lower surface. This flow separation is due to the high camber and thickness of the airfoil, which creates an adverse pressure gradient that induces flow separation at low angles of attack. Because of the flow separation occuring on the lower surface, both the coefficient of drag and of lift are increased, as seen in Figure 4.8.

Notably, the UIUC and Baylor experimental data do not agree on the angle of attack at which deep stall and flow separation on the lower surface occurs nor the magnitude of the lift and drag coefficients in these regions. Because of the sensitivity of

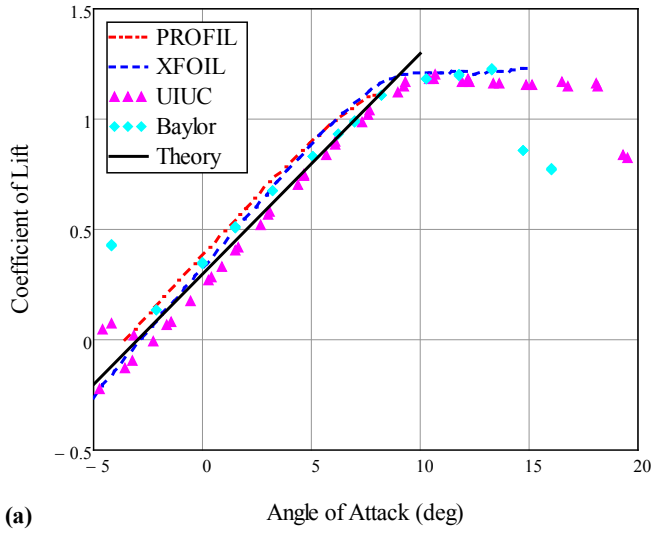

(a)

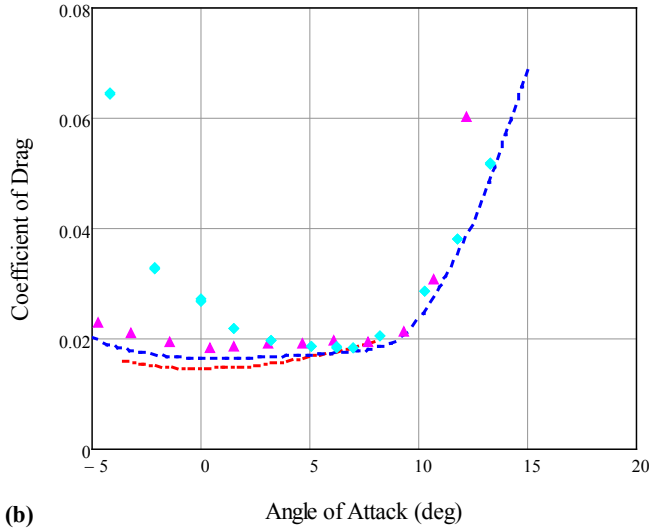

(b)

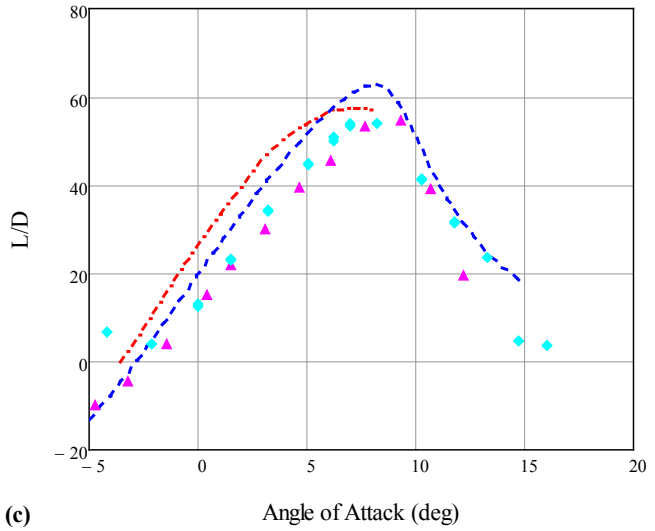

(c)

Figure 4.8: S823 Airfoil Data Comparison for a Reynolds number of 200,000 [48, 71]

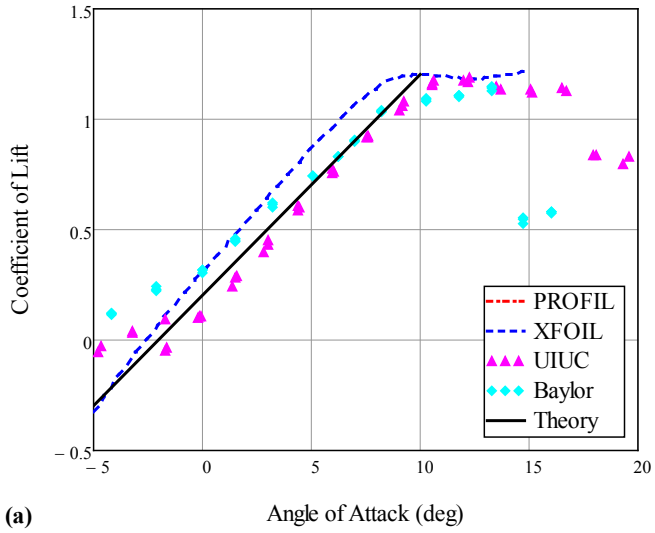

(a)

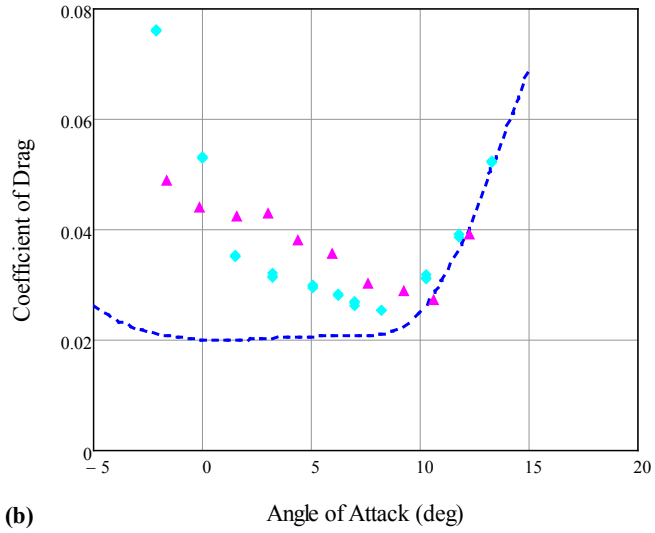

(b)

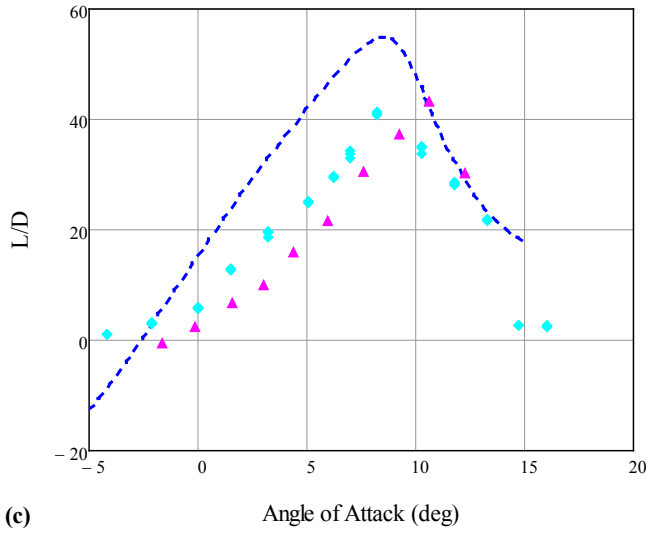

(c)

Figure 4.9: S823 Airfoil Data Comparison for a Reynolds number of 100,000 [71]

Table 4.1: Comparison of Distinct Angles of Attack (deg) for the S823 Airfoil at a Reynolds Number of 200,000

Airfoil Data	Onset of Stall	Onset of Deep-Stall	Location of Max L/D
PROFIL	N/A	N/A	7.6
XFOIL	9.5	N/A	8.0
UIUC	10.4	19.3	9.3
Baylor	10.3	14.7	8.2

Table 4.2: Comparison of Distinct Angles of Attack (deg) for the S823 Airfoil at a Reynolds number of 100,000

Airfoil Data	Onset of Stall	Onset of Deep-Stall	Location of Max L/D
XFOIL	8.0	N/A	8.5
UIUC	12.0	18.0	12.2
Baylor	11.8	14.7	8.2

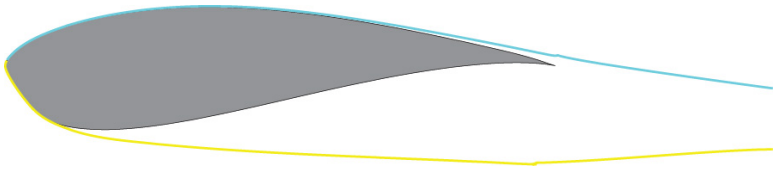

Figure 4.10: XFOIL Streamline Visualization of the S823 Airfoil at a Reynolds number of 2000,000 and Angle of Attack of -8 deg, showing Flow Separation on the Lower Surface

low Reynolds numbers flows to turbulence intensity, it is possible that the minor differences between the two test methods account for the differences in experimental data. Flow visualization studies could provide more insight into the discrepancies between the data sets.

Comparing the L/D curves for a Reynolds number of 200,000, the agreement is very reasonable. For a Reynolds number of 100,000 however, the XFOIL data peak more than 10% higher than the experimental data. Table 4.1 and Table 4.2 document a comparison of distinct angles in the airfoil data, showing agreement within 2 deg for a

Reynolds number of 200,000 and within 4 deg for a Reynolds number of 100,000 except for the onset of stall.

In addition to Reynolds numbers of 200,000 and 100,000, 75,000, and 50,000 were tested. At these Reynolds numbers, the effect of a separation bubble or even full separation reduced the lift produced significantly. In order to design a wind turbine to produce more power, reducing the effects of separated flow is beneficial to wind turbine performance. Because forcing the flow in the boundary layer to transition from laminar to turbulent can reduce separation over the airfoil, a trip strip was added at 25% of the chord from the leading edge, the thickest part of the airfoil, on the upper surface. The trip strips were applied and tested for all Reynolds numbers (50,000 to 200,000) but for Reynolds number of 100,000 and 200,000 the trip strip was detrimental to airfoil performance. The thickest part of the airfoil was chosen because as the flow moves past this location, it will naturally begin to have a negative pressure gradient and be more susceptible to flow separation. The goal was to place the trip strip just upstream of separation to force the boundary layer to transition as late as possible on the airfoil surface while still reducing the effect of separation. This prevents the added drag present in a turbulent boundary layer in the attached region as opposed to a laminar boundary layer while still reducing separation over the airfoil surface. Three trip strip heights—0.021, 0.035, and 0.080 inches—were applied and tested to determine which height improved the airfoil performance the most. The minimum thickness of 0.021 inches was chosen based on the momentum thickness over the range of Reynolds numbers predicted by XFOIL. However, at a Reynolds number of 50,000, the trip strips applied at 25% of the chord did not improve performance because separation occurred upstream of the trip strip. Thus, the 0.035 inch trip strip was moved to 2% of the chord from the leading edge

on the upper surface. While only the 0.035 inch trip strip was applied at the 2% chord location and this is not a complete testing matrix, the goal was not to determine the optimum trip strip location or height for each Reynolds number, but to improve performance over the range of Reynolds numbers tested. Additionally, a trip strip of 0.035 inches rather than 0.021 inches was chosen in order to improve the performance at Reynolds numbers of 50,000, 25,000, and 15,000. Since the L/D curve is directly related to torque and power production, the L/D curve is all that is displayed for the trip strip study. A higher peak L/D curve will give better performance at the design condition than a lower peak, and a higher L/D curve in general will result in better off-design performance than a lower L/D curve. Figure 4.11 (a-c) shows the L/D curves for Reynolds numbers of 100,000, 75,000, and 50,000 for a smooth surface and with a trip strip on the upper surface. The Reynolds number of 200,000 is not shown because the results are similar to that of 100,000. Analyzing the data for 100,000 in Figure 4.11 (a), every trip strip added decreased performance. However, for a Reynolds number of 75,000, shown in Figure 4.11 (b), the trip strips of 0.021 and 0.035 inches applied at 25% of the chord peak at approximately the same magnitude. Additionally, for angles between 2.5 and 7 degrees, the trip strips keep the flow attached and the L/D values are higher than for the smooth airfoil. Figure 4.11 (c) shows the data from a Reynolds number of 50,000. While the trip strips of 0.021 and 0.035 inches at 25% of the chord improve the performance from the smooth airfoil, the trip strip of 0.035 inches applied at 2% of the chord on the upper surface increased the peak of the L/D curve more than three times the peak of the two trip strips previously mentioned.

Figure 4.12 shows the airfoil data that was chosen to be used for wind turbine design in the BET and BEMT models. For Reynolds numbers of 200,000 and 100,000,

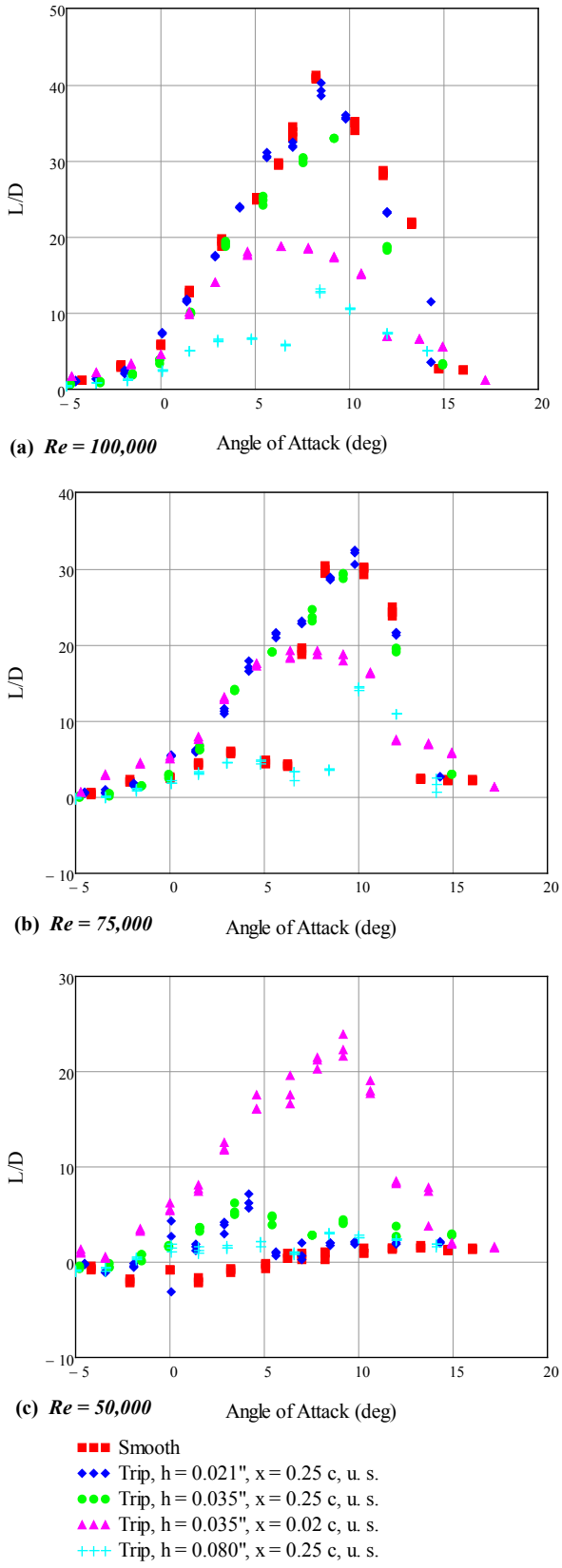

Figure 4.11: S823 Airfoil Data for Trip Strip Comparison at Various Reynolds Numbers

the airfoil data from the smooth surface was used. For a Reynolds number of 75,000, the data from the airfoil with the 0.035 inches at 25% of the chord trip strip was chosen. For a Reynolds number of 50,000, the data from the airfoil with the 0.035-inch trip strip at 2% of the chord was chosen. The coefficient of lift curves in Figure 4.12 (a) show the expected trend of decreasing magnitude with decreasing Reynolds number, which occurs because of the separation bubbles that form on the upper surface of the airfoil. However, for a Reynolds number of 50,000 the flow separation on the upper surface is reduced but there is likely still a separation bubble on the lower surface of the airfoil, which increased both the lift and the drag. The drag coefficient, shown in Figure 4.12 (b), shows the expected trend of increasing magnitude with decreasing Reynolds number. Finally, the L/D curve in Figure 4.12 (c) shows the expected trend of decreasing magnitude and the peak shifting towards higher angles of attack with decreasing Reynolds number. The decrease in peak occurs because of increased drag. The shifting of the peak occurs because the shape of the drag curve changes with Reynolds number.

Wind Turbine Study

The purposes of the wind turbine study were two-fold. First, to determine the validity of the wind tunnel corrections applied through a scaling study. Secondly, to determine the experimental difference in power output for a scaled 1.15 m diameter turbine when optimizing the angle of twist using BET and BEMT.

Scaling Study

Generally speaking, the results of the scaling study using Reynolds number matching validated the wind tunnel corrections applied. For all conditions tested the power curves of the small and medium turbines agree very reasonably, within 6.0%. For

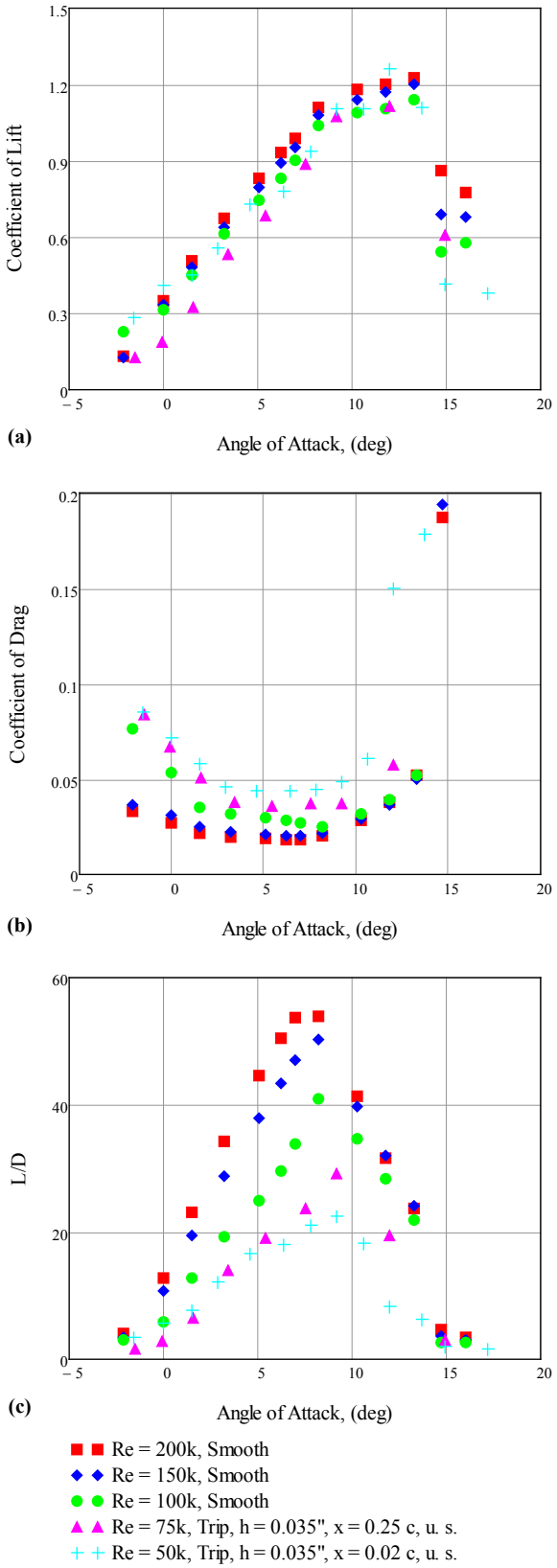

Figure 4.12: S823 Airfoil Data for Use in Wind Turbine Design

wind speeds of 5.5 m/s and greater, the large turbine also agreed reasonably well, within 9.2% of the data from the medium turbine. However, for wind speeds less than 5.5 m/s, the power curve of the large turbine differs by as much as 60.5% from the medium turbine data. Examining the Reynolds numbers distribution over the blades, power curves, as well as blockage factors at each wind speed provides insight and a likely explanation to this discrepancy.

Analyzing two wind speeds that are representative of the lower speeds tested (2.5 and 3.5 m/s), Figure 4.13 and Figure 4.14 shows the Reynolds number distributions over the blades for the unloaded and MPP cases as well as the corresponding power curves. Notably, there is no data for the small turbine at a wind speed of 2.5 m/s because it had not yet started spinning. At these speeds, the majority of the blades are experiencing Reynolds number less than 100,000, the value of Reynolds number below which a trip strip has been shown to significantly affect airfoil performance in Figure 2.12. In this Reynolds number range, any surface roughness on the blade has the potential to make a significant difference on the wind turbine performance because of the sensitivity of flow transition and separation to surface roughness, as noted previously [68, 139]. Comparing the Reynolds numbers over the blades of each of the turbines, there is a measureable difference between the large turbine and the other two, particularly when the turbine is unloaded at a wind speed of 3.5 m/s. Figure 4.13 (b) shows that while the MPP for the large and medium turbine are the same at 2.5 m/s, the curves are slightly different, suggesting that the aerodynamics are slightly different as well. Figure 4.14 (b) shows a similar behavior in that the small and medium turbines are nearly identical in performance over the whole range of loadings, but the large turbine is significantly different from the other two turbines and produces much less power.

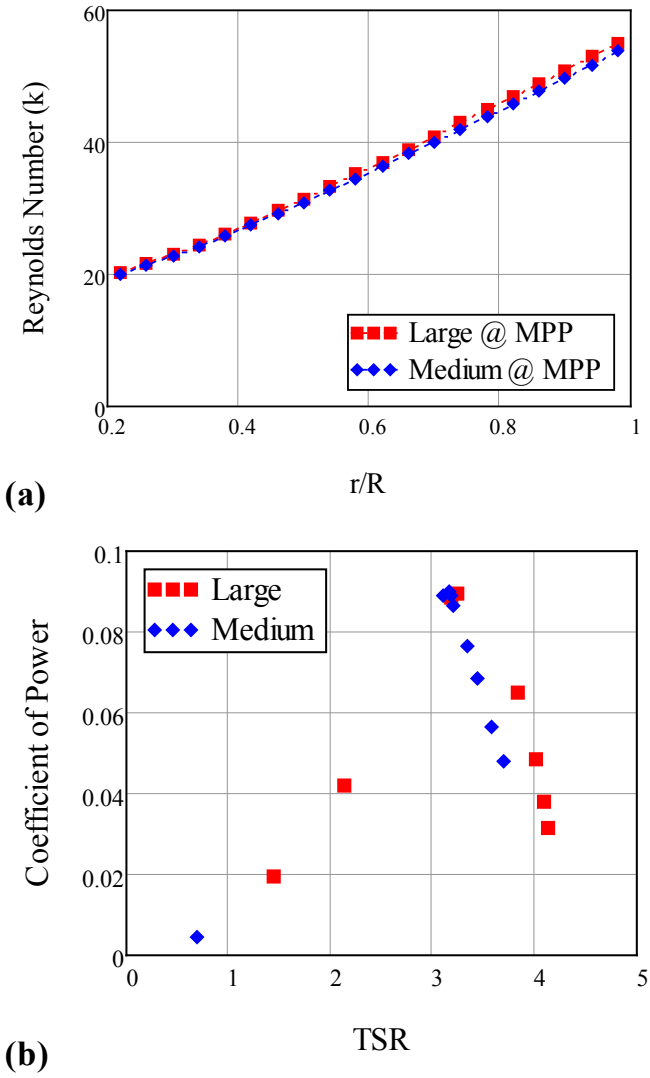

Figure 4.13: (a) Reynolds Number Distribution and (b) Coefficient of Power vs. TSR at $U = 2.5$ m/s

At this point, it is important to know that the surfaces of the turbine blades have minor roughness as a result of the printing process. While the resolution of the Objet30 is very low, at 0.0011 in (27.9 μm), the surfaces still have this minor roughness that could influence experimental results. Assuming the roughness height is on the order of the resolution of the printer, the roughness height can be compared to the height of the trip strip used in the S823 airfoil study shown in Figure 2.12. As the chord of the wind

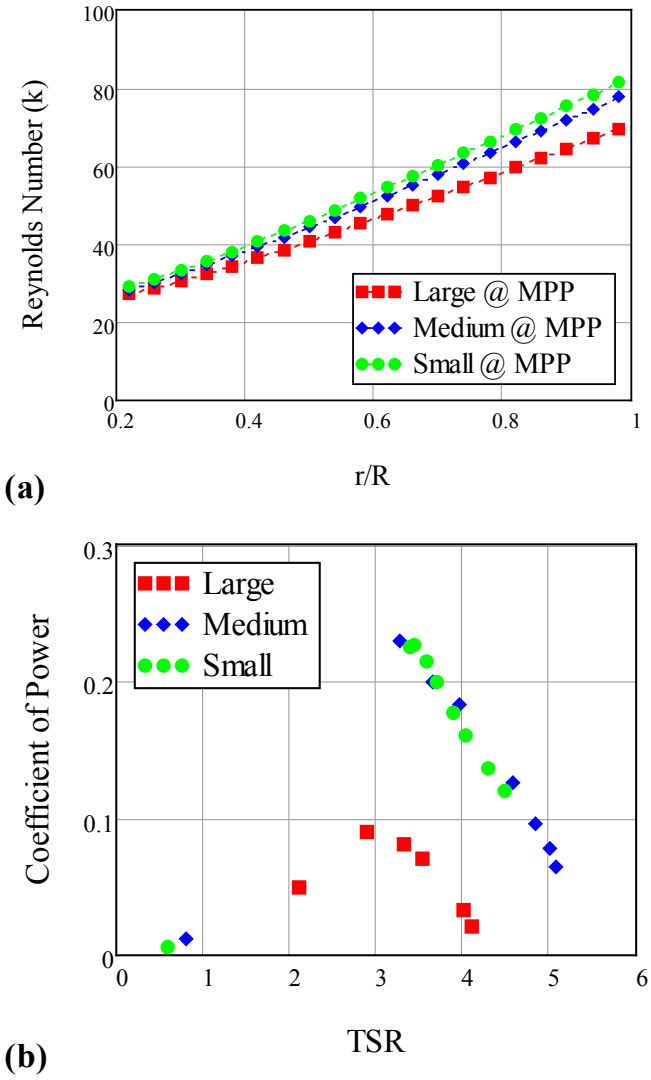

Figure 4.14: (a) Reynolds Number Distribution and (b) Coefficient of Power vs. TSR at U = 3.5 m/s

turbine blade increases, the surface roughness from the Objet30 printer remains constant and, thus, the relative roughness height decreases, as seen in Table 4.3. Studies have shown that surface roughness can reduce flow separation by forcing the boundary layer to transition from laminar to turbulent flow if the roughness protrudes far enough into the boundary layer. Because the Reynolds numbers over the blades has been scaled, the boundary layer size is scaled as well. However, the relative roughness height is not

scaled. Thus, it is possible that the roughness on the large turbine is not protruding far enough into the boundary layer at these wind speeds to induce flow transition from laminar to turbulent for the large scale turbine, but the roughness is protruding far enough into the boundary layer for the medium and small turbines. Because of the sensitivity of transition and separation to surface roughness at Reynolds numbers this low, the surface roughness on the blades is a likely explanation of why the small and medium turbines have nearly identical power curves but the large turbine is significantly lower.

Table 4.3: Relative Roughness Height Comparison

Parameter	Large	Medium	Small	S823 airfoil
Roughness Height (% c)	0.070%	0.087%	0.116%	0.350%
Location on Surface (% c)	even distribution			25%, upper surface

Analyzing two wind speeds that are representative of the higher speeds tested (5.5 and 6.5 m/s), Figure 4.15 and Figure 4.16 show the Reynolds number distributions of the blades for the unloaded and MPP cases as well as the corresponding power curves. The small turbine was not tested under unloaded conditions at a scaled wind speed of 6.5 m/s in order to prevent high rotational velocities that could have caused structural failure of the blades. Thus, there is no Reynolds number data for this case; however, the small turbine was tested under loaded conditions at a wind speed of 6.5 m/s. For all the turbines, the Reynolds number agreement is very good. Additionally, the Reynolds number ranges over the blade are significantly higher, with all the Reynolds numbers being higher than approximately 50,000. At least half of blade is experiencing Reynolds numbers higher than 100,000 for all of the tests, suggesting that the blades are not experiencing Reynolds numbers in which surface roughness would increase performance. Analyzing the power curves for both wind speeds shows very good agreement. At 5.5

m/s, there is only a minor difference in the region of the maximum power point, where the coefficient of power for both the small and medium turbines decreases just prior to full stall. At 6.5 m/s, the same trend occurs. However, for this case the small turbine decreases in performance more than the medium turbine does. Again, this is likely due to the surface roughness, which, for an already turbulent boundary layer, will increase drag and the susceptibility to flow separation. As seen in Figure 2.12, for a Reynolds number greater than 150,000, the trip strip no longer reduces drag but actually increases it by a small amount. This increase in drag becomes greater as Reynolds number increases. Because the non-dimensionalized roughness height is larger for the medium and small turbines, it seems logical that they would experience more drag at higher Reynolds numbers than the large turbine, particularly just prior to stall when the flow becomes even more sensitive to roughness. This also explains the difference between the amount that the small and medium turbine power output decreases just prior to stall.

Figure 4.17 (a) shows the coefficient of power curves for all three turbines. While the small and medium turbine agree over all the wind speeds tested and the large turbine agrees with the other data for a wind speed of 5.5 m/s and greater, below a wind speeds of 5.5 m/s the large turbine differs significantly from the other two turbines. As mentioned previously, the surface roughness from the printing process is causing the flow to stay attached for the small and medium turbines at these low wind speeds, but not for the large turbine. At higher wind speeds, particularly 5.5 m/s and higher, the performance of all the turbines have the same trend, but there is a measureable difference between the power curves. This offset is likely due to an increase in drag for the increased scale of roughness of the turbine blades. Figure 4.17 (b) shows the TSR for the unloaded and MPP cases for different wind speeds. This figure shows the same trends as

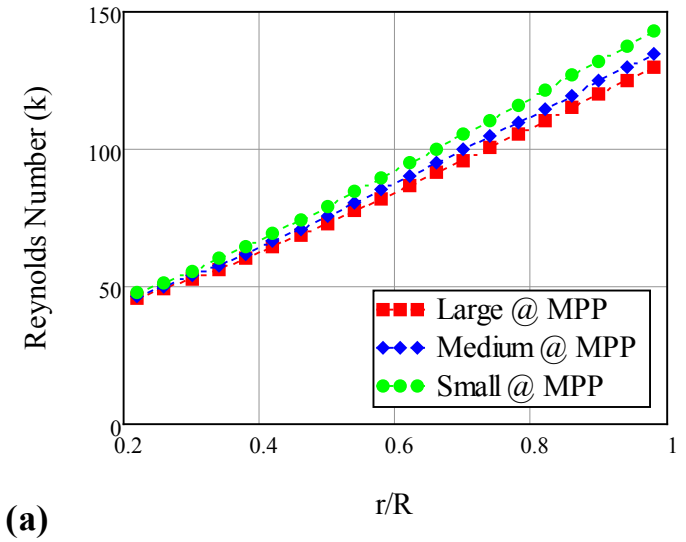

(a)

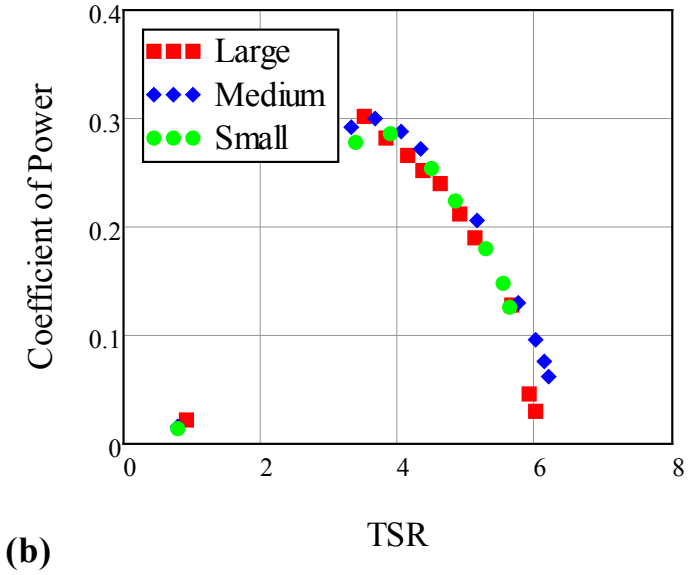

(b)

Figure 4.15: (a) Reynolds Number Distribution and (b) Coefficient of Power vs. TSR at U = 5.5 m/s

the power curve for the unloaded TSRs, seen in Figure 4.17 (a). The MPP TSR curves in Figure 4.17 (b) show that the all three turbines stall at approximately the same TSRs, indicating the success of the scaling procedure.

Figure 4.18 shows the blockage factor for each turbine at the unloaded and MPP conditions. For the small turbine, the blockage factor is relatively constant for both the

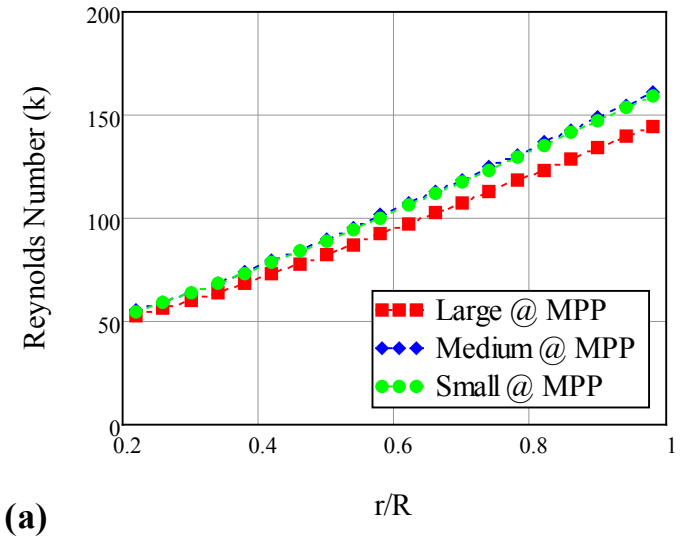

(a)

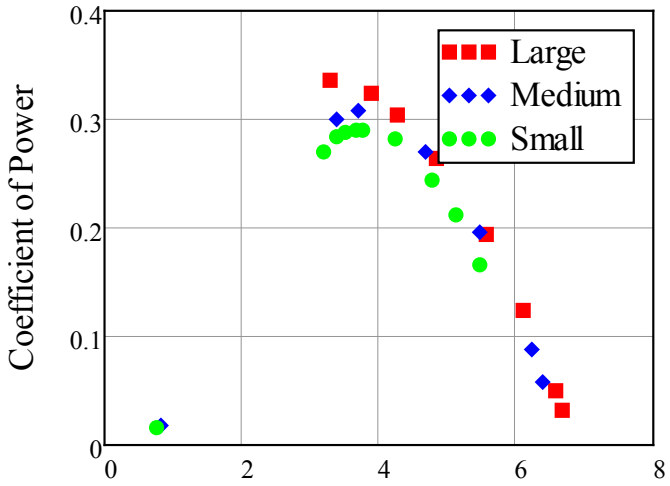

(b)

Figure 4.16: Reynolds Number Distribution and Coefficient of Power vs. TSR at U = 6.5 m/s

unloaded and MPP conditions. The medium turbine blockage factor is also relatively constant but at a lower blockage factor, indicating higher blockage. However, at the lowest wind speed of 2.5 m/s, the blockage factor for both the unloaded and MPP conditions decrease significantly. For the large turbine, however, the blockage factor varies significantly over the wind speeds tested. Additionally, the change in trend of the

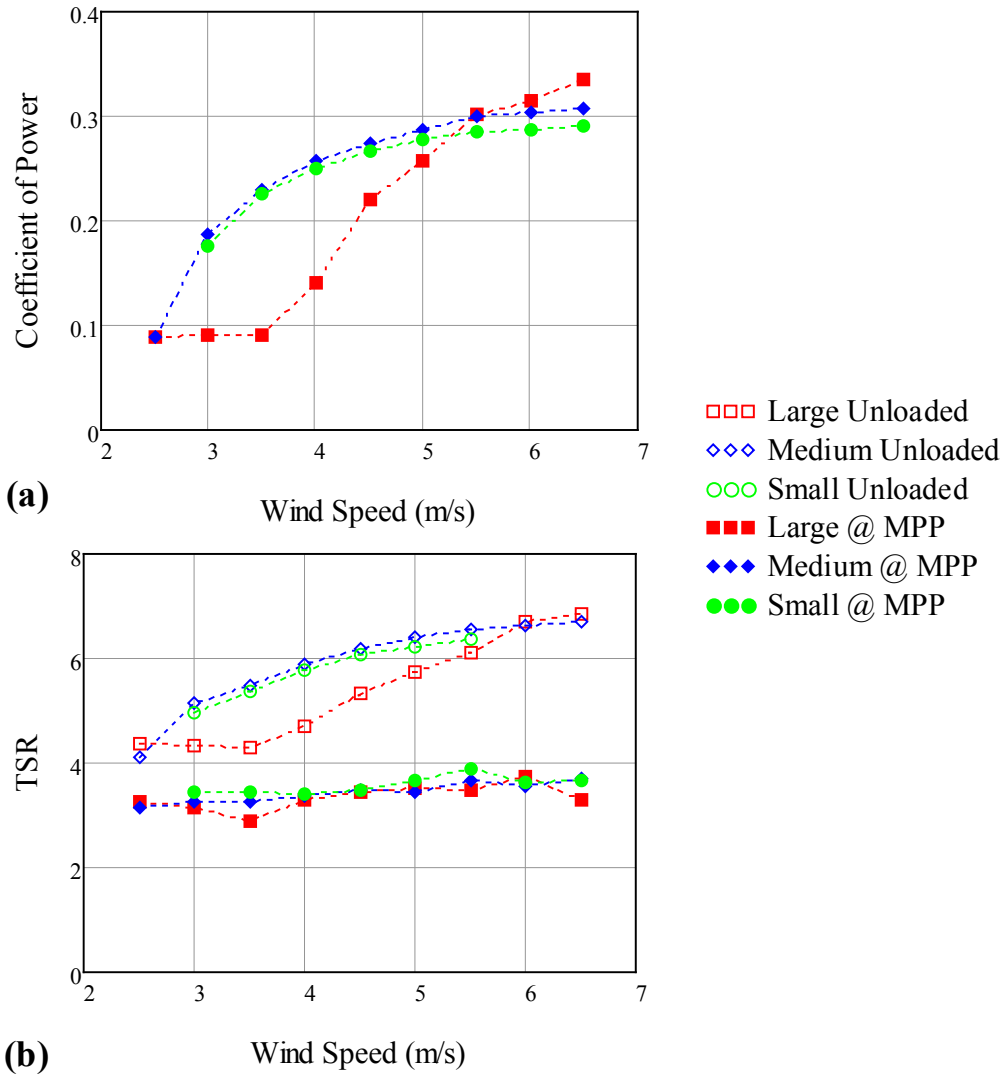

Figure 4.17: (a) Coefficient of Power and (b) TSR vs. Wind Speed

blockage factor curves at 3.5 m/s seems to correlate to the change in trend of the coefficient of power curve. Notably, the blockage factor at the MPP levels out at wind speeds of 4.5 m/s and higher, but the blockage factor for the unloaded condition does not level out until wind speeds of 6 m/s and higher. When both blockage factors for the large turbine have leveled out, the coefficient of power curve for the large turbine also reasonably matches the data from the other two turbines. These correlations between the blockage factor and the large wind turbine performance suggest that blockage as well as

roughness may be causing the discrepancy between power curves of the large turbine with the other two turbines. However, further study is necessary to determine the true cause of the discrepancy, which should include testing completely smooth, scaled wind turbine blades as well as a detailed analysis of the flow in the wake and its effect on the blockage factor.

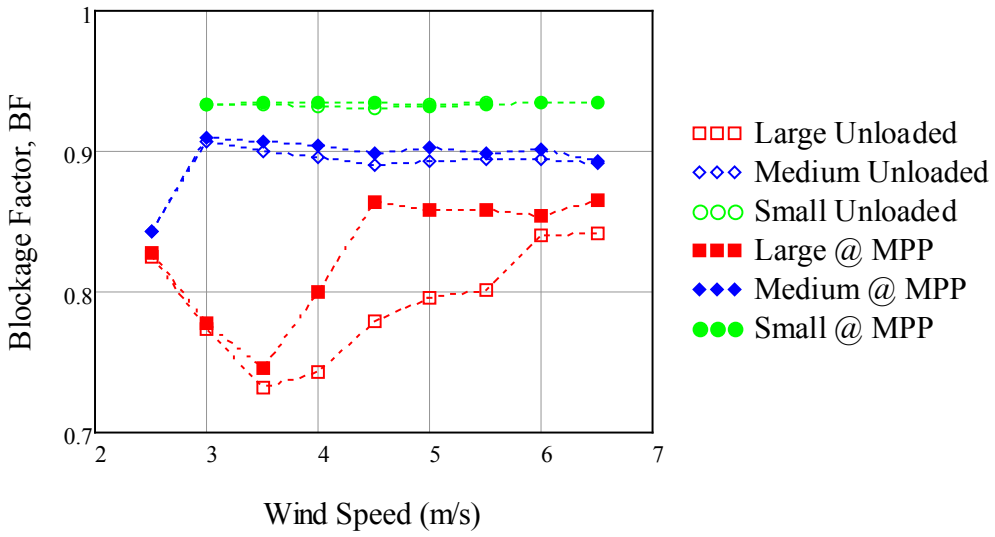

Figure 4.18: Blockage Factor for Unloaded and MPP Conditions

Comparison of Optimal BET and BEMT Designs

Using the BET and BEMT models, the wind turbine blade was divided into 18 elements and a theoretical optimum angle of twist was determined at a TSR of 5 for each element, as detailed previously. The BET design was also evaluated with the BEMT model for comparison. These two rotors have been compared experimentally to quantify the difference in performance and determine which model is better. Finally, the BEMT model was used to optimize both TSR and angle of twist for maximum power output, as mentioned previously. Because a trip strip was seen to improve performance in the

airfoil study, a trip strip was applied to the wind turbine blades when the blade experienced Reynolds numbers near 50,000 and 75,000. The trip strip dimensions were scaled and applied to the wind turbine blade for Reynolds numbers under 85,000, and the location of the trip strip was linearly interpolated for Reynolds numbers above 50,000 between 2% and 25% of the chord from the leading edge. The resulting trip-strip location can be seen in Figure 4.19 based on the BET and BEMT calculation of Reynolds number. Table 4.4 includes the optimal angle of attack for each Reynolds number used for the BET optimal design.

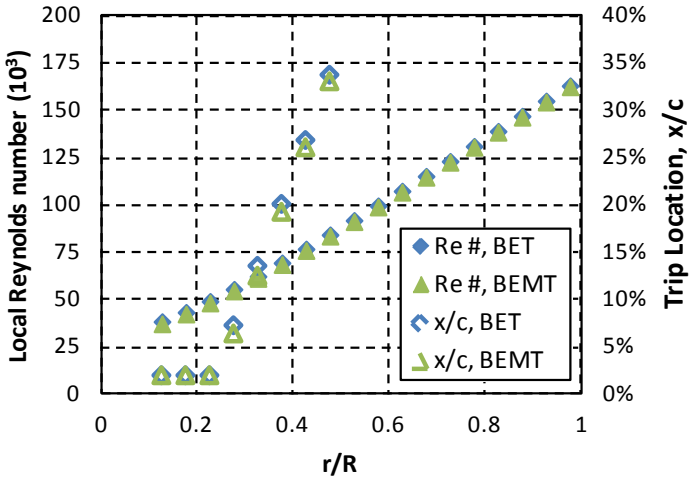

Figure 4.19: Reynolds Number and Trip Strip Location

Table 4.4: Optimal Angles of Attack at each Reynolds Number

Re (10^3)	α (deg)	C_L	C_D	L/D
50	8.89	1.0879	0.0476	22.865
75	9.26	1.0768	0.0369	29.160
100	8.41	1.0465	0.0254	41.163
150	8.05	1.0697	0.0213	50.292
200	7.62	1.0541	0.0192	55.012

Theoretical comparison of optimal BET and BEMT designs. An optimal angle of twist was determined using both BET and BEMT, as seen in Figure 4.20. The resulting

twist distributions are significantly different for the inner half of the blade, over 15 degrees for one of the elements. Figure 4.21 and Figure 4.22 show the elemental flow angle and angle of attack. The first data set in these figures, labeled BET, is the flow conditions over the BET-optimized design predicted by BET. The second data set, labeled BET/BEMT, is the flow conditions over the BET-optimized design predicted by the BEMT model. The third data set, labeled BEMT, is the flow conditions over the BEMT-optimized design predicted by the BEMT model. The flow angles for BET and BET/BEMT differ by as much as 8.53 degrees, pointing to the significant effect including the momentum theory has on the aerodynamic prediction. Additionally, the flow angles for BET/BEMT and BEMT differ by as much as 6.34 degrees, demonstrating the difference that the axial and tangential momentum factors have on the flow angle. Analyzing the angle of attack distributions in Figure 4.22, BET shows the angle of attack at which the lift to drag ratio is maximized. The BEMT optimized design keeps the angle of attack near this optimum from the root of the blade to an r/R value of nearly 0.3. After this radial value, however, the angle of attack cannot be kept near the angle of maximum lift to drag ratio because of momentum and tip-loss effects. The BET/BEMT distribution suggests that the BET-optimized design does not actually keep the angle of attack at the maximum lift to drag ratio, but is at least 4.8 degrees lower. Figure 4.23 plots the local coefficient of power for each element, which has been non-dimensionalized using the total theoretical power available to the entire rotor. The BET power prediction is not included on this plot because it is not realistic, as shown by the total coefficient of power listed in Table 4.5. While the elemental power coefficient of BET/BEMT is shown, the total power coefficient could not be evaluated because the innermost (radial) element did not converge.

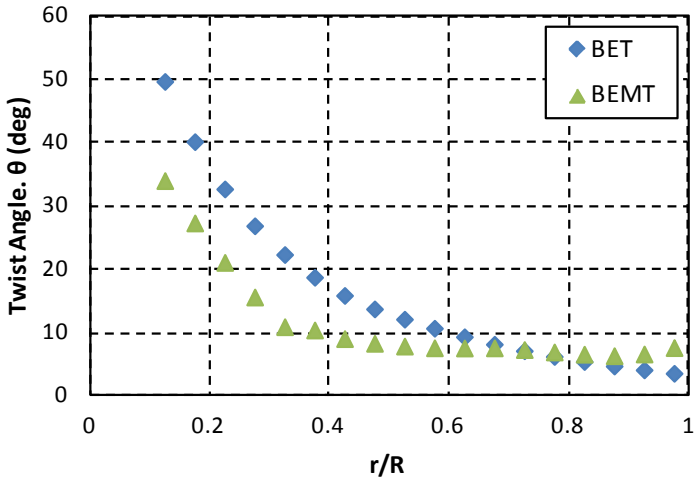

Figure 4.20: Twist Angle for Optimal Design under Design Conditions

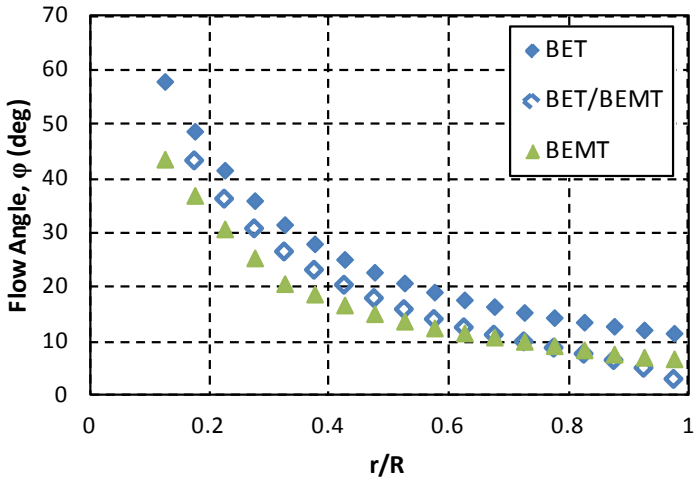

Figure 4.21: Flow Angle for Optimal Design under Design Conditions

Further optimization was performed using BEMT by varying the TSR while still optimizing the angle of twist. The results of this optimization can be seen in Figure 4.24 with the maximum coefficient of power being at a TSR of 3.9. The low optimal TSR may be due to the relatively large chord, and, thus, high solidity of the turbine. The two BEMT designs, optimized for a TSR of 5 and a TSR of 3.9, differ in predicted coefficient of power at the design speed by nearly 0.04 (Table 4.6), an increase of 10%.

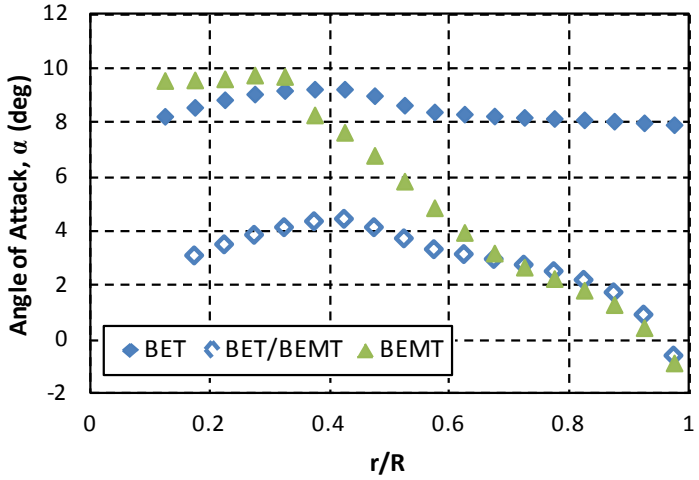

Figure 4.22: Angle of Attack for Optimal Design under Design Conditions

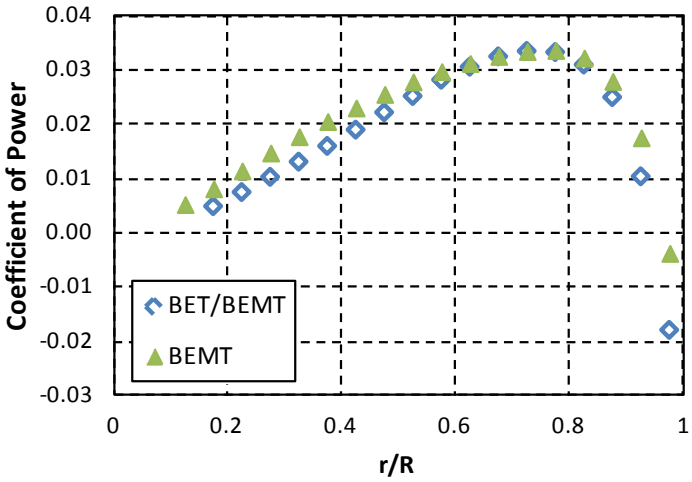

Figure 4.23: Coefficient of Power for Optimal Design under Design Conditions

Table 4.5: Rotor Power Prediction of Optimal Designs

Model	C_P
BET	1.3634
BEMT	0.3901

Additionally, the two designs have significantly different angles of twist, the difference being as much as 10.03 degrees (Figure 4.25). Analyzing the predicted angle

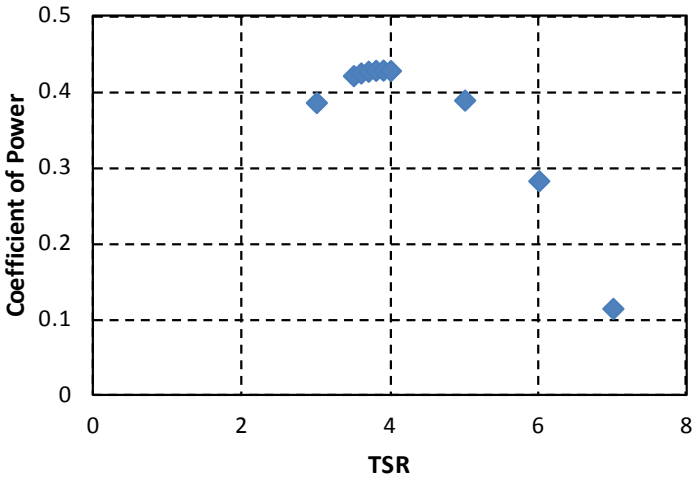

Figure 4.24: Maximum Coefficient of Power for a Given TSR

Table 4.6: Rotor Power of Optimal Designs Predicted with BEMT

Design	C_P
BEMT, TSR = 5	0.3901
BEMT, TSR = 3.9	0.4295

of attack, as seen in Figure 4.26, the rotor optimized for a TSR of 3.9 has an angle of attack that is within one degree of the angle that produces the maximum lift to drag ratio (as listed in Table 4.4) over more of the blade, up to an r/R value of 0.5. Figure 4.27 shows the local coefficients of power for both BEMT designs. For radial locations above r/R equal to 0.5, the angle of attack was moved much closer to the optimum and the coefficient of power is increased, resulting in a 10% increase in total rotor power.

Experimental comparison of optimal BET and BEMT designs. The experimental testing demonstrated a measureable difference in power production between the two rotors. However, due to the electrical current limitations of the generator used in testing, the full power curve could not be developed. Figure 4.28 shows the performance of the two rotors at wind speeds of 1.5, 2.5, and 3.5 m/s, which are representative of the

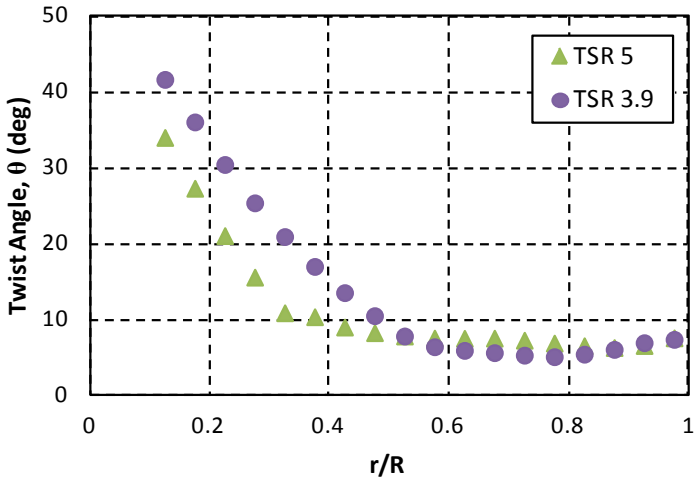

Figure 4.25: Twist Angle for Optimal Design using BEMT

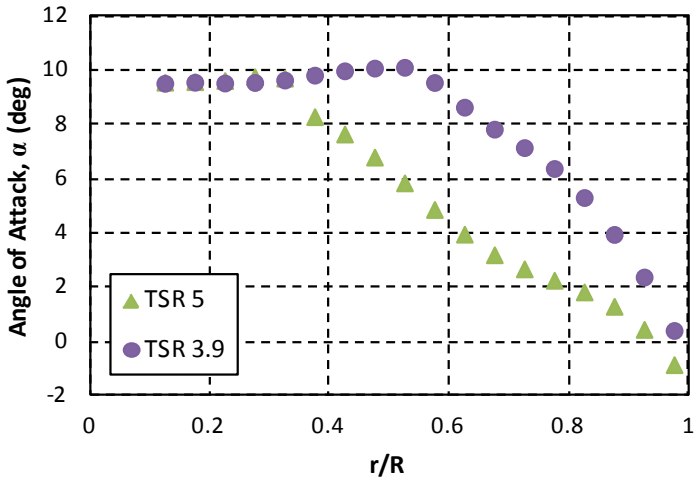

Figure 4.26: Angle of Attack for Optimal Design using BEMT

wind speeds tested. Analyzing the turbine performance at these wind speeds, it is clear that for the wind speeds tested, the BEMT rotor produces less power at its peak (for each individual wind speed) than the BET rotor.

Figure 4.29 represents the portion of the power curves that were tested, plotting the maximum coefficient of power as well as the actual power at each wind speed. For wind speeds of 1.5 to 3.5 m/s, the coefficient of power curve makes it clear that the BET

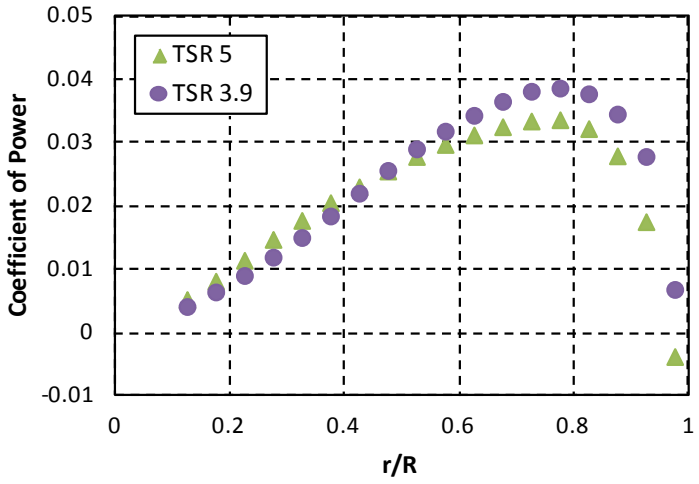

Figure 4.27: Coefficient of Power for Optimal BEMT Designs

rotor performs better than the BEMT rotor. The power curve, however, shows that there is not a significant difference in actual power produce at the wind speeds that were experimentally tested. However, from the coefficient of power experimental data alone it appears that the BET rotor may have reached a maximum while the BEMT rotor performance is still increasing.

For comparison, a BEMT simulation of the BEMT-designed rotor optimized for a TSR of 5 was performed off-design, at wind speeds as low at 3 m/s. The result can be seen in Figure 4.29. Running the BEMT simulation off-design requires having off-design airfoil data. Off-design airfoil data includes having data over a greater range of Reynolds numbers for airfoils with and without a trip strip. Since the off-design airfoil data necessary to generate a full power curve is not available, simulations using the on-design airfoil data were run within 2 m/s of the design wind speed of 5 m/s. However, for winds

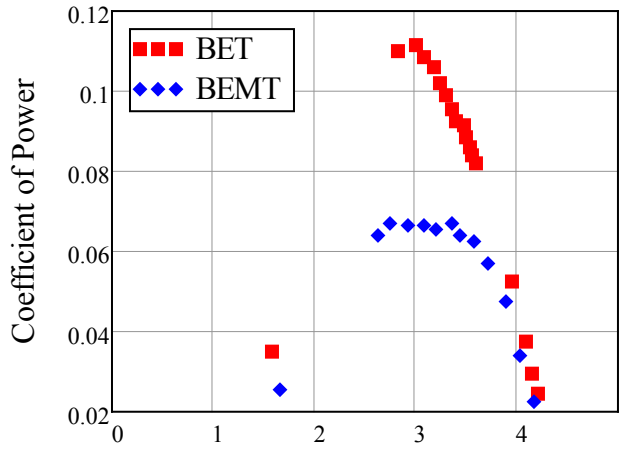

(a) $U = 1.5$ m/s

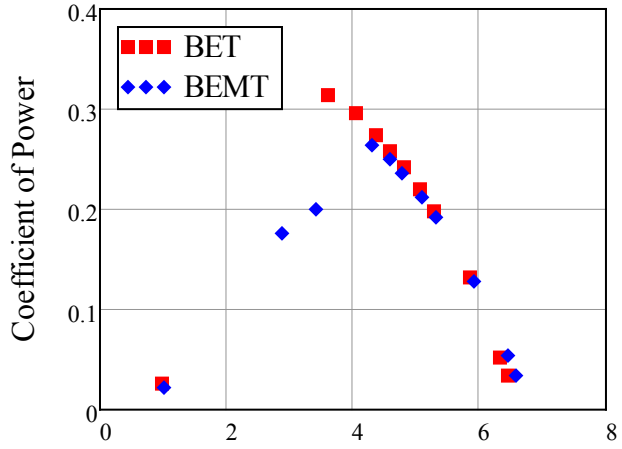

(b) $U = 2.5$ m/s

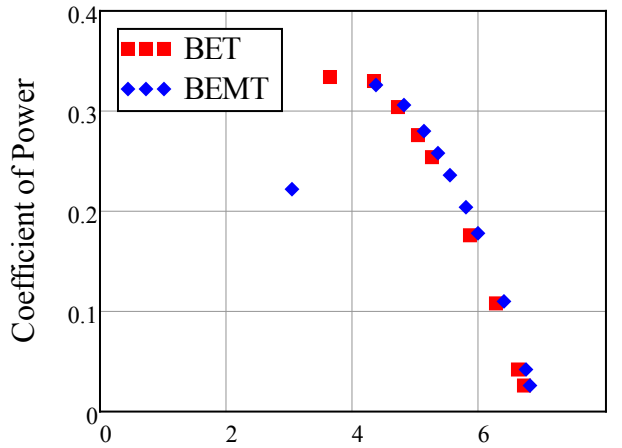

(c) $U = 3.5$ m/s

Figure 4.28: Coefficient of Power vs. TSR for Multiple Wind Speeds

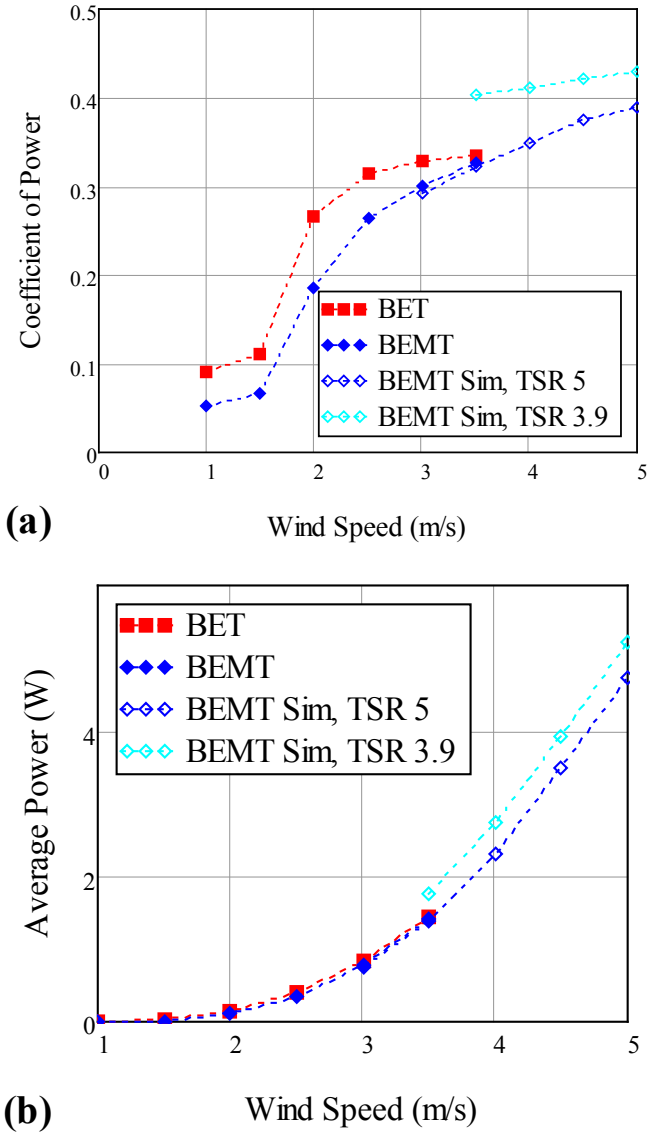

Figure 4.29: (a) Coefficient of Power and (b) Power vs. Wind Speed

speed of 3.0 and 3.5 m/s, the simulation matches the experimental data within 2%. Notably, the simulation predicts that the power curve will continue to increase, surpassing what appears to be the maximum power output from the BET simulation. Finally, data from the simulation of the BEMT design optimized for a TSR of 3.9 is plotted to show the power increase that would be expected after optimizing the TSR using BEMT.

Without a full power curve and an AEP estimate, however, a quantitative conclusion cannot be drawn as to which optimization method is better. Nonetheless, the trends of the experimental data and the theoretical BEMT curve for a TSR of 5 suggest that the BEMT design will produce more power than the BET design at wind speeds above 3.5 m/s, making BEMT the better optimization tool. Additionally, the fact that BEMT is a better theoretical model and can be used to optimize TSR as well as angle of twist makes it a better optimization tool.

Figure 4.30 (a) shows the TSR when the turbine is both unloaded and at the Maximum Power Point (MPP) for a given wind speed. Although it is expected that the MPP would be at or very near the design TSR of 5, at a wind speed of 3.5 m/s the BEMT model is close with a TSR of 4.36 at the MPP. The BET TSR at the MPP is significantly lower than the design, which may be due to the low angles of attack present on the blade at the design TSR as shown by the BEMT evaluation of the BET design in Figure 4.22 (a). Figure 4.30 (b) shows the blockage factor for both the unloaded and MPP conditions over the range of wind speeds tested. Notably, the blockage factor is relatively constant over the range of wind speeds. However, at a wind speed of 1.5 m/s, the blockage factor has decreased compared to both higher wind speed and a wind speed of 1 m/s. This suggests greater separation over the blades, but warrants further investigation.

One topic of interest when designing small-scale, fixed-pitch HAWTs is how the design TSR compares with the experimental TSR. By optimizing the angle of twist for power production at the design TSR and wind speed using either BET or BEMT, the underlying assumption is that at the design TSR and wind speed the wind turbine will produce the most power. At this point, it must be noted that the TSR controls the flow angle, and thus, the angle of attack that each element on the blade sees. Since the angle

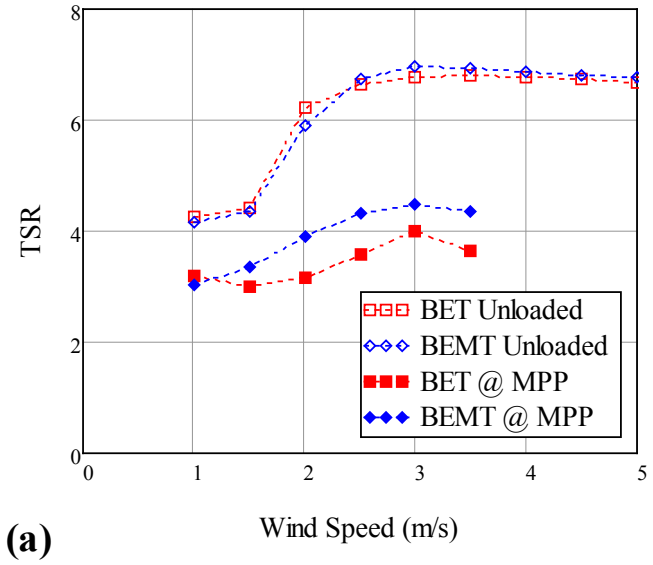

Figure 4.30: TSR (a) and BF (b) vs. Wind Speed

of attack that produces the most power output only varies a couple of degrees with Reynolds number, the TSR should be near the design wind speed at the MPP for most wind speeds. While the design wind speed was not reached in the experimental testing, the TSR at the MPP of both wind turbines seem to have somewhat leveled off between 2.5 and 3.5 m/s. If this assumption is true, the BET-optimized blade set will likely have a TSR at the MPP between 3.5 and 4, and the BEMT-optimized blade set will likely have a

TSR at the MPP between 4.3 and 4.5. Also, if the TSRs at the MPP fall into the previously listed ranges, it would suggest that BEMT more accurately models the aerodynamics as expected. Also, depending on the experimental uncertainty, the TSR at the MPP being lower than the design TSR may suggest three-dimensional effects being present on the blade such as stall-delay. Thus, the discrepancy between the design and experimentally measured TSR warrants further testing to determine the accuracy of the two models.

Comparison of BEMT-Optimized Turbine with Southwest Windpower's Air X Turbine

The BET- and BEMT-optimized blades were designed to have the same diameter as Southwest Windpower's Air X wind turbine and eventually be tested by replacing the blades on an Air X turbine. Thus, for comparison purposes, the performance of the designed wind turbine blades will be compared with published NREL data on the Air X wind turbine, pictured in Figure 4.31.

Figure 4.31: Southwest Windpower's Air X Wind Turbine [140]

However, since the experimental data for the BET- and BEMT-optimized blades does not include wind speeds higher than 3.5 m/s, the performance of the BEMT-optimized blades must be simulated. As noted previously, off-design airfoil data necessary to develop a full power curve is not available. To generate a full power curve, the BEMT-model was used to simulate wind speeds higher than the limit of the experimental data of 3/5 m/s. In terms of simulating the flow over sections of the blade that have the trip strip, the simulation will predict a higher power output than what will actually occur because "off-design" airfoil data is not included in the model. However, Reynolds numbers greater than 200,000 also occur over the blade at wind speeds higher than the design wind speed. Since data at 200,000 is used for Reynolds numbers greater than 200,000, the model will predict a lower power output than what will actually occur. A simple way to show this is by analyzing the L/D curve for multiple Reynolds numbers. An L/D curve with a higher Reynolds number will have a higher magnitude and higher peak value than an L/D curve with a lower Reynolds number. Because of the opposite effect of using the on-design airfoil data, the resulting error of the model should be minimized, and the predicted power curve should be reasonable. However, both further experimental testing and improvements to the model should be a part of future research. Figure 4.32 shows the power predictions for the BEMT-optimized blade up to a wind speed of 15 m/s.

While multiple sets of published data are available for the Air X wind turbine, two have been chosen that are representative. Both experimental field tests quantified the performance of the Air X turbine, rated for 400 W at 12.5 m/s, and compared with the manufacturer's "turbulent" power curve. The first data set, taken with a 12-V, marine version, was published in 2003 by NREL. The results match previously published field-

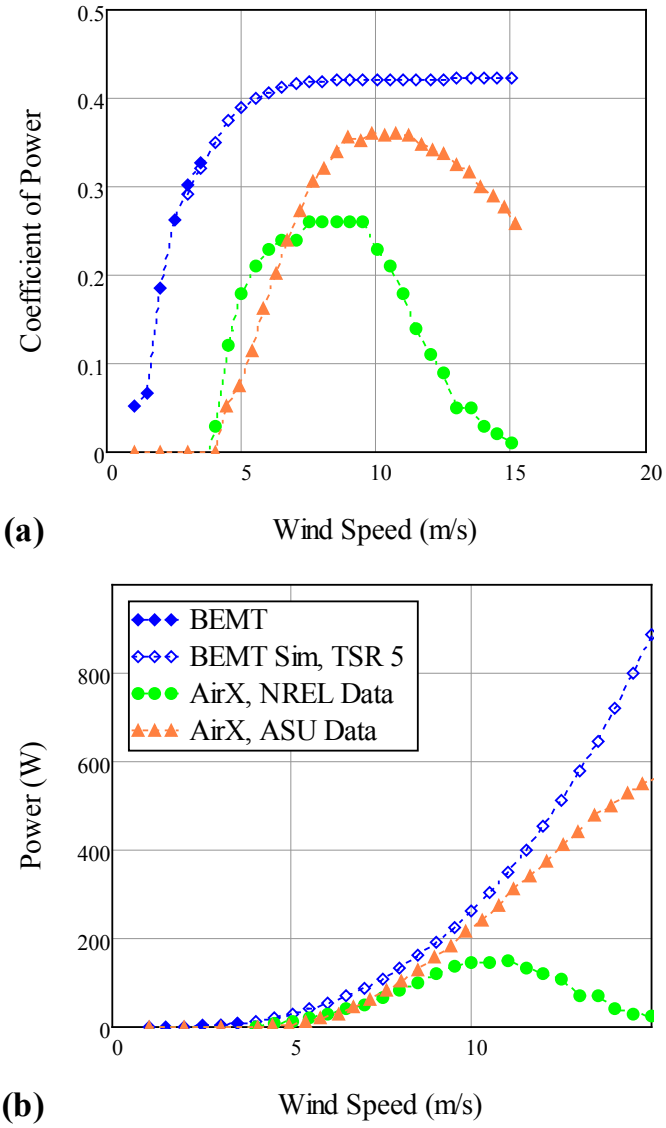

Figure 4.32: Comparison of BEMT-design blades with Air X (a) Coefficient of Power and (b) Power Curves [141, 142]

tested power curves but not the manufacturer's published power curve [141]. The second data set, taken with a 24-V Air X, was published in 2005 by Summerville at Appalachian State University (ASU) and closely matches the manufacturer's published power curve [142]. Both the NREL and ASU power curves can be seen in Figure 4.32. No explanation is given by Summerville for why the ASU power curve differs from the other

published curves [142]. However, the NREL document reports that at the end of the NREL field test, Southwest Windpower implemented a number of software upgrades to the turbine. The NREL report also notes one of the major causes of the discrepancy between the NREL test and the manufacturer's power curves to be due to a control system issue. This is shown in a plot of 10-second averaged data from the NREL test in Figure 4.33, in which the turbine was operating in the stall and automatic shutdown mode when it should have been operating in normal power production. Modifying the control system may have been able to reduce the time spent in the stall or automatic shutdown mode. Being a control issue, it was likely resolved with the software upgrades.

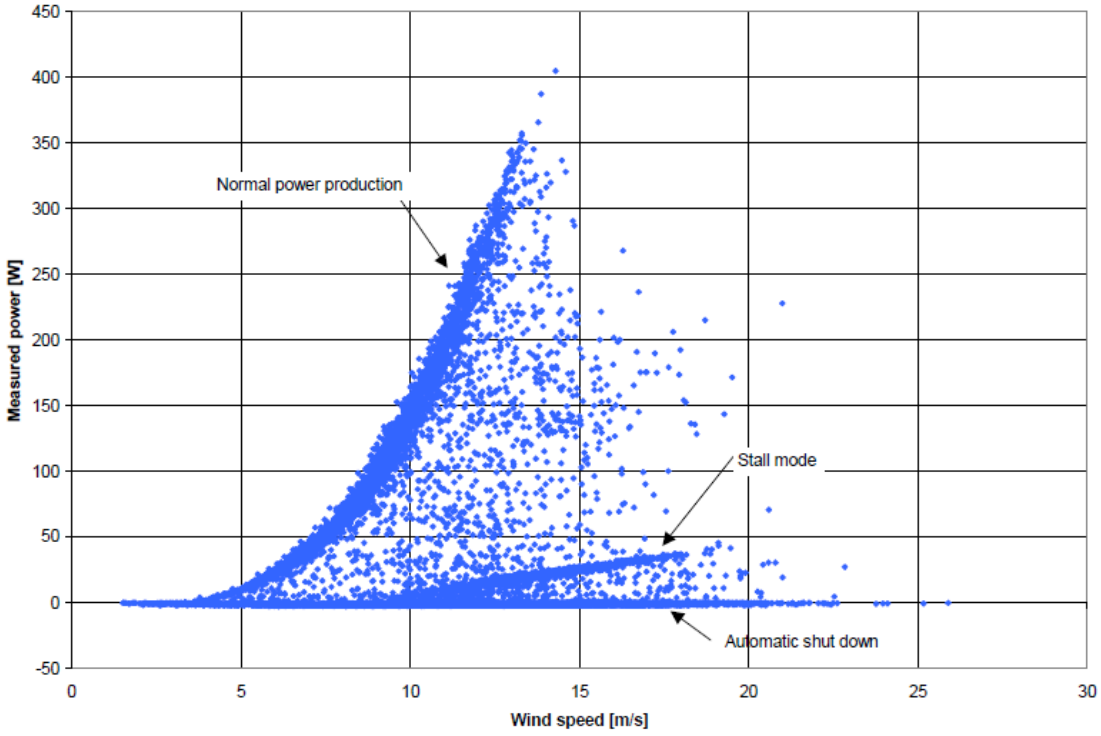

Figure 4.33: Ten-Second Averaged Data from NREL Air X Field Test [141]

Using each of the power curves seen in Figure 4.32 (b) and the data from the wind site survey at Region 12, the AEP can be predicted. Figure 4.34 (a) shows the average

wind turbine power at each wind speed, P_W, using the Weibull fit parameters. The wind distribution at 50 ft (15.24 m) was used because the Air X was installed at 13 m by NREL and 13.7 m by ASU in their respective studies. Figure 4.34 (b) shows the average wind turbine power calculated using the measured wind distribution data. The calculated AEP, the area under the curve, is listed in Table 4.7 for each of the power curves using the AEP from both the Weibull curve fit and using the measured data. The increase in AEP of the BEMT-designed turbine over the Air X AEP based on the two power curves is also listed in the table. The AEP results demonstrate two things. First, that fitting a Weibull curve to the measured wind site survey data produces an AEP calculation within 2.0% of the AEP calculation using the measured wind data. Second, the AEP calculated for the BEMT-optimized blades indicates an improvement of at least 58.8% over the Air X wind turbine, suggesting the importance of designing for the site wind conditions. This theoretical result indicates the need for both wind tunnel and field testing of the designed turbine to validate the results. Additionally, it is expected that further gains in the AEP are possible by optimizing more parameters than simply the twist angle as well as optimizing for the AEP rather than for power production at a particular wind speed.

Design Angle Study

Because of the sensitivity of the L/D value to the angle of attack, a study was undertaken to analyze the effect of using a non-optimum angle of attack in the designing a wind turbine blade. As can be seen in Figure 4.11 (f), a change in angle of attack of just 2 degrees from the angle at which the maximum L/D value occurs can decrease performance by as much as 25%. Changing the design angle of attack by the same

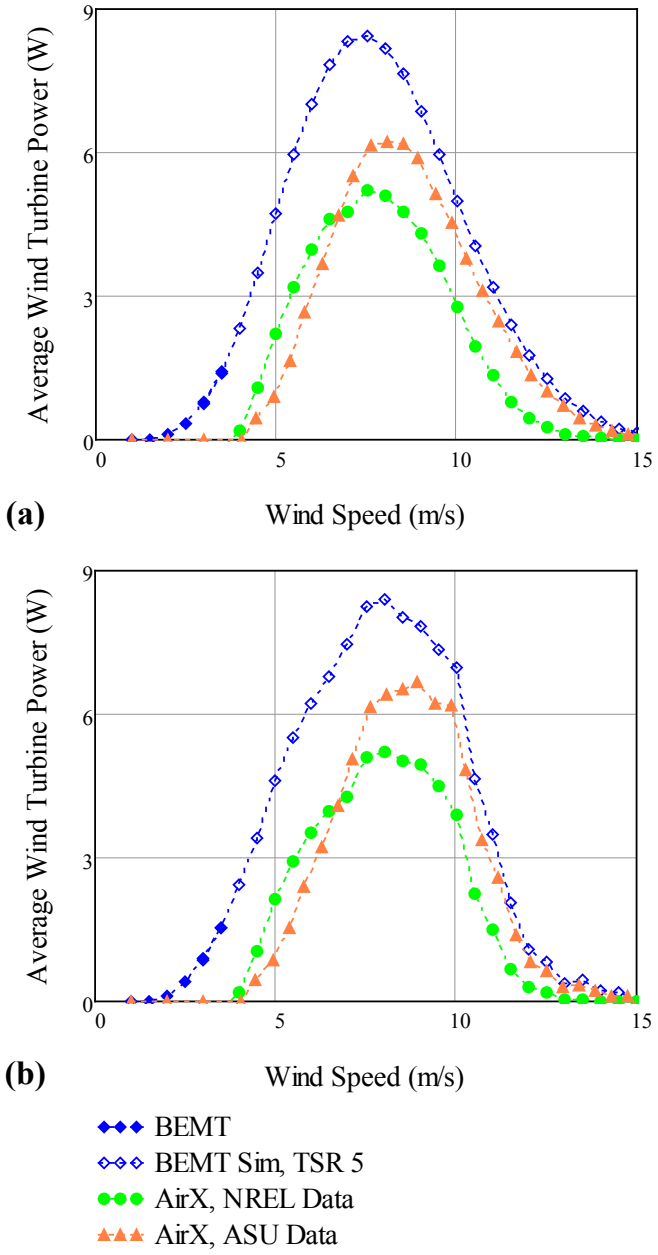

Figure 4.34: Average Wind Turbine Power Curves at 50 ft using (a) Weibull Curve Fit and (b) Measured Wind Data

Table 4.7: Comparison of Predicted AEP (kWh/yr)

Data Set	Weibull Curve Fit	Increase of BEMT-designed	Measured Data	Increase of BEMT-designed
BEMT-designed	435.2	0.0%	436.7	0.0%
NREL Air X	217.8	99.8%	221.6	97.1%
ASU Air X	269.8	61.3%	275.1	58.8%

amount over each element on a blade does not change the blade shape, but effectively rotates the entire blade and changes the pitch angle, as defined in Figure 2.16 (b).

Figure 4.35 shows the Reynolds number distribution over the blades used in this study. Because the Reynolds number is always lower than 75,000, the trip strip was simply applied at 2% from leading edge of the blade along the chord. Additionally, the angle of attack that was used in designing the blade was based off the airfoil data at 50,000, an angle of 8.89 deg. BET theory was used to optimize the blade shape for this study, primarily because accurate airfoil data was not available to input into the BEMT model. For the blades designed using an angle of 8.89 deg as the design angle of attack, the pitch is zero. The results from testing this blade set can be identified as P-00. The results from the blade set with a pitch of +2 deg can be identified at P-02, and the results from the blade set with a pitch of -2 deg can be identified as P-M2.

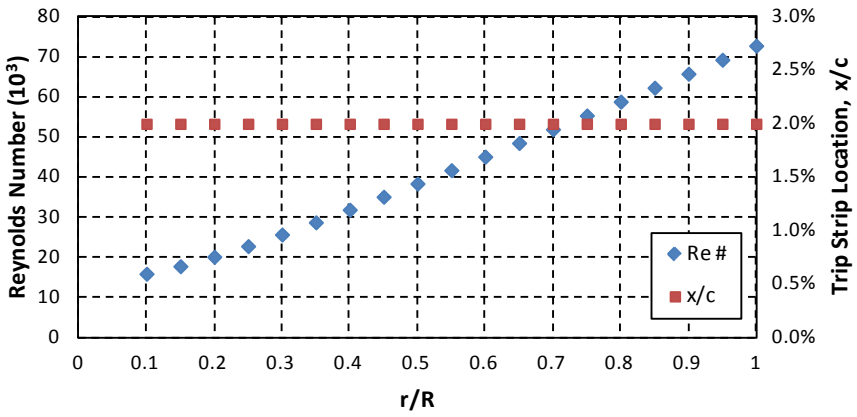

Figure 4.35: Reynolds Number Distribution and Trip Strip Location

Changing the pitch angle of the blades should have multiple effects on wind turbine performance. For a given TSR, decreasing the pitch angle will increase the angle of attack. This has an effect both on the cut-in speed of the wind turbine as well as the stall point of the wind turbine. Increasing the pitch angle will decrease the cut-in speed

because the angle of attack in decreased. Decreasing the pitch angle will have the opposite effect. Since reducing the TSR increases the effective angle of attack of the blades, increasing the pitch angle, which decreases the angle of attack, will cause stall to occur at a lower TSR. However, these general trends are what would occur over a wind turbine blade with fully two-dimensional flow.

As expected, P-00 had a lower cut-in speed than P-M2, of 2 m/s compared with 2.5 m/s, because increasing the pitch angle should decrease the cut-in speed. However, it also has a lower cut-in speed than P-02, which was expected to have a cut-in speed of 2 m/s or lower but had a cut-in speed of 2.5 m/s. While this is counter-intuitive, it may be due to three-dimensional effects. Analyzing the two low wind speeds of 2.5 m/s and 3.5 m/s, seen in Figure 4.36 (a, b), there is a very clear distinction between the blade sets. P-M2 stalls at the higher TSR, and P-00 stalls at the lowest TSR, as expected. There is a similar trend in the maximum coefficient of power, P-M2 producing the highest value and P-02 producing the least. However, at a wind speed of 4.5 m/s (Figure 4.36, c), the trend in coefficient of power is reversed, and all three blade sets stall at approximately the same TSR. This may be due to unique three-dimensional flows occurring over the blade. For wind speeds of 5.5, 7, and 9 m/s (Figure 4.36, d-f), there is no measurable difference between TSRs and coefficients of power at the MPP.

Figure 4.37 (a) shows the coefficient of power curves for each of the blade sets with wind speed. Noticeably, while there is a scatter in the data at low wind speeds, the data converges at wind speeds higher than 4.5 m/s. Analyzing the power curve in Figure 4.37 (b), there is very little measurable difference in the power curves at all. This is because the largest difference in coefficient of power occurs at the lower speeds when the

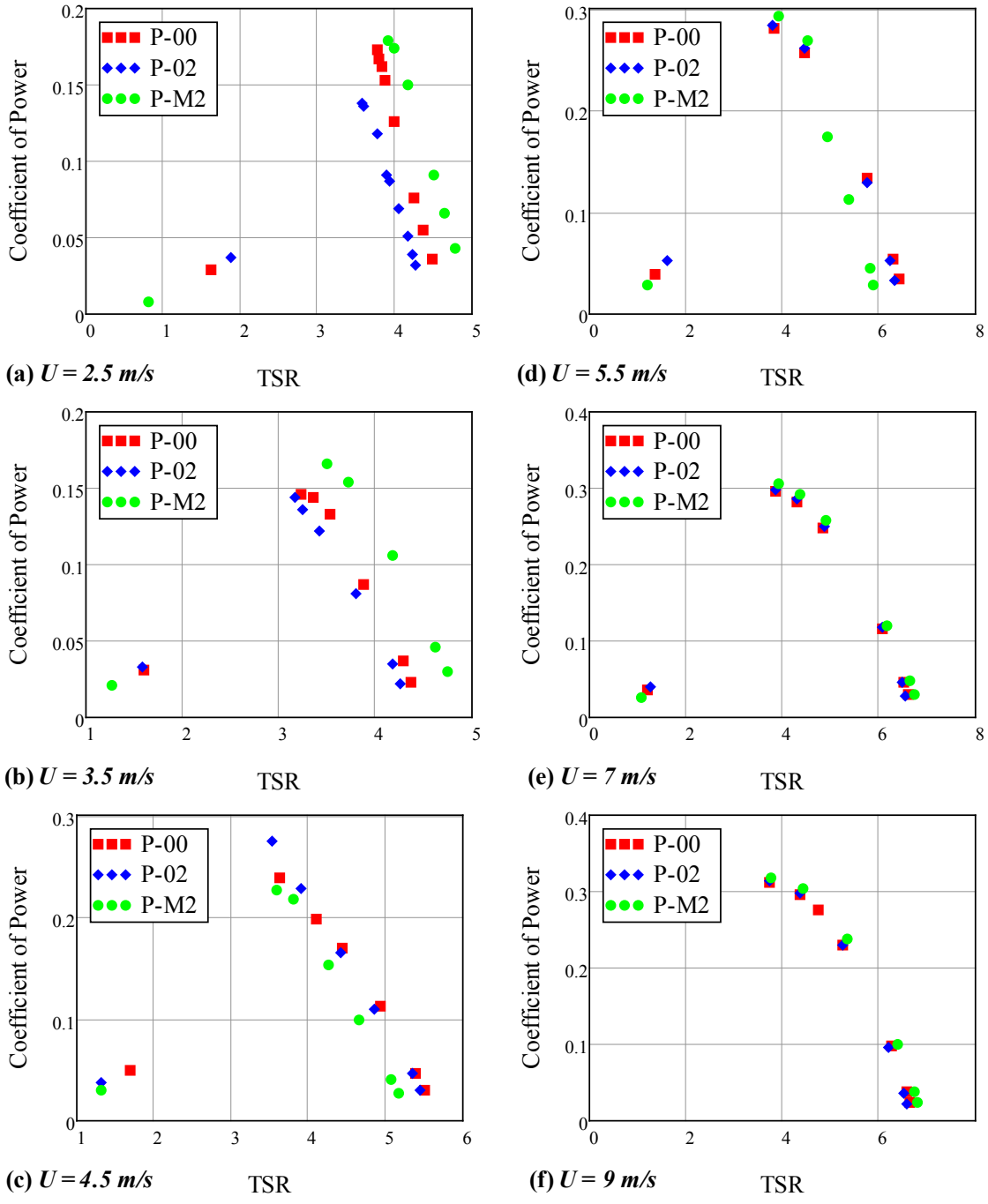

Figure 4.36: Coefficient of Power vs. TSR at Multiple Wind Speeds

actual power produced is very low. Wind speeds higher than 9 m/s were not tested due to the electrical current limitations of the generator used in the test.

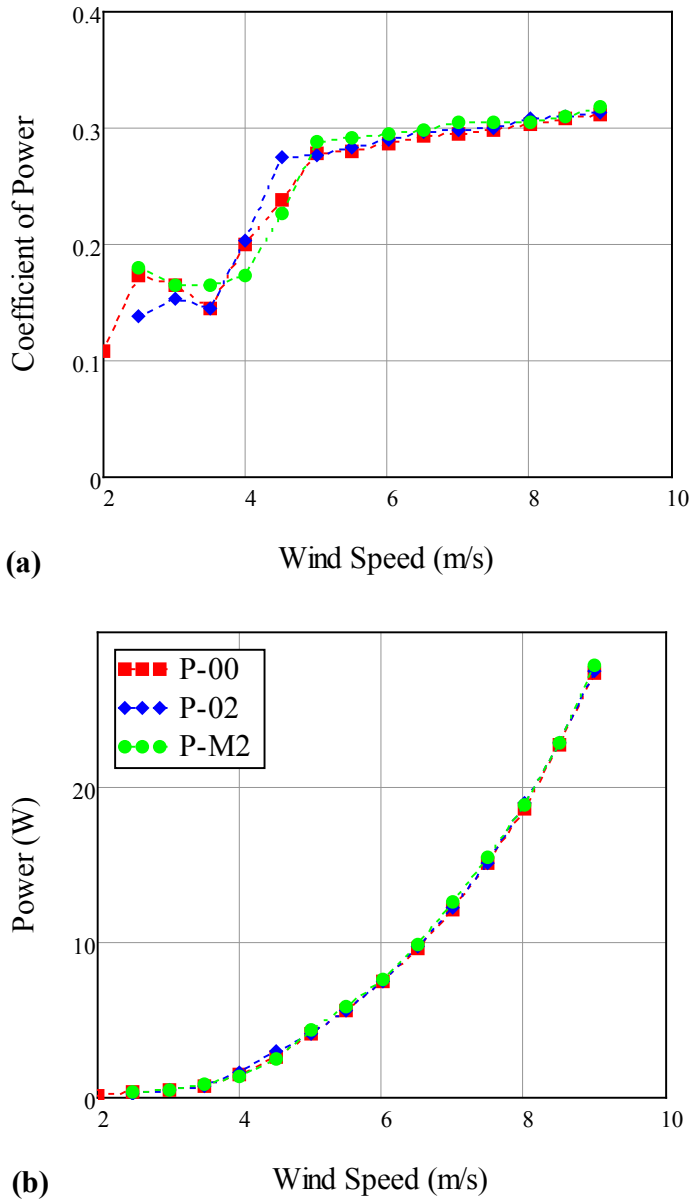

Figure 4.37: Coefficient of Power (a) and Power (b) vs. Wind Speed

The TSR ratios at each wind speed for the loaded and unloaded conditions can be seen in Figure 4.38. For the unloaded TSR curves, there are three distinct regions. At wind speeds between 2 and 4 m/s, the P-M2 blades have the highest TSR and the P-02 have the lowest. At wind speeds between 4 and 7 m/s, this trend is reversed, and the P-M2 blades have the lowest TSR and the P-02 have the highest. This is possibly due to

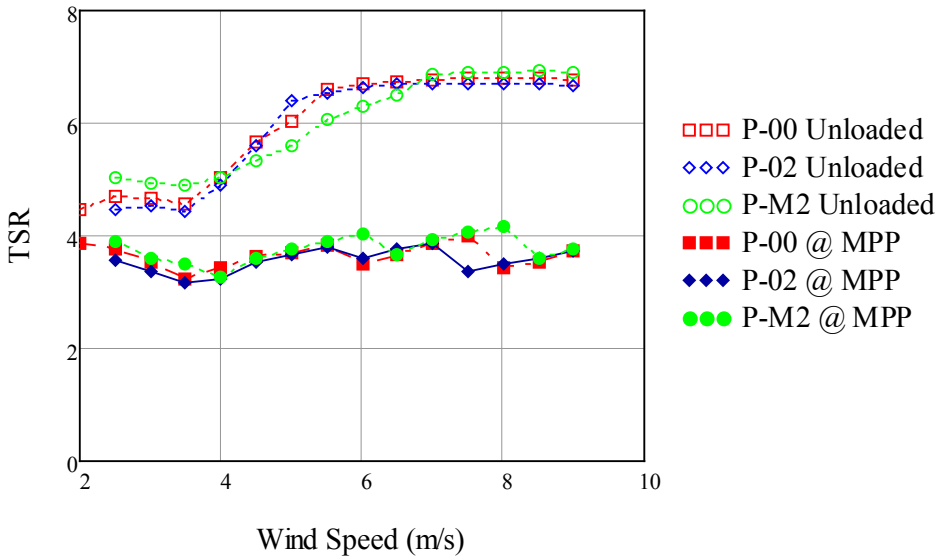

Figure 4.38: TSR vs. Multiple Wind Speed

three-dimensional flow conditions and flow separation occurring over the blades. For wind speeds higher than 7 m/s, the unloaded TSRs are experimentally indistinguishable. However, the TSR curves at the MPP for wind speeds lower than 6 m/s are very similar. For wind speeds of 6 m/s and higher, there are discreet drops in the TSR for each of the turbines, not necessarily occurring at the same wind speed. The second time this happens, the P-02 blade set stalls at 7.5 m/s, the P-00 blade set stalls at 8 m/s, and the P-M2 blade set stalls at 8.5 m/s. At this point it is likely that the true MPP is occurring at a TSR of approximately 3.75, but for each wind speed stall was occurring between either 2 Ω and 1 Ω (for 6 and 6.5 m/s) and 1 Ω and 0 Ω for wind speeds higher than 7 m/s. Because the resolution of the decade box is 1 Ω, the TSR and coefficient of power was not captured as accurately at wind speed above 6 m/s as it was at lower speeds.

Figure 4.39 shows the blockage factor curves during each test for the unloaded (a) and MPP (b) conditions. Notably, there are trends very similar to the blockage factor during the scaling study, seen in Figure 4.18. The decrease in blockage factor as the

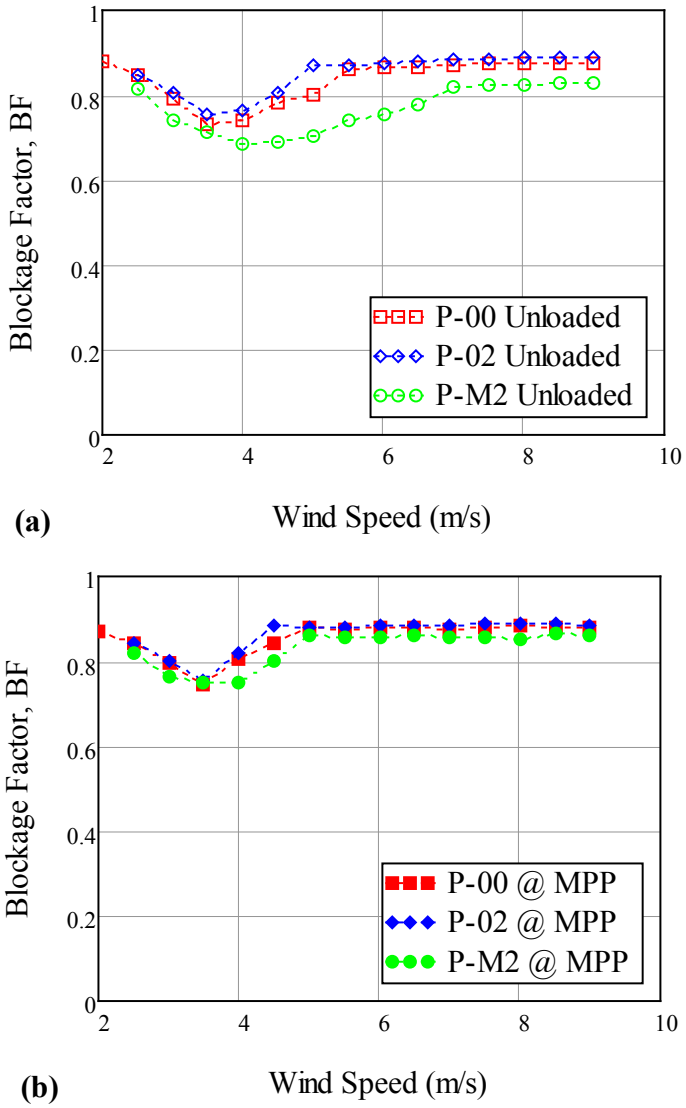

Figure 4.39: BF vs. Wind Speed for the (a) Unloaded and (b) MPP Conditions

wind speed decreases, between 7 and 4 m/s for the unloaded condition and between 5 and 3.5 m/s for the MPP condition, suggests flow separation increasing. However, the blockage factor increases with decreasing wind speed below 3.5 or 4 m/s, depending on the turbine and the loading (unloaded or MPP). The trends in the blockage factor suggest the need for further flow field study to determine its cause.

Figure 4.40 shows the average wind turbine power using both the Weibull curve fit and the measured wind data. From these figures, it is clear that no significant

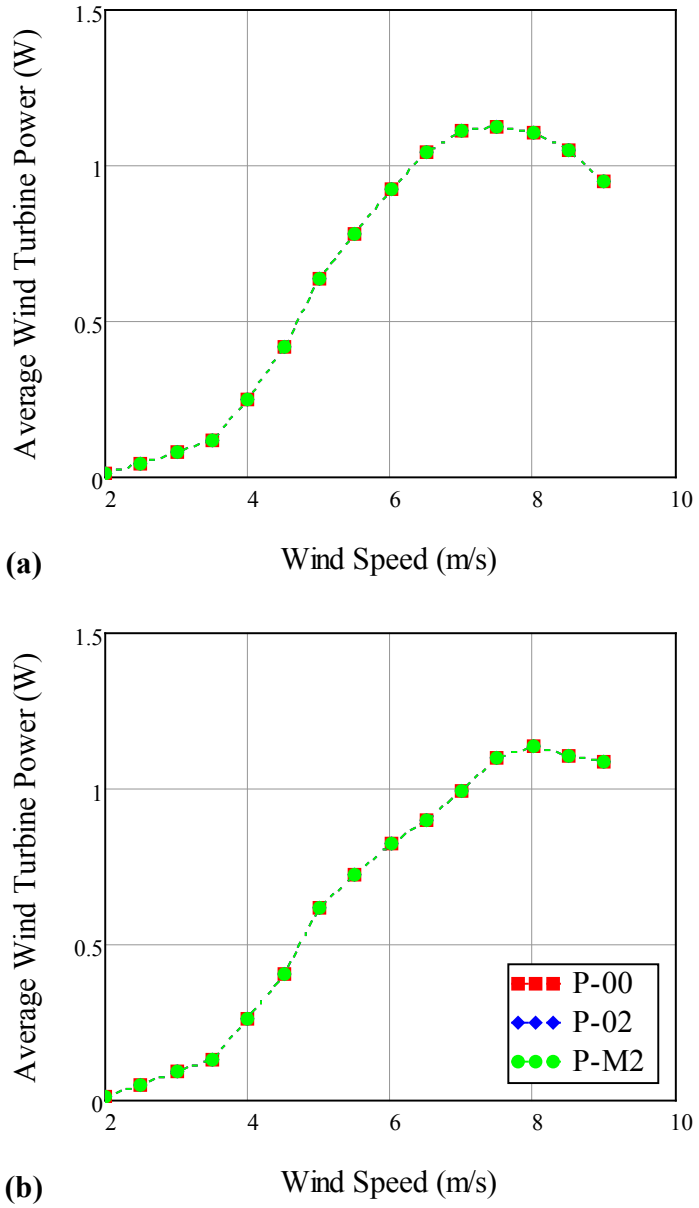

Figure 4.40: Average Wind Turbine Power vs. Wind Speed using Weibull Curve Fit (a) and Measured Wind Data (b)

difference exists between the performances of the three blade sets. This is supported by comparing the calculated AEPs for each blade set, which are listed in Table 4.8. The difference between the results for each blade set is less than 0.3% when considering either the Weibull curve fit or the measured data. For a given blade set, the AEP values

generated using the Weibull fit are within 3% of the AEP calculated using measured data, showing that using a Weibull fit to the measured data is reasonable. Figure 4.40 also shows that to fully complete this test, all three turbines would need to be tested at wind speeds higher than 9 m/s to truly determine whether or not there is no difference in the performance for the three blade sets. However, this was not possible given the current limitation of the generator used in testing.

Table 4.8: Comparison of Predicted AEP (kWh/yr)

Data Set	Weibull Curve Fit	Measured Data
P-02	40.1	38.9
P-00	40.2	40.0
P-M2	40.1	38.9

CHAPTER FIVE

Conclusions

Summary of the Current Work

In this work, multiple aspects of wind turbine design have been addressed in an effort to improve the design process for small-scale HAWT designers, particularly with application to Class 2 wind sites. The first part of this work included an analysis of one full year of data from a wind site survey in Waco, TX. In the analysis, a Weibull fit of the data as well as the measured data were used in predicting AEP. Using the measured data was shown to yield a 53.7% increase in predicted AEP over the AEP predicted using the Weibull fit. This discrepancy is due to the fact that the AEP is very sensitive to differences between the Weibull curve fit and the measured data at higher speeds because the turbine is producing more power.

The second part of this work experimentally studies various aspects of airfoil performance at low Reynolds numbers in order to quantify S823 airfoil performance under conditions that small-scale wind turbines experience and that have not been tested before. The experimental results were compared with the aerodynamic codes PROFIL and XFOIL. Additionally, a trip strip has been applied and shown to improve performance for Reynolds numbers of 50,000 and 75,000, although airfoil performance was not improved for Reynolds numbers of 100,000 and 200,000.

The final part of this work involved three experimental wind turbine tests of wind turbines design using BET and BEMT. The first of these three experimental tests validated a scaling technique involving Reynolds number matching used in later testing.

Additionally, the blockage correction applied has been shown valid for blockage ratios up to 52.8%. However, further study is necessary to ascertain whether the discrepancy at lower wind speeds with a blockage ratio of 52.8% is due to blockage or roughness. The second experimental test applied the scaling relationships and blockage correction to compare the optimal angle of twist arrived at using BET and BEMT for a 1.15-m diameter turbine. While the experimental test was not completed at the design point due to experimental limitations, the trends of the data and the prediction of the BEMT model suggest that the BEMT model produces more power at the design point and would be the better design tool. Additionally, the full power curve of the BEMT-optimized blade was predicted to produce twice the amount of power when compared to the Southwest Windpower's Air X turbine, largely because the BEMT-designed turbine was designed for a lower wind speed. The third and final experimental wind turbine test analyzed the effect of changing the design angle of attack by ±2 deg and this small variation was shown not to produce a significant difference in the AEP between the three turbines tested.

Recommendations for Improving the Current Experiment

A number of recommendations can be made for improving the multiple experiments performed. For the airfoil testing, two options exist for fully automating the system: either modifying the angle of attack adjustment so it can be automated or using a new force balance with that functionality built-in. Additionally, the angle of attack measurement should be automated, which can be done with either an inclinometer or a potentiometer that can interface both with the experimental setup and with data acquisition hardware. For the wind turbine testing, the test stand as well as the speed

control needs to be modified so that a full power curve can be measured. This could simply include a new generator with a higher current rating and a variable resistor with finer resolution than 1 Ω. Another option is eliminating the generator and measure the torque and controlling the wind turbine speed directly.

Design Recommendations

Additionally, multiple design recommendations should be made as a result of this study. In determining the correct airfoil data to use with BET or BEMT, a number of considerations should be kept in mind. First, the data needs to be at the correct Reynolds number, particularly if the Reynolds number is below 700,000. Second, experimental data should be used until a numerical model can be validated for low Reynolds numbers, particularly below 100,000. Finally, some type of flow control, such as applying a trip strip as a passive technique, should be utilized to reduce the effect of a laminar separation bubble or laminar separation at low Reynolds numbers. In scaling a small-scale wind turbine for wind tunnel testing, Reynolds number matching should be applied, and the effects of surface roughness should be kept in mind and scaled when possible. Blockage corrections should be applied for wind tunnel testing if the blockage ratio is greater than 10%. From the comparison of BET- and BEMT-optimized blades, BEMT is the recommended model for optimizing performance. Additionally, designing a wind turbine specifically for the site in which it will be installed can improve performance significantly. This can be done by designing for a particular wind speed or for the AEP of the site. Also, when using BET to design wind turbine blades, being off in the design angle of ±2 deg does not change performance significantly. Finally, in using a wind distribution to predict AEP, the results of the wind site survey should be used rather than

the Weibull curve fit because a minor discrepancy at the higher wind speed can produce significant differences in average wind turbine power and AEP.

Recommendations for Future Study

As a result of the multiple studies aimed at improving wind turbine performance, a number of recommendations can be made for further investigation. First, a more extensive experimental airfoil study can be performed. This should include a larger test matrix for the locations and dimensions of the trip strip to determine optimum placement, which may include placing a trip strip on the lower surface as well as the top. However, if a CFD model can be generated and validated for low Reynolds numbers, a wider range of roughness parameters could be simulated. Nonetheless, validating a CFD model that captures the effects of transition and flow separation is not trivial. Additionally, the steady-state nature of the airfoil wind tunnel testing merits further investigation. In testing Reynolds numbers below 50,000 for the S823 airfoil and at 60,000 and lower, the lift and drag forces were seen to drift more than 200% over a period of 20 minutes. Second, multiple aspects of the wind turbine experimental testing warrant further study. With the modified wind turbine test stand discussed in the recommendations for improving the current experiment, completing the testing of the BET- and BEMT-optimized blades and comparing their AEP is needed to truly evaluate which design is better. A number of improvements can and should be made to the BEMT model. For example, a stall-delay model and off-design functionality (in terms of airfoil data) should be implemented. Also, the model should be fully validated with the Phase VI data. Finally, the optimization method can be improved by using a genetic algorithm, optimizing angle of twist, chord distribution, and TSR, and optimizing the wind turbine

for the AEP rather than simple a design wind speed. To validate the results of the scaling study, an experimental test with lightly sanded blades should be performed. Additionally, some form of flow visualization should be performed to determine the wind turbine wake and wind tunnel wall flow interactions. Additionally, a design angle study should be performed with the current BET design but with a change of ±4 deg and a similar study should be performed with BEMT-optimized blades such as the scaled blades designed for a 1.15-m diameter turbine. Finally, full-scale outdoor testing of the design BEMT rotor should be performed for comparison with the Air X wind turbine. This will require some type of wind turbine controller as well as a method for manufacturing the full-scale wind turbine blades. Additionally, the specifications of the generator used must be determined.

APPENDICES

APPENDIX A

MATLAB® Code used for Aerodynamic Modeling

Multiple MATLAB® scripts were written in order to run both BET and BEMT codes to determine the optimum angle of twist. Both the BET and BEMT codes used the same input file. The BET model, because of simplicity of the theory, was written into a single script file. The BEMT model, however, was spread across multiple script files. The main BEMT algorithm is contained in the bemt_loop function. This function was called by the file bemt.m to simulate the performance of a defined blade design. It was also called by the file bemt_opt.m to determine the twist distribution that produced the most power at the design wind speed. The subprograms are also included, one with conversion factors, conversions.m, and one that was used to determine the bounding Reynolds number that experimental data was available for a given Reynolds number present on a particular blade element. A sample input file as well as the other files used for evaluating performance and optimized angle of twist are included below.

Sample Input File: AirX_Input.m

```
% AirX_Input.m
% This file is the input file used for BET and BEMT simulations.  It
% contains all the input data necessary for a turbine the size of the
% AirX.


%% Load conversion factors and airfoil data

cd ..

conversions

i = 1;
af{i}.renum = 50;
af{i}.data  = load('Airfoil Data\Experimental\S823_50k.txt');
```

```
i = i + 1;
af{i}.renum = 75;
af{i}.data  = load('Airfoil Data\Experimental\S823_75k.txt');
i = i + 1;
af{i}.renum = 100;
af{i}.data  = load('Airfoil Data\Experimental\S823_100k.txt');
i = i + 1;
af{i}.renum = 150;
af{i}.data  = load('Airfoil Data\Experimental\S823_150k.txt');
i = i + 1;
af{i}.renum = 200;
af{i}.data  = load('Airfoil Data\Experimental\S823_200k.txt');

af = [af{:}];

cd AirX


%% Input Parameters

% Simulation paramters
maxiter = 1000;             % Maximum number of iterations
ATol    = 1E-6;             % Tolerance for induction loop

% Air Properties
rho = 1.225;                % air density, kg/m^3
nu  = 1.464E-05;            % kinematic viscosity, m^2/s, at 15 deg C

% General Turbine Parameters
B     = 3;                  % number of blades
R     = 0.575;              % rotor radius, m
rhub  = 0.0575;             % hub radius, m
U     = 15;                  % wind velocity, m/s
TSR   = 5;                  % tip speed ratio at that rpm
omega = TSR*U/R;            % rotational speed, rad/s
rpm   = omega/rpm2rps;      % rotational speed, rpm

% Elemental Turbine Parameters
n    = 18;                  % number of elements
c    = 0.096*ones(1,n+1);   % local chord betwen elements, m
r    = zeros(1,n+1);        % local radius between elements, m
delr = (R-rhub)/n;          % radial length of each element, m
for i = 1:n+1
    % loop for calculating radial divisions of the element
    r(i) = delr*(i-1)+rhub;
end

%%  Corrections

% WT_Perf Corrections
corr.tip_loss  = true;  % use tip loss correction?
corr.hub_loss  = false;  % use hub loss correction?
% not added, "most engineers" use the advaced brake-state model...
corr.adv_brake = false;  % use advanced brake-state model?
% not added... ???
```

```
corr.ind_prop  = false;  % use prop-pc instead of propx induction
algorithm?

% Wind Turbine Technology Corrections
% not added, probably similar to hub loss correction
corr.cascade   = false;  % use cascade correction on airfoil data?

%% Calculate Elemental Turbine Parameters at Center of Elements

% Local Radius
r_old = r;
clear r
for i = 1:n
    r(i) = ( r_old(i+1) - r_old(i) )/2 + r_old(i);
end

% Local Chord
c_old = c;
clear c
c = pchip(r_old,c_old,r);
```

BET Code: bet.m

```
% bet.m
% This code runs the simple BET for analyzing wind turbine performance.

clear all
close all
clc

disp('>> bet')

conversions

%% Input File

cd('ECTC')
ECTC_Input
cd ..

%% Calculate BET Performance

data = load('Airfoil Data\Experimental\S823_BET.txt');

SpdRatio = zeros(1,n);
phi      = zeros(1,n);
VelLoc   = zeros(1,n);
ReLoc    = zeros(1,n);
alpha    = zeros(1,n);
CL       = zeros(1,n);
CD       = zeros(1,n);
twist    = zeros(1,n);
Felem    = zeros(1,n);
```

```
Qelem    = zeros(1,n);
Pelem    = zeros(1,n);

fprintf([' r/R \t  r  \t  Vel \t  Re   \t twist \t  phi \t alpha ',...
         '\t   CL \t   CD \t   CP \n'])
fprintf(['(--) \t (m) \t (m/s) \t(10^-3)\t (deg) \t (deg) \t (deg)
',...
         '\t  (--) \t  (--) \t  (--) \n'])

Pwind = 1/2*rho*pi*R^2*U^3;

for i = 1:n
    SpdRatio(i) = TSR*r(i)/R;              % local speed ratio
    phi(i)      = atan2(1,SpdRatio(i));    % flow angle
    VelLoc(i)   = U*sqrt(1+SpdRatio(i)^2); % local relative velocity
    ReLoc(i)    = VelLoc(i)*c(i)/nu;       % local Re #
    % assign optimum angle of attack, CL, and CD from data
    alpha(i) = pchip(data(:,1),data(:,2),ReLoc(i)/1000)*d2r;
    CL(i)    = pchip(data(:,1),data(:,3),ReLoc(i)/1000);
    CD(i)    = pchip(data(:,1),data(:,4),ReLoc(i)/1000);
    alpha(i) = 8.89*d2r;
    twist(i) = phi(i) - alpha(i);        % calculating the twist angle
    % Force on the element in the direction of rotation
    Felem(i) = 1/2*rho*VelLoc(i)^2*c(i)*delr*...
               (CL(i)*sin(phi(i))-CD(i)*cos(phi(i)));
    % Torque
    Qelem(i) = Felem(i)*r(i);
    % Power for all three blades
    Pelem(i) = B*Qelem(i)*omega;
    CPelem(i) = Pelem(i)/Pwind;
    fprintf(['%5.3f \t %5.3f \t %5.2f \t%6.2f \t %5.2f \t %5.2f ',...
             '\t %5.2f \t %5.3f \t %5.3f \t %7.4f \n'], ...

r(i)/R,r(i),VelLoc(i),ReLoc(i)/1000,twist(i)/d2r,phi(i)/d2r,...
            alpha(i)/d2r,CL(i),CD(i),CPelem(i))
end

P = sum(Pelem);
CP = sum(CPelem);
disp(['Power Output  = ',num2str(P),' W'])
disp(['Power in Wind = ',num2str(Pwind),' W'])
disp(['Power Coeff   = ',num2str(CP)])
```

BEMT Iteration Loop: bemt_loop.m

```
function [CP,alpha,a,ap,CL,CD,F] =
bemt_loop(twist,corr,p1,p2,print_errors)
% this function interates to find the induction factors for a specified
% element. twist is the twist angle of the blade. p1 and p2 are cell
arrays
% of other wind turbine parameters

conversions         % conversion factors
```

```
rho      = p1{1};    % density, kg/m^3
nu       = p1{2};    % kinematic viscosity, kg/(m*s)
R        = p1{3};    % turbine radius, m
rhub     = p1{4};    % hub radius, m
U        = p1{5};    % freestream velocity, m/s
TSR      = p1{6};    % tip speed ratio
omega    = p1{7};    % rotational speed, rad/s
B        = p1{8};    % number of blades
maxiter  = p1{9};    % max number of iterations
ATol     = p1{10};   % tolerance to exit induction loop
af       = p2{1};    % airfoil data
renum    = [af.renum]; % Reynolds numbers of airfoil data
data     = {af.data};  % Cell array of airfoil data
n        = p2{2};    % number of elements
r        = p2{3};    % radius to center of each element, m
SpdRatio = p2{4};    % local speed ratio
c        = p2{5};    % chord, m
solidity = p2{6};    % solidity...

% initial guess values
Urel  = U*sqrt(1+SpdRatio^2);    % Relative velocity
Re    = Urel*c/nu;               % Reynolds number
[h,~] = re_find(renum,Re/1000); % Find airfoil data to use
[~,i] = max(data{h}(:,4));
alpha = data{h}(i,1)*d2r;                    % Angle of attack, radians
phi   = twist + alpha;                       % Local flow angle, radians
% CL    = spline(data{h}(:,1),data{h}(:,2),alpha/d2r);  % CL based on
alpha
% CD    = spline(data{h}(:,1),data{h}(:,3),alpha/d2r);  % CD based on
alpha
% a     = 1./( 1+4*sin(phi).^2./( solidity.*(CL.*cos(phi)+CD.*sin(phi))
) );
%                                              % axial induction factor
%ap    = (1-3*a)./(4*a-1);                    % tangential induction
factor
a = 1/3;
ap = 0;

% Induction loop
i = 0;
while(1)
    i = i + 1;

    % tip and hub loss corrections
    if corr.tip_loss == true
        F_Tip = 2/pi * acos( exp( -( B/2*(1-r/R)/(r/R*sin(phi)) ) ) );
% tip loss factor
    else
        F_Tip = 1;
    end
    if corr.hub_loss == true
        F_Hub = 2/pi * acos( exp( -( B/2*(r/R-rhub/R)/(rhub/R*sin(phi))
) ) );  % hub loss factor
    else
        F_Hub = 1;
    end
    F = F_Tip*F_Hub;
```

```
    Urel  = sqrt(((1-a)*U)^2+(omega*r*(1+ap))^2);   % Relative velocity
    Re    = Urel*c/nu;              % Reynolds number
    [h,l] = re_find(renum,Re/1000); % Find airfoil data to use
    hmin  = min(data{h}(:,1))*d2r;
    lmin  = min(data{l}(:,1))*d2r;
    hmax  = max(data{h}(:,1))*d2r;
    lmax  = max(data{l}(:,1))*d2r;

    % check if F has an imaginary part or if alpha is outside limits of
    % given airfoil data or if number of iterations is greater than
1000
    % and return NaN if so
    if alpha < hmin || alpha < lmin
        if print_errors == true
            disp(['for the next element, the current angle of attack
(',...
                num2str(alpha/d2r),') is outside the domain of your
data.'])
            disp(['iteration number ',num2str(i)])
        end
        CP    = NaN;
        alpha = NaN;
        CL    = NaN;
        CD    = NaN;
        return
    elseif alpha > hmax || alpha > lmax
        if print_errors == true
            disp(['for the next element, the current angle of attack
(',...
                num2str(alpha/d2r),') is outside the domain of your
data.'])
        end
        CP    = NaN;
        alpha = NaN;
        CL    = NaN;
        CD    = NaN;
        return
    end

    if imag(F) ~= 0 || isnan(alpha) == 1
        if print_errors == true
            disp('Iterating pushed the data to unreal values')
        end
        CP    = NaN;
        alpha = NaN;
        CL    = NaN;
        CD    = NaN;
        return
    end

    if i >= maxiter
        if print_errors == true
            disp(['Reached maximum number of iterations (',...
                  num2str(maxiter),') without reaching convergence'])
        end
        CP    = NaN;
```

```
        alpha = NaN;
        CL    = NaN;
        CD    = NaN;
        return
    end

    % Determining lift and drag coefficient (CL and CD)
    if h == l
        CL = spline(data{h}(:,1),data{h}(:,2),alpha/d2r);
        CD = spline(data{h}(:,1),data{h}(:,3),alpha/d2r);
    else
        CLh = spline(data{h}(:,1),data{h}(:,2),alpha/d2r);
        CLl = spline(data{l}(:,1),data{l}(:,2),alpha/d2r);
        CDh = spline(data{h}(:,1),data{h}(:,3),alpha/d2r);
        CDl = spline(data{l}(:,1),data{l}(:,3),alpha/d2r);
        CL  = interp1([renum(l),renum(h)],[CLl,CLh],Re/1000);
        CD  = interp1([renum(l),renum(h)],[CDl,CDh],Re/1000);
    end

    % coefficient of torque calculation
    CT = solidity*(1-a)^2*...
            (CL*cos(phi)+CD*sin(phi))/...
            sin(phi)^2;
    % new axial induction factor calculation
    if CT < 0.96
        anew = 1/( 1+...
                  4*F*sin(phi)^2/...
                  ( solidity*CL*cos(phi) ) );
    else
        anew = 1/F * ( 0.143 + ...
                  sqrt(0.0203 - 0.6427 * ( 0.889 - CT ) ) );
    end
    % new tangential induction factor calculation
    apnew = 1/( 4*F*cos(phi) / ( solidity*CL ) - 1 );
    % calculation of error
    err = abs( (anew-a)/anew );
    if err < ATol
        break
    else
        a = anew;
        ap = apnew;
        phi = atan2((1-a),(1+ap)*SpdRatio);
        alpha = phi - twist;
    end
end

% if  a >= 0.55
%     disp(['a (',num2str(a),') is greater than 0.55'])
%     CP = NaN;
%     return
% end

% Coefficient of power calculation from textbook
CP = 8/(TSR*n)*F .* sin(phi).^2 .* ...
                        (cos(phi)-SpdRatio.*sin(phi)) .* ...
                        (sin(phi)+SpdRatio.*cos(phi)) .* ...
                        (1-CD./CL.*cot(phi)) .* SpdRatio.^2;
```

```
end
```

BEMT Code: bemt.m

```
% bemt.m
% Generalized Rotor Design Algorithm, from Wind Energy Explained
Textbook

clear all
close all
clc

disp('>> bemt')

%% Input File and Data

cd('AirX')
AirX_Input
load('Twist_Tip_TSR5')
cd ..


%% Evaluate Performance

SpdRatio = omega*r/U;   % local speed ratio
solidity = B*c./(2*pi*r);   % Local solidity

p1 = {rho,nu,R,rhub,U,TSR,omega,B,maxiter,ATol};
disp(' ')
fprintf([' r/R \t  r  \t  Vel \t  Re   \t   F  \t AxInd \t TanInd'...
         '\t twist \t  phi \t alpha \t   CL \t   CD \t   CP \n'])
fprintf(['(--) \t (m) \t (m/s) \t(10^-3)\t  (--) \t (--) \t (--) '...
         '\t (deg) \t (deg) \t (deg) \t  (--) \t  (--) \t  (--) \n'])

CP    = zeros(1,n);
alpha = zeros(1,n);
a     = zeros(1,n);
ap    = zeros(1,n);
Uax   = zeros(1,n);
Urot  = zeros(1,n);
Urel  = zeros(1,n);
Re    = zeros(1,n);
phi   = zeros(1,n);

for i = 1:n
    p2 = {af,n,r(i),SpdRatio(i),c(i),solidity(i)};
    [CP(i),alpha(i),a(i),ap(i),CL,CD,F] =
bemt_loop(twist(i),corr,p1,p2,true);
    Uax(i)  = U*(1-a(i));              % Axial velocity, m/s
    Urot(i) = omega*r(i)*(1+ap(i));      % Rotational Velocity, m/s
    Urel(i) = sqrt(Uax(i)^2+Urot(i)^2);  % Relative Velocity, m/s
    Re(i)   = Urel(i)*c(i)/nu;           % Reynolds number
```

```
    phi(i)   = atan2(Uax(i),Urot(i));
    fprintf(['%5.3f \t %5.3f \t %5.2f \t%6.2f \t% 5.3f \t% 5.3f \t%
5.3f ',...
             '\t %5.2f \t %5.2f \t %5.2f \t %5.3f \t %5.3f \t %7.4f
\n'],...
            r(i)/R,r(i),Urel(i),Re(i)/1000,F,a(i),ap(i),...
            twist(i)/d2r,phi(i)/d2r,alpha(i)/d2r,CL,CD,CP(i))
end

disp(' ')
disp(['CP = ',num2str(sum(CP))])
disp(' ')
```

BEMT Optimization Algorithm: bemt_opt.m

```
% bemt.m
% Generalized Rotor Design, from Wind Energy Explained

clear all
close all
clc

disp('>> bemt_opt')

ttotal_start = tic;

%% Input File

cd AirX
AirX_Input_mod
cd ..


%% Optimize Performance (Find Optimum Angle)

SpdRatio = omega*r/U;   % local speed ratio
solidity = B*c./(2*pi*r);   % Local solidity

p1 = {rho,nu,R,rhub,U,TSR,omega,B,maxiter,ATol};

alpha = zeros(1,n);
CP    = zeros(1,n);
Urel  = zeros(1,n);
Re    = zeros(1,n);

% initialize...
tmin  = 0;
tmax  = 50;
step  = [1,0.1,0.01];
range = [50,10,1];
twist = (tmax - tmin)/2*ones(1,n)*d2r;

for j = 1:length(step)
```

```
    t_iter_start = tic;

    disp(' ')
    disp(['step = ',num2str(step(j))])
    disp(['range = ',num2str(range(j))])
    fprintf(' i \t  a  \t  ap \t twist \t alpha \t   Re \t   CP \t
elasp time \n')

    for i = 1:n
        tmin = twist(i)/d2r - range(j)/2;
        tmax = twist(i)/d2r + range(j)/2;
        t_elem_start = tic;
        p2 = {af,n,r(i),SpdRatio(i),c(i),solidity(i)};
        CP(i) = -1;
        for p = tmin:step(j):tmax
            twist(i) = p*d2r;
            %disp(twist(i)/d2r)
            [cp,aa,a(i),ap(i),~] =
bemt_loop(twist(i),corr,p1,p2,false);
            %disp([p,cp,aa])
            if cp >= CP(i)
                CP(i) = cp;
                opt_p = twist(i);
                alpha(i) = aa;
                Urel(i)  = sqrt((1-
a(i))*U)^2+(omega*r(i)*(1+ap(i)))^2);   % Relative velocity
                Re(i)    = Urel(i)*c(i)/nu;              % Reynolds
number
            end
        end
        twist(i) = opt_p;
        t_elem_elasp = toc(t_elem_start);
        fprintf('%2i \t %5.2f \t %5.2f \t %5.2f \t %5.2f \t %5.1f \t
%7.4f \t %5.3f \n', ...

i,a(i),ap(i),twist(i)/d2r,alpha(i)/d2r,Re(i)/1000,CP(i),t_elem_elasp)
    end

    disp(' ')
    disp(['CP = ',num2str(sum(CP))])
    disp(' ')

    t_iter_elasp = toc(t_iter_start);
    disp(['Elasped time is ',num2str(t_iter_elasp/60),' minutes'])

end

ttotal_elasp = toc(ttotal_start);
disp(['Elapsed time is ',num2str(ttotal_elasp/60),' minutes.'])

% save('AirX\AirX_Twist','twist')
```

conversions.m

```
% conversions.m

rpm2rps = 2*pi/60;  % RPM to rad/s
mph2mps = 0.44704;  % mph to m/s
d2r = pi/180;       % degrees to radians
```

re_find.m

```
function [l,h] = re_find(red,re)
% this function finds the reynolds numbers in red that it lies between
% the reynolds number in the cell array red must be in order from
greatest
% to least

[remax,h] = max(red);    % re max from data and index
[remin,l] = min(red);    % re min from data and index
n         = length(red); % number of reynolds numbers in data

if re > remax
    l = h;
    return
%     error(['Reynolds number of ',num2str(re),' is greater than ',...
%            'maximum Reynolds number of airfoil data'])
elseif re < remin
    h = l;
    return
%     error(['Reynolds number of ',num2str(re),' is lower than ',...
%            'minimum Reynolds number of aifoil data'])
end

for i = 1:n
    if re == red(i)
        h = i;
        l = i;
        break
    elseif re < red(i) && red(i) <= red(h)
        h = i;
    elseif re > red(i) && red(i) >= red(l)
        l = i;
    end
end

end
```

APPENDIX B

MATLAB® Code for Importing and Analyzing Wind Site Survey Data

Two scripts were written to analyze the raw wind data. The first script file, import_data.m, imported the raw data from the text files and compiled the data into matrices of data per month. These matrices of monthly data were saved into files for each month, and each file had five columns of the mean values for each of the four anemometers and the wind vane. The files were named based on year and month, like the following file name for January 2011: Y2011M01.txt. The second script file, analyze_data.m, analyzes the wind data, performs the processing mentioned in Chapter 3, and generates the plots of wind data shown in Figure 3.3 through Figure 3.12, and Figure 4.1, and Figure 4.2. The code in each of the files is shown below.

import_data.m

```
%import_data.m

clear all
close all
clc

disp('>> import_data')

%% Creating Filename

type = '0639';
start = [2010,10,13,0,0,0];
dv = start;
disp([datestr(dv,'mmmm'),' ',datestr(dv,'yyyy')])
n = daysdif(datestr(start),datestr(dv)) + 8;
% size = daysdif(datestr(dv),datestr(dv+[0,1,1-dv(3),0,0,0]));
i = 1;


%% Importing data

tic
```

```
while(1)
    % assign filename of file to open
    yyyy = num2str(dv(1),'%4.4i');
    mm = num2str(dv(2),'%2.2i');
    mmstr = datestr(dv,'mmmm');
    dd = num2str(dv(3),'%2.2i');
    filename = [type,yyyy,mm,dd,num2str(n,'%3.3i'),'.txt.'];
    % disp(filename)

    % open file if it exists
    fid = fopen([yyyy,'\',mm,' ',mmstr,'\',filename]);
    % if file does not exist
    if fid == -1
        % try incrementing file number
        for kk = 1:10
            n = n + 1;
            filename = [type,yyyy,mm,dd,num2str(n,'%3.3i'),'.txt.'];
            fid = fopen([yyyy,'\',mm,' ',mmstr,'\',filename]);
            if fid ~= -1
                disp(['   ',num2str(kk),' file numbers were skipped'])
                break
            end
        end
        % if the file still does not exist, end program
        if fid == -1
            disp(['  ','The file for ',datestr(dv),' is not complete'])
            savefile = ['Y',yyyy,'M',mm,'.txt'];
            dummy = [datev,datam];
            save(savefile,'dummy','-ASCII','-tabs')
            clear dummy datam datev
            fprintf('   ')
            toc
            break
        end
    end

    % skip all data in file until header for data is reached
    header = ['Date & Time Stamp   CH1Avg  CH1SD   CH1Max  CH1Min',...
                                  'CH2Avg  CH2SD   CH2Max  CH2Min',...
                                  'CH3Avg  CH3SD   CH3Max  CH3Min',...
                                  'CH4Avg  CH4SD   CH4Max  CH4Min',...
                                  'CH5Avg  CH5SD   CH5Max  CH5Min',...
                                  'CH6Avg  CH6SD   CH6Max  CH6Min',...
                                  'CH7Avg  CH7SD   CH7Max  CH7Min',...
                                  'CH8Avg  CH8SD   CH8Max  CH8Min',...
                                  'CH9Avg  CH9SD   CH9Max  CH9Min',...
                                  'CH10Avg CH10SD  CH10Max CH10Min',...
                                  'CH11Avg CH11SD  CH11Max CH11Min',...
                                  'CH12Avg CH12SD  CH12Max CH12Min'];
    dummy = '';
    while strcmp(dummy,header) == false
        dummy = fgetl(fid);
    end

    % read data out of file
    while(1)
        date = fscanf(fid,'%19c',1);
```

```
        data = fscanf(fid,'%f',24);
        if strcmp(date,'')
            % at end of file, stop reading
            break
        end
        % convert to matlab date string
        datev(i,:) = [str2double(date(7:10)),...
                      str2double(date(1:2)),...
                      str2double(date(4:5)),...
                      str2double(date(12:13)),...
                      str2double(date(15:16)),...
                      str2double(date(18:19))];
        % make matrix of pertinent data
        datam(i,:) = data(1:17);
        fgetl(fid);
        i = i + 1;
    end

    % close file
    fclose(fid);

    % increment file number and date
    n = n + 1;
    if (datev(i-1,4) == 22 || datev(i-1,4) == 23) && datev(i-1,5) == 50
        % if the end of the day was reached, increment the date
        month_old = dv(2);
        dv = datevec(daysadd(datestr(dv),1,0));
        if month_old ~= dv(2)
            savefile = ['Y',yyyy,'M',mm,'.txt'];
            dummy = [datev,datam];
            save(savefile,'dummy','-ASCII','-tabs')
            clear dummy datam datev
            i = 1;
            fprintf('   ')
            toc
            disp([datestr(dv,'mmmm'),' ',datestr(dv,'yyyy')])
            tic
        end
    else
        disp(['   ',datestr(dv),' has two data files'])
        % data for the whole day was not taken, so do nothing (the next
        % file should complete the data from that day)
    end
end


clear all
```

analyze_data.m

```
% analyze_data.m
% this file analyzes the data imported from the original text files.
It
% imports the data from the text files created in the import process,
% smooths the data, determines the weibull distribution constants, and
```

```
% plots the data vs. the weibull curve fit.


clear all
% close all
clc

set(0,'DefaultFigureWindowStyle','docked')

mps2mph = 2.23693629;

disp('>> analyze_data')

%% Import data from created txt files

disp(' ')
disp('Importing data from text files...')

        name = {...
                'Y2011M01.txt'...
                ,...
                'Y2011M02.txt'...
                ,...
                'Y2011M03.txt'...
                ,...
                'Y2011M04.txt'...
                ,...
                'Y2011M05.txt'...
                ,...
                'Y2011M06.txt'...
                ,...
                'Y2011M07.txt'...
                ,...
                'Y2011M08.txt'...
                ,...
                'Y2011M09.txt'...
                ,...
                'Y2011M10.txt'...
                ,...
                'Y2011M11.txt'...
                ,...
                'Y2011M12.txt'...
                };

d = [[],[],[],[],[]];

for i = 1:length(name)
    tic
    disp(name{i})
    data = load(name{i});
    months(i) = length(data);
    d = vertcat(d,data(:,[7,11,15,19,23]));
    toc
end
```

```
%% Figure Setup

disp(' ')
disp('Setting up figures...')
tic

num_figures = 9;

for ff = 1:num_figures
    figure(ff);
end

toc

%% Pre-smoothing plots

nn = length(d);          % number of samples

disp(' ')
disp('Plotting raw data...')
tic

% Plot two 100 ft anemometers vs. each other
figure(6)
subplot(3,2,1)
plot(d(:,3),d(:,4),'.')
% title: Pre-Smoothed 100 ft Data
plot_options(6,'',...
    '100 ft (A) Anemometer (m/s)','100 ft (B) Anemometer (m/s)')
grid on

% Plot primary 100 ft vs. 75 ft
figure(6)
subplot(3,2,3)
plot(d(:,3),d(:,2),'.',d(:,4),d(:,2),'.')
% title: Pre-Smoothed 100 ft vs. 75 ft Data
plot_options(6,'',...
    '100 ft Anemometer (m/s)','75 ft Anemometer (m/s)')
legend('75 ft vs. 100 ft (A)','75 ft vs. 100 ft (B)')
legend location northwest
grid on

% Plot primary 50 ft vs. 75 ft
figure(6)
subplot(3,2,5)
plot(d(:,1),d(:,2),'.')
% title: Pre-Smoothed 50 ft vs. 75 ft Data
plot_options(6,'',...
    '50 ft Anemometer (m/s)','75 ft Anemometer (m/s)')
grid on

exp2 = log2(10);
ba = 10^(-5);
bb = 10^5;
dummy = -5:1:5;
```

```
ytick = 10.^dummy;
yticklabeldummy = {'     ','     ','     ','     ','     ','     ',...
                   '     ','     ','     ','     ','     '};
yticklabel = {'2^-^5','2^-^4','2^-^3','2^-^2','2^-^1','2^0',...
              '2^1','2^2','2^3','2^4','2^5'};

% plot 100 ft anemometer ratio vs. time
figure(7)
gca = subplot(3,2,1);
semilogy(1:size(d,1),(d(:,3)./d(:,4)).^exp2,'.')
% title: Pre-Smoothed anemometer ratio vs. sample number
plot_options(7,'','Sample Number','100 ft (A) / 100 ft (B)')
xlim([0,nn])
ylim([ba,bb])
set(gca,'ytick',ytick,'yticklabel',yticklabeldummy)
grid on
set(gca,'YMinorGrid','off')
for i = dummy
    text(-1000,10^i,yticklabel(i+6),'HorizontalAlignment','Right')
end

% plot 100 ft / 75 ft anemometer ratio vs. time
figure(7)
gca = subplot(3,2,3);
semilogy(1:size(d,1),(d(:,3)./d(:,2)).^exp2,'.',...
         1:size(d,1),(d(:,4)./d(:,2)).^exp2,'.')
% title: Pre-Smoothed anemometer ratio vs. sample number
plot_options(7,'','Sample Number','100 ft / 75 ft')
xlim([0,nn])
ylim([ba,bb])
set(gca,'ytick',ytick,'yticklabel',yticklabeldummy)
legend('100 ft (A) / 75 ft','100 ft (B) / 75 ft')
legend location northwest
grid on
set(gca,'YMinorGrid','off')
for i = dummy
    text(-1000,10^i,yticklabel(i+6),'HorizontalAlignment','Right')
end

% plot 50 ft / 75 ft anemometer ratio vs. time
figure(7)
gca = subplot(3,2,5);
semilogy(1:size(d,1),(d(:,1)./d(:,2)).^exp2,'.')
% title: Pre-Smoothed anemometer ratio vs. sample number
plot_options(7,'','Sample Number','50 ft / 75 ft')
xlim([0,nn])
ylim([ba,bb])
set(gca,'ytick',ytick,'yticklabel',yticklabeldummy)
grid on
set(gca,'YMinorGrid','off')
for i = dummy
    text(-1000,10^i,yticklabel(i+6),'HorizontalAlignment','Right')
end

% Plot 100 ft data vs. time (sample number, for now)
figure(8)
gca = subplot(3,2,1);
```

```
plot(1:size(d,1),d(:,3:4),'.')
plot_options(8,'','Sample Number','100 ft Anemomenter (m/s)')
xlim([30000,35000])
legend('100 ft (A)','100 ft (B)')
legend location northwest
grid on

% Plot 75 ft data vs. time (sample number, for now)
figure(8)
gca = subplot(3,2,3);
plot(1:size(d,1),d(:,2),'.')
plot_options(8,'','Sample Number','75 ft Anemomenter (m/s)')
xlim([[30000,35000]])
grid on

% Plot 50 ft data vs. time (sample number, for now)
figure(8)
gca = subplot(3,2,5);
plot(1:size(d,1),d(:,1),'.')
plot_options(8,'','Sample Number','50 ft Anemomenter (m/s)')
xlim([10000,15000])
grid on

toc

%% Smooth data

disp(' ')
disp('Smoothing data...')
tic

rat75 = mean([mean(d(:,2)./d(:,4)),mean(d(:,2)./d(:,3))]);
rat50 = mean([mean(d(:,1)./d(:,4)),mean(d(:,1)./d(:,3))]);

np = 0;
np2 = 0;
n1 = 0;
n11 = 0;
n12 = 0;
n3 = 0;
n4 = 0;
n32 = 0;
n42 = 0;
n5 = 0;
d_old = d(:,1)';

for i = 1:length(d)
    % compare data at 100 ft, if quotient of two anemoemters is > 2,
    % data is bad... (assumes one of the anemometers is reading
    % properly)
    if abs( d(i,3) - d(i,4) ) > 0.45*2
        if d(i,3)/d(i,4) > 2
            d(i,4) = d(i,3);
            n4 = n4 + 1;
        elseif d(i,4)/d(i,3) > 2
            d(i,3) = d(i,4);
```

```
            n3 = n3 + 1;
        end
    end

    % solve for the power in the power law for turb, boundary layers
    pow(i)      = log( d(i,2)/mean(d(i,3:4)) ) / log( 25/34 );
    if pow(i) > 0 && pow(i) < 0.75
        np = np + 1;
    end
    dummypow(i) = d(i,3)*(50/75)^pow(i);

    if abs(dummypow(i) - d(i,1)) > 0.45*2
        if dummypow(i)/d(i,1) > 2
            d(i,1) = round(dummypow(i)*10)/10;
            n1 = n1 + 1;
            if pow(i) > 0 && pow(i) < 0.75
                np2 = np2 + 1;
            end
        end
    end

    if abs(dummypow(i) - d(i,1)) < 0.45
        n11 = n11 + 1;
    elseif abs(dummypow(i) - d(i,1)) > 2
        n12 = n12 + 1;
    end

    % check angle (if wind speed is 0.4 m/s, don't include angle data)
    if mean(d(i,1:4)) == 0.4
        d(i,5) = NaN;
        n5 = n5 + 1;
    end

end

% noting % of data modified
disp('Percent of data modified')
fprintf('100 ft (A)  \t %6.3f \n',n3 /nn*100)
fprintf('100 ft (B)  \t %6.3f \n',n4 /nn*100)
fprintf('50 ft pred \t %6.3f \n',n11/nn*100)
fprintf('50 ft pred \t %6.3f \n',n12/nn*100)
fprintf('50 ft      \t %6.3f \n',n1 /nn*100)
fprintf('BL Exp     \t %6.3f \n',np /nn*100)
fprintf('BL Exp app \t %6.3f \n',np2/n1*100)
fprintf('Angle      \t %6.3f \n',n5 /nn*100)

toc

%% Post-smoothing plots

disp(' ')
disp('Plotting smoothed data...')
tic

% Plot two 100 ft anemometers vs. each other
```

```
figure(6)
subplot(3,2,2)
plot(d(:,3),d(:,4),'.')
% title: Smoothed 100 ft Data
plot_options(6,'',...
    '100 ft (A) Anemometer (m/s)','100 ft (B) Anemometer (m/s)')
grid on

% Plot primary 100 ft vs. 75 ft
figure(6)
subplot(3,2,4)
plot(d(:,3),d(:,2),'.',d(:,4),d(:,2),'.')
% title: Smoothed 100 ft vs. 75 ft Data
plot_options(6,'',...
    '100 ft Anemometer (m/s)','75 ft Anemometer (m/s)')
legend('75 ft vs. 100 ft (A)','75 ft vs. 100 ft (B)')
legend location northwest
grid on

% Plot primary 75 ft vs. 50 ft
figure(6)
subplot(3,2,6)
plot(d(:,1),d(:,2),'.')
% title: Smoothed 50 ft vs. 75 ft Data
plot_options(6,'',...
    '50 ft Anemometer (m/s)','75 ft Anemometer (m/s)')
grid on

% plot anemometer ratio vs. time
dummy = -5:1:5;

figure(7)
gca = subplot(3,2,2);
semilogy(1:size(d,1),(d(:,3)./d(:,4)).^exp2,'.')
% title: Smoothed anemometer ratio vs. sample number
plot_options(7,'',...
    'Sample Number','100 ft (A) / 100 ft (B)')
xlim([0,nn])
ylim([ba,bb])
set(gca,'ytick',ytick,'yticklabel',yticklabeldummy')
grid on
set(gca,'YMinorGrid','off')
for i = dummy
    text(-1000,10^i,yticklabel(i+6),'HorizontalAlignment','Right')
end

% plot 100 ft / 75 ft anemometer ratio vs. time
figure(7)
gca = subplot(3,2,4);
semilogy(1:size(d,1),(d(:,3)./d(:,2)).^exp2,'.',...
         1:size(d,1),(d(:,4)./d(:,2)).^exp2,'.')
% title: Smoothed anemometer ratio vs. sample number
plot_options(7,'',...
    'Sample Number','100 ft / 75 ft')
xlim([0,nn])
ylim([ba,bb])
```

```
set(gca,'ytick',ytick,'yticklabel',yticklabeldummy')
legend('100 ft (A) / 75 ft','100 ft (B) / 75 ft')
legend location southwest
grid on
set(gca,'YMinorGrid','off')
for i = dummy
    text(-1000,10^i,yticklabel(i+6),'HorizontalAlignment','Right')
end

% plot 50 ft / 75 ft anemometer ratio vs. time
figure(7)
gca = subplot(3,2,6);
semilogy(1:size(d,1),(d(:,1)./d(:,2)).^exp2,'.')
% title: Smoothed anemometer ratio vs. sample number
plot_options(7,'',...
    'Sample Number','50 ft / 75 ft')
xlim([0,nn])
ylim([ba,bb])
set(gca,'ytick',ytick,'yticklabel',yticklabeldummy')
grid on
set(gca,'YMinorGrid','off')
for i = dummy
    text(-1000,10^i,yticklabel(i+6),'HorizontalAlignment','Right')
end

% Plot 100 ft data vs. time (sample number, for now)
figure(8)
gca = subplot(3,2,2);
plot(1:size(d,1),d(:,3:4),'.')
plot_options(8,'','Sample Number','100 ft Anemomenter (m/s)')
xlim([30000,35000])
legend('100 ft (A)','100 ft (B)')
legend location northwest
grid on

% Plot 75 ft data vs. time (sample number, for now)
figure(8)
gca = subplot(3,2,4);
plot(1:size(d,1),d(:,2),'.')
plot_options(8,'','Sample Number','75 ft Anemomenter (m/s)')
xlim([30000,35000])
grid on

% Plot 50 ft data vs. time (sample number, for now)
figure(8)
gca = subplot(3,2,6);
plot(1:size(d,1),d_old,'.',1:size(d,1),d(:,1),'.')
plot_options(8,'','Sample Number','50 ft Anemomenter (m/s)')
xlim([10000,15000])
legend('Uncorrected','Corrected')
legend location northwest
grid on

%% other plots

% plot figure of power law predicted data to real data at 50 ft
```

```
figure(9);
a = 2;
step = 0.05;
bins = -a:step:a;
gca = subplot(2,2,1);
hist(dummypow-d_old,bins);
plot_options(9,'Histogram of Predicted Wind Speed at 50 ft',...
    'Difference of Predicted Wind Speed and Measured Wind Speed
(m/s)',...
    'Frequency')
grid on
xlim([-a,a])

% plot figure of original 50 ft data
gca = subplot(2,2,2);
% plot histogram
step = 0.5;
bins = 0:step:25;
hist(d_old,bins)
% add labels
plot_options(9,'Wind Data at 50 ft','Wind Speed (m/s)','Probability')
% adjust limits and tick marks
mm = 0.2;
prob = linspace(0,mm,11);
xm = 12;
xtick = 0:2:xm;
xlim([0,xm])
set(gca,'xtick',xtick,'xticklabel',xtick)
ylim([0,mm*nn*step])
set(gca,'ytick',prob*nn*step,'yticklabel',prob)
% legend and grid
grid on

% plot histogram of exp from power law
gca = subplot(2,2,3);
a = -1;
b = 2;
bins = linspace(a,b,100);
hist(pow,bins)
plot_options(9,'Histogram of Power Values','Exponent','Frequency')
xlim([a,b]);
text(1.9,4800,['Mean Value = ',num2str(mean(pow))],...
    'BackgroundColor',[1 1 1],'EdgeColor',[0 0 0],'Margin',5,...
    'HorizontalAlignment','Right','VerticalAlignment','Top')
grid on

toc

%% Find the Weibull Constants

disp(' ')
disp('Finding the Weibull constants...')

A = zeros(size(d,2)-1,2);
Avar = A;
for i = 1:size(d,2)-1
```

```
    [A(i,:),dummy] = wblfit(d(:,i));
    Avar(i,1) = dummy(2,1)-A(i,1);
    Avar(i,2) = dummy(2,2)-A(i,2);
end
clear dummy


%% Comparison of Weibull curve fit and actual data (mean and std dev)

disp(' ')
disp('Comparison of Data and Weibull Curve Fit...')

[wmean,wvar] = wblstat(A(:,1),A(:,2));
wstd  = sqrt(wvar);
dmean = mean(d(:,1:4))';
dstd  = std(d(:,1:4))';
dmode = mode(round(d(:,1:4)*10)/10)';
amean = mean(d(:,5));
astd  = std(d(:,5));
amode = mode(d(:,5));

ttl = {'50 ft','75 ft','100 ft','100 ft'};
fprintf('Height \t Data Mean \t Fit Mean \t Data Std \t Fit Std \n')
for i = 1:4
    fprintf('%s \t %7.4f \t %7.4f \t %7.4f \t %7.4f \n',...
            ttl{i},dmean(i),wmean(i),dstd(i),wstd(i))
end

%% Plot Weibull Distributions

disp(' ')
disp('Plotting data vs. Weibull curve fit...')

step = 0.5;                          % step size, m/s
bins = 0:step:25;                    % bins for histogram
xm   = 12;                           % xmax for plot, m/s
U    = linspace(0,xm);               % wind speed, m/s
func = zeros(length(U),length(A));   % probability for each wind speed
for i = 1:length(A)
    [func(:,i),~] = prob_func(U',A(i,:));
end
% find midpoints of bins
for i = 1:(length(bins)-1)
    midbins(i) = ( bins(i) + bins(i+1) ) / 2;
end

% scaling for plots
mm    = 0.2;                 % max probability
prob  = linspace(0,mm,11);   % probability at tick
xtick = 0:2:xm;              % x value at ticks
figure(1)
for i = 1:4
    gca = subplot(2,2,i);
    % plot histogram
    hist(d(:,i),bins)
    n = hist(d(:,i),bins);
```

```
    hold on
    % plot curve fit
    plot(U,func(:,i)*nn*step,'r-','LineWidth',2);
    % add labels
    plot_options(1,['Wind Data at ',ttl{i}],'Wind Speed
(m/s)','Probability')
    % add k and c values
    [~,imax] = max(func(:,i));
    text(U(imax),nn*step*0.02,...
        {['k = ',num2str(A(i,2)),' \pm ',num2str(Avar(i,2))],...
         ['c = ',num2str(A(i,1)),' \pm ',num2str(Avar(i,1))]},...
        'BackgroundColor',[1 1 1],'EdgeColor',[0 0 0],'Margin',5,...
        'HorizontalAlignment','Center')
    % disp bin size on plot
    text(0.02*xm,mm*.97*nn*step,{'Bin Size',...
        [num2str(step,'%5.3f'),' m/s'],...
        'Mean (Data)',[num2str(dmean(i),'%5.3f'),' m/s'],...
        'Mean (Fit)',[num2str(wmean(i),'%5.3f'),' m/s']},...
        'BackgroundColor',[1 1 1],'EdgeColor',[0 0 0],'Margin',5,...
        'HorizontalAlignment','Left','VerticalAlignment','Top')
    % adjust limits and tick marks
    xlim([0,xm])
    set(gca,'xtick',xtick,'xticklabel',xtick)
    ylim([0,mm*nn*step])
    set(gca,'ytick',prob*nn*step,'yticklabel',prob)
    % legend and grid
    legend('Data','Weibull Fit')
    legend location northeast
    grid on
    hold off
end

%% Plot Wind Rose

disp(' ')
disp('Building Wind Rose...')
fprintf('Mode Angle: %5.3f degrees \n',amode)

for i = 1:4
    figure(i+1)
    wind_rose(d(:,5),d(:,i),'lablegend','Wind Speed (m/s)',...
                  'ci',[4,8,12],'n',36,'dtype','meteo',...
                  'di',[0,2.5,5,7.5,10,12.5,15,17.5])
    plot_options(i+1,['Wind Data at ',ttl{i}],'','')
end

% go back to figure 1
figure(1)

% percent of data
disp('Percent of wind coming from north')
disp((length(find(315 < d(:,5))) + length(find(d(:,5) < 45)))/nn*100)
disp('Percent of wind coming from the north')
disp(length(find(135 < d(:,5) & d(:,5) < 225))/nn*100)
```

```
%% Monthly Data

index = 1;

monthly_avg = zeros(length(name),4);

for i = 1:length(name)
    monthly_avg(i,1:4) = mean(d(index:(months(i)+index-1),1:4));
    index = index + months(i);
end

disp(' ')
disp('Monthly Averages (m/s)')
disp(['YYYY-MMM',' 50 ft ',' 75 ft ','100 ft ','100 ft '])
for i = 1:length(name)
    [~,mm] = month([name{i}(7:8),'/','1/',name{i}(2:5)]);
    disp([name{i}(2:5),'-',mm,...
        ' ',num2str(monthly_avg(i,:),'%7.3f')])
end
disp(['Average  ',...
      num2str(mean(d(:,1)),'%5.3f'),'  ',...
      num2str(mean(d(:,2)),'%5.3f'),'  ',...
      num2str(mean(d(:,3)),'%5.3f'),'  ',...
      num2str(mean(d(:,4)),'%5.3f')])
disp(' ')
```

APPENDIX C

Front Panel of LabVIEW® Program for Wind Tunnel Controller

The LabVIEW® code for the wind tunnel is relatively simple. The inputs, seen in Figure C.1, include a folder name (a file with wind speed data is named based on the date), the physical channels for the thermocouple, relative humidity sensor, the timing inputs for the thermocouple and relative humidity sensor sampling. Additionally, the number of samples to be taken and averaged for the PCL-2A as well as the module being used must be input. Finally, the characteristic length for a Reynolds number calculation can be input.

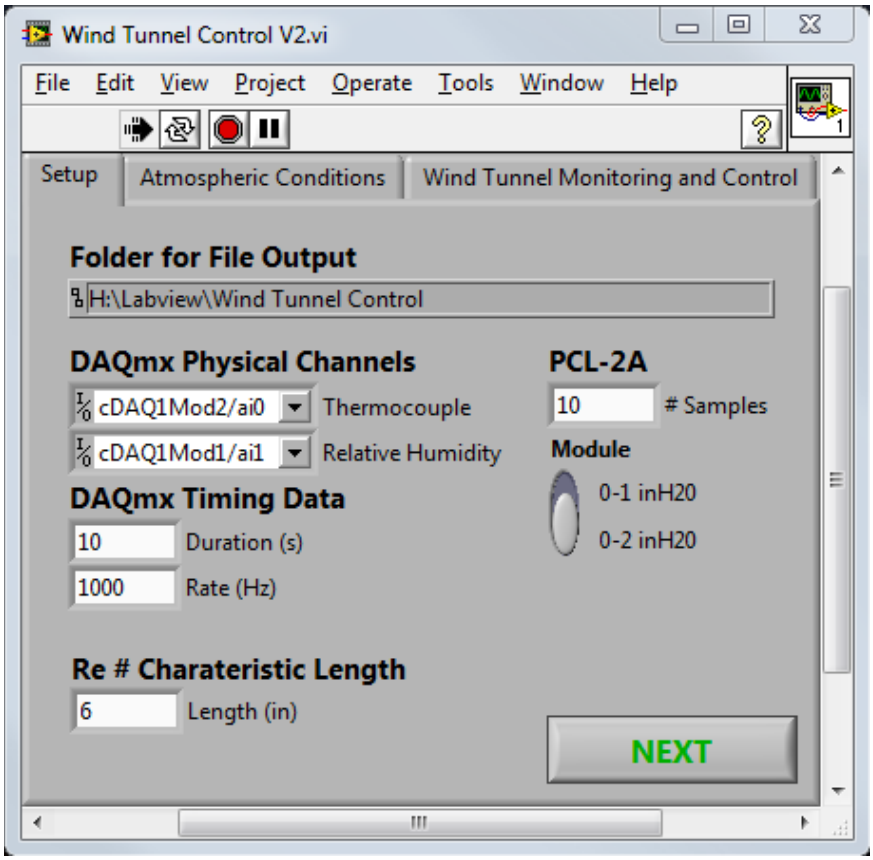

Figure C.1: "Setup" Tab of Wind Tunnel Controller Program

Figure C.2 shows the atmospheric conditions tab of the program, which allows the input of the atmospheric pressure through a dialog box. After the pressure is entered into the dialog, the program calculates the air density and viscosity based on the measured temperature and relative humidity.

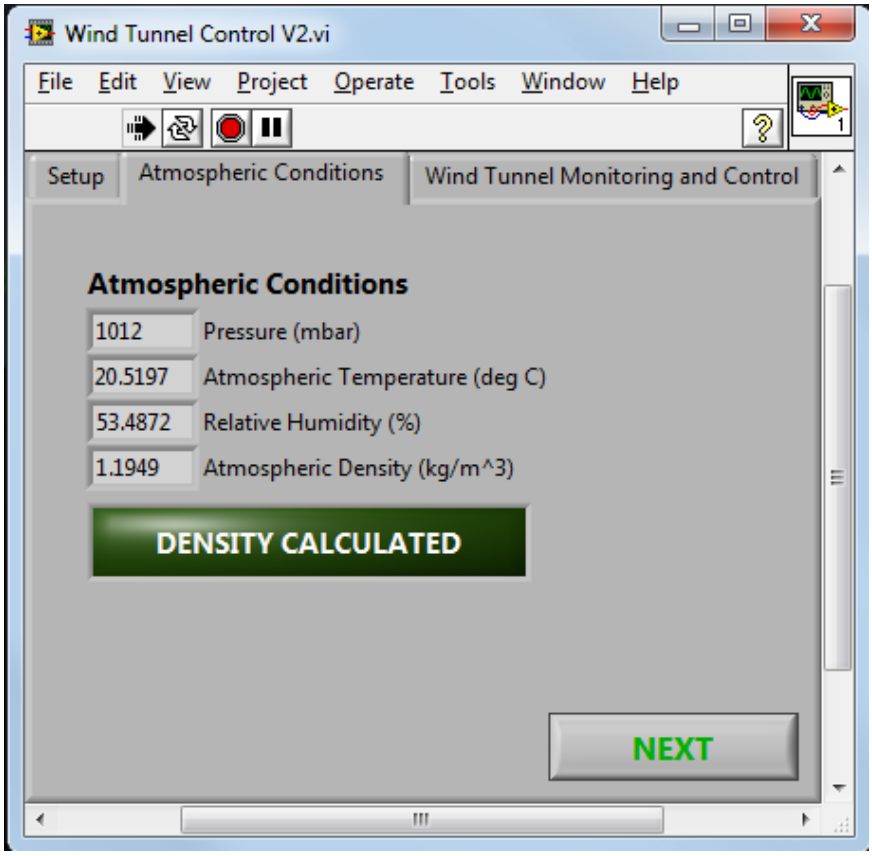

Figure C.2: "Atmospheric Conditions" Tab of Wind Tunnel Controller Program

Finally, the "Wind Tunnel Monitoring and Control" tab can be seen in Figure C.3. This tab shows a slider that controls the voltage signal sent to the wind tunnel. Additionally, the dynamic pressure, velocity, and Reynolds numbers are display for monitoring the wind tunnel condition. This assumes that a pitot-static tube is connected to the PCL-2A. Also, the current conditions can be stored into an array, which is written to a file when the program is stopped. This array includes the outputs previously

mentioned as well as the number of samples taken for the dynamic pressure and the standard deviation for uncertainty calculations.

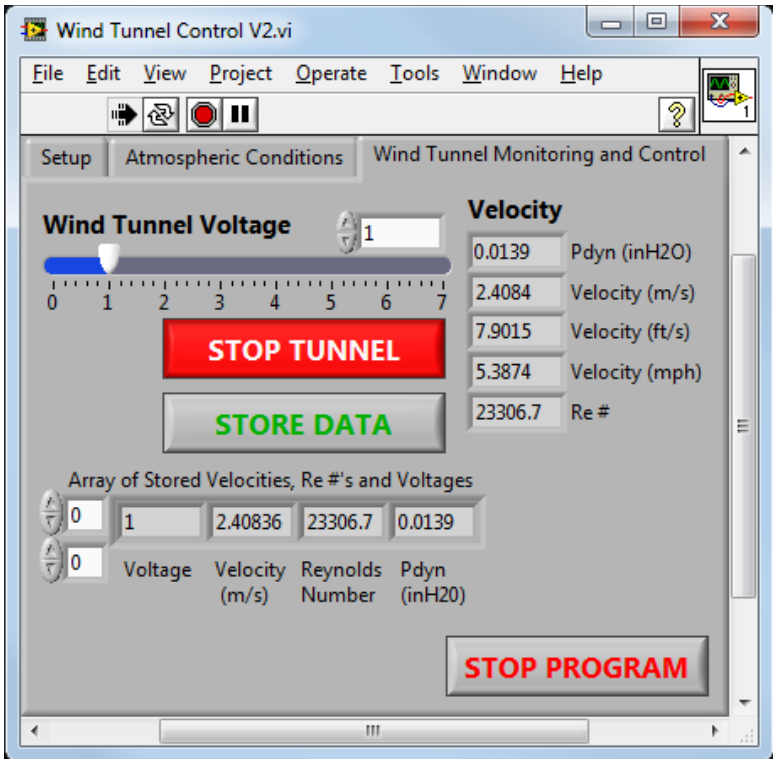

Figure C.3: "Wind Tunnel Monitoring and Control" Tab of Wind Tunnel Controller Program

APPENDIX D

Airfoil Manufacture

The airfoils used in this study have a 6-inch chord and were manufactured out of Spyderfoam using a CNC hot wire. The surface was finished to be more rigid and smooth. The original airfoil material and surface can be seen in Figure D.1. The materials used in finishing the airfoil surface are listed below.

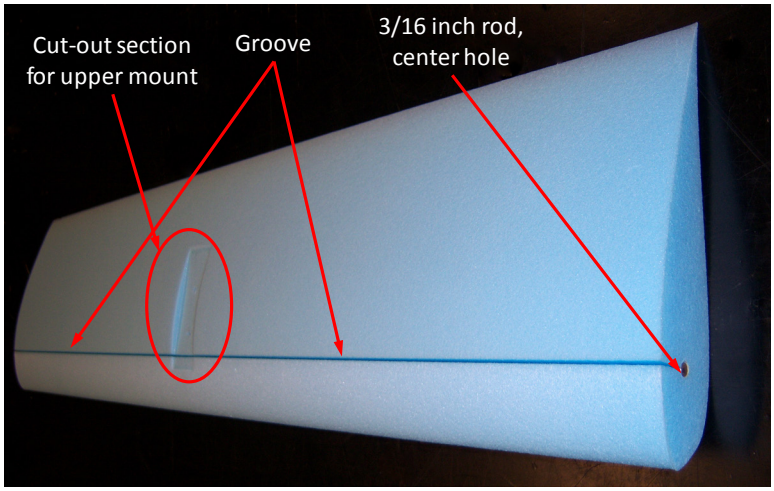

Figure D.1: Original Foam Airfoil (S823 Airfoil)

1. Foam airfoil with 6-inch chord and 24-inch width
2. Top and bottom airfoil mount and two #6-32 1 inch long screws
3. Masking tape
4. 1/16 inch sheet of balsa wood
5. 1-inch wide, Worktools International paint brush
6. West System epoxy resin 105
7. West System epoxy hardener 207

8. Solo P3A 3 oz. plastic cup and stirring stick for mixing epoxy
9. Methyl Ethyl Ketone (MEK)
10. 1/8 inch diameter, 3 ft long steel rod
11. 180 grit sandpaper (multiple 3 ¾ inch by 9 inch sheets)
12. 400, 600, 1000, and 2000 grit wet or dry sandpaper (multiple 3 ¾ inch by 9 inch sheets)
13. 3M Bondo professional glazing and spot putty (automotive putty)
14. Plastic putty knife
15. Rustoleum professional aerosol primer, 15 oz.
16. Rustoleum flat black protective enamel spray paint, 15 oz.
17. 3/16 inch, 24 inch long diameter steel rod
18. X-ACTO knife
19. Metal ruler, 12 inches long
20. Cut off wheel
21. Shurtape double sided duct tape

Using the materials listed above, the following procedure was followed to obtain a smooth airfoil surface.

1. First, the airfoil mounts were placed into the cut-out sections, of the original foam airfoil to determine if they fit properly. The cut-out sections were 1-inch wide and located in the spanwise center of the airfoil. The cut-out section for the upper mount is circled in red in Figure D.1. If the either mount was not tall enough to be flush with the airfoil surface, layers of masking tape were added to increase thickness and keep the mount flush. If either mount was too tall to be flush with

the airfoil surface, the foam was sanded using 180 grit sandpaper until the mount fit flush with the outer surface of the airfoil (as seen in Figure D.2).

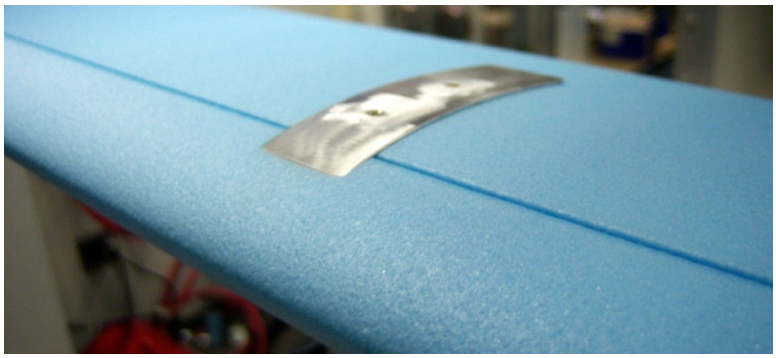

Figure D.2: Original Foam Airfoil with Upper Mount Inserted Flush

2. With the upper mount held firmly in the top cut-out section, both screws were screwed from the top down through the airfoil. This made the through holes in the foam for both screws.
3. Both mounts were placed in their respective cut-out sections and screwed in from the bottom into the top mount. A cut off wheel was used to take off the excess length of screw and make it flush with the upper mount. The mounts were then removed.
4. A groove (seen in Figure D.1) was cut in the airfoil by the manufacturer in order to produce a spanwise hole for a 3/16-inch steel rod. The purpose of the steel rod was to provide stiffening support for the airfoil. The groove interrupted the smooth surface of the airfoil, therefore, two ¼-inches wide, 11-inch long strips were cut from the balsa wood sheet and lightly sanded with 400 grit sandpaper until they fit snugly into the groove on either side of the upper airfoil mount cut-out (Figure D.1). Then the two strips of balsa wood were fit into the groove so that they were flush with the top surface of the airfoil, as seen in Figure D.3.

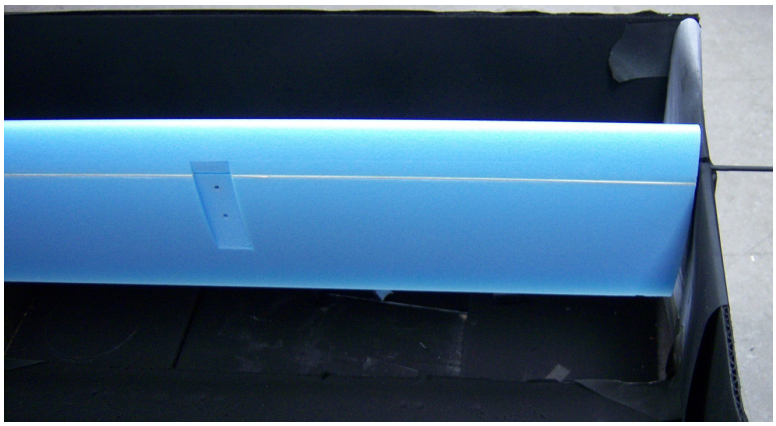

Figure D.3: Hanging Foam Airfoil with Balsa Wood Inserted

5. Before applying the epoxy, loose bristles were pulled out of the paint brush (if the paint brush was new).
6. The airfoil was hung with a 30-inch long, 1/8-inch diameter steel rod through the center hole on the airfoil (Figure D.3).
7. Three parts West Systems 105 epoxy resin and one part West Systems 207 epoxy hardener were mixed into a plastic cup and with the stirring stick.
8. The entire surface of the airfoil was coated with a very thin layer of epoxy except for the cut-out sections.
9. The epoxy was cleaned out of the paint brush with methyl ethyl ketone (MEK) in order to be used in applying another coat.
10. After drying for at least 10 hours, the epoxy was lightly sanded with 180 grid sandpaper and steps 2 through 9 were repeated to apply a total of three coats.
11. After drying, the epoxy surface had an orange-peel texture (seen in Figure D.4) and the groove was not completely smooth. To make the surface smoother, 3D Bondo professional glazing and spot putty was spread over the airfoil surface (not the ends of the airfoil or the cut-out sections) and wet sanded using 180 grit

sandpaper. To ensure the shape of the airfoil is maintained, the putty was sanded until spots of epoxy could be seen. The addition of the spot putty can be seen in Figure D.5.

Figure D.4: Airfoil with Epoxy Coating

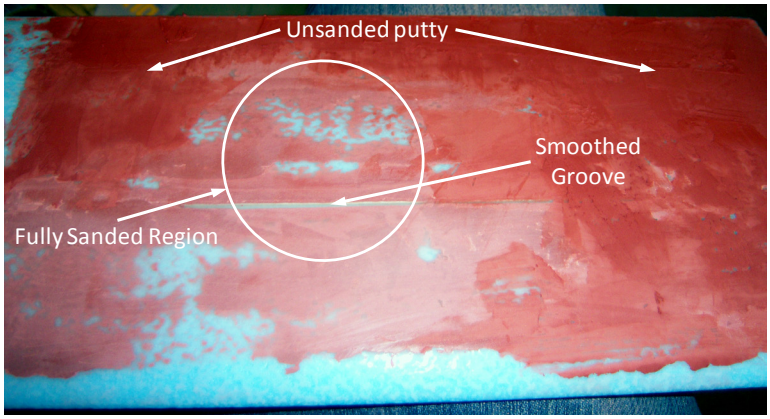

Figure D.5: Airfoil with Putty

12. After the airfoil surface was smooth to the touch from wet sanding, the cut-out sections were covered with masking tape so that there was no foam exposed (oil-based paints will eat away the foam). Two coats of Rustoleum primer were applied over the entire airfoil twenty minutes apart.
13. After about six hours the primer was dry and the surface was sanded lightly with 400 grit sandpaper.

14. Two coats of Rustoleum flat black protective enamel spray paint were applied to the surface twenty minutes apart.
15. After about six hours the paint was completely dry and the surface was wet sanded with 600 grit sandpaper. If the orange-peel texture has been completely covered and the surface is smooth to the touch, the surface can be wet sanded using 1000 grit then 2000 grit sandpaper. Otherwise, two more coats were added and this step was repeated.
16. The 3/16 inch diameter steel rod was inserted into the hole in the center of the airfoil and the mounts were placed into the cut-outs and screws attached. The upper mount can be seen in Figure D.2 and the lower mount can be seen in Figure D.6.

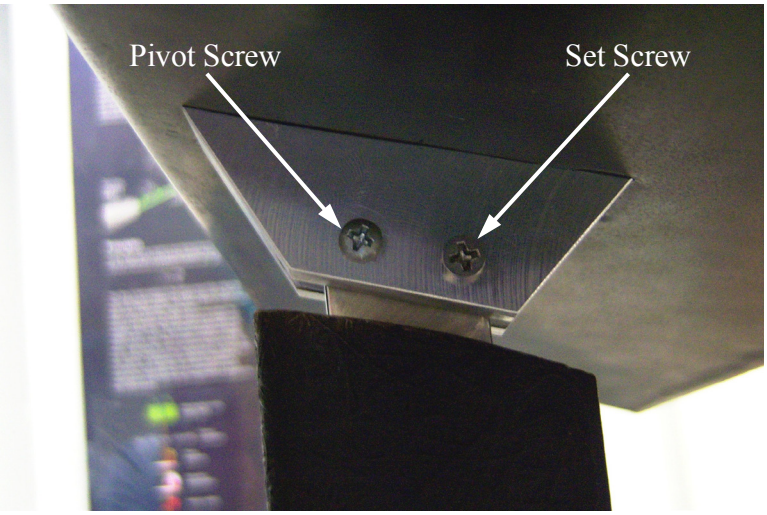

Figure D.6: Lower Airfoil Mount and Interface with Dynamometer (E37 Airfoil)

17. For some tests, a trip strip was added to the upper airfoil surface. Depending on the test, it was applied at either 2% or 25% of the chord from the leading edge. To make the trip strip, a piece of Shurtape double stick duct tape was applied to

the backside of a sheet of 180 grid sandpaper. Depending on the desired thickness, multiple layers of tape can be applied. The thickness of the sandpaper was approximately 0.009 inches, and the thickness of one layer of tape was approximately 0.012 inches. The strips were cut into 1/8 inch wide strips the length of the sandpaper sheet using an X-ACTO knife and metal ruler, then applied to the airfoil surface with the leading edge of the trip strip at the specified location (2% or 25%). A trip strip thickness of 0.021 inches was achieved with one layer of tape, a thickness 0.035 inches was achieve with two layers of tape, and a thickness of 0.080 inches was achieved with six layers of tape. The finished S823 airfoil with a trip strip applied at 2% of the chord on the upper surface can be seen in Figure D.7.

Figure D.7: Finished Airfoil Surface with Trip Strip Applied at 2% Chord (S823 Airfoil)

APPENDIX E

An Experimental Comparison of Multiple Airfoil Surfaces on the S823 Airfoil

A comparison was made of three different surface types to determine the best technique for airfoil surfacing. The first surface type was the original foam surface shown in Figure D.1. The second surface type was a thin plastic known as MonoKote® that was ironed onto the airfoils surface, shown in Figure E.1. The third surface type was developed by the process described in Appendix D. For this discussion, it will be referred to as the epoxy surface. The finished airfoil can be seen in Figure D.7, although no trip strip was added in this study.

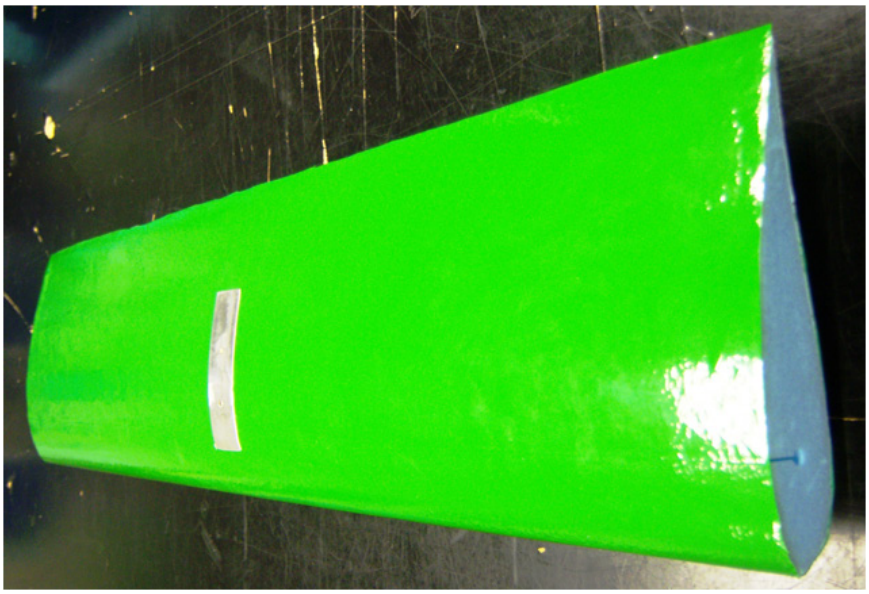

Figure E.1: MonoKote® Covered S823 Airfoil

Data for the foam and MonoKote® surfaces was taken for a Reynolds number of 175,000 and compared because both the coefficients of lift and drag did not change significantly with Reynolds number near this value. Additionally, an XFOIL simulation

was run for comparison with the experimental data. The results can be seen in Figure E.2. For the coefficient of lift, the data from the foam surface matches the XFOIL simulation very closely. The data from the MonoKote® surface, on the other hand, matches for most of the XFOIL simulation. However, for angles of attack greater than approximately 7 deg, the lift coefficient continues to increase. The maximum lift coefficient of the MonoKote® surface is nearly 1.5, but the maximum lift coefficient for the XFOIL simulation and foam surface only reaches approximately 1.2. The drag coefficient of both experimental sets is higher than the XFOIL simulation, partly due to the fact that wind tunnel corrections have not been applied to the data. Nonetheless, because the airfoil with the MonoKote® surface produced lift coefficients that are significantly higher than the simulation and other experimental data at similar Reynolds numbers, the airfoil with the foam surface as used in further comparisons with the epoxy-surfaced airfoil.

A second comparison was made between the XFOIL simulation data with the foam and epoxy surface data for Reynolds numbers of 200,000 and 100,000, shown in Figure E.3 and Figure E.4. While a comparison could be made at this point to published data for these Reynolds numbers, this data has not been included in the comparison because no wind tunnel corrections have been applied. A comparison of data taken with epoxy surface and UIUC data can be seen in Figure 4.8 and Figure 4.9. In both Figure E.3 and Figure E.4, the coefficient of lift and drag curves for the epoxy-surfaced airfoil match the XFOIL simulation data much better and is the surfacing used in all airfoil results presented in the body of this work.

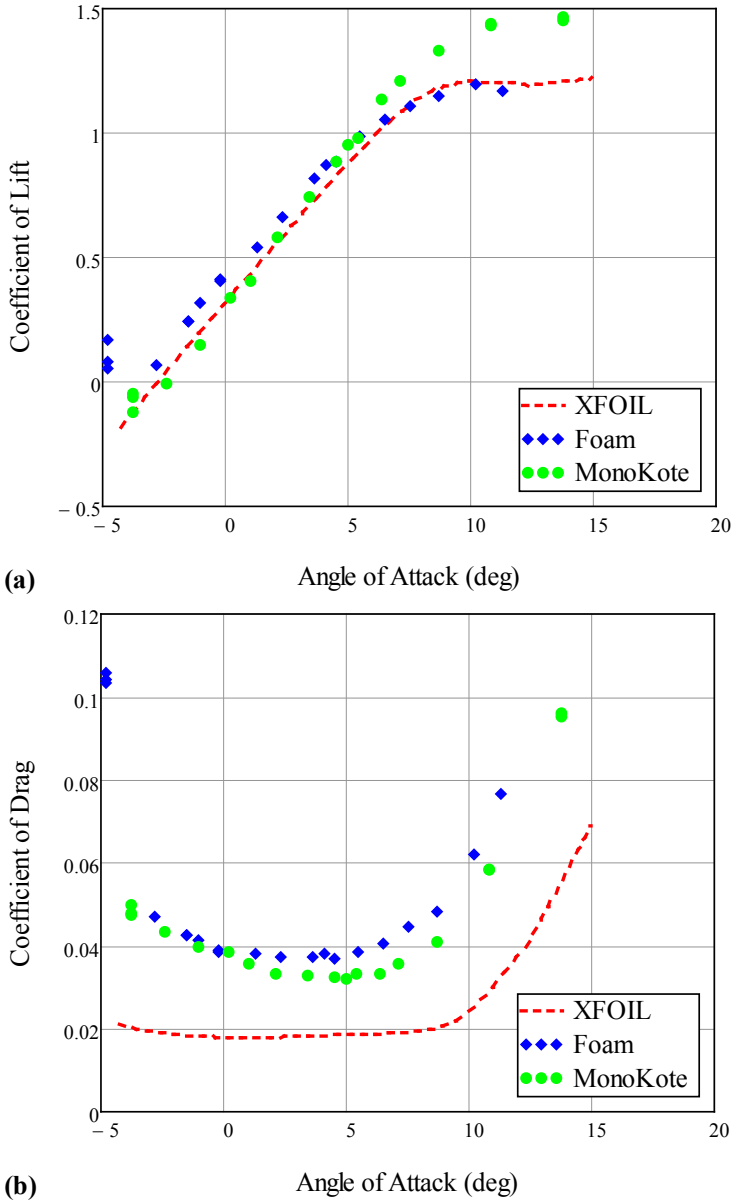

Figure E.2: Comparison of XFOIL with a foam and MonoKote ® surface on the S823 Airfoil at a Reynolds number of 175,000 (no wind tunnel corrections have been applied)

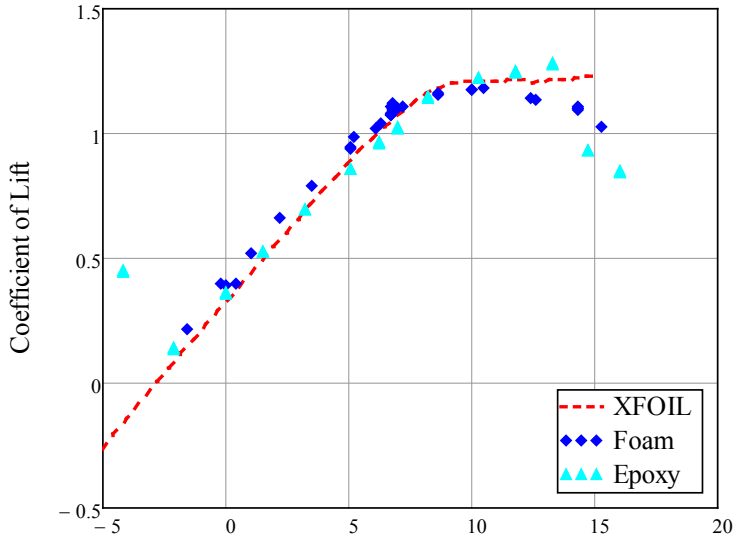

(a)

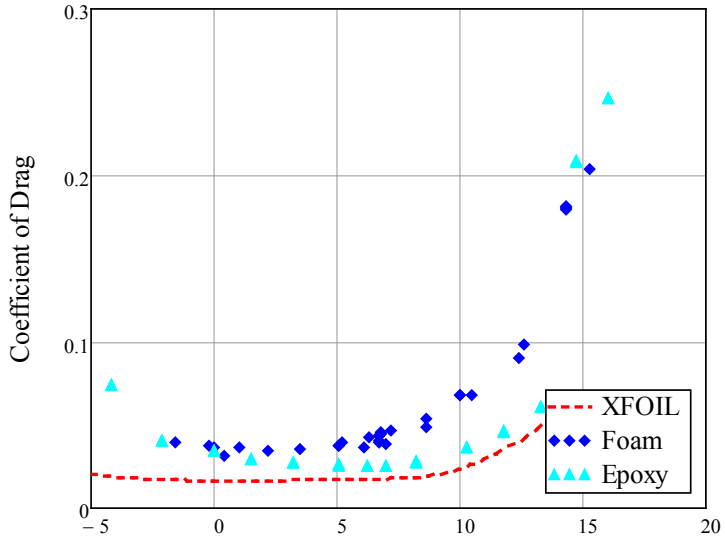

(b)

Figure E.3: Comparison of XFOIL with a foam and epoxy surface on the S823 Airfoil at a Reynolds number of 200,000 (no wind tunnel corrections have been applied)

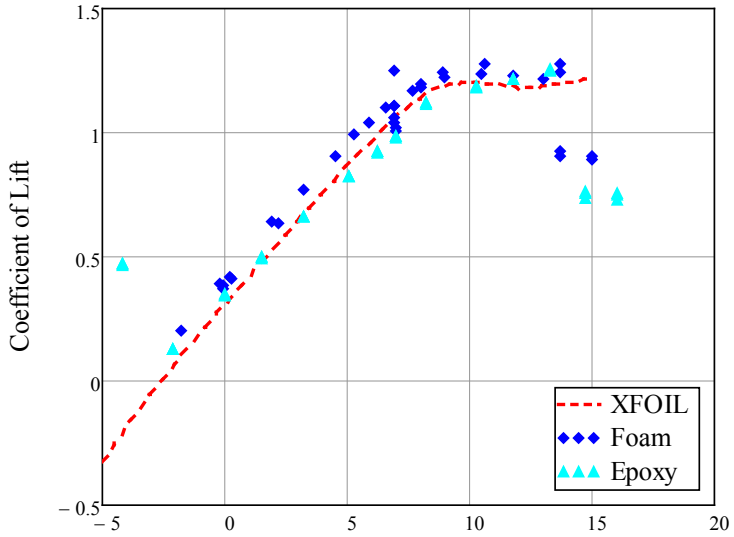

(a)

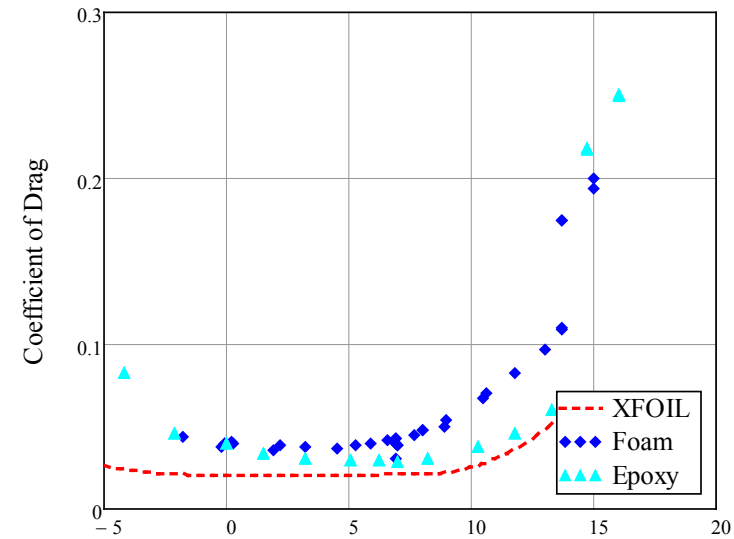

(b)

Figure E.4: Comparison of XFOIL with a foam and epoxy surface on the S823 Airfoil at a Reynolds number of 100,000 (no wind tunnel corrections have been applied)

APPENDIX F

Front Panel of LabVIEW® Program used in Automated Airfoil Data Acquisition

The front panel of the LabVIEW® program used in the automated airfoil data acquisition has four tabs. The first tab contains instructions for using the program. The second tab contains all the data acquisition inputs as well as constants for calculating coefficients and Reynolds number. Additionally, the angle of attack can be input on this screen, and the nominal Reynolds numbers to be tested and their corresponding voltages are input on this screen, as seen in Figure F.1. Notably, the "INPUTS" tab also has some outputs on it, such as the measured atmospheric temperature, relative humidity and air density. Figure F.2 shows a screen shot of the third tab, which contains the measured and calculated outputs, such as voltage generated by the force balance and the corresponding forces and coefficients. Additionally, this tab has a few inputs, such as the time to wait for the tunnel to reach steady state as well as the slopes to use as the steady criteria. The fourth tab contains graphs of the freestream velocity, lift force, and drag force for steady state monitoring.

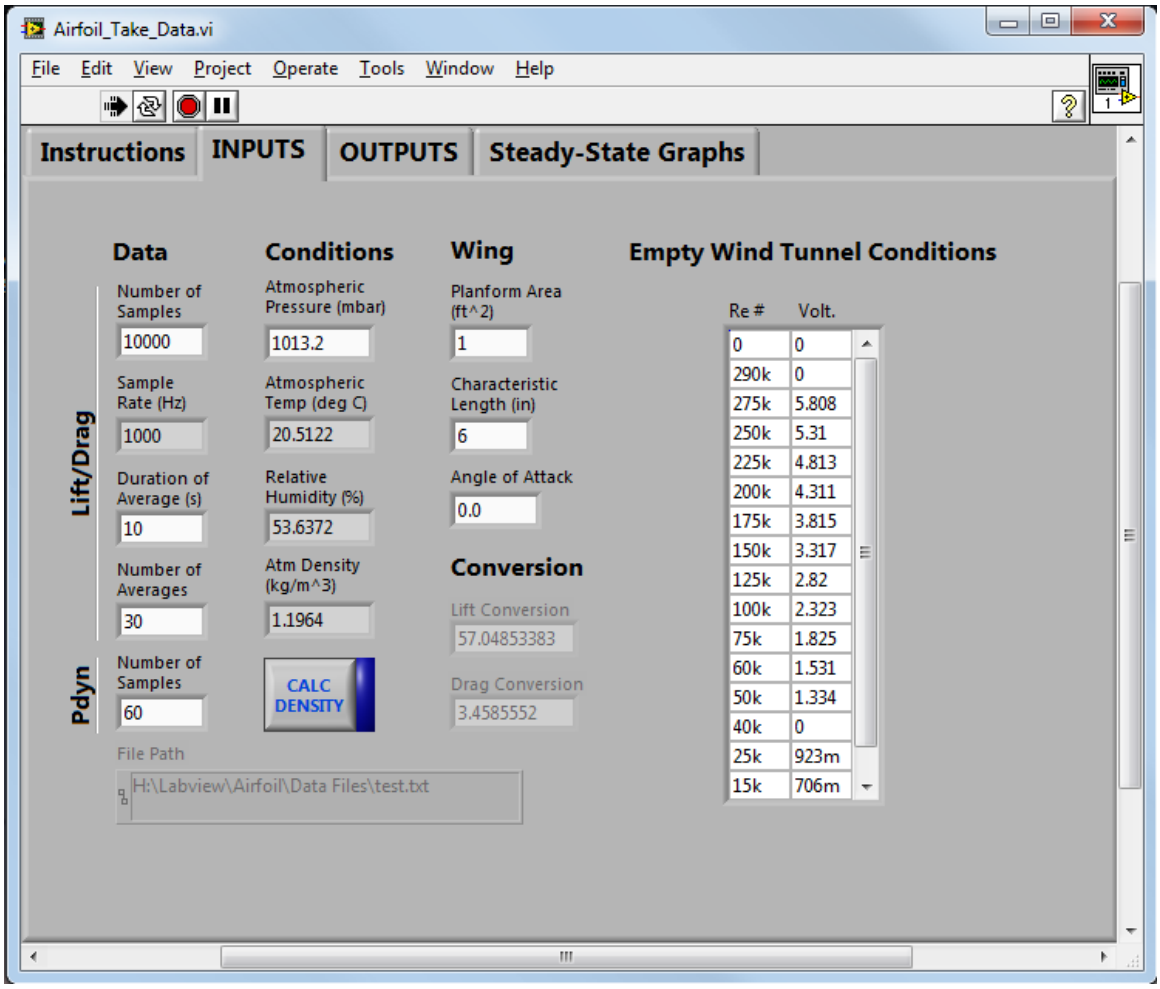

Figure F.1: “INPUTS” Tab of Automated Airfoil Data Acquisition Program

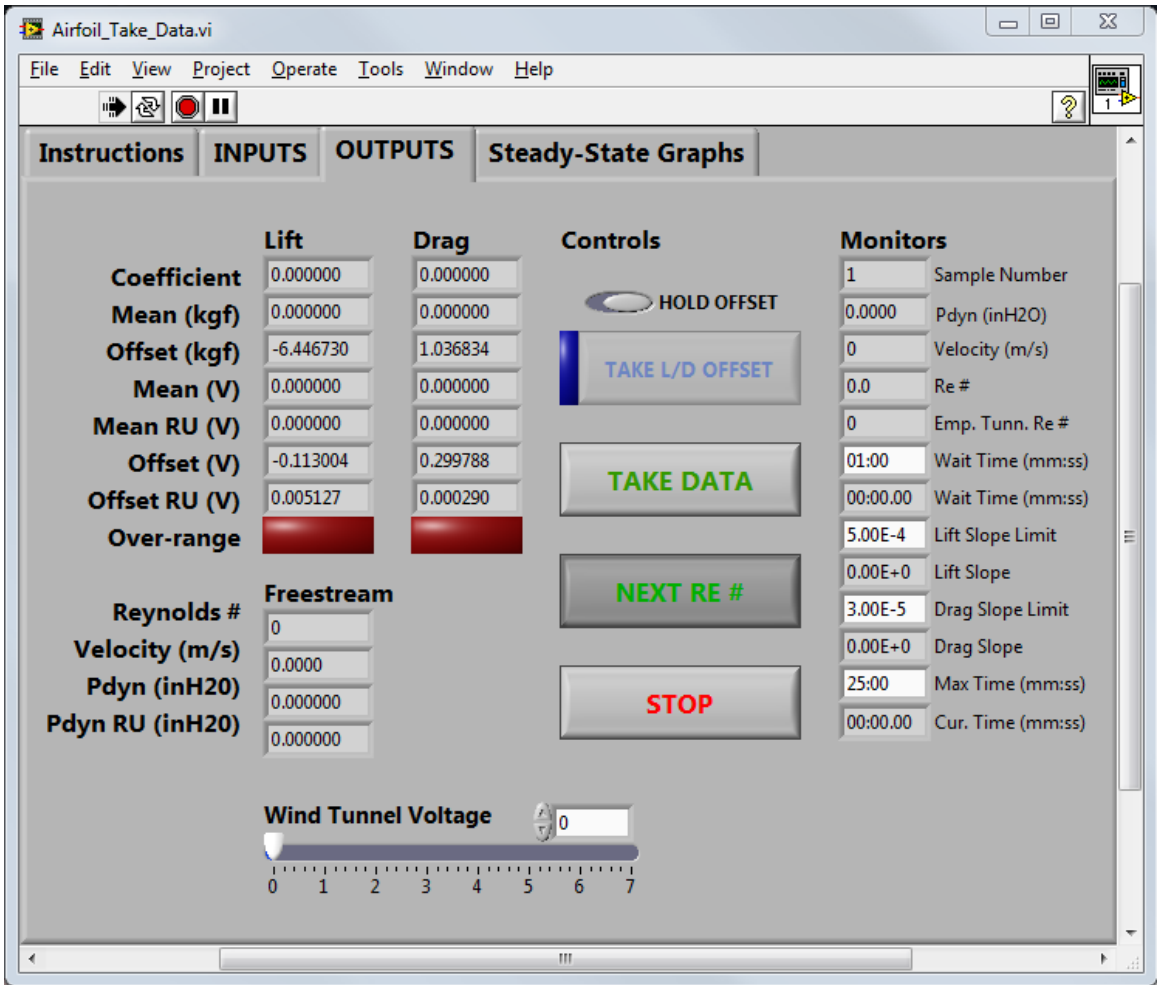

Figure F.2: “OUTPUTS” Tab of Automated Airfoil Data Acquisition Program

APPENDIX G

Sample Airfoil Data Reduction File

Mathcad® was used in calculating the experimental uncertainty in airfoil measurements as well as apply the wind tunnel corrections described in Chapter 2. Figure G.1 shows a sample uncertainty calculation for the S823 airfoil and a Reynolds number of 200,000, which was determined using the Kline and McClintock method [137]. Notably, the uncertainty calculations were performed before the wind tunnel corrections were applied, but the effect on the uncertainty estimation is minimal. Figure G.2 shows a sample calculation of wind tunnel corrections using the method described by Barlow et al. as mentioned previously [59].

Uncertainty Calculation

Function for Combining Random and Fixed Uncertainty Function

$$U_{tot}(n, var_{SD}, var_{fixed}) := \overrightarrow{\sqrt{\left(\frac{qt(.975, n-1)\cdot var_{SD}}{\sqrt{n}}\right)^2 + var_{fixed}^2}}$$

Velocity

$$U_{Pdyn} := U_{tot}(N_{Pdyn}, P_{dyn.SD}, P_{dyn.f})$$

$$U_{Vel} := \overrightarrow{\left(\frac{1}{\sqrt{2}\cdot\sqrt{P_{dyn}\cdot\rho}}\cdot U_{Pdyn}\right)}$$

Lift and Drag

Voltage

$$U_{V.L} := U_{tot}(N_{LD}, V_{L.SD}, V_{L.f})$$

$$U_{V.D} := U_{tot}(N_{LD}, V_{D.SD}, V_{L.f})$$

$$U_{Force}(V, m, U_V) := \overrightarrow{\sqrt{(V\cdot U_T(m))^2 + (m\cdot U_V)^2}}$$

$$U_L := U_{Force}(V_L, m_L, U_{V.L})$$

$$U_D := U_{Force}(V_D, m_D, U_{V.D})$$

Coefficients:

$$U_c(LD, U_{LD}, Vel, U_V) := \overrightarrow{\sqrt{\left(\frac{2}{\rho\cdot Vel^2\cdot A_p}\cdot U_{LD}\right)^2 + \left(\frac{-4\cdot LD}{\rho\cdot Vel^3\cdot A_p}\cdot U_V\right)^2}}$$

$$U_{c.l} := U_c(L, U_L, Vel, U_{Vel})$$

$$U_{c.d} := U_c(D, U_D, Vel, U_{Vel})$$

$i := 0$

$$\min\left(\overrightarrow{\frac{U_{c.l}^{\langle i\rangle}}{\left|c_l^{\langle i\rangle}\right|}}\right) = 1.165\cdot\% \qquad \min\left(\overrightarrow{\frac{U_{c.d}^{\langle i\rangle}}{c_d^{\langle i\rangle}}}\right) = 1.221\cdot\% \qquad \min\left(\overrightarrow{\frac{U_{Vel}^{\langle i\rangle}}{Vel^{\langle i\rangle}}}\right) = 0.562\cdot\%$$

$$\max\left(\overrightarrow{\frac{U_{c.l}^{\langle i\rangle}}{\left|c_l^{\langle i\rangle}\right|}}\right) = 3.147\cdot\% \qquad \max\left(\overrightarrow{\frac{U_{c.d}^{\langle i\rangle}}{c_d^{\langle i\rangle}}}\right) = 1.492\cdot\% \qquad \max\left(\overrightarrow{\frac{U_{Vel}^{\langle i\rangle}}{Vel^{\langle i\rangle}}}\right) = 0.603\cdot\%$$

Figure G.1: Uncertainty Analysis for S823 Smooth Airfoil Data at a Reynolds Number of 200,000

Wind Tunnel Corrections

Solid Blockage:

$K_1 := 0.74$

$M_v := (110.663 + 2.1 \cdot .75 \cdot 12)\text{in}^3$

$A_{ts} := (24\text{in})^2$

$$\varepsilon_{sb} := \frac{K_1 \cdot M_v}{A_{ts}^{\frac{3}{2}}} = 6.936 \times 10^{-3}$$

Wake Blockage:

$h_{ts} := 24\text{in}$

$$\varepsilon_{wb} := \left(\frac{c}{2 \cdot h_{ts}}\right) \cdot c_d$$

Streamline curvature:

$$\sigma := \frac{\pi^2}{48} \cdot \left(\frac{c}{h_{ts}}\right)^2$$

$nj := \text{rows}(c_d) = 42$ $\quad j := 0 .. nj - 1$

$nk := \text{cols}(c_d) = 6$ $\quad k := 0 .. nk - 1$

Barlow method:

$\varepsilon_b := \varepsilon_{sb} + \varepsilon_{wb}$

$\overrightarrow{Vel_c} := \overrightarrow{\left[Vel \cdot \left(1 + \varepsilon_b\right)\right]}$

$\overrightarrow{c_{l.c}} := \overrightarrow{\left[c_l \cdot \left(1 - \sigma - 2 \cdot \varepsilon_b\right)\right]}$

$\overrightarrow{c_{d.c_{j,k}}} := \overrightarrow{\left[\left(c_{d_{j,k}} - c_{d.tare_k}\right) \cdot \left(1 - 3 \cdot \varepsilon_{sb} - 2 \cdot \varepsilon_{wb_{j,k}}\right)\right]}$

$i := 0$

$$\min\left(\frac{\overrightarrow{c_l^{\langle i \rangle} - c_{l.c}^{\langle i \rangle}}}{c_l^{\langle i \rangle}}\right) = 3.311 \cdot \%$$

$$\min\left(\frac{\overrightarrow{c_d^{\langle i \rangle} - c_{d.tare_i} - c_{d.c}^{\langle i \rangle}}}{c_d^{\langle i \rangle} - c_{d.tare_i}}\right) = 2.719 \cdot \%$$

$$\min\left(\frac{\overrightarrow{Vel_c^{\langle i \rangle} - Vel^{\langle i \rangle}}}{Vel^{\langle i \rangle}}\right) = 1.013 \cdot \%$$

$$\max\left(\frac{\overrightarrow{c_l^{\langle i \rangle} - c_{l.c}^{\langle i \rangle}}}{c_l^{\langle i \rangle}}\right) = 8.823 \cdot \%$$

$$\max\left(\frac{\overrightarrow{c_d^{\langle i \rangle} - c_{d.tare_i} - c_{d.c}^{\langle i \rangle}}}{c_d^{\langle i \rangle} - c_{d.tare_i}}\right) = 8.232 \cdot \%$$

$$\max\left(\frac{\overrightarrow{Vel_c^{\langle i \rangle} - Vel^{\langle i \rangle}}}{Vel^{\langle i \rangle}}\right) = 3.769 \cdot \%$$

Figure G.2: Calculation of Wind Tunnel Corrections for S823 Smooth Airfoil Data at a Reynolds Number of 200,000

APPENDIX H

LabVIEW®-Controlled Decade Box

The LabVIEW®-controlled decade box in this work was developed in previous research at Baylor University. Figure H.1 shows a schematic of the system. The decade box utilized a Seeeduino Mega microcontroller to control relays which varied the resistance. Essentially, a number of resistors were connected in series and each resistor could be eliminated from the circuit by short circuiting it with a relay. In this way, any combination of the installed resistances could be achieved. The resistances used in the decade box were nominally 1, 2, 3, 4, 10, 20, 30, and 40 Ω. With these resistors any resistance between 0 and 100 Ω could be attained.

For this research, multiple modifications were necessary. The first issue was integration with the LabVIEW®. This was achieved by configuring one of the input pins on the microcontroller to monitor analog voltage. The microcontroller could then be programmed to receive an analog VDC signal from 0 to 5 V which linearly corresponded with a resistance from 0 to 99 Ω. The code resulting code, which is similar to C++, is contained on the following pages. The second issue was that the resistance was not consistent. High power thin film resistors were purchased and installed, however, the resistance of the unit was still not consistent. After troubleshooting the circuit, it was realized that the relays used in the circuit were not closing the contact consistently, and thus would add some resistance to the circuit. The added resistance would depend upon the how well the particular relay made the contact. The relays were replaced with the same model, but eventually other relays began to add an unpredictable resistance to the

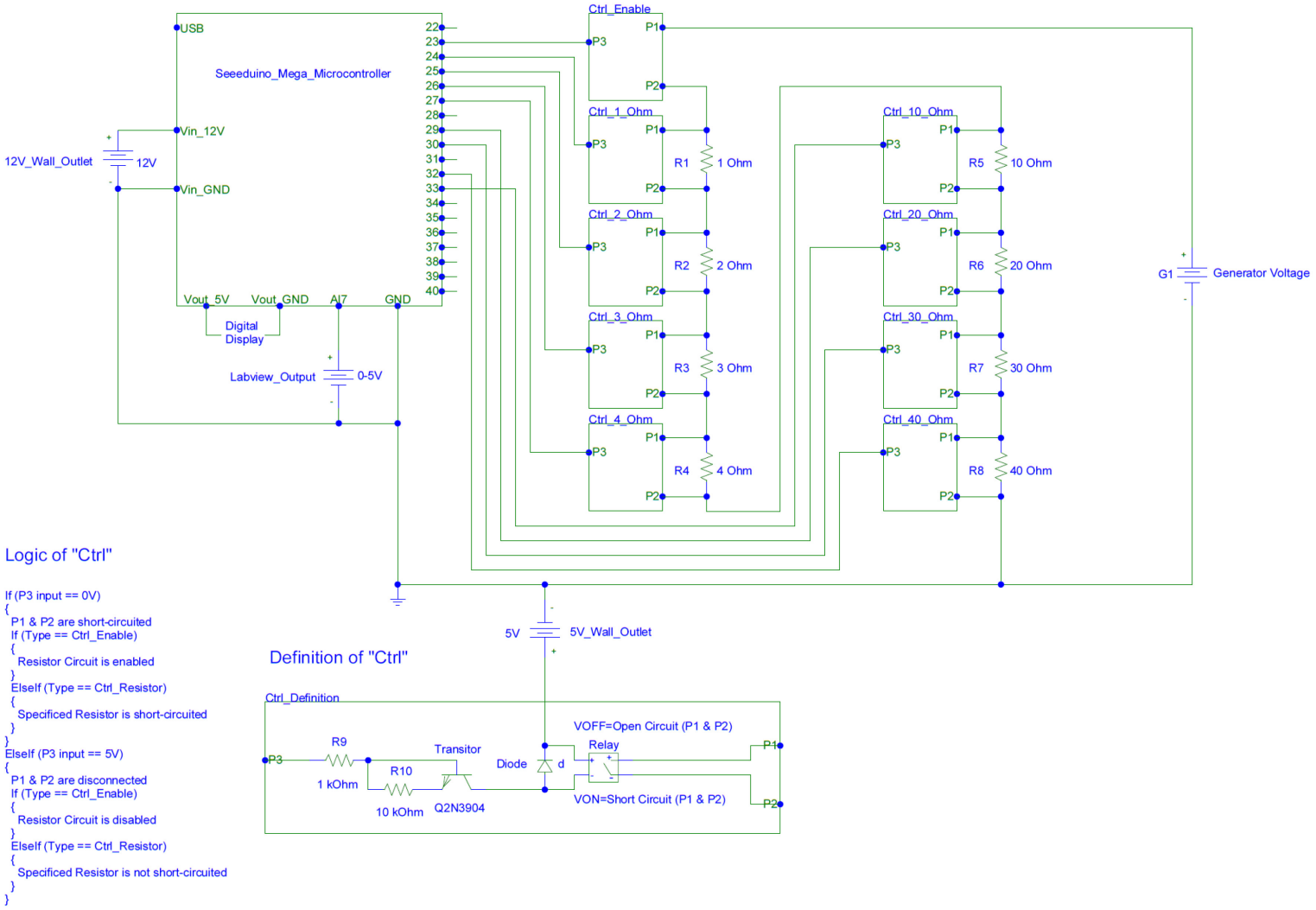

Figure H.1: Schematic of Custom-Designed Decade Box

circuit. The degradation of the relays may be due to the high current of the system, but this should not be the problem because the relays are rated for 30 Amps. The maximum current generated in the circuit was less than 3.33 Amps due to the limitations of the generator.

```
/*****************************************************/
/*****************Program Overview********************/
/*****************************************************/

// Program Algorithm:
// - Setup all constants and hardware
// - Measure voltage from Labview (0-5V)
// - Determine resistance based on voltage signal
// Note: Resistance will be an integer from 0 to 100
// - Change resistance to determined value
// - Measure voltage from Labview
// - Change resistance if different


/*****************************************************/
/*************Resistance Determination***************/
/*****************************************************/

const int NUM_SAMPLES = 50;     // number of samples of voltage
measurements
const int VOLT_DURATION = 500;  // duration of voltage measurement (ms)
const int RSCAL = 100;          // used in converting labview voltage
to resistance


/*****************************************************/
/*******************Pin Assignments*******************/
/*****************************************************/
// Note: changing this code requires changing hardware
// Note: pins 0 and 1 are reserved for serial communication

const int  _1_OHM = 24;
const int  _2_OHM = 25;
const int  _3_OHM = 26;
const int  _4_OHM = 27;
const int _10_OHM = 33;
const int _20_OHM = 29;
const int _30_OHM = 30;
const int _40_OHM = 32;
const int ENABLE  = 23;  // enable relay pin
const int AI_VOLT =  7;  // voltage measurement pin


/*****************************************************/
/*****************Hardware Constants******************/
/*****************************************************/
```

```
const int ON    = 1;    // enable control
const int OFF   = 0;    // disable control
const int R_ON  = LOW;  // resistance control
const int R_OFF = HIGH; // resistance control
const int RMAX  = 110;  // max resistance possible with resistor box

// Resistance values, obtained by measuring the resistance at the
generator
// ground/voltage, and then subtracting out the short circuit
resistance (.65 Ohms).

const double  _0_Ohm_rActual = 0.369;
const double  _1_Ohm_rActual = 0.966;
const double  _2_Ohm_rActual = 1.974;
const double  _3_Ohm_rActual = 2.966;
const double  _4_Ohm_rActual = 3.979;
const double _10_Ohm_rActual = 9.974;
const double _20_Ohm_rActual = 19.968;
const double _30_Ohm_rActual = 29.944;
const double _40_Ohm_rActual = 39.985;


/*****************************************************/
/***************Function Declarations*****************/
/*****************************************************/

void   setEnable  ( int    ); // sets enable relay (enabling
resistances)
double setR       ( double ); // input nominal resistance, set
resistance, output actual resistance
double getR       (        ); // measures voltage


/*****************************************************/
/***************Board Initialization******************/
/*****************************************************/

void setup()
{

  // defining pin mode as output
  pinMode( _1_OHM,OUTPUT);
  pinMode( _2_OHM,OUTPUT);
  pinMode( _3_OHM,OUTPUT);
  pinMode( _4_OHM,OUTPUT);
  pinMode(_10_OHM,OUTPUT);
  pinMode(_20_OHM,OUTPUT);
  pinMode(_30_OHM,OUTPUT);
  pinMode(_40_OHM,OUTPUT);
  pinMode( ENABLE,OUTPUT);

  // turning off resistor circuit relay
  setEnable(OFF);
  delay(20);

  // turning on individual resistor relays
```

```
  digitalWrite( _1_OHM,R_ON);
  digitalWrite( _2_OHM,R_ON);
  digitalWrite( _3_OHM,R_ON);
  digitalWrite( _4_OHM,R_ON);
  digitalWrite(_10_OHM,R_ON);
  digitalWrite(_20_OHM,R_ON);
  digitalWrite(_30_OHM,R_ON);
  digitalWrite(_40_OHM,R_ON);

  // turn on serial communication to LCD
  Serial2.begin(9600);
  Serial.begin(9600);
  delay(100);
  // turn display off
  Serial2.print(0xFE, BYTE);  //command flag
  Serial2.print(0x08, BYTE);
  delay(100);
  // clear screen
  Serial2.print(0xFE,BYTE);
  Serial2.print(0x01,BYTE);
  delay(100);
  // turn display on
  Serial2.print(0xFE,BYTE);
  Serial2.print(0x0C,BYTE);
  delay(100);
  // move to first line and print
  Serial2.print(0xFE,BYTE);
  Serial2.print(128,BYTE);
  Serial2.print("Resistance");
  // move to second line and print
  Serial2.print(0xFE, BYTE);
  Serial2.print(192, BYTE);
  Serial2.print("Controller");
  delay(2000);

}


/*****************************************************/
/******************Main Program Loop*****************/
/*****************************************************/

// initializing variables
int r_old = RMAX;
int r;
double actualR;

void loop()
{

  // measure voltage and convert to resistance value
  r = getR();

  if (r == r_old)
  {
    // do nothing
  }else
```

```
  {
    // check next resistance
    delay(100);
    r = getR();

    // set next resistance
    actualR = setR(r);

    // clear screen
    Serial2.print(0xFE,BYTE);
    Serial2.print(0x01,BYTE);
    delay(100);
    // move to first line and print
    Serial2.print(0xFE,BYTE);
    Serial2.print(128,BYTE);
    Serial2.print("R (nom) = ");
    Serial2.print(r);
    // move to second line and print
    Serial2.print(0xFE, BYTE);
    Serial2.print(192, BYTE);
    Serial2.print("R (act) = ");
    Serial2.print(actualR,3);
  }

  r_old = r;

}



/*****************************************************/
/*******************Functions*************************/
/*****************************************************/


/******************setEnable************************/
/*This function sets the enable relay to high or low*/

void setEnable(int e)
{
  if (e == ON)
  {
    digitalWrite(ENABLE,HIGH);
  }else
  if (e == OFF)
  {
    digitalWrite(ENABLE,LOW);
  }
}


/******************getR************************/
/*This function measures the voltage off analog pin 7 and returns
desired resistance*/

double getR()
{
```

```
  double v    = 0; // stores voltage measurement
  double nd_v = 0; // non-dimensional voltage
  int    r    = 0; // stores resistance (0-5 V correlates to 0-100
Ohms)

  analogReference(DEFAULT);  // sets reference voltage to 5V, more info
online
  delay(10);

  // sums voltage reading, average is taken later
  for (int i = 0; i < NUM_SAMPLES; i++)
  {
    v += analogRead(AI_VOLT);
    delay(VOLT_DURATION/NUM_SAMPLES);
  }

  v    = v/NUM_SAMPLES; // average voltage
  nd_v = v/1023.0;      // changes from 0 - 1023 (which correlates to 0
- 5V) to 0 - 1
  //v    = nd_v*5;      // only necessary if you want to print out
measured voltage

  r = nd_v*RSCAL+0.5; // adding 0.5 changes from trunication to
rounding
  r += -1; // this accounts for the fact that 0.00 V is an open
circuit, and 0.05 V is a short circuit (0 Ohms)

  return r;

}


/*****************setShort************************/
/*This function turns off every relay and shorts out every resistor*/

double setShort()
{
  digitalWrite( _1_OHM,R_OFF);
  digitalWrite( _2_OHM,R_OFF);
  digitalWrite( _3_OHM,R_OFF);
  digitalWrite( _4_OHM,R_OFF);
  digitalWrite(_10_OHM,R_OFF);
  digitalWrite(_20_OHM,R_OFF);
  digitalWrite(_30_OHM,R_OFF);
  digitalWrite(_40_OHM,R_OFF);
}


/*****************setR************************/
/*This function turns on  hardware resistance and calculates actual
resistance*/

double setR( double r)
{

  int ones = 0;
```

```
  int tens = 0;
  double rActual = _0_Ohm_rActual; // initial value is short circuit
resistance

  ones = (int)r%10;
  tens = (int)r%100 - ones;

  setEnable(OFF); //
  setShort();     // Set all resistances off before you can set them
on.

  if( (r < 0) || (r > RMAX) )
  {
    // set to open circuit
    // this case occurs if r = -1
    // since the enable relay is not turned on, this stays an open
circuit
    rActual = -1;
  }
  else
  {

    /*This sets the ones place*/
    if(ones == 0)
    {
    }else
    if(ones == 1)
    {
      digitalWrite(_1_OHM, R_ON);
      rActual += _1_Ohm_rActual;
    }else
    if(ones == 2)
    {
      digitalWrite(_2_OHM, R_ON);
      rActual += _2_Ohm_rActual;
    }else
    if(ones == 3)
    {
      digitalWrite(_3_OHM, R_ON);
      rActual += _3_Ohm_rActual;
    }else
    if(ones == 4)
    {
      digitalWrite(_4_OHM, R_ON);
      rActual += _4_Ohm_rActual;
    }else
    if(ones == 5)
    {
      digitalWrite(_4_OHM, R_ON);
      rActual += _4_Ohm_rActual;
      digitalWrite(_1_OHM, R_ON);
      rActual += _1_Ohm_rActual;
    }else
    if(ones == 6)
    {
      digitalWrite(_4_OHM, R_ON);
      rActual += _4_Ohm_rActual;
```

```
  digitalWrite(_2_OHM, R_ON);
  rActual += _2_Ohm_rActual;
}else
if(ones == 7)
{
  digitalWrite(_4_OHM, R_ON);
  rActual += _4_Ohm_rActual;
  digitalWrite(_3_OHM, R_ON);
  rActual += _3_Ohm_rActual;
}else
if(ones == 8)
{
  digitalWrite(_4_OHM, R_ON);
  rActual += _4_Ohm_rActual;
  digitalWrite(_3_OHM, R_ON);
  rActual += _3_Ohm_rActual;
  digitalWrite(_1_OHM, R_ON);
  rActual += _1_Ohm_rActual;
}else
if(ones == 9)
{
  digitalWrite(_4_OHM, R_ON);
  rActual += _4_Ohm_rActual;
  digitalWrite(_3_OHM, R_ON);
  rActual += _3_Ohm_rActual;
  digitalWrite(_2_OHM, R_ON);
  rActual += _2_Ohm_rActual;
}

/*This sets the ten place*/
if(tens == 0)
{
}else
if(tens == 10)
{
  digitalWrite(_10_OHM, R_ON);
  rActual += _10_Ohm_rActual;
}else
if(tens == 20)
{
  digitalWrite(_20_OHM, R_ON);
  rActual += _20_Ohm_rActual;
}else
if(tens == 30)
{
  digitalWrite(_30_OHM, R_ON);
  rActual += _30_Ohm_rActual;
}else
if(tens == 40)
{
  digitalWrite(_40_OHM, R_ON);
  rActual += _40_Ohm_rActual;
}else
if(tens == 50)
{
  digitalWrite(_40_OHM, R_ON);
  rActual += _40_Ohm_rActual;
```

```
      digitalWrite(_10_OHM, R_ON);
      rActual += _10_Ohm_rActual;
    }else
    if(tens == 60)
    {
      digitalWrite(_40_OHM, R_ON);
      rActual += _40_Ohm_rActual;
      digitalWrite(_20_OHM, R_ON);
      rActual += _20_Ohm_rActual;
    }else
    if(tens == 70)
    {
      digitalWrite(_40_OHM, R_ON);
      rActual += _40_Ohm_rActual;
      digitalWrite(_30_OHM, R_ON);
      rActual += _30_Ohm_rActual;
    }else
    if(tens == 80)
    {
      digitalWrite(_40_OHM, R_ON);
      rActual += _40_Ohm_rActual;
      digitalWrite(_30_OHM, R_ON);
      rActual += _30_Ohm_rActual;
      digitalWrite(_10_OHM, R_ON);
      rActual += _10_Ohm_rActual;
    }else
    if(tens == 90)
    {
      digitalWrite(_40_OHM, R_ON);
      rActual += _40_Ohm_rActual;
      digitalWrite(_30_OHM, R_ON);
      rActual += _30_Ohm_rActual;
      digitalWrite(_20_OHM, R_ON);
      rActual += _20_Ohm_rActual;
    }

    if(r == 100)
    {
      digitalWrite(_40_OHM, R_ON);
      rActual += _40_Ohm_rActual;
      digitalWrite(_30_OHM, R_ON);
      rActual += _30_Ohm_rActual;
      digitalWrite(_20_OHM, R_ON);
      rActual += _20_Ohm_rActual;
      digitalWrite(_10_OHM, R_ON);
      rActual += _10_Ohm_rActual;
    }

    delay(100);
    setEnable(ON);

  }

  return rActual;

}
```

APPENDIX I

Front Panel of LabVIEW® Program used in Automated Wind Turbine Data Acquisition

For the automated wind turbine program in LabVIEW®, the user interface was divided into three tabs. The first contained most of the inputs as well as a number of outputs. These are all discussed in Chapter 3. A screenshot of this tab can be seen in Figure I.1. The second tab contained most of the outputs, as well as a graph for steady-state monitoring. Finally, the final tab contained multiple graphs for in-situ monitoring.

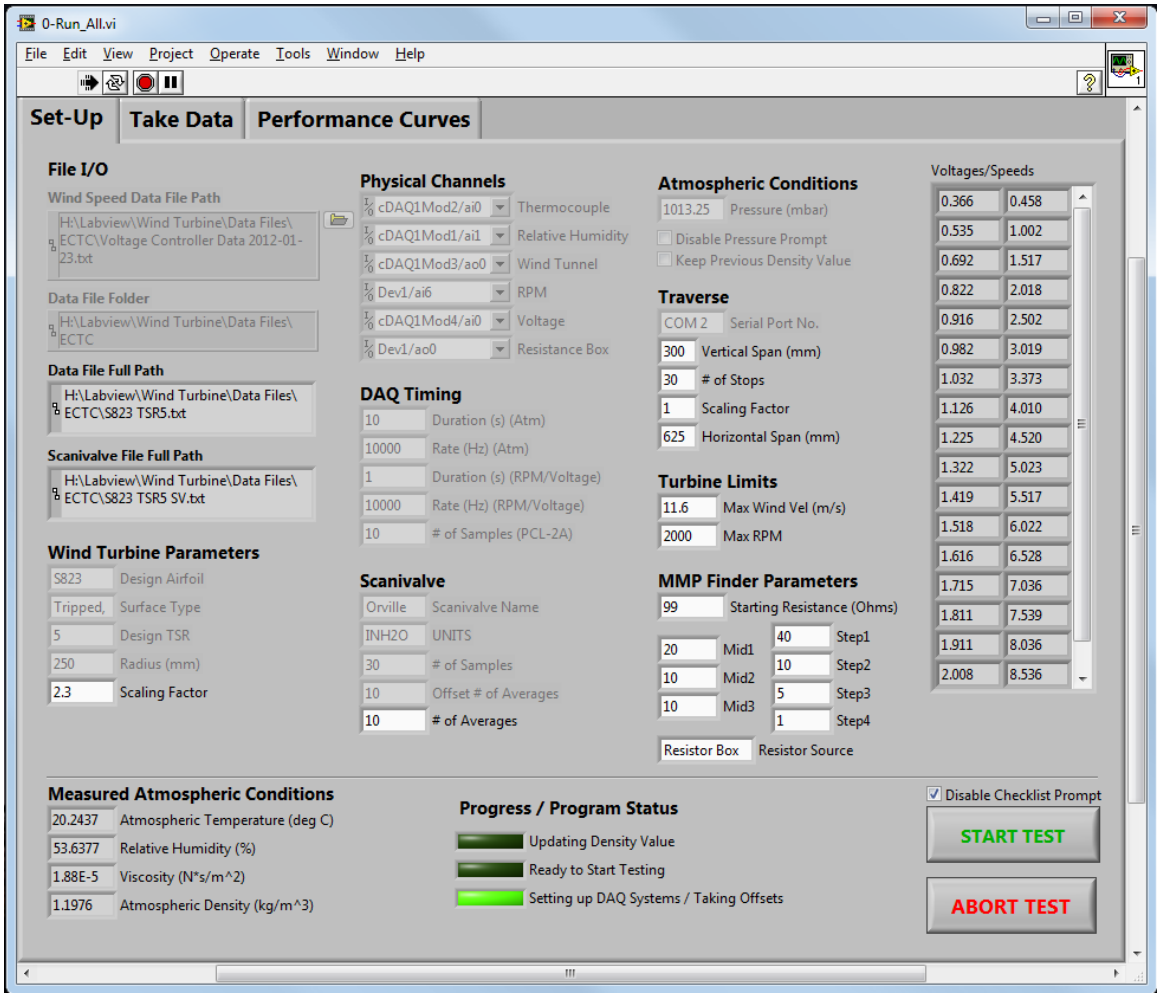

Figure I.1: "Set-Up" Tab of Automated Wind Turbine Data Acquisition Program

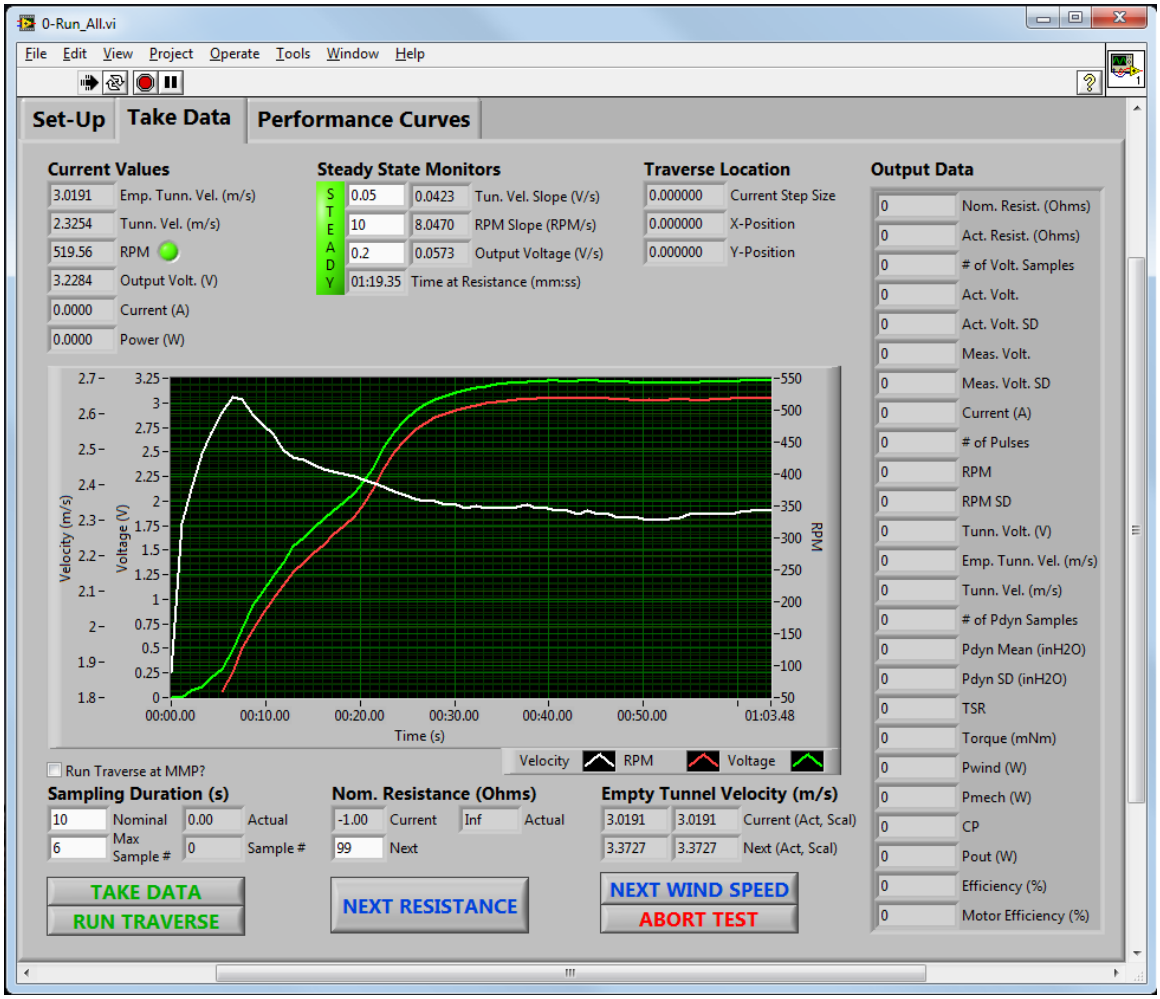

Figure I.2: “Take Data” Tab of Automated Wind Turbine Data Acquisition Program

APPENDIX J

Sample Wind Turbine Data Reduction File

The following pages include sample calculations performed in Mathcad® for analyzing the wind turbine data. The first two pages contain a derivation of the scaling factor for different parameters, but specifically arriving at the scaling factor for the resistance. The following page shows the general data processing and reduction performed on all the wind turbine data to average out the samples taken. The next page shows a sample calculation of the blockage factor at the maximum power point and unloaded conditions. The remaining four pages are a sample of the uncertainty calculations performed for the medium-sized turbine in the scaling study.

Determining the scaling factor for Resistance Measurements

$sc = \frac{Rad_{sc}}{Rad}$ sc is the geometric scaling factor or $Rad_{sc} = Rad \cdot sc$

$sc = \frac{c_{sc}}{c}$ and the chord of the wind turbine is scaled by it

Since Reynolds number must be kept the same and the fluid for both tests will be the same, we can determine velocity scaling based on geometric scaling

$\rho_{sc} = \rho$ $\mu_{sc} = \mu$ $c_{sc} = c \cdot sc$

$$\frac{Re_{sc}}{Re} = 1 = \frac{\left(\frac{\rho_{sc} \cdot U_{sc} \cdot c_{sc}}{\mu_{sc}}\right)}{\left(\frac{\rho \cdot U \cdot c}{\mu}\right)} = \frac{U_{sc} \cdot c_{sc}}{U \cdot c} = \frac{U_{sc} \cdot (c \cdot sc)}{U \cdot c} = \frac{U_{sc} \cdot sc}{U}$$

Rearranging yields:

$\frac{U_{sc}}{U} = \frac{1}{sc}$ or $U = U_{sc} \cdot sc$

For the turbines to be alike, the TSR must also be kept the same

$$\frac{TSR_{sc}}{TSR} = 1 = \frac{\left(\frac{\Omega_{sc} \cdot Rad_{sc}}{U_{sc}}\right)}{\left(\frac{\Omega \cdot Rad}{U}\right)} = \frac{\left[\frac{\Omega_{sc} \cdot (Rad \cdot sc)}{U_{sc}}\right]}{\left(\frac{\Omega \cdot Rad}{U_{sc} \cdot sc}\right)} = \frac{\left(\Omega_{sc} \cdot sc\right)}{\left(\frac{\Omega}{sc}\right)} = \frac{\Omega_{sc}}{\Omega} \cdot sc^2$$

Rearranging yields:

$\frac{\Omega_{sc}}{\Omega} = \frac{1}{sc^2}$ or $\Omega = \Omega_{sc} \cdot sc^2$

Analyzing the power available in the wind:

$$\frac{Pwind_{sc}}{Pwind} = \frac{\left(\frac{1}{2} \cdot \rho_{sc} \cdot \pi \cdot Rad_{sc}^2 \cdot U_{sc}^3\right)}{\left(\frac{1}{2} \cdot \rho \cdot \pi \cdot Rad^2 \cdot U^3\right)} = \frac{\left(Rad_{sc}^2 \cdot U_{sc}^3\right)}{\left(Rad^2 \cdot U^3\right)} = \frac{\left[(Rad \cdot sc)^2 \cdot U_{sc}^3\right]}{\left[Rad^2 \cdot \left(U_{sc} \cdot sc\right)^3\right]} = \frac{sc^2}{sc^3} = \frac{1}{sc}$$

So,

$\frac{Pwind_{sc}}{Pwind} = \frac{1}{sc}$ or $Pwind = Pwind_{sc} \cdot sc$

Since

$CP_{sc} = CP$

for a geometrically scaled rotor operating under like flow conditions

$$\frac{Protor_{sc}}{Protor} = \frac{1}{sc} \quad \text{or} \quad Protor = Protor_{sc} \cdot sc$$

Analyzing the rotor power:

$$\frac{Protor_{sc}}{Protor} = \frac{1}{sc} = \frac{(\tau_{sc} \cdot \Omega_{sc})}{(\tau \cdot \Omega)} = \frac{(\tau_{sc} \cdot \Omega_{sc})}{\left[\tau \cdot \left(\Omega_{sc} \cdot sc^2\right)\right]} = \frac{(\tau_{sc})}{\left[\tau \cdot \left(sc^2\right)\right]}$$

Rearranging yields:

$$\frac{\tau_{sc}}{\tau} = sc \quad \text{or} \quad \tau_{sc} = \tau \cdot sc$$

For a DC motor, torque is proportional to current, thus:

$$\frac{I_{sc}}{I} = sc \quad \text{or} \quad I_{sc} = I \cdot sc$$

Analyzing the electrical power output of the turbine:

$$\frac{Protor_{sc}}{Protor} = \frac{1}{sc} = \frac{Pelec_{sc} \cdot \eta sys_{sc}}{Pelec \cdot \eta sys}$$

Note: $\eta sys_{sc} \neq \eta sys$

Rearranging and apply:

$$\frac{P_{sc}}{P} = \frac{\eta sys}{\eta sys_{sc}} \cdot \frac{1}{sc} = \frac{I_{sc}^2 \cdot R_{sc}}{I^2 \cdot R} = \frac{(I \cdot sc)^2 \cdot R_{sc}}{I^2 \cdot R} = \frac{sc^2 \cdot R_{sc}}{R}$$

Rearranging yields:

$$\frac{R_{sc}}{R} = \frac{\eta sys}{\eta sys_{sc}} \cdot \frac{1}{sc^3} \quad \text{or} \quad R_{sc} \cdot \eta sys_{sc} \cdot sc^3 = R \cdot \eta sys$$

Data Processing

$n := 6 \qquad sc_L := 1 \qquad sc_M := 0.8 \qquad sc_S := 0.6$

$$AVG(param, n) := \left| \begin{array}{l} k \leftarrow 0 \\ \text{for } i \in 1..\left(\frac{\text{length}(param)}{n} - 1\right) \\ \quad \left| \begin{array}{l} j \leftarrow i \cdot n..(i \cdot n + n - 1) \\ param_{ave_k} \leftarrow \frac{\sum_j param_j}{n} \\ k \leftarrow k + 1 \end{array} \right. \\ param_{ave} \end{array} \right.$$

$$proc\_data(data, sc) := \left| \begin{array}{l} \text{for } j \in 0..(\text{rows}(data) - 1) \\ \quad \left| \begin{array}{l} CP_j \leftarrow AVG\left[\left(data_j\right)^{\langle 21 \rangle}, n\right] \\ TSR_j \leftarrow AVG\left[\left(data_j\right)^{\langle 17 \rangle}, n\right] \\ R_j \leftarrow AVG\left[\left(data_j\right)^{\langle 1 \rangle}, n\right] \\ \eta mot_j \leftarrow AVG\left[\left(data_j\right)^{\langle 24 \rangle}\ \%, n\right] \\ R_{sc_j} \leftarrow \overrightarrow{\left(R_j \cdot sc^3 \cdot \eta mot_j\right)} \end{array} \right. \\ \left(CP \quad TSR \quad R_{sc} \quad R\right) \end{array} \right.$$

$LA := proc\_data(Large, sc_L)$

$MA := proc\_data(Med, sc_M)$

$SA := proc\_data(Small, sc_S)$

$$TSR_{unloaded}(data) := \left| \begin{array}{l} \text{for } k \in 0..(\text{rows}(data) - 1) \\ \quad \left| \begin{array}{l} j \leftarrow 0..n - 1 \\ TSR_k \leftarrow \frac{\sum_j \left[\left(data_k\right)^{\langle 17 \rangle}\right]_j}{n} \end{array} \right. \\ TSR \end{array} \right.$$

$TSR_{LU} := TSR_{unloaded}(Large)$

$TSR_{MU} := TSR_{unloaded}(Med)$

$TSR_{SU} := TSR_{unloaded}(Small)$

Blockage Factor Calculation

$$BF_{data}(data, index) := \left| \begin{array}{l} \text{for } k \in 0..(\text{rows}(data) - 1) \\ \quad \left| \begin{array}{l} j \leftarrow 0..n-1 \\ U_{k,0} \leftarrow \dfrac{\sum_j \left[\left(data_k \right)^{\langle 12 \rangle} \right]_j}{n} \\ UM_{k,0} \leftarrow \dfrac{\sum_j \left[\left(data_k \right)^{\langle 13 \rangle} \right]_j}{n} \\ BF_{k,0} \leftarrow \dfrac{UM_{k,0}}{U_{k,0}} \\ U_{dummy_k} \leftarrow AVG\left[\left(data_k \right)^{\langle 12 \rangle}, n \right] \\ U_{k,1} \leftarrow \left(U_{dummy_k} \right)_{\left(index_k \right)} \\ UM.dummy_k \leftarrow AVG\left[\left(data_k \right)^{\langle 13 \rangle}, n \right] \\ UM_{k,1} \leftarrow \left(UM.dummy_k \right)_{\left(index_k \right)} \\ BF_{k,1} \leftarrow \dfrac{UM_{k,1}}{U_{k,1}} \end{array} \right. \\ BF \end{array} \right.$$

$$BF_L := BF_{data}\left(Large, i_L\right)$$

$$BF_M := BF_{data}\left(Med, i_M\right)$$

$$BF_S := BF_{data}\left(Small, i_S\right)$$

Uncertainty Calculations

Calculate the partial derivatives of wind speed:

$$U := \sqrt{\frac{Pdyn}{\frac{1}{2}\rho}}$$

$$dUd\rho(\rho, Pdyn) := \frac{d}{d\rho}U \rightarrow -\frac{\sqrt{2}\cdot Pdyn}{2\cdot\rho^2\cdot\sqrt{\frac{Pdyn}{\rho}}}$$

$$dUdPdyn(\rho, Pdyn) := \frac{d}{dPdyn}U \rightarrow \frac{\sqrt{2}}{2\cdot\rho\cdot\sqrt{\frac{Pdyn}{\rho}}}$$

$$U := U$$

Calculate the partial derivatives of torque

$$\tau := \frac{V}{R}\cdot k_\tau$$

$$d\tau dV\left(V, R, k_\tau\right) := \frac{d}{dV}\tau \rightarrow \frac{k_\tau}{R}$$

$$d\tau dR\left(V, R, k_\tau\right) := \frac{d}{dR}\tau \rightarrow -\frac{V\cdot k_\tau}{R^2}$$

$$d\tau dk_\tau\left(V, R, k_\tau\right) := \frac{d}{dk_\tau}\tau \rightarrow \frac{V}{R}$$

$$\tau := \tau$$

Calculate the partial derivative of the tip speed ratio:

$$TSR := \frac{\Omega\cdot R}{U}$$

$$dTSRd\Omega(\Omega, R, U) := \frac{d}{d\Omega}TSR \rightarrow \frac{R}{U}$$

$$dTSRdR(\Omega, R, U) := \frac{d}{dR}TSR \rightarrow \frac{\Omega}{U}$$

$$dTSRdU(\Omega, R, U) := \frac{d}{dU}TSR \rightarrow -\frac{R\cdot\Omega}{U^2}$$

$$TSR := TSR$$

Calculate the partial derivatives of the coefficient of power:

$$CP := \frac{\tau\cdot\Omega}{\frac{1}{2}\rho\cdot\pi\cdot R^2\cdot U^3}$$

$$dCPd\tau(\tau, \Omega, \rho, R, U) := \frac{d}{d\tau}CP \rightarrow \frac{2\cdot\Omega}{\pi\cdot R^2\cdot U^3\cdot\rho}$$

$$dCPd\Omega(\tau, \Omega, \rho, R, U) := \frac{d}{d\Omega}CP \rightarrow \frac{2\cdot\tau}{\pi\cdot R^2\cdot U^3\cdot\rho}$$

$$dCPd\rho(\tau, \Omega, \rho, R, U) := \frac{d}{d\rho}CP \rightarrow -\frac{2\cdot\tau\cdot\Omega}{\pi\cdot R^2\cdot U^3\cdot\rho^2}$$

$$dCPdR(\tau, \Omega, \rho, R, U) := \frac{d}{dR}CP \rightarrow -\frac{4\cdot\tau\cdot\Omega}{\pi\cdot R^3\cdot U^3\cdot\rho}$$

$$dCPdU(\tau, \Omega, \rho, R, U) := \frac{d}{dU}CP \rightarrow -\frac{6\cdot\tau\cdot\Omega}{\pi\cdot R^2\cdot U^4\cdot\rho}$$

$$CP := CP$$

Fixed uncertainties

$\rho_f := 0.02 \frac{kg}{m^3}$ assumed

$Pdyn_f := 2 \cdot 0.07\% \, inH2O$

$V_f := 0.003925V$ not sure...

$R_f := 5\%$

$k_{\tau.f} := 1\% \cdot 60.3 \frac{mNm}{A}$ assumed

$\Omega_f := 0$ assumed

defining constants

$inH2O := 0.249088908333kPa$

$mNm := N \cdot 10^{-3} \cdot m$

$k_\tau := 60.3 \frac{mNm}{A}$

Functions

$$STAT(param, n) := \left| \begin{array}{l} \text{for } i \in 1..\left(\frac{length(param)}{n} - 1\right) \\ \quad \left| \begin{array}{l} start \leftarrow i \cdot n \\ \text{for } j \in [start..\, start + (n-1)] \\ \quad dummy_{j-start} \leftarrow param_j \\ param_{ave_{i-1}} \leftarrow mean(dummy) \\ param_{stdev_{i-1}} \leftarrow stdev(dummy) \end{array} \right. \\ augment\left(param_{ave}, param_{stdev}\right) \end{array} \right.$$

$$proc\_data(data, n) := \left| \begin{array}{l} \text{for } i \in 0..\,(rows(data) - 1) \\ \quad \left| \begin{array}{l} R_i \leftarrow STAT\left[\left(data_i\right)^{\langle 1 \rangle}, n\right] \\ V_i \leftarrow STAT\left[\left(data_i\right)^{\langle 3 \rangle}, n\right] \\ RPM_i \leftarrow STAT\left[\left(data_i\right)^{\langle 9 \rangle}, n\right] \\ TSR_i \leftarrow STAT\left[\left(data_i\right)^{\langle 17 \rangle}, n\right] \\ \tau_i \leftarrow STAT\left[\left(data_i\right)^{\langle 18 \rangle}, n\right] \\ CP_i \leftarrow STAT\left[\left(data_i\right)^{\langle 21 \rangle}, n\right] \end{array} \right. \\ augment(R, V, RPM, TSR, \tau, CP) \end{array} \right.$$

$Pdyn_L := Data_{Vel.L} \cdot inH2O$ $Pdyn_M := Data_{Vel.M} \cdot inH2O$ $Pdyn_S := Data_{Vel.S} \cdot inH2O$

$n := 6$

$Data_L := Large$ $Data_M := Med$ $Data_S := Small$

$Large := proc\_data(Large, n)$ $Med := proc\_data(Med, n)$ $Small := proc\_data(Small, n)$

Other Definitions

$$U_{tot}(n, var_{SD}, var_{fixed}) := \sqrt{\left(\frac{qt(.975, n-1) \cdot var_{SD}}{\sqrt{n}}\right)^2 + var_{fixed}^2}$$

$$U(\rho, Pdyn) := \sqrt{\frac{Pdyn}{\frac{1}{2}\rho}}$$

$Rad := 250mm$

Medium Rotor Uncertainty Analysis

$$U(\rho, Pdyn) := \overrightarrow{\sqrt{\frac{Pdyn}{\frac{1}{2}\rho}}}$$

$i := 0$

$\rho := \rho_M$

$Pdyn := Pdyn_M$

$U := U\left(\rho, Pdyn^{\langle 0 \rangle}\right)$

$R := \left(Med^{\langle 0 \rangle}\right)_i \cdot ohm$

$Volt := \left(Med^{\langle 1 \rangle}\right)_i \cdot V$

$\tau := \left(Med^{\langle 4 \rangle}\right)_i mNm$

$\Omega := \left(Med^{\langle 2 \rangle}\right)_i \cdot rpm$

$TSR := \left(Med^{\langle 3 \rangle}\right)_i$

$CP := \left(Med^{\langle 5 \rangle}\right)_i$

Velocity

$U_{Pdyn} := U_{tot}\left(n, Pdyn^{\langle 1 \rangle}, Pdyn_f\right)$

$U_\rho := U_{tot}\left(100, 0, \rho_f\right) = 0.02 \frac{kg}{m^3}$

$$U_U := \frac{\overrightarrow{\sqrt{\left(dUdPdyn\left(\rho, Pdyn^{\langle 0 \rangle}\right) \cdot U_{Pdyn}\right)^2 ... + \left(dUd\rho\left(\rho, Pdyn^{\langle 0 \rangle}\right) \cdot U_\rho\right)^2}}}{U}$$

Torque

$U_R := R_f \cdot R^{\langle 0 \rangle}$

$U_V := U_{tot}\left(n, Volt^{\langle 1 \rangle}, V_f\right)$

$U_{k.\tau} := k_{\tau.f}$

$$U_\tau := \frac{\overrightarrow{\sqrt{\left(d\tau dV\left(Volt^{\langle 0 \rangle}, R^{\langle 0 \rangle}, k_\tau\right) \cdot U_V\right)^2 ... + \left(d\tau dR\left(Volt^{\langle 0 \rangle}, R^{\langle 0 \rangle}, k_\tau\right) \cdot U_R\right)^2 ... + \left(d\tau dk_\tau\left(Volt^{\langle 0 \rangle}, R^{\langle 0 \rangle}, k_\tau\right) \cdot U_{k.\tau}\right)^2}}}{\tau^{\langle 0 \rangle}}$$

Medium Rotor Uncertainty Analysis

$$U(\rho, Pdyn) := \sqrt{\frac{Pdyn}{\frac{1}{2}\rho}}$$

$i := 0$

$\rho := \rho_M$

$Pdyn := Pdyn_M$

$U := U\left(\rho, Pdyn^{\langle 0 \rangle}\right)$

$R := \left(Med^{\langle 0 \rangle}\right)_i \cdot ohm$

$Volt := \left(Med^{\langle 1 \rangle}\right)_i \cdot V$

$\tau := \left(Med^{\langle 4 \rangle}\right)_i mNm$

$\Omega := \left(Med^{\langle 2 \rangle}\right)_i \cdot rpm$

$TSR := \left(Med^{\langle 3 \rangle}\right)_i$

$CP := \left(Med^{\langle 5 \rangle}\right)_i$

Velocity

$U_{Pdyn} := U_{tot}\left(n, Pdyn^{\langle 1 \rangle}, Pdyn_f\right)$

$U_\rho := U_{tot}\left(100, 0, \rho_f\right) = 0.02 \frac{kg}{m^3}$

$$U_U := \frac{\sqrt{\left(dUdPdyn\left(\rho, Pdyn^{\langle 0 \rangle}\right) \cdot U_{Pdyn}\right)^2 + \left(dUd\rho\left(\rho, Pdyn^{\langle 0 \rangle}\right) \cdot U_\rho\right)^2}}{U}$$

Torque

$U_R := R_f \cdot R^{\langle 0 \rangle}$

$U_V := U_{tot}\left(n, Volt^{\langle 1 \rangle}, V_f\right)$

$U_{k.\tau} := k_{\tau.f}$

$$U_\tau := \frac{\sqrt{\left(d\tau dV\left(Volt^{\langle 0 \rangle}, R^{\langle 0 \rangle}, k_\tau\right) \cdot U_V\right)^2 + \left(d\tau dR\left(Volt^{\langle 0 \rangle}, R^{\langle 0 \rangle}, k_\tau\right) \cdot U_R\right)^2 + \left(d\tau dk_\tau\left(Volt^{\langle 0 \rangle}, R^{\langle 0 \rangle}, k_\tau\right) \cdot U_{k.\tau}\right)^2}}{\tau^{\langle 0 \rangle}}$$

Tip Speed Ratio

$$U_\Omega := U_{tot}\left(n, \Omega^{\langle 1\rangle}, \Omega_f\right)$$

$$U_{TSR} := \left[\frac{\sqrt{\left(dTSRd\Omega\left(\Omega^{\langle 0\rangle}, Rad, U_i\right)\cdot U_\Omega\right)^2 ... + \left(dTSRdU\left(\Omega^{\langle 0\rangle}, Rad, U_i\right)\cdot U_{U_i}\cdot U_i\right)^2}}{TSR^{\langle 0\rangle}}\right]$$

Coefficient of Power

$$U_{CP} := \frac{\sqrt{\left(dCPd\tau\left(\tau^{\langle 0\rangle}, \Omega^{\langle 0\rangle}, \rho_i, Rad, U_i\right)\cdot U_\tau\cdot\tau^{\langle 0\rangle}\right)^2 ... + \left(dCPd\Omega\left(\tau^{\langle 0\rangle}, \Omega^{\langle 0\rangle}, \rho_i, Rad, U_i\right)\cdot U_\Omega\right)^2 ... + \left(dCPd\rho\left(\tau^{\langle 0\rangle}, \Omega^{\langle 0\rangle}, \rho_i, Rad, U_i\right)\cdot U_\rho\right)^2 ... + \left(dCPdU\left(\tau^{\langle 0\rangle}, \Omega^{\langle 0\rangle}, \rho_i, Rad, U_i\right)\cdot U_{U_i}\cdot U_i\right)^2}}{CP^{\langle 0\rangle}}$$

$$U_{U_i} = 1.106\cdot\%$$

$$U_{TSR} = \begin{pmatrix} 1.388 \\ 1.43 \\ 1.395 \\ 1.394 \\ 1.425 \\ 1.421 \\ 1.404 \\ 1.467 \\ 1.674 \end{pmatrix}\cdot\%$$

$$U_{CP} = \begin{pmatrix} 4.047 \\ 4.05 \\ 4.047 \\ 4.047 \\ 4.058 \\ 4.049 \\ 4.049 \\ 4.056 \\ 4.094 \end{pmatrix}\cdot\%$$

$$\max\left(U_{TSR}\right) = 1.674\cdot\% \qquad \max\left(U_{CP}\right) = 4.094\cdot\%$$

$$\min\left(U_{TSR}\right) = 1.388\cdot\% \qquad \min\left(U_{CP}\right) = 4.047\cdot\%$$

$$\text{augment}\left(U_{U_i}, \min\left(U_{TSR}\right), \max\left(U_{TSR}\right), \min\left(U_{CP}\right), \max\left(U_{CP}\right)\right) = (1.106 \quad 1.388 \quad 1.674 \quad 4.047 \quad 4.094)\cdot\%$$

REFERENCES

[1] Institute for Energy Research, 2011, "North American Energy Inventory," Institute for Energy Research, Washington DC.

[2] Energy Information Administration, 2011, "Annual Energy Review 2010," DOE/EIA-0384, U.S. Department of Energy, Washington DC.

[3] BP Statistical Review of World Energy, June 2010.

[4] Fronk, B. M., Neal, R., Garimella, S., 2010, "Evolution of the Transition to a World Driven by Renewable Energy," ASME: Journal of Energy Resource Technology, Vol. 132, No.2, pp. 021009 1-7.

[5] Energy Information Administration, 2011, "International Energy Outlook 2011," DOE/EIA-0484, U.S. Department of Energy, Washington DC.

[6] Tonn, B., Healy, K. C., Gibson, A., Ashish, A., Cody, P., Beres, D., Lulla, S., Mazur, J., and Ritter, A. J., 2009, "Power from Perspective: Potential Future United States Energy Portfolios," Elsevier: Energy Policy, pp. 1432-1443.

[7] Goldstein, R., 2011, "Water Use for Electricity Generation and Other Sectors: Recent Changes (1985-2005) and Future Projections (2005-2030)," Electric Power Research Institute.

[8] Energy Information Administration, 2011, "Annual Energy Outlook 2011 with Projections to 2035," DOE/EIA-0383, U.S. Department of Energy, Washington DC.

[9] Wiser, R., Bolinger, M., 2011, "Wind Technologies Market Report," U.S. Department of Energy: Energy Efficiency and Renewable Energy, June 2011.

[10] Energy Information Administration, 2010, "Levelized Cost of New Generation Resources in the Annual Energy Outlook 2011," U.S. Department of Energy, Washington DC.

[11] Elliot, D. L., Holladay, C. G., Barchet, W. R., Foote, H. P., and Sandusky, W. F., 1986, "Wind Energy Resource Atlas of the United States," Solar Technical Information Program, DOE/CH 10093-4.

[12] Calvert, S., Thresher, R., Hock, S., Laxson, A., and Smith, B., 2002, "U.S. Department of Energy Wind Energy Research Program for Low Wind Speed Technology of the Future," ASME, J. of Solar Energy Engineering, Vol. 124, pp. 445-458.

[13] Williams, R., 2011, "Wind Energy: The Engineering, Economics and Benefits of Renewable Energy," Baylor University, Waco, Seminar, 31 January.

[14] 2009, "United States – Wind Resource Map," U.S. Department of Energy, National Renewable Energy Laboratory, Web, 23 November 2011, http://www.nrel.gov/gis/pdfs/windsmodel4pub1-1-9base200904enh.pdf.

[15] U.S. Census Bureau, 2011, "2010 Census: United States Profile," U.S. Census Bureau: Geography Division, New York.

[16] Department of Energy, 2008, "20% Wind Energy by 2030," DOE/GO-102008-2567, U.S. Deptartment of Energy, Oak Ridge.

[17] Womeldorf, C. A., 2012, "Design of an Extra-Tall Mast Above Blade-Tip Heights for Wind Resource Assessments Across Complex Terrain Regions," ASME: Journal of Solar Energy Engineering, Vol. 134, pp. 1-7.

[18] Sangpanich, U., Ault, G. A., and Low, K. L., 2009, "Economic Feasibility of Wind Farm Using Low Wind Speed Turbine," IEEE: Proceedings of the 44th International Universities Power Engineering Conference, pp. 1-5.

[19] "Wind Turbines – Wind Power," GE Power & Water, Web, 26 January 2012, http://www.ge-energy.com/products_and_services/products/wind_turbines/.

[20] GE Power & Water, 2011, "GE's 1.5-77 (Class I)," GE Power & Water: Renewable Energy, Web, 16 January 2012, http://www.ge-energy.com/content/multimedia/_files/downloads/GEA18768_Wind_1.5-77_Broch_r7.pdf.

[21] "Skystream | Southwest Windpower," Southwest Windpower, Web, 26 January 2012, http://www.windenergy.com/products/skystream.

[22] Sachse, A., 2009, "Excerpts from: Performance, Duration and Acoustic Test Reports for the Skystream 3.7 Wind Generator," WINDTEST Kaiser-Wilhelm-Koog, WT 7650/09.

[23] Flowers, L., 2011, "2010 U.S. Small Wind Turbine Market Report," American Wind Energy Association.

[24] Srikanth, N., and Funk, J. L., 2011, "Geometric Scaling and Long-Run Reductions in Cost: The Case of Wind Turbines," 2011 International Technology Management Conference, San Jose, CA, 27-30 June, pp. 691-696.

[25] Sorenson, J. N., 2011, "Aerodynamic Aspects of Wind Energy Conversion," Annual Review of Fluid Mechanics, Vol. 43, pp. 427-448.

[26] Manwell, J. F., McGowan, J. G., and Rogers, A. L., 2009, *Wind Energy Explained: Theory, Design, and Application*, Second Edition, John Wiley and Sons.

[27] Burton, T., Sharpe, D., Jenkins, N., and Bossanyi, Ervin, 2001, *Wind Energy Handbook*, John Wiley and Sons.

[28] Gipe, P., 1995, *Wind Energy Comes of Age*, Wiley, New York.

[29] Matthews, Clifford, 2002, *Aeronautical Engineer's Data Book*, Elsevier, Boston, pp. 99.

[30] Incropera, F. and DeWit, D., 2007, *Fundamentals of Heat and Mass Transfer*, Fifth Edition, John Wiley & Sons.

[31] Carmichael, B. H., 1982, "Low Reynolds Number Airfoil Survey, Volume 1," NASA Contractor Report 165803, Low Energy Transportation Systems Capistrano Beach, California.

[32] Santhanakrishnan, A. and Jacob, J. D., 2005, "Effect of Regular Surface Perturbation on Flow Over an Airfoil, 35th Fluid Dynamics Conference, Toronto, Canada, 6-9 June.

[33] Huber II, A. F. and Mueller, T. J., 1987, "The Effect of Trip Wire Roughness on the Performance of the Wortmann FX 63-137 Airfoil at Low Reynolds Numbers," Springer-Verlag, Experiments in Fluids, Vol. 5, pp. 263-272.

[34] Lyon, C., Selig, M., and Broeren, A., 1997, "Boundary layer Trips on Airfoils at Low Reynolds Numbers," 35th Aerospace Sciences Meeting & Exhibit, Reno, NV, 6-10 January.

[35] Giguere, P. and Selig, M. S., 1999, "Aerodynamic Effects of Leading-edge Tape on Aerofoils at Low Reynolds Numbers," Wind Energy, Vol. 2, pp. 125-136.

[36] Wieck, T. D., 1990, "Effect of Riblets on Flow Separation from a Cylinder and an Airfoil in Subsonic Flow," Thesis, Air Force Institute of Technology.

[37] Wheeler, G. O., 1991, "Low Drag Vortex Generators," Patent 5,058,837, 22 October.

[38] Schatz, M., Knacke, T., Thiele, F., Meye, R., Hage, W., and Bechert, D. W., 2004, "Separation Control by Self-Activated Movable Flaps," 42nd AIAA Aerospace Sciences Meting & Exhibit, Reno, NV, 5-8 January.

[39] Bons, J. P., Sondergaard, R., and Rivir, R. B., 2001, "Turbine Separation Control Using Pulsed Vortex Generator Jets," Transactions of the ASME, Vol. 123, pp. 198-206.

[40] Huang, J., Corke, T. C., and Thomas, F. O., 2006, "Unsteady Plasma Actuators for Separation Control of Low-Pressure Turbine Blades," AIAA Journal, Vol. 44, No. 7, pp. 1477-1487.

[41] Seifert, A., Eliahu, S., Greenblatt, D., and Wygnanski, I., 1998, "Use of Piezoelectric Actuators for Airfoil Separation Control," AIAA Journal, Vol. 36, No. 8, pp. 1535-1537.

[42] Zaman, K., Bar-Seve, A., and Mangalam, S. M., 1987, "Effect of Acoustic Excitation on the Flow Over a Low-Re Airfoil," Cambridge University Press, Journal of Fluid Mechanics, Vol. 182, pp. 127-148.

[43] Menter, F. R., Langtry, R. B., Likki, S. R., Suzen, Y. B., Huang, P. G., Volker, S., 2006, "A Correlation-Based Transition Model Using Local Variables Part I: Model Formulation," ASME: Journal of Turbomachinery, Vol. 128, pp. 413-422.

[44] Munson B. R., Young, D. F., and Okiishi, T. H., 2006, *Fundamentals of Fluid Mechanics*, Fifth Edition, John Wiley & Sons.

[45] Gregg, J. R., Burdett, T. A., Van Treuren, K. W., and McClain, S. T., 2011, "Design Considerations, Performance Enhancing Techniques, and Wind Tunnel Testing for Small-Scale, Low Reynolds Number Wind Turbines," Proceedings of the ASME International Mechanical Engineering Congress and Exposition, Denver, Colorado, 11-17 November.

[46] Gross, A. and Fasel, H. F., 2011, "Flow Control for Wind Turbine Airfoil," Proceedings of the ASME 2011 5th International Conference on Energy Sustainability, Washington D.C., 7-10 August.

[47] Lissaman, P. B. S., 1983, "Low-Reynolds-Number Airfoils," Annual Review of Fluid Mechanics, Vol.15, pp. 223-239.

[48] Somers, Dan M., 2005, "The S822 and S823 Airfoils," NREL/SR-500-36333, National Renewable Energy Laboratory.

[49] Selig, M. S. and Guglielmo, J. J., 1997, "High-Lift Low Reynolds Number Airfoil Design," Journal of Aircraft, Vol. 34, No. 1, pp. 72-79.

[50] Fujino, M., Yoshizaki, Y., and Kawamura, Y., 2003, "Natural-Laminar-Flow Airfoil Development for a Lightweight Business Jet," Journal of Aircraft, Vol. 40, No. 4, pp. 609-615.

[51] Eppler, R., 2000, "Eppler Airfoil Design and Analysis Code," Airfoils Incorporated.

[52] McGhee, R. J. and Millard, B. F., 1988, "Experimental Results for the Eppler 387 Airfoil at Low Reynolds Numbers in the Langley Low-Turbulence Pressure Tunnel," NASA Technical Memorandum 4062.

[53] Tangler, J. L. and Somers, D. M., 1995, "NREL Airfoil Families for HAWTs," NREL/TP-442-7109, National Renewable Energy Laboratory.

[54] Drela, M., and Giles, M. B., 1987, "Viscous-Inviscid Analysis of Transonic and Low Reynolds Number Airfoils," AIAA Journal, Vol 2, No. 10, pp. 1347-1355.

[55] Drela, M., 1986, "Two-Dimensional Transonic Aerodynamic Design and Analysis Using the Euler Equations," Ph.D. Dissertation, Dept. of Aeronautics and Astronautics, Massachusetts Institute of Technology, Cambridge, MA.

[56] McGranahan, B. D. and Selig, M. S., 2003 "Surface Oil Flow Measurements on Several Airfoils at Low Reynolds Numbers," *21st AIAA Applied Aerodynamics Conference*, AIAA 2003-4067, Orlando, FL.

[57] Lyon, C. A., Broeren, A. P., Giguere, P., Gopalarathnam, A., and Selig, M. S., 1997, *Summary of Low-Speed Airfoil Data*, Vol. 3, SoarTech Publications, Virginia Beach, VA.

[58] Maughmer, M. D. and Coder, J. D., 2010, "Comparisons of Theoretical Methods for Predicting Airfoil Aerodynamic Characteristics," RDECOM TR 10-D-106.

[59] Barlow, J. B., Rae Jr., W. H., and Pope, A., 1999, *Low-Speed Wind Tunnel Testing*, Third Edition, John Wiley and Sons, Inc., New York.

[60] Spera, D. A., 2009, *Wind Turbine Technology*, New York: ASME.

[61] Somers, D. M., 1997, "Design and Experimental Results for the S809 Airfoil," NREL/SR-440-6918, National Renewable Energy Laboratory.

[62] Burdett, T., Gregg, J., and Van Treuren, K., 2011, "An Examination of the Effect of Reynolds Number on Airfoil Performance," Proceedings of ASME 2011 5th International Conference on Energy Sustainability, Washington DC, 7-10 August.

[63] Hand, M. M., Simms, D. A., Fingersh, L. J., Jager, D. W., Cotrell, J. R., Schreck, S., and Larwood, S. M., 2001, "Unsteady Aerodynamics Experiment Phase VI: Wind Tunnel Test Configurations and Available Data Campaigns," NREL/TP-500-29955, National Renewable Energy Laboratory.

[64] Anderson, M. B., Milborrow, D. J., and Ross, J. N., 1982, "Performanace and Wake Measurements on a 5 m Diameter Horizontal Axis Wind Turbine. Comparison of Theory, Wind Tunnel and Field Test Data," 4th International Symposium on Wind Energy Systems, September 21-24, Stockholm, Sweden.

[65] Simms, D., Schreck, S., Hand, M., and Fingersch, L. J., 2001, "NREL Unsteady Aerodynamics Experiment in the NASA-Ames Wind Tunnel: A Comparison of Predictions to Measurements," NREL/TP-5029494, National Renewable Energy Laboratory.

[66] Zhang, C. and Hu, J., 2010, "The UAE Wind Turbine Performance Prediction Using Wind Tunnel Airfoil Data," World Non-Grid-Connected Wind Power and Energy Conference, Nanjing, China, November 5-7.

[67] Martinez, J., Bernabini, L., Probst, O., and Rodriquez, C., 2005, "An Improved BEM Model for the Power Curve Prediction of Stall-Regulated Wind Turbines," Wind Energy, Vol. 8, pp. 385-802.

[68] Snel, H., Schepers, J. G., and Montgomerie, B., 2007, "The MEXICO Project (Model Experiments in Controlled Conditions): The Database and First Results of Data Processing and Interpretation," Journal of Physics, Conference Series, Vol. 75.

[69] Snel, H., Schepers, J. G., and Siccama, N. B., 2009, "Mexico Project: The Database and Results of Data Processing and Interpretation," 47th AIAA Aerospace Sciences Meeting, Orlando, Florida, 5-8 January.

[70] Tangler, J. L., 2002, "The Nebulous Art of Using Wind Tunnel Aerofoil Data for Predicting Rotor Performance," Wind Energy, Vol. 5, pp. 245-257.

[71] Selig, M. S., Guglielmo, J. J., Broeren, A. P., and Giguère, P., 1995, *Summary of Low-Speed Airfoil Data*, Vol. 1, SoarTech Publications, Virginia Beach, VA.

[72] Selig, M.S., Lyon, C. A., Giguère, P., Ninham, C.N., and Guglielmo, J.J., 1996, *Summary of Low-Speed Airfoil Data*, Vol. 2, SoarTech Publications, Virginia Beach, VA.

[73] Viterna, L. A., and Corrigan, R. D., 1981, "Fixed Pitch Rotor Performance of Large Horizontal Axis Wind Turbines," Presented at DOE/NASA Workshop on Large HAWTs, Cleveland, Ohio.

[74] Tangler, J. L., 2004, "Insight into Wind Turbine Stall and Post-Stall Aerodynamics," Wind Energy, Vol. 7, pp. 247-260.

[75] Tangler, J., and Kocurek, J. D., 2004 "Wind Turbine Post-Stall Airfoil Performance Characteristics for Blade-Element Momentum Methods," NREL/CP-500-36900, National Renewable Energy Laboratory.

[76] Betz, A., 1919, "Schraubenpropeller mit geringstem Energieverlust," Diss. Gottingen Nachrichten, Gottingen.

[77] Glauert, H., 1935, "Airplane Propellers: In Aerodynamic Theory," ed. W. F. Durand, IV, Division L, New York: Springer, pp. 191-269.

[78] Sant, T., 2007, "Improving BEM-based Aerodynamic Models in Wind Turbine Design Codes," PhD. Thesis, Delft University.

[79] Ronsten, G., 1992, "Static Pressure Measurements in a Rotating and non-Rotating 2.375 m Wind Turbine Blade. Comparison with 2D Calculations," Journal of Wind Engineering and Industrial Aerodynamics, Vol 39, No. 1-3, pp. 105-118.

[80] Snel, H., Houwindk, R., Bosschers, R., Piers, W. J., Van Bussel, G. J. W., and Bruining, A., 1993, "Sectional Prediction of 3-D Effects for Stalled Flow on Rotating Blades and Comparison with Measurements," Proceedings of the European Community Wind Energy Conference, Germany, 8-12 March.

[81] Snel, H., Houwink, R.,and Bosschers, J., 1994, "Sectional Prediction of Lift Coefficients on Rotating Wind Turbine Blades in Stall," ECN-C-9052.

[82] Hansen, A. C. and Butterfield, C. P., 1993, "Aerodynamics of Horizontal-Axis Wind Turbines," Annual Review of Fluid Mechanics, Vol. 25, pp. 115-49.

[83] Du, Z. and Selig, M. S., 2000, "The Effect of Rotation on the Boundary Layer of a Wind Turbine Blade," Elsevier: Renewable Energy, Vol. 20, pp. 167-181.

[84] Eggers Jr., A. J., Chaney, K., and Digumarthi, R., 2003, "An Assessment of Approximate Modeling of Aerodynamic Loads on the UAE Rotor," AIAA Journal, pp. 283-292.

[85] Du, Z. and Selig, S., 1998, "A 3-D Stall-Delay Model for Horizontal Axis Wind Turbine Performance Prediction," 36th Aerospace Sciences and Meeting Exhibit and 1998 ASME Wind Energy Symposium, Reno, Nevada, 12-15 January.

[86] Bak, C., Johansen, J. and Andersen, P. B., 2006, "Three-Dimensional Corrections of Airfoil Characteristics Based on Pressure Distributions," European Wind Energy Conference and Exhibition, Athens, Greece, 27 February - 2 March.

[87] Tangler, J. L., and Selig, M. S., 1997, "An Evaluation of an Empirical Model for Stall Delay Due to Rotation for HAWTS," Windpower 1997 Conference, Austin, Texas, 15-18 June.

[88] Glauert, H., 1926, "The Analysis of Experimental Results in the Windmill Brake and Vortex Ring States of an Airscrew," Report 1026, Aeronautical Research Committee Reports and Memoranda, London: Her Majesty's Stationery Office.

[89] Buhl, Jr., M. L., 2005, "A New Empirical Relationship between Thrust Coefficient and Induction Factor for the Turbulent Windmill State," NREL/TP-500-36834, National Renewable Energy Laboratory.

[90] Moriarty, P. J. and Hansen, A. C., 2005, "Aerodyn Theory Manual," NREL/TP-500-36811, National Renewable Energy Laboratory.

[91] Hansen, M. O. L., 2008, *Aerodynamics of Wind Turbines*, Second Edition, Martin O. L. Hansen, Sterling.

[92] De Bellis, F. and Catalano, L. A., 2011, "Single and Multi Objective CFD Optimization of Horizontal Axis Wind Turbines," Proceedings of the ASME Turbo Expo 2011, Vancouver, British Columbia, Canada, 6-10 June.

[93] Tangler, J. L. and Somers, D. M., 1995, "Root Region Airfoil for Wind Turbine," Midwest Research Institute, Assignee, Patent 5,417,548, 23 May.

[94] Tangler, J. L. and Somers, D. M., 1996, "Airfoils for Wind Turbine," Midwest Research Institute, Assignee, Patent 5,562,420, 8 October.

[95] Tangler, J. L. and Somers, D. M., 2009, "Quiet Airfoils for Small and Large Wind Turbines," Midwest Research Institute, Assignee, Patent US 20090123289Al, 14 May.

[96] Giguere, P. and Selig, M. S., 1998, "New Airfoils for Small Horizontal Axis Wind Turbines," Transactions of the ASME, Vol. 120, pp. 108-114.

[97] Fuglsang, P. and Bak, C., 2004, "Development of the Riso Wind Turbine Airfoils," Wind Energy, Vol. 7, pp. 145-162.

[98] Giguere, P. and Selig, M. S., 1997, "Low Reynolds Number Airfoils for Small Horizontal Axis Wind Turbines," Wind Engineering, Vol. 21, No. 6, pp. 367-380.

[99] Selig, M. S. and McGranahan, B. D., 2004, "Wind Tunnel Aerodynamic Tests of Six Airfoils for Use on Small Wind Turbines," NREL/SR-500-34515, National Renewable Energy Laboratory.

[100] Somers, Dan M., 2005, "The S833, S834, and S835 Airfoils," NREL/SR-500-36340, National Renewable Energy Laboratory.

[101] Ceyhan, O., Sezer-uzol, N., Tuncer, I. H., 2009, "Optimization of Horizontal Axis Wind Turbines by Using BEM Theory and Genetic Algorithm," Ankara International Aerospace Conference, 17-19 August.

[102] Clifton-Smith, M. J. and Wood, D. H., 2007, "Further Dual Purpose Evolutionary Optimization of Small Wind Turbine Blades," Journal of Physics: Conference Series, Vol. 75, pp. 1-9.

[103] Mendez, J. and Greiner, D., 2006, "Wind Blade Chord and Twist Angle Optimization Using Genetic Algorithms," Proceedings of the 5th International Conference on Engineering Computational Technology, Las Palmas de Gran Canaria, Spain, 12-15 September.

[104] Dossing, M., Madsen, H A., and Bak, C., 2011, "Aerodynamic Optimization of Wind Turbine Rotors Using a BEM Method with Corrections for Wake Rotation and Expansion," Wind Energy, doi: 10.1002/we.487, pp. 1-10.

[105] Xuan, H., Weimin, Z., Xiao, L., and Jieping, L., 2008, "Aerodynamic and Aeroacoustic Optimization of Wind Turbine Blade by a Genetic Algorithm," 46th AIAA Aerospace Sciences Meeting and Exhibit, Reno, NV, 7-10 January.

[106] Xudong, W., Shen, W. Z., Zhu, W. J., Sorenson, J. N., and Jin, C., 2009, "Shape Optimization of Wind Turbine Blades," Wind Energy Vol. 12, pp. 781-803.

[107] Benini, E. and Toffolo, A., 2002, "Optimal Design of Horizontal-Axis Wind Turbines Using Blade-Element Theory and Evolutionary Computation," ASME Journal of Solar Energy Engineering Vol. 124, pp. 357-363.

[108] Eke, G. B. and Onyewudiala, J. I., 2010, "Optimization of Wind Turbine Blades Using Genetic Algorithm," Global Journal of Researches in Engineering, Vol. 10, No. 7, pp. 22-26.

[109] Raju, B., 2011 "Design Optimization of a Wind Turbine Blade," Thesis, University of Texas Arlington.

[110] Selig, M. S., Deters R. W., and Williamson, G. A., 2011, "Wind Tunnel Testing Airfoils at Low Reynolds Numbers," 49th AIAA Aerospace Sciences Meeting, Orlando, FL, 4-7 January.

[111] Miley, S. J., 1982, "A Catalog of Low Reynolds Number Airfoil Data for Wind Turbine Applications," DE-AC04-76DP03533.

[112] Selig, M. S. and McGranahan, B. D., 2004, "Wind Tunnel Aerodynamic Tests of Six Airfoils for Use on Small Wind Turbines," Journal of Solar Energy Engineering, Vol. 126, pp. 986-1001.

[113] Bahaj, A. S., Molland, A. F., Chaplin J. R., and Batten, W. M. J., 2007, "Power and Thrust Measurements of Marine Current Turbines under Various Hydrodynamic Flow Conditions in a Cavitation Tunnel and a Towing Tank," Elsevier: Renewable Energy, Vol. 32, pp. 407-426.

[114] Chen, T. Y. and Liou, L. R., 2011, "Blockage Corrections in Wind Tunnel Tests of Small Horizontal-Axis Wind Turbines," Elsevier: Experimental Thermal and Fluid Science, Vol. 35, pp. 365-569.

[115] Cho, T., Chealwan K., and Duckjoo, L., 2010, "Acoustic Measurements for 12% Scaled Model of NREL Phase VI Wind Turbine by Using Beamforming," Elsevier: Current Applied Physics, Vol. 10, pp. 320-325.

[116] Jackson, K. L., 1994, "Scaling Wind Turbine Fatigue Design Loads," Wind Energy, Vol. 15, pp. 189-196.

[117] Hulskamp, A. W., Van Wingerden, J. W., Barlas, T., Champliaud, H., Van Kuik, G. A. M., Bersee, H. E. N., and Verhaegen, M., 2010, "Design of a Scaled Wind Turbine with a Smart Rotor for Dynamic Load Control Experiments," Journal of Wind Energy, Vol. 14, No. 3, pp. 339-354.

[118] Gao, X. and Hu, J., 2009, "Numerical Research of Reynolds Number Impact on Scale Model of Wind Turbine," IEEE World Non-Grid-Connected Wind Power and Energy Conference, Nanjing, China, pp. 1-4.

[119] Burdett, T. A., Van Treuren, K. W., 2012, "Scaling for Small-Scale Wind Tunnel Testing," Proceedings of ASME Turbo Expo 2012, Copenhagen, Denmark, 11-15 June.

[120] Burdett, T. A., Van Treuren, K. W., 2012, "A Theoretical and Experimental Comparison of Optimized BET and BEMT Blade Designs," Proceedings of ASME Turbo Expo 2012, Copenhagen, Denmark, 11-15 June.

[121] Wainauski, H. S., 1979, "Wind Tunnel Tests of a 1/30 Scale Model of a 3.5 Megawatt Wind Turbine," Proceedings of the 14th Intersociety Energy Conversion Engineering Conference, Boston, Massachusetts, 5-10 August.

[122] Petersen, H., 1984, "The Scaling Laws Applied to Wind Turbine Design," Wind Engineering, Vol. 8. No. 2, pp. 99-108.

[123] "Wind Roses," Texas Commission on Environmental Quality, 4 January 2012, Web, 26 January 2012 http://www.tceq.texas.gov/airquality/monops/windroses.html.

[124] Cohen, A. C., 1965, "Maximum Likelihood Estimation in the Weibull Distribution Based on Complete and on Censored Samples," Journal of Technometrics, Vol. 7, No. 4, pp. 579-588.

[125] Prasad, R. D., Bansal, R. C, and Sauturaga, M., 2009, "Some of the Design and Methodology Considerations in Wind Resource Assessment," IET Renewable Power Generation, Vol. 3, No. 1, pp. 53-64.

[126] Ozgur, M. A. and Kose, R., 2006, "Assessment of the Wind Energy Potential of Kutahya, Turkey," Energy Exploration and Exploitation, Vol. 24, No. 4-5, pp. 331-348.

[127] Kalogirou, S., Neocleous, C., Paschiardis, S. and Schizas, C., 1999, "Wind Speed Prediction Using Artificial Neural Networks," Proceedings of the European Symposium on Intelligent Techniques ESIT'99, Crete, Greece.

[128] Kline, J. and Milligan, M., 1998, "An Evaluation of Hourly Average Wind-Speed Estimation Techniques," Windpower '98, Bakersfield, CA.

[129] Celik, A. N., 2003, "A Statistical Analysis of Wind Power Density Based on the Weibull and Rayleigh Models at the Southern Region of Turkey," Elsevier: Renewable Energy, Vol. 29, pp. 593-604.

[130] "NRG Systems – NRG #40C Anemometer," NRG Systems, Web, 26 January 2012, http://www.nrgsystems.com/sitecore/content/Products/1900.aspx.

[131] "NRG Systems – NRG #200P Wind Direction Vane," NRG Systems, Web, 26 January 2012, http://www.nrgsystems.com/sitecore/content/Products/1904.aspx.

[132] "NRG Systems – NRG SymphoniePlus®3 Logger," NRG Systems, Web, 26 January 2012, http://www.nrgsystems.com/sitecore/content/Products/5504.aspx.

[133] The International Association for the Properties of Water and Steam, 2007, "Revised Release on the IAPWS Industrial Formulation 1997 for the Thermodynamic Properties of Water and Steam," http://www.iapws.org/

[134] Sutherland, W., 1893, "The Viscosity of Gases and Molecular Force," Philosophical Magazine, Series 5, Vol. 36, No. 223, pp. 507-531.

[135] Wilke, C. R., (1950), "A Viscosity Equation for Gas Mixtures," Journal of Chemical Physics, Vol. 18, No. 4, pp. 517-519.

[136] 2003, "24" Wind Tunnel Instrumentation and Model Set: Installation, Operation and Maintenance Instructions," Engineering Laboratory Design, Inc., Lake City, Minnesota.

[137] Kline, S.J. and McClintock, F.A., 1953, "Describing Uncertainties in Single Sample Experiments," Mechanical Engineering, Vol. 75, pp. 3-8.

[138] Gregg, J. R., Merchant, J. S, and Van Treuren, K. W., "Experimental Analysis of a Counter-Rotating Wind Turbine," ASME International Mechanical Engineering Congress and Exposition 2009 Conference, Lake Buena Vista, FL. 13-19 November.

[139] Burdett, T. A., Gregg, J. R., Van Treuren, K. W., 2012, "A Numerical Study on Improving Airfoil Performance at Low Reynolds Numbers for Small-Scale Wind Turbines Using Intentional Roughness," Proceedings of 50th AIAA Aerospace Sciences Meeting, Nashville, January 9-12.

[140] "A Personal Wind Turbine for $500: The Air-X," TreeHugger, http://www.treehugger.com/renewable-energy/a-personal-wind-turbine-for-500-the-air-x.html.

[141] van Dam, J., Meadors, M., Link, H., and Migliore, P., 2003, "Power Performance Test Report for the Southwest Windpower Air-X Wind Turbine," NREL/TP-500-34756, National Renewable Energy Laboratory.

[142] Summerville, B., 2005, "Small Wind Turbine Performance in Western North Carolina," Appalachian State University.